VILNIUS UNIVERSITY
CENTER FOR PHYSICAL SCIENCES AND TECHNOLOGY

Paulius
BARONAS

Exciton dynamics in bifluorene crystals for laser applications

DOCTORAL DISSERTATION

Natural Sciences,
Physics N 002

VILNIUS 2020

This dissertation was written between 2015 and 2019 at the Institute of Photonics and Nanotechnology, Vilnius University.
The research was supported by the Research Council of Lithuania: scholarships for academical accomplishments (DOK-16364 and P-DAP-18-391), funding from joint Lithuania-Japan research project (No. LJB-3/2015) and the European Social Fund project SMART (No. 09.3.3-LMT-K-718-01-0026).

Academic supervisor:

Prof. Habil. Dr. Saulius Juršėnas (Vilnius University, Natural sciences, Physics – N 002).

Dissertation Defense Panel:
Chairman – **Prof. Habil. Dr. Gintaras Valušis** (Center for Physical Sciences and Technology, Natural sciences, Physics – N 002).
Members:
Dr. Andrius Devižis (Center for Physical Sciences and Technology, Natural sciences, Physics – N 002),
Research Prof. Dr. Johannes Gierschner (IMDEA Nanociencia, Natural sciences, Chemistry – N 003),
Prof. Dr. Edvinas Orentas (Vilnius University, Natural sciences, Chemistry – N 003),
Prof. Dr. Mikas Vengris (Vilnius University, Natural sciences, Physics - N 002).

The dissertation shall be defended at a public meeting of the Dissertation Defense Panel at 2 pm on April 24th, 2020, in the A101 auditorium of the Center for Physical Sciences and Technology. Address: Saulėtekio av. 3, LT-10257, Vilnius, Lithuania, tel. +37052648884; e-mail: office@ftmc.lt.

The text of this dissertation can be accessed at the libraries of Vilnius University and the Center for Physical Sciences and Technology, as well as on the website of Vilnius University: www.vu.lt/lt/naujienos/ivykiu-kalendorius.

VILNIAUS UNIVERSITETAS
FIZINIŲ IR TECHNOLOGIJOS MOKSLŲ CENTRAS

Paulius
BARONAS

Eksitonų dinamika bifluoreno kristaluose skirtuose lazerių taikymams

DAKTARO DISERTACIJA

Gamtos mokslai,
Fizika N002

VILNIUS 2020

Disertacija rengta 2015 – 2019 metais Vilniaus universiteto Fotonikos ir nanotechnologijų institute.
Mokslinius tyrimus rėmė Lietuvos mokslo taryba: stipendijos už akademinius pasiekimus (DOK-16364 ir P-DAP-18-391), jungtinis Lietuvos-Japonijos mokslo projektas (Nr. LJB-3/2015) ir ES SF projektas SMART (Nr. 09.3.3-LMT-K-718-01-0026).

Mokslinis vadovas:
Prof. habil. dr. Saulius Juršėnas (Vilniaus universitetas, gamtos mokslai, fizika – N 002).

Gynimo taryba:
Pirmininkas – **Prof. habil. dr. Gintaras Valušis** (Fizinių ir technologijos mokslų centras, gamtos mokslai, fizika – N 002).
Nariai:
Dr. Andrius Devižis (Fizinių ir technologijos mokslų centras, gamtos mokslai, fizika – N 002),
Prof. dr. Johannes Gierschner (IMDEA Nanociencia, gamtos mokslai, chemija – N 003),
Prof. dr. Edvinas Orentas (Vilniaus universitetas, gamtos mokslai, chemija – N 003),
Prof. dr. Mikas Vengris (Vilniaus universitetas, gamtos mokslai, fizika – N 002).

Disertacija ginama viešame Gynimo tarybos posėdyje 2020 m. balandžio mėn. 24 d. 14 val. Nacionalinio fizinių ir technologijos mokslų centro A101 auditorijoje. Adresas: Saulėtekio al. 3, LT-10257, Vilnius, Lietuva, tel. +37052648884; el. paštas office@ftmc.lt.

Disertaciją galima peržiūrėti Vilniaus universiteto ir Fizinių ir technologijos mokslų centro bibliotekose ir Vilniaus universiteto interneto svetainėje adresu: https://www.vu.lt/naujienos/ivykiu-kalendorius

Acknowledgements

I would like to thank my family, friends and colleagues without whose support this Thesis would have not been possible. First of all, I was really lucky to have prof. Saulius Juršėnas as my supervisor, who despite my average performance during my undergraduate years still convinced me to pursue a career in science. Thank you for all “crazy ideas” and extracurricular activities that made four years fly by. I believe I have learned so much in those years and our projects developed further than I thought was possible.

I also can‘t thank enough to all the people at the Institute of Photonics and Nanotechnology and Vilnius University. Dr. Gediminas Kreiza for ingeniously improvised solutions to problems that made this PhD project possible. Dr. Karolis Kazlauskas for lessons on discipline in scientific writing. Dr. Tomas Serevičius for bridging communication with Japan and daily news reports. Special thanks to Dr. Regimantas Komskis for crash courses on lab work and endless scientific discussions. Prof. Mikas Vengris and dr. Saulius Nargelas for technical tips on how to tame Harpia. Justina Jovaišaitė for all the fun at conferences. Dr. Steponas Raišys for setting high PhD standards for the upcoming generations and for all the technical support in the lab. Also, thanks to my students Tadas, Vladislavas, Džiugas and Eglė who constantly made me question my competence by exceeding expectations.

A special thanks goes to my ex-colleagues Paulius and Karolina for “science is cool” credo and all the laughs. Thanks to dr. Almantas Pivrikas for intense scientific discussions during a short, but memorable stay in Australia.

Thanks to people I met at Lund University for inspiration to continue on my scientific journey as a PhD and Helena for joining me on this crazy adventure. Thanks to my former supervisors Arkady and Tobias for proving that science can be fun. Thanks to Chris for preparing the ground for my future start-ups.

Thanks to teachers Vida, Onutė, Neringa and Aušra who laid a solid background for Lithuanian, English, math and most importantly physics.

A special thanks goes to friends Juozapas, Kazimieras, Ugnius, Petras, Lukas and Deividas for showing somewhat genuine interest in my work.

Last but definitely not least, I am most grateful to my soulmate Elena - for managing my emotional intelligence, my sister Kristina – for providing medical care, my mother Rasa - for spiritual support and father Arūnas - for encouragement to keep moving forward.

Contents

LIST OF ABBREVIATIONS

ASE	Amplified spontaneous emission
CW	Continuous-wave
CT	Charge transfer
DBR	Distributed Bragg reflectors
DFB	Distributed feedback
DSC	Differential scanning calorimetry
DT	Differential transmission
ESA	Excited state absorption
FRET	Förster resonant energy transfer
GSA	Ground state absorption
GSB	Ground state bleach
HOMO	Highest occupied molecular orbital
IC	Internal conversion
ISC	Intersystem crossing
LITG	Light induced transient grating
LUMO	Lowest unoccupied molecular orbital
OLED	Organic light emitting diode
OSLD	Organic semiconductor laser diode
PL	Photoluminescence
PVT	Physical vapor transport
QY	Quantum yield
SE	Stimulated emission
SPA	Singlet-polaron annihilation
SSA	Singlet-singlet annihilation
STA	Singlet-triplet annihilation
TA	Transient absorption
TADF	Thermally activated delayed fluorescence
TPA	Triplet-polaron annihilation
TRPL	Time-resolved photoluminescence
TTA	Triplet-triplet annihilation
XRD	X-ray diffraction

k_r	Radiative rate
k_{nr}	Non-radiative rate
τ	Lifetime
Φ_{PL}	Quantum yield
σ_{SE}	Stimulated emission cross section
N_{coh}	Coherence length
λ^2	Huang-Rhys (HR) factor
R_{PL}	Ratio of 0-0 and 0-1 PL peaks
R	Radius
κ^2	Orientation factor
J_F	Förster spectra overlap integral
ε	Extinction coefficient
d	Sample thickness
A	Absorbance
ΔA	Differential absorbance
μ	Absorption length
α	Absorption coefficient
Λ	Grating period
η	Diffraction efficiency
I_{th}^{ASE}	Amplified spontaneous emission threshold
g	Net gain
ΔN	Population inversion
L	Stripe length
t_{hop}	Hopping time

INTRODUCTION

The emergence of organic semiconductors promised a new generation of flexible, low-cost and bio-compatible electronics.[1,2] Organic materials combine the plastic-like mechanical and chemical properties, but behave like semiconductor, which allows to have a functionality of absorbing and emitting light or conducting electricity. However, unlike inorganic semiconductor technologies that require highly sophisticated manufacturing techniques, organic electronics offer low cost and large-scale processing methods such as printing from solution.[3] In the era of brittle crystalline inorganic semiconductors, they were deemed as soft disordered materials, that required new theories to describe phenomena rarely observed in inorganic crystals.[4] And while today organic materials are often used to replicate functionality of traditional semiconductors at a lower cost, in a near future these new materials may offer some unique technologies.

One of the remarkable features of organic materials is that they can function on the many levels of order and disorder. In principle, order of mostly carbon atoms in organic molecule determines all its chemical, photophysical and conductive properties contained within nanometer sized structure. For example, specific arrangement of atoms in conjugated molecules allows for strong interaction with photons, and that's what determines colors (and their perception) in naturally occurring chromophores. The disorder on the molecular level is dictated by relatively weak forces that hold atoms together allowing molecular structures to vibrate, disintegrate and form new compounds, which makes up a foundation for organic chemistry.[5] Another level of order and disorder can be observed when molecules are tightly packed to form a macroscopic entity performing specific function. Excitation of molecular solid with light creates a quasiparticle called an exciton, which is responsible for energy dynamics in natural photosynthetic systems as well as artificial electronic devices.[6,7] The way molecules are packed together can have dramatic effects on the photophysical properties, which is well utilized in optimizing processes in natural systems. For example, cable bacteria have been shown to have unprecedented conductivity comparable to best organic semiconductors.[8] However, even state-of-the-art technologies today have little control of how molecules are packed in a film, and thus technologies like OLEDs or solar cells are based on mostly disordered amorphous molecular films.

One of the ways how molecular electronics could benefit from highly ordered molecular systems is enhanced energy transport and electrical conductivity, which would lead to faster and more efficient device operation. This is extremely important for new generation of plastic transistors and with recent advances in production technologies integration of crystalline organic materials became available at almost no expense of production cost or device flexibility.[9] Furthermore, just in last few years new record efficiencies (over 16%) were achieved in fully organic solar cells, emphasizing the importance of fine-tuning the morphology, i.e. the ratio between disorder and order in molecular films.[10–13] Apart from that, after years of research phenomenon of exciton fission (unique to organic crystalline films) was utilized to boost efficiency of silicon solar cells from 29% to 35%, which could result in dramatic savings in energy generation.[14,15] OLEDs were also shown to benefit from increased order, where something as simple as control of emitter orientation has helped to achieve over 30% external quantum efficiency by improved outcoupling.[16] These are only few examples how higher order already leads to more efficient devices.

While most of electronic components have been reproduced using organic materials and are on the verge of changing electronics as we view it today, organic current-injected lasers are just at their infancy. Just last year multiple challenges related to strong excitation of organic materials were overcome to demonstrate first functioning organic laser prototypes.[17–19] It might be surprising, but ever since first demonstrations of laser action in the 1960s organic molecules were material of choice in optically-pumped dye lasers for their high gain coefficient, wide emission color tunability and temperature stability.[20] The later emergence of compact electrically-pumped inorganic diode lasers rendered inefficient and bulky organic dye lasers obsolete. However, inorganic laser technologies opened a $14-billion market for major applications in material processing, communication and medicine.[21] While the demand for lasers is high, their current production price and versatility limits their applications for consumer use. To put that in perspective, currently OLED display market alone surpassed lasers reaching $31-billion in 2019.[22] The projected OLED market growth signifies the importance of organic semiconductor materials in future consumer electronics and may as well be promising a breakthrough in organic laser technology.

Limitations set by fragile organic materials suggest that organic lasers will never offer intensities of coherent light comparable to inorganic semiconductor technologies, but they might open a market for emerging technologies. The ability to process organic materials into complex networks is already interesting for micro- and nano- lasers delivering coherent emission at nanoscale systems for applications in biology or computing.[23–25] Optically active organic lasers have already been tested for high resolution intracellular bio-imaging paving a way for implantable and wearable photonic healthcare devices.[26–28] Another unique market for organic lasers is quantum computing, where organic materials excel at producing another quasiparticle called polariton appearing due to strong interactions of excitons with light.[29] A team at the IBM Research Lab has just proven polariton lasers based on organic materials are a breakthrough technology for all-optical transistors.[29–31] Technologies like these promise a bright future for organic materials in laser applications when the precise nanoscale manufacturing techniques will catch up.

Sometimes it is easy to forget that carbon-based systems evolved into complex self-assembled molecular machinery such as photosynthetic system or body's DNA replication mechanism.[6,32] Todays efforts to produce organic electronic devices may appear brute compared to nature's delicate machinery. And while it took millions of years for such sophisticated and efficient machinery to develop, there are many things to learn on how relatively simple molecules can be used to build macro structures. Here, supramolecular chemistry holds a great promise for utilizing intermolecular interactions in completely new synthetic systems that incorporate functionality of electronic devices.[33] In a similar way, new evolutionary chemistry methods based on biological design principles (an idea that won a Nobel prize in 2018) may expand the organic synthesis toolbox for building complex nano-materials.[34] Whereas now tools for building bio-compatible nano-lasers are out of reach, the gap between biological systems and electronics may shrink in a near future making such disruptive technologies possible.

Aim and novelty

This dissertation is aimed at improving stimulated emission characteristics in organic fluorene-based single crystals and thereby demonstrating their potential for applications in organic lasers. Up to this day the best laser performance is achieved in amorphous organic gain medium, while strong intermolecular (excitonic) coupling in highly ordered crystalline phase leads to effects degrading laser performance. In this work it was important to show that excitonic coupling, and thus characteristics of gain material can be controlled via modifications of molecular and crystal structure. To achieve the objective the following tasks were formulated:

- To characterize photophysical properties in the range of differently substituted fluorene derivatives in dispersed, solid amorphous and crystalline environments.
- To evaluate effects of excitonic coupling on ASE properties in bifluorene crystals as a function of varying rigidity of molecular structures.
- To determine direction and rate of exciton transport in bifluorene crystals by various complementary techniques.
- To investigate the enhanced exciton transport enabling ultrafast exciton transfer dynamics in doped bifluorene crystals.
- To evaluate the effects of reduced SSA and reabsorption losses in doped crystals for improved ASE performance.

The thesis contains five chapters that are each based on papers I-V in the order of appearance. In the first chapter (based on Paper I) fluorene-based compounds are investigated in amorphous medium that allows to disregard excitonic coupling and evaluate intramolecular structure-properties relations for optimal lasing performance. In the second chapter (based on Paper II) molecular structure with strong vibrational coupling is tested for production of low loss crystals. Detailed spectroscopic analysis of intramolecular and intermolecular properties allowed to show that strong vibrational coupling can cancel out excitonic coupling in crystals resulting in monomer-like stimulated emission properties. Third chapter (based on Paper III) was initially aimed at showing the opposite behavior to the one presented in Chapter 2, where reduced vibrational coupling and enhanced excitonic coupling would cause degraded lasing characteristics, however serendipitous discovery of self-doping phenomenon instead led to significantly improved lasing characteristics of organic crystals. In depth investigation of self-doping revealed superior energy transport properties unique to bifluorene crystals. In the fourth chapter (based on Paper IV) analysis of exciton transport were performed to show an inverse relation of energy transfer rate to a strength of vibrational coupling. Weak vibrational coupling together with J-type excitonic coupling was found to result in highly anisotropic and partly coherent exciton motion. In the final chapter (based on Paper V) bifluorene crystals with superior energy transport properties were intentionally doped to control ultrafast host-dopant energy transfer rate aiming to optimize amplified spontaneous emission performance. It was demonstrated that doping at optimal concentration eliminated exciton annihilation and emission reabsorption losses, which allowed to improve ASE photostability and achieve extremely low threshold values that were comparable to the best performing organic laser crystals.

Key findings

A. Enhanced electron-vibronic coupling and conformational disorder of phenyl and biphenyl bridged bifluorene molecules reduces excitonic coupling strength in single crystals, hence improving ASE performance.
B. Self-doping of molecular crystals via acetylene-ethylene bond modification in bifluorenes is a promising cost-saving strategy to obtain highly emissive and low ASE threshold doped crystals.
C. Highly anisotropic singlet exciton transport with diffusion coefficients of up to 1 cm^2/s in bifluorene single crystals is enabled by J-type excitonic coupling. Reduced conformational disorder in crystals containing rigid acetylene and ethylene linked bifluorene derivatives leads to coherent enhancement of exciton transport as evidenced by inverse temperature dependence.
D. Long-range exciton transport in doped bifluorene crystals mediates ultrafast exciton transfer to highly emissive dopants allowing to significantly reduce reabsorption and exciton annihilation losses at optimal doping concentration, and thus improved ASE performance and photostability can be achieved.

LIST OF PUBLICATIONS

On the dissertation topic

I. **P. Baronas**, K. Kazlauskas, G. Kreiza, V. Jankauskas, A. Tomkevičienė, J. Simokaitienė, J. V. Grazulevicius, S. Juršėnas, “Differently linked fluorene-carbazole triads for light amplification”, *Dyes and Pigments*, 123, 370-379 (2015).

II. G. Kreiza, **P. Baronas**, E. Radiunas, P. Adomėnas, O. Adomėnienė, K. Kazlauskas, J. C. Ribierre, C. Adachi, S. Juršėnas, “Bifluorene single crystals with extremely low-threshold amplified spontaneous emission”, *Adv. Opt. Mater.* 5, 1600823 (2017).

III. **P. Baronas**, G. Kreiza, P. Adomėnas, O. Adomėnienė, K. Kazlauskas, C. Adachi and S. Juršėnas, “Low-Threshold Light Amplification in Bifluorene Single Crystals: Role of the Trap States”, *ACS Appl. Mater. Interfaces* 10, 2768-2775 (2018).

IV. **P. Baronas**, P. Ščajev, V. Čerkasovas, G. Kreiza, P. Adomėnas, O. Adomėnienė, K. Kazlauskas, J. C. Ribierre, C. Adachi and S. Juršėnas, “Exciton Diffusion in Bifluorene Single Crystals Studied by Light Induced Transient Grating Technique”, *Appl. Phys. Lett.* 112, 033302 (2018).

V. **P. Baronas**, G. Kreiza, M. Mamada, S. Maedera, P. Adomėnas, O. Adomėnienė, K. Kazlauskas, C. Adachi and S. Juršėnas, “Enhanced energy transfer in doped bifluorene single crystals: prospects for organic lasers”, *Adv. Opt. Mater.* 1901670 (2019).

Other publications

VI. **P. Baronas**, K. Kazlauskas, J. Simokaitienė, A. Gruodis, V. Jankauskas, A. Tomkevičienė, J. V. Grazulevicius, S. Juršėnas, “High-Triplet-Energy Carbazole and Fluorene Tetrads”, *Journal of Luminescence*, 169, 256-265 (2016).

VII. R. Komskis, **P. Baronas**, P. Adomėnas, O. Adomėnienė, T. Serevičius and S. Juršėnas, “Suppression of charge transfer states in aryl substituted 9,9’ – bianthryl derivatives”, *J. Phys. Chem. C* 121, 23618-23625 (2019).

VIII. T. Matulaitis, P. Imbrasas, N. A. Kukhta, **P. Baronas**, T. Bučiūnas, D. Banevičius, K. Kazlauskas, J. V. Gražulevičius, and S. Juršėnas, “Impact of Donor Substitution Pattern on the TADF Properties in the Carbazolyl-Substituted Triazine Derivatives”, *J. Phys. Chem. C* 121, 23618-23625 (2017).

IX. P. Ščajev, R. Aleksiejunas, **P. Baronas**, D. Litvinas, M. Kolenda, C. Qin, T. Fujihara, T. Matsushima, C. Adachi and S. Juršėnas, “Carrier Recombination and Diffusion in Wet-Cast Tin Iodide Perovskite Layers Under High Intensity Photoexcitation” *J. Phys. Chem. C,* 123, 19275 (2019).

X. P. Ščajev, C. Qin, R. Aleksiejunas, **P. Baronas**, S. Miasojedovas, T. Fujihara, T. Matsushima, C. Adachi and S. Juršėnas, “Diffusion Enhancement in Highly Excited MAPbI3 Perovskite Layers with Additives” *J. Phys. Chem. Lett.* 9, 3167 (2018).

XI. E. Gaubas, **P. Baronas**, T. Čeponis, L. Deveikis, D. Dobrovolskas, E. Kuokstis, J. Mickevičius, V. Rumbauskas, M. Bockowski, M. Iwinska, T. Sochacki, “Study of spectral and recombination characteristics of HVPE GaN grown on ammono substrates” *Mater. Sci. Semicond. Process.* 91, 341 (2019).

Popular science articles

I. P. Baronas "Optoelektronikos revoliucija veda organinio lazerio link", *Spectrum*, 27, p. 14-19 (2018).

Conference presentations

1. P. Baronas, G. Kreiza, P. Ščajev, P. Adomėnas, K. Kazlauskas, C. Adachi and S. Juršėnas, “Effects of vibrational coupling on energy transport in bifluorene single crystals”, Progress in Organic Optoelectronics and Energy Conversion (Malaga, Spain, 12-13 December 2019). **Poster presentation.**
2. P. Baronas, G. Kreiza, P. Ščajev, P. Adomėnas, K. Kazlauskas, C. Adachi and S. Juršėnas, “Doped bifluorene crystals for laser applications: The role of ultrafast energy transfer”, SPIE Organic Photonics + Electronics (San Diego, United States, 11-15 August 2019). **Poster presentation.**
3. P. Baronas, G. Kreiza, P. Ščajev, P. Adomėnas, K. Kazlauskas, C. Adachi and S. Juršėnas, “Enhanced exciton transport in bifluorene single crystals” 13th International Conference on Optical Probes of Organic and Hybrid Optoelectronic Materials and Applications (Vilnius, Lithuania 7-12 July 2019). **Oral presentation.**
4. P. Baronas, G. Kreiza, P. Adomėnas, K. Kazlauskas, M. Mamada, S. Maedera, C. Adachi and S. Juršėnas, “Doped bifluorene crystals for laser applications: the role of ultrafast energy transfer on triplet quenching” 14th International symposium on Functional pi-electron systems (Berlin, Germany, 2-7 June 2019). **Poster presentation.**
5. P. Baronas, G. Kreiza, K. Kazlauskas, P. Ščajev, P. Adomėnas, C. Adachi, S. Juršėnas, „Doped bifluorene crystals for laser applications: the role of ultrafast energy transfer“ Open Readings 2019, (Vilnius, Lithuania, 19-22 March, 2019). **Poster presentation.**
6. P. Baronas, G. Kreiza, P. Adomėnas, K. Kazlauskas, C. Adachi and S. Juršėnas, “Organic single crystals for laser applications” 7th EuCheMS Chemistry Congress (Liverpool, England, 26-30 August 2018). **Poster presentation.**
7. P. Baronas, G. Kreiza, P. Scajev, P. Adomėnas, K. Kazlauskas, C. Adachi and S. Juršėnas, “Bifluorene single crystals for organic lasers” ICSM2018: International conference on science and technology of synthetic metals (Busan, Korea, 1-6 July 2018). **Oral presentation.**
8. P. Baronas, P. Scajev, V. Čerkasovas, G. Kreiza, P. Adomėnas, K. Kazlauskas, J.Ch. Ribierre, Ch. Adachi and S. Juršėnas, „Exciton diffusion in bifluorene single crystals“, 42th Lithuanian national physics conference, (Vilnius, Lithuania, October 4-6 2017). **Oral presentation.**

9. P. Baronas, P. Scajev, V. Čerkasovas, G. Kreiza, P. Adomėnas, K. Kazlauskas, J.Ch. Ribierre, Ch. Adachi and S. Juršėnas, “Exciton diffusion in bifluorene single crystals”, 14th European Conference on Molecular Electronics (29 August – 2 September, 2017, Dresden, Germany). **Poster presentation.**
10. P. Baronas, G. Kreiza, P. Ščajev, V. Čerkasovas, E. Radiūnas, P. Adomėnas, O. Adomėnienė, K. Kazlauskas, J.C. Ribierre, C. Adachi, S. Juršėnas, „Bifluorene Single Crystals For Organic Lasers“, 60th International Conference for Students of Physics and Natural Sciences - Open Readings 2017, (Vilnius, Lithuania, 14-17 March, 2017). **Oral presentation.**
11. P. Baronas, T. Matulaitis, T. Buciunas, J. V. Grazulevicius and S. Jursenas, “Highly Efficient TADF in Triazine-carbazole Derivatives”, Organic Semiconductors Conference 2016 (Cavtat, Croatia, 22-25 September, 2016). **Poster presentation.**
12. P. Baronas, T. Harlang, V. Sundström, S. Juršėnas, „Ultrafast Dynamics Of Photo Induced Electron Transfer In Iron Complex Based Solar Cells“, 59th International Conference for Students of Physics and Natural Sciences - Open Readings 2016 (Vilnius, Lithuania, 15-18 March, 2016). **Oral presentation.**

Participation in scientific projects

1. “Control of the photophysical properties of multifunctional molecular systems“, (Global Grant, The Research Council of Lithuania, 2012-2015).
2. “Flexible structure bearing bifluorene compounds for optoelectronics industry, BiFluorenas“, (EU structural funds, 2013-2015).
3. “Towards Organic Laser Transistor” (Joint Lithuania-Japan research project, The Research Council of Lithuania, 2015-2017).
4. “Enhancing light upconversion efficiency in organic films for optoelectronic applications” (The Research Council of Lithuania, 2017-2020).
5. “Triplet state engineering in organic optoelectronic compounds” (Global Grant, The Research Council of Lithuania, 2017-2022).
6. “Development of advanced optoelectronic materials using smart molecular engineering.” (EU structural funds, 2017-2022).

Author's contribution

The author carried out all ultrafast TA and TRPL and most of the steady-state spectroscopy measurements and performed data analysis. The author also significantly contributed to preparation of all manuscripts on the dissertation topic and actively participated in the discussions of other publications.

Synthesis of fluorene-based materials presented in the dissertation was carried out by the research groups lead by prof. Juozas V. Gražulevičius (Kaunas University of Technology) and dr. Povilas Adomėnas (Vilnius University). DSC measurements and analysis was performed by dr. Regimantas Komskis (Vilnius University). Crystal growth, XRD analysis and ASE measurements were performed by dr. Gediminas Kreiza (Vilnius University). Additional XRD analysis was performed by dr. Sandra Stanionytė (FTMC). Exciton diffusion measurements with LITG technique were carried out by Patrik Ščajev (Vilnius University). The author is very grateful for all contributions to this work.

1 ORGANIC CRYSTALS FOR LASER APPLICATIONS

Although to this day most of organic optoelectronic devices are based on thin films, in the past years organic crystals have drawn great research interest due to new processing techniques allowing to effortlessly produce highly crystalline films. Here, long-range molecular order of crystals makes them advantageous to be employed as a superior gain medium and charge conductor in laser devices. However, despite decades of research, some phenomena occurring in molecular aggregates are under debate.

In this chapter, current technological advances towards realizing current-injection organic lasing will be reviewed together with loss mechanisms. Later, history of organic solid-state laser materials will be revisited to point out key ingredients for molecular structures and crystal growth. Lastly, photophysical properties specific to ordered molecular aggregates will be discussed.

1.1 Organic solid-state lasers

The complexity of organic semiconductor laser diode (OSLD) problem is well reflected in the progress of organic light emitting devices (OLED) research. To this day OLED operation is still facing major challenges concerning efficiency roll-off at high current densities and long-term device stability, while organic lasers would require orders of magnitude higher excitation densities to achieve population inversion. The underlying causes of high excitation density effects in organic light emitting devices are unavoidable generation of optically dark states at electrical pumping and various bimolecular annihilation and absorption processes leading to emission quenching.[35]

Primary issue limiting the emission efficiency of organic semiconductor devices is the formation of non-emissive triplet states at electrical excitation.[36] The simplified scheme of charge-to-photon conversion in OLEDs is presented in Figure 1.1. Electrons and holes injected into organic material are first subjected to strong electron-vibronic coupling of organic molecules leading to polaron formation and low charge mobility.[4] Recombination of positive and negative polarons form an exciton, where spin statistics dictate that 75% of the generated excitons are triplets and rest 25% are singlets.[4,37] In addition, some of the emissive singlet excitons can spontaneously change into triplet state via intersystem-crossing (ISC) further increasing triplet yield. The spin-allowed nature of transition from singlet state resulting in photon emission (i.e. fluorescence) leads to several orders of magnitude higher radiative rate ($k_r(S) = 10^{-7}$-10^{-9} s^{-1}) compared to spin-forbidden triplet transition (i.e. phosphorescence) ($k_r(T) = 10^{-6}$-10^{0} s^{-1}). Due to direct competition between non-radiative internal conversion (IC) induced by strong electron-vibrational coupling, phosphorescence is rarely observed at room-temperature.[38] Therefore, intrinsic singlet-triplet ratio in organic semiconductors limits internal charge-to-photon conversion efficiency to 25% in first generation OLEDs employing only singlet emitters. To utilize the triplet excitations room-temperature phosphorescent materials containing rare-earth metals (e.g. iridium) were developed, which boosted the internal OLED efficiency to 100% enabling applications in state-of-the-art display technologies.[39] Research interest is now focused on developing 3rd generation of OLED technologies that are based on thermally activated delayed fluorescence (TADF) mechanism allowing to convert almost 100% of triplet excitations to emissive singlets via reverse ISC in materials containing no rare-earth metals.[36] Nevertheless, possibility of harnessing triplet excitations in organic lasers is still highly debated as phosphorescent and TADF emitters exhibit poor ASE properties owing to relatively low radiative rates compared to best singlet emitters.[40–42]

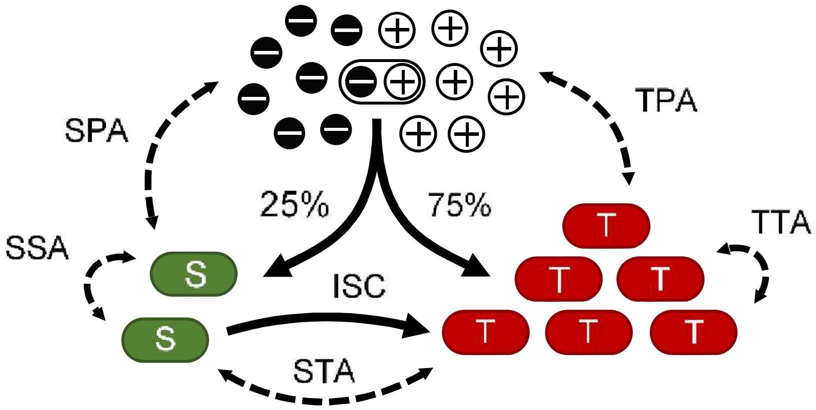

Figure 1.1. Schematic illustration of charge-to-exciton conversion and possible annihilation mechanisms leading to efficiency roll-off in organic devices.

Another major factor limiting OLED efficiency at high excitation densities is multitude of bimolecular annihilation processes presented in Figure 1.1. The annihilation events result in charges quenching excitons: singlet-polaron annihilation (SPA) and triplet-polaron annihilation (SPA); or excitons quenching other excitons: singlet-singlet annihilation (SSA), triplet-triplet annihilation (TTA) and singlet-triplet annihilation (STA). Most of these reactions occur through Förster energy transfer, where only TTA is mediated by Dexter transfer.[35] The only difference in Dexter reaction is that it requires direct charge transfer, where Förster reactions rely on dipole interactions. In the event of annihilation reaction, energy of the exciton is transferred to the higher excited state of the other exciton. Excess energy is either dissipated as heat due to efficient IC or leads to autoionization of a molecule. These were found to be primary causes of material degradation.[43,44] Furthermore, singlet or triplet excitations are lost in annihilation reactions.

The rate of these annihilation processes depends on population density, lifetime and diffusivity of the participating species.[35] Therefore, most probable are reactions including long-lived triplet states that show diffusion length exceeding several micrometers.[45] Consequently, OLEDs harnessing triplet energy via TADF or phosphorescent emitters suffer from stronger roll-off at high current densities due to TTA reactions. In contrast, fluorescence-based OLEDs can harness TTA reactions to produce delayed fluorescence boosting internal quantum efficiency from 25% to 62.5%.[46,47] This signifies the use of fluorescent emitters for OSLD applications not only for their generally lower ASE threshold, but also for lower roll-off at high current densities. However, even in fluorescence-based devices STA is a remaining source of losses and degradation. To suppress STA in organic lasers, numerous triplet quenching strategies (i.e. addition of low triplet level compounds such as 9,10-di(naphtha-2-yl)anthracene (ADN) or oxygen) have been successfully tested.[43,48,49]

Considering orders of magnitude higher excitation densities required to achieve population inversion in organic lasers compared to typical operation of OLED for display or lighting applications, roll-off becomes a major factor further increasing current density requirements (Figure 1.2). Currently, lowest lasing thresholds obtained by optical pumping of organic thin films are in the range of 100 W/cm^2.[23] However, it must be pointed out that electrical pumping will introduce additional losses (i.e. polaron annihilation or absorption at metal electrodes).[50] Therefore, even the best estimates of lasing threshold would still require driving OSLDs with electrical current densities of 1 kA/cm^2.

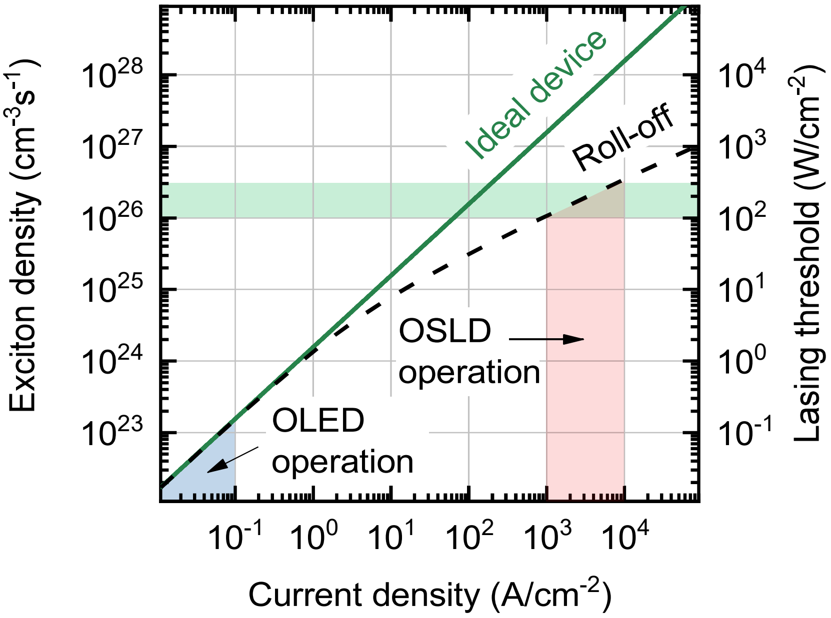

Figure 1.2. Exciton density as a function of current density in ideal and real (with roll-off) OLED devices. Lowest achieved lasing thresholds are indicated with green area.

High current densities are difficult to achieve in layered OLED architecture, where low charge mobility and large device area lead to substantial Joule heating and eventual degradation.[44] Fortunately, these problems can be mitigated in the light-emitting field-effect transistors (LEFET) based on organic crystals.[51–53] Unlike in typical layered sandwich structure of OLED, where charge recombination occurs within the area of the device, in LEFETs charges injected from opposing electrodes accumulate in the thin interface between active material and gate insulator (Figure 1.3). This results in thin recombination zone (~10 μm) within length of the LEFET device.[51,54] Furthermore, organic single crystals show high carrier mobilities (over 1 $cmV^{-1}s^{-1}$) as well as ambipolar charge transport, which eliminate the need for multiple charge transport and blocking layers to achieve charge balance.[55,56] High current densities (>1 kA/cm^2) have been achieved in crystal based LEFET devices.[57] Recently, first evidence of lasing in LEFET based on 5,5”-bis(biphenyl-4-yl)-2,2’:5’,2”-terthiophene single crystal with optical feedback (DFB) construction was demonstrated by Tanigaki’s group.[19] The lasing threshold current density of 1 kA cm^{-2} was observed for narrow emission line at 610 nm.

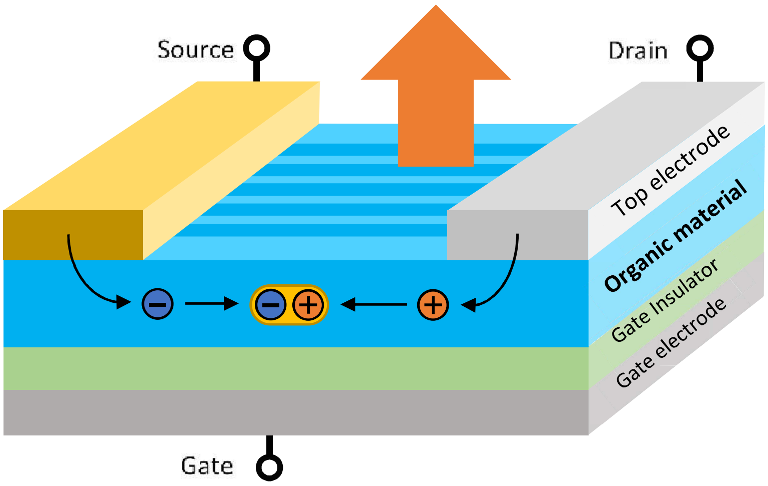

Figure 1.3. Scheme of light-emitting transistor.

1.2 Requirements for organic gain materials

The three principal components of any laser are an excitation source, an optical feedback structure and gain medium. Although electrical excitation is desirable, most of the organic lasers to this day are tested using external optical pumping sources. In terms of optical feedback, organic materials are attractive due to their compatibility with different resonator structures. Optical feedback can be provided by variety of methods: external planar cavities (e.g. metal mirrors or distributed Bragg reflectors (DBR)),[50,58] distributed feedback (DFB) structures (imprinted onto organic films[59–61] or crystals[62]) or simply by internal reflection of high refractive index organic crystals.[63,64] Quality factor of the optical feedback structures plays an important role in determining laser threshold in organic lasers devices. For example, microcrystals with highly defined smooth facets that act as Fabry-Perot cavities showed lasing thresholds down to hundreds of nJ/cm^2.[63,65,24,66,67] However, fundamental threshold limit is set by gain and absorption losses of the organic medium. In this case, amplified spontaneous emission (ASE) process, where spontaneously emitted photons are amplified by stimulated transitions in a single pass through excited gain medium, is often used to characterize gain properties of the material independently of the optical feedback.

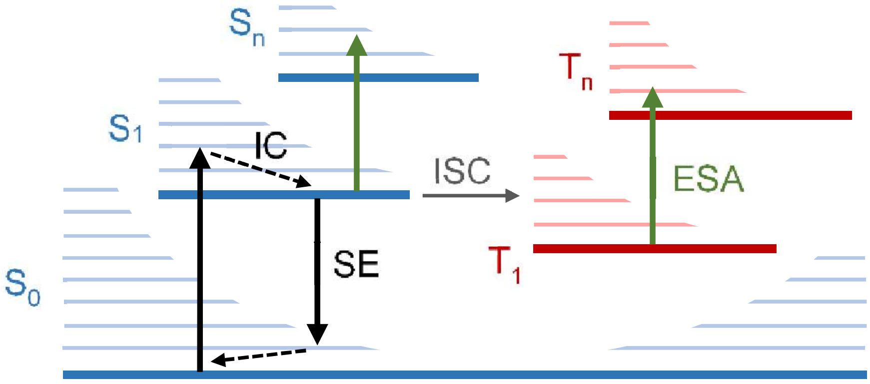

Figure 1.4. Schematic illustration of Jablonski diagram showing how an organic molecule can act as a four-level laser system. Singlet (S) or triplet (T) electronic levels have vibronic structure allowing for fast internal conversion (IC). Stimulated emission is most likely to occur from S_1 excited state bottom to the first vibrational level of the S_0 ground state. Excitation from S_1 can undergo intersystem crossing (ISC) to long-lived triplet states. At high excitation densities, singlet or triplet excited state absorption (ESA) becomes a possible loss channel.

The attractive feature of the organic materials to be used as gain medium is the predominantly efficient quasi four-level system functioning on a level of single molecule. As seen from Jablonski diagram in Figure 1.4, the optical excitation from singlet ground state (S_0) to higher vibrational level of singlet excited (S_1) results in ultrafast vibrational relaxation to the bottom of S_1 level occurring within sub-picosecond timescale. Stimulated emission from S_1 bottom occurs as a transition to the first or second vibrational levels of the ground state to avoid self-absorption and is determined by SE cross-section. Therefore, ASE bands usually correspond to 0-1 or 0-2 vibrational bands of the fluorescence spectrum. Stimulated transition is followed by another ultrafast relaxation to the bottom of the S_0 state. This signifies that conditions for population inversion in organic materials are controlled by the strength of vibrational coupling, which prevents buildup of excitations in vibrational levels of the ground state. It is obvious that superior lasing properties are recorded for molecules with lower torsional rigidity, for example coumarin or rhodamine commercial dyes used in dye lasers.[68] The main implication of the efficient four-level system in organic materials is that it allows to avoid emission reabsorption losses due to considerable Stokes shift (i.e. energy difference between ground state absorption and excited state emission spectra).

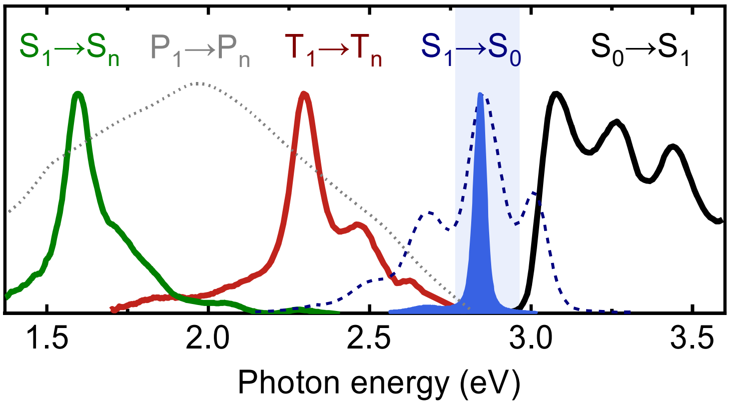

Figure 1.5. Typical ground and excited state absorption spectra (solid lines) plotted together with fluorescence spectra (dashed line). ASE occurring at the 0-1 vibronic band of the fluorescence spectra (colored area) has least overlap with absorption components. Energy window for absorption free emission is highlighted.

Other absorption loss mechanisms are related to absorption at singlet (S_n) or triplet (T_n) higher excited states (Figure 1.5). Absorption at polaron states (P_n) should also be considered for electrical excitation or in the events of annihilation resulting in autoionization.[18,69] At high excitation densities needed for laser operation, excited state absorption can amount to substantial losses if it overlaps with ASE emission. In some cases singlet excited state absorption overlapping emission was found to completely suppress ASE in organic materials.[70] Meanwhile the long-lived triplet excited state absorption inhibits continuous-wave (CW) operation of organic lasers.[49,71] Furthermore, absorption of high energy emission to higher excited states leads to formation of high energy excitons (in the range of 5-6 eV), which may induce photodegradation as it is above ionization energy of most organic molecules.[43] Transient absorption measurements proved to be a reliable method to determine the effects of excited state absorption.

The ASE threshold of a laser is achieved when all the optical losses in the material are compensated by the gain. If net gain is possitive, narrow emission amplified by stimulated transitions begins to dominate fluorescence spectrum. Relatively high net gain values of 10^2-10^4 cm^{-1} enable significant amplification at a distance of several micrometers, which is relevant to miniaturization of laser devices.[24] Such high gain is determined by large stimulated emission cross sections ($\sigma_{SE} \sim 10^{-15}$ cm^2) of organic molecules.[72,73] It is important to point out that stimulated emission cross-section is directly related to radiative rate of the molecule. Therefore, radiative recombination rate and ASE threshold are one of the most commonly used parameters for screening potential organic gain materials.

1.3 Molecular design for solid-state lasing material

One of the persistent challenges when designing organic solid-state emitters is the introduction of additional losses appearing due to strong intermolecular coupling. For optically pumped lasers effects of intramolecular coupling can be mitigated by increasing spacing between chromophores. It can be implemented by either functionalizing molecules with inert non-conjugated groups, creating twisted molecular structures that prevent close packing or embedding emitters into solid host matrix. However, close packing is necessary for transport of charges in current-injection lasers. This creates special requirement for solid-state laser materials to be an efficient emitter and ambipolar charge transporter.

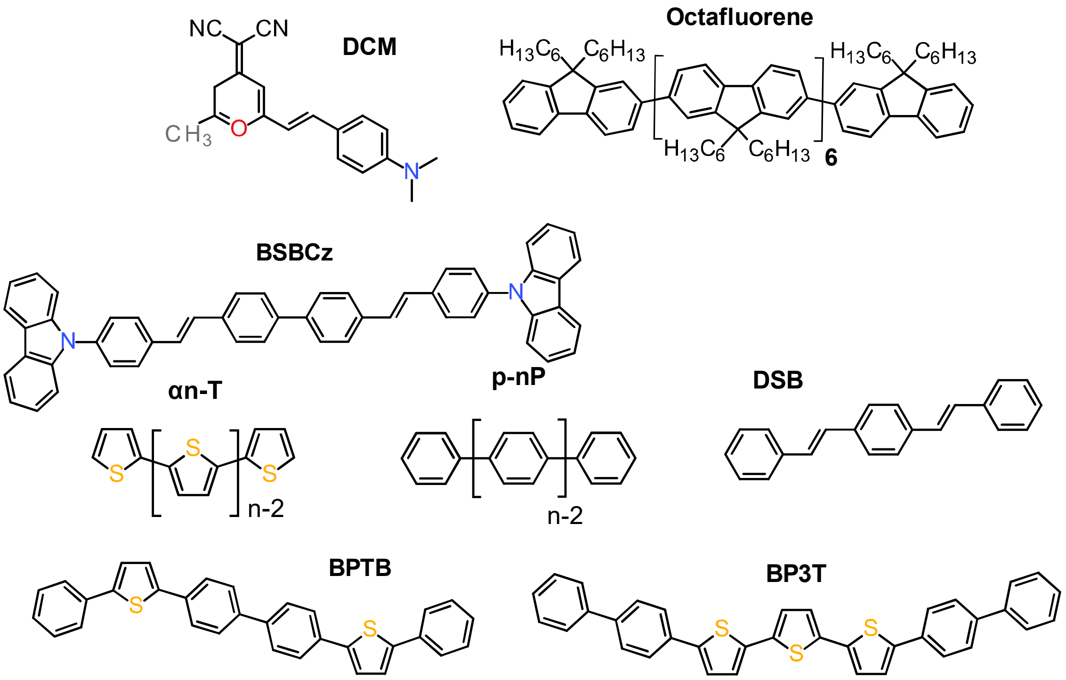

Figure 1.6. Best performing organic compounds for solid-state laser applications.

First of all, for a molecule to be considered for lasing applications it should exhibit large oscillator strength, which ensures high radiative rate (in the range of 1 ns^{-1}) and strong absorption and stimulated emission cross-sections.[72] This can be achieved in highly conjugated linear molecules showing strong transition dipole moments oriented along long molecular axis (Figure 1.6). One of the early examples was red emitting DCM possessed polar groups typically found in laser dyes for wavelength tunability with change of solvent polarity. However, polar groups were also associated with relatively low radiative rate (0.2 ns^{-1}) and strong emission quenching in solid films.[74] The latter limitation was bypassed by embedding DCM into active host-guest matrix, where the efficient energy transfer process eliminated quenching and reabsorption losses and resulted in ASE threshold values down to 1 μJ/cm^2 (500 W/cm^2).[75] Since then research was focused on finding novel laser emitters, which would maintain radiative properties even in neat films. Easy functionalization of relatively inexpensive fluorene units in oligomer and polymer derivatives in combination with superior charge transport properties made them of the most popular gain materials.[23,73,76–81] Interestingly, highly conjugated fluorene-based linear molecules show enhancement of radiative rates (up to 1.8 ns^{-1}) with increasing number of fluorene units.[78] This feature allows to achieve deep blue emission at 450 nm with ASE thresholds as low as 0.1 μJ/cm^2 in neat films of octafluorene derivatives.[76] Similar ASE properties were also recorded for polyfuorene, where highly conjugated nature of polymer also improved charge transport properties in thin films.[79] However, large molecular weight of the polymers limit their application to only solution processed devices, where high performance devices are produced by evaporating ultrathin (<100 nm) films using small molecules.

One of the main strategies to improve charge transport in organic films is to incorporate electron donating heteroatoms (e.g. nitrogen, oxygen or sulfur) into molecular structure and optimize geometry for dense packing. Generally, these changes are known to cause non-radiative losses due to enhanced ISC to triplets or formation of low energy charge transfer (CT) states that act as excitation traps. However, fine molecular design adjustments can lead to optimized emission and charge transport properties. The gold standard of the organic gain material was set by C. Adachi's group, who developed BSBCz compound.[82] Vacuum deposition of BSBCz resulted in high quality amorphous films maintaining almost 100% quantum yield at high radiative rate (0.6 ns^{-1}) and low ASE threshold (0.6 μJ/cm^2) together with moderate ambipolar charge transport mobility in the range of 10^{-3} cm^{2}V^{-1}s^{-1}.[83] These features proved sufficient for this compound to perform functions of charge transport and gain within a single amorphous layer in a first electrically driven

OSLD showing 600 A/cm^2 current threshold for 480 nm laser emission.[18] Recent molecular design improvements of BSBCz towards higher stability under intense excitation are extremely important for the future of organic lasers.[84]

Although amorphous organic materials are attractive for their easy and controllable deposition techniques, long-range molecular order in organic crystals can produce superior features such as enhanced charge and exciton transport, polarized emission or improved stability. Thiophene-based compounds are among the most popular building blocks for crystals with superior ambipolar charge mobility surpassing 1 cm^{2}V^{-1}s^{-1}.[85] On the other hand, sulfur produces heavy atom effect that is known to induce strong non-radiative losses due to ISC to triplets, and thus low quantum efficiency values are observed for oligothiophenes.[86] Interestingly, these non-radiative losses can be suppressed by extending conjugation, which allowed to observe ASE in α6-T and α8-T crystals.[87,88] Combination of charge transport and luminescent properties in oligothiophene crystals initiated research on lasing in electrically driven organic LEFETs in the early 2000s. This was also the basis for the infamous false realization of the electrically driven organic laser prototype by J. H. Schön.

Oligophenylene is another class of molecules known for crystals exhibiting superior emission properties. One of the most studied examples are p-6p molecules forming crystalline nanofibers.[89] Large stimulated emission cross-section of 2x10^{-16} cm^2 allowed to achieve low ASE thresholds in the range of 10 μJ/cm^2.[69,90] Further structural modification of phenylene oligomers with vinylene linkers unlocked a new class of distirylbenzene (DSB) compounds.[91] Unlike other oligophenylenes, DSBs formed large area platelet crystals showing ambipolar charge transport with hole and electron mobilities of 0.1 cm^{2}V^{-1}s^{-1} and ASE thresholds down to 10 μJ/cm^2.[92–94] Large variation of crystal emission color (from blue to red) could be achieved with introduction of peripheral units.[91,95]

Particularly interesting class of crystal forming materials integrating charge transport and light-emitting properties for lasing applications are thiophene/phenylene co-oligomers (TPCOs).[96,97] Large atomic radius of sulfur atoms embedded in the core of BP3T molecules ensures superior ambipolar charge transport in single crystal with mobility values of 0.1 - 1 cm^{2}V^{-1}s^{-1}.[98] Peripheral phenylene units extending the conjugation in BP3T derivative enabled superior optical properties. PB3T crystals showed high PLQY of 80% and 0.5 ns^{-1} radiative rate leading to low ASE threshold of 8 μJ/cm^2 for

610 nm emission.[99–101] In addition, extremely high current densities reaching 12 kA/cm^2 have been achieved in BP3T crystal based LEFETs.[102] Even lower ASE threshold of 1.8 μJ/cm^2 was recorded for green emitting BPTB crystal, however isolation of sulfur atoms in a molecule was found to degrade charge transport properties.[103] Recently, PB3T crystals coupled to DFB resonator were used to produce the first electrically driven laser transistor showing 2 μJ/cm^2 optical lasing threshold and 1 kA/cm^2 injection current threshold.[19]

Despite common belief that close molecular packing should result in strong intermolecular coupling that in turn induces emission quenching, most of the materials presented in this section show excellent solid-state emission properties. There has also been large effort toward improving charge transport properties of organic crystals for applications in light emitting transistors.[52] While charge transport properties are beyond the scope of the thesis, recent reviews on the topic can be recommended for further reading.[104–106] In the further sections, the optimization of optical properties in ordered organic systems will be discussed as a function of intramolecular and intermolecular interactions.

1.4 Excitonic coupling in molecular crystals

Control of excitonic coupling in molecular aggregates allows to achieve different photophysical properties from those of a monomer. Although the term exciton (i.e. correlated electron-hole pair) is sometimes used to refer to an excitation in a monomer, here it will be reserved for description of a collective response of a molecular aggregate. In most cases, the weak Van der Walls bonds holding together molecular solids is the reason for weak intermolecular interactions. Therefore, optical properties of amorphous organic solids are mostly determined by molecular structure. On the other hand, close molecular packing in aligned aggregates can induce coherent phenomenon leading to significantly changes of optical or charge transport properties. Furthermore, recently developed theory of short-range interactions between charges in aggregated molecules promise the new generation of highly emissive and conductive crystals.[107]

The changes of photophysical properties in molecular aggregates are presented in Figure 1.7. If the molecules in a solid medium are separated at intermolecular distances larger than molecular size (~5 Å), i.e. beyond the point of their molecular orbital overlap, the exciton is thought to be localized on a single molecule. This localized hole-electron pair is referred to as Frenkel exciton and can be represented by point-dipole with molecular dipole moment (μ) corresponding to $S_0 \rightarrow S_1$ transition. Despite small exciton radius, Coulombic interactions with other dipoles in the environment stabilize the ground and excited states due to Van der Walls attraction. Such non-resonant interactions lead to dispersive "gas-to-solid" energy shift when comparing molecular solid to monomers in gas phase (Figure 1.7). This shift is usually observed as absorption and emission redshift in amorphous media and is related to solvation effect in solutions.

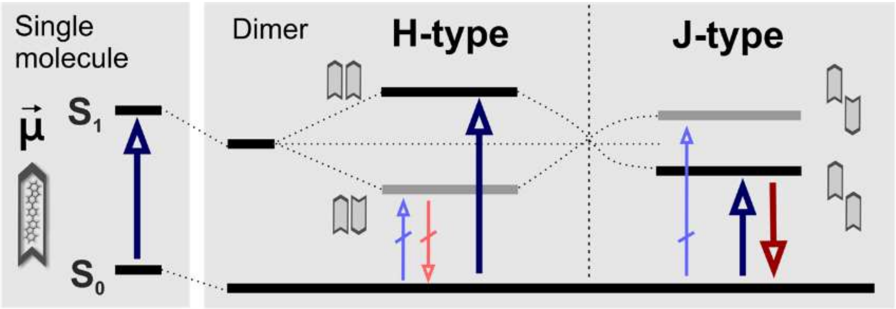

Radiative decay rate	Reduced k_r	Increased k_r
Exciton transport	Low (self-trapping)	Coherently enhanced
Vibronic coupling	Increases k_r	Reduces k_r
Main restrictions	Low oscillator strength	Reabsorption

Figure 1.7. Kasha's exciton model showing dependence of energy levels on intermolecular arrangements.

In molecular aggregates or crystals, where identical dipoles are placed in long-range order, resonant Coulombic interactions are possible. The in-phase and out-of-phase interactions between molecular dipole moments of the neighboring molecules lead to splitting of the excitonic band (i.e. Davydov splitting), where the relative orientation of dipole moments determines the distribution of the collective oscillator strength within these states. According to Kasha molecular dimer model, molecular aggregates are classified in respect to the relative orientation.[108,109] Although this is an oversimplified model to determine excitonic coupling between molecular dipoles in crystal, to some extent it has been shown to agree with experiments.[91] Side-by-side alignment of dipoles forms a so-called H-aggregate, where the coupling of opposite dipoles cancels the oscillator strength of the lower level and enhances the upper one. This is observed as blueshift of the absorption maximum in aggregates compared to monomers. The head-to-tail alignment of dipole moments results in J-aggregates, which leads to coherent enhancement of the lowest energy level oscillator strength and absorption redshift. As the emission always occurs from the lowest level due to ultrafast intraband IC, the radiative rate of an exciton is suppressed in H-aggregates. In contrast, in J-aggregates superradiance is observed when radiative rate is enhanced by the number of coherent neighbors.[109–111] However, reduced Stokes shift and strong absorption of the lowest level in J-aggregates induces strong reabsorption losses in bulk crystals.[91] This makes both, strong J-type and H-type excitonic coupling undesirable in crystals for laser applications, where high radiative rate an low reabsorption are essential to maintain superior gain properties. Therefore, weak excitonic coupling in crystals is desirable opting for best ASE performance.[91,112]

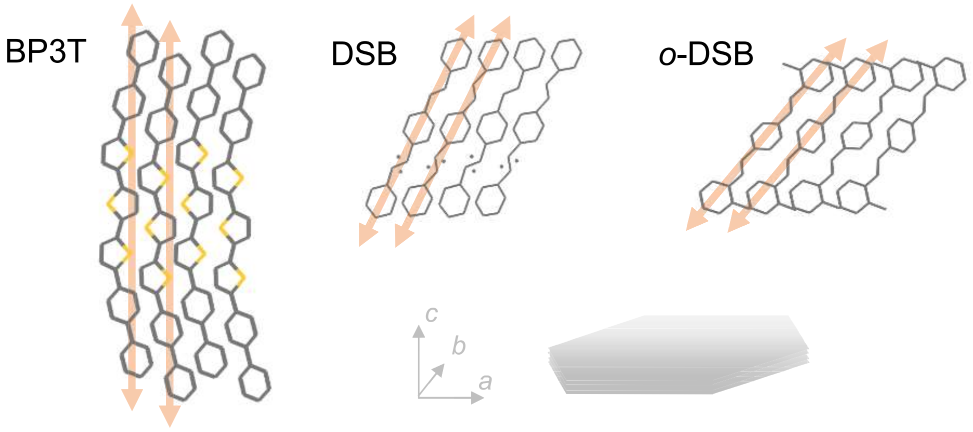

Figure 1.8. Intralayer molecular packing in BP3T,[113] DSB[114] and o-DSB[93] single crystals. All compounds formed layered platelet-like crystals with molecular layers in *ab* plane were stacked in *c* crystallographic direction. Arrows indicate molecular transition dipole moments.

From a practical point of view, effects of excitonic coupling can be controlled via molecular modification with steric groups that either act as spacers increasing intermolecular distances in crystal or promote slip-stacked packing canceling out contributions of dipole-dipole interaction (Figure 1.7). General packing motive for linear molecules with dipole moment coinciding with long molecular axis is H-type aggregates as displayed in Figure 1.8. To enable packing at an ange, and thus reduce H-type coupling, substituents of simple methyl groups in modified DSB compounds have been shown to promote higher radiative rate and improved ASE properties in single crystals.[93,114] More complex modifications of DSB has even produced J-aggregate crystals with high intralayer packing angle.[115]

Another way to reduce excitonic coupling in crystalline medium is by increasing exciton-vibronic coupling and static disorder.[109] This can be achieved by designing molecular structures with singly-bonded fragments allowing for higher torsional disorder as well as enhanced coupling to vibrational modes. The conventional Kasha model of dipole-dipole interaction presented in Figure 1.7 does not include the contribution of vibronic coupling. However, if vibrational coupling (i.e. nuclear relaxation energy) is comparable to the exciton bandwidth (i.e. Davydov splitting), it can strongly influence spectral signatures of the excitonic states. This is true for many organic aggregates as magnitude of the excitonic coupling rarely exceeds the energy of dominating vinyl stretching mode (~1600 cm^{-1}). Examples of strong excitonic coupling can be found in one dimensional polymers such as polydiacetylene (PDA) chains, where dipole interactions lead to exciton delocalization on 20-50 closely linked fragments.[109,116] Furthermore, the energy of intramolecular torsional modes (~100 cm^{-1}) or phonons in the solid state are comparable to $k_B T$ at room temperature (~200 cm^{-1}), which strongly influences the coherent function between interacting dipoles, and thus the excitonic coupling. The theory behind vibronic Frenkel excitons is well explained in the recent review by Hestand and Spano.[109] Here, only main spectroscopic features that allow to determine type and strength of excitonic coupling will be presented.

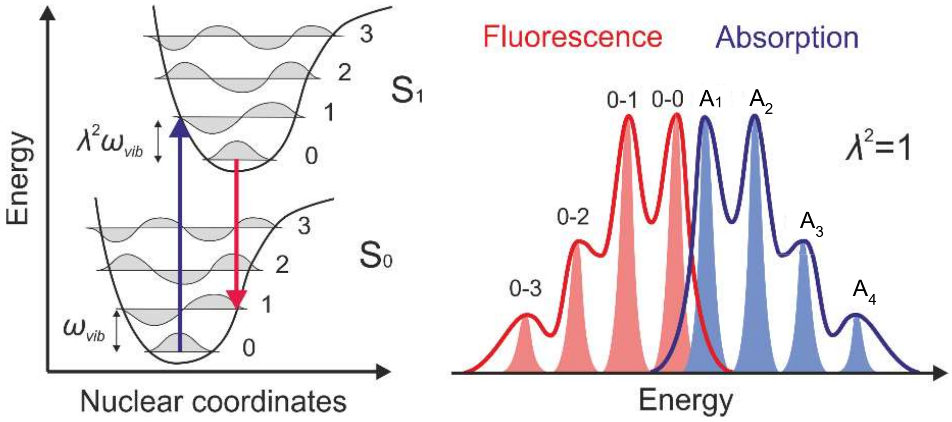

Figure 1.9. (Left) ground and excited state nuclear potential wells. Relative shift of the excited state potential is proportional to nuclear relaxation energy $\lambda^2\omega_{vib}$. (Right) Monomer absorption and fluorescence spectra for $\lambda^2 = 1$.

Highly elastic nature of carbon bonds forming organic molecules allow for nuclear relaxation along multiple vibrational modes. Dominant high energy modes such as symmetric vinyl stretching ($\omega_{vib} \sim 0.2$ eV) represent dominant peaks in the absorption and emission spectra of organic molecule (Figure 1.9). The strength of nuclear relaxation is given by dimensionless Huang-Rhys (HR) factor (λ^2), which can be obtained from absorption or fluorescence spectra of a monomer as a ratio of the first two peaks. HR parameter determines the relative shift and shape of the nuclear potentials. In molecular aggregates, where the nuclear relaxation energy is comparable to exciton bandwidth ($\lambda^2\omega_{vib} \approx W$), formation of separate vibronic bands with excitonic character leads to similar spectral structure of absorption and emission spectra as that of a monomer. However, in weakly coupled aggregate the lowest band (corresponding to A_1 or 0-0 transitions) is sensitive to exciton coherence.[109] Therefore, the absorption band ratio $R_{\mathrm{abs}} = A_1/A_2$ allows to determine the type and strength of excitonic coupling in aggregates. The increased/decreased ratio of aggregate absorption compared to monomer signals J-/H-type coupling, while the magnitude of R_{abs} is directly proportional to strength of excitonic coupling. In contrast, the emission from band bottom exciton retains the information on exciton coherence function. This allows to derive the coherence number (number of molecules over which exciton is delocalized) as an intensity ratio of the first two PL vibronic peaks $N_{\mathrm{coh}} = \lambda^2 R_{\mathrm{PL}}$, where $R_{\mathrm{PL}} = I_{0\text{-}0}/I_{0\text{-}1}$. As the vibronic sidebands are largely incoherent, only the $I_{0\text{-}0}$ band receives coherent enhancement of the radiative rate k_{r} in J-aggregates and is suppressed in H-aggregates. In ideal aggregates, where all molecules share the same electronic structure, N_{coh} can exceed tens of molecules at temperatures approaching 0 K. However, in real aggregates coherent function is highly sensitive to static energetic disorder arising from defects in crystal lattice or dynamic disorder due to thermal activation of low frequency torsional modes. Therefore, superradiant enhancement in large aggregates such as single crystals is usually completely suppressed at room temperature. For example, superradiant 0-0 band emission at low temperatures has been observed in rigid tetracene J-aggregates.[110,117]

Another instance where the conventional Kasha theory brakes down is when intermolecular distances become comparable to the molecular size (3-4 Å). At this point, overlap of molecular orbitals gives rise to short-range charge transfer (CT) interactions.[107] Most recent theories show that short-range interactions can produce H-/J-aggregate photophysical features that interfere with long-range coupling contribution. As a result, destructive interference can produce monomer-like optical features in molecular aggregates, where charge transport properties are facilitated by CT interactions. However, CT interactions are also the basis for formation of trap states that induce emission quenching in some aggregates. If the CT exciton state is comparable in energy to Frenkel exciton state, resonant mixing between these states may lead to the formation of low-energy excimers.[118] The distinct features of excimer states are strongly redshifted featureless emission spectra and low radiative rate, which allow to efficiently trap energy in aggregates. In special cases, such as α8-T crystals, CT states are higher in energy preventing formation of excimers in closely packed aggregates.[119] Similarly, short range interactions may explain the combination of ambipolar charge transport and high radiative rate in BP3T crystals despite side-by-side alignment of molecular dipoles (see Figure 1.8). One of the negative features of short-range coupling is high sensitivity to sub-Å molecular displacements appearing due to temperature change.

A more straightforward approach to reduce the effects of strong excitonic coupling is to dope crystals showing superior charge transport with highly emissive molecules. It is worth noting that in this work we refer to doping as a method to enhance light emitting properties and not to control conductivity of the material. In this case, excitation energy in the host material can be transferred to a dopant. The dopant must have lower energy gap for energy transfer to occur, which also eliminates possibility for resonant excitonic coupling with the surrounding media. Such doping strategy is widely used in amorphous host-guest active layers of OLEDs and solid state lasers.[120,121] One of the major issues is that emissive dopants act as charge traps, reducing charge mobility of the material.[101,122–124] However, it is yet unclear whether charge trapping at the dopant may lead to direct exciton formation, and thus improved electroluminescence efficiency.[125] Therefore, low doping concentrations are desirable not only for better charge transport properties, but also for lower dopant reabsorption losses considering laser applications. To achieve efficient energy transfer from host to dopant at low doping concentrations, host material must exhibit long-range energy transport prior to energy trapping at the dopant.

1.5 Energy transfer

The mechanism of excitation energy transfer in organic solids is important for function of optoelectronic devices as well as natural photosynthetic systems.[45,126,127] Unfortunately, similarly to charge transport strong vibronic coupling and disorder of organic materials determines the localized nature of the excitons leading to incoherent energy transport with short exciton diffusion distance rarely exceeding several nanometers. This limitation can be overcome by designing ordered systems, where strong excitonic coupling enables coherent enhancement of energy transport. Artificial one dimensional aggregates have been shown to exhibit long-range energy transfer of several hundred nanometers.[128,129] Similarly, highly anisotropic excitonic coupling in organic crystals can lead to long-range energy transport with coherent and incoherent components.

Typically, in organic materials exciton migration is viewed as incoherent hopping between localized sites due to fast dephasing caused by static or dynamic disorder. A probability for a single hop is defined by Förster resonant energy transfer (FRET) theory.[6,130] In a similar fashion to the exciton theory described in the previous section, interaction between transition dipole moments of donor and the acceptor promotes non-radiative energy transfer. However, unlike a delocalized excitation between several molecules in a coherent exciton, incoherent hop occurs with time constant that can vary in the range of 0.1 - 10 ps. The resonance condition implies that energy transfer is promoted by the overlap of transition dipole moment of the donor and dipole moment of the acceptor. Former is encoded in the radiative rate of the donor and latter is the absorption coefficient of the acceptor. Therefore, the magnitude of FRET rate is dictated by the overlap of the donor emission spectra and acceptor absorption spectra. This indicates that FRET can occur between same and different donor and acceptor pairs as long as spectra overlap. The general expression for FRET rate was expressed as:

$$k_{FRET} = \frac{9(\ln 10)\kappa^2 k_r J_F}{128\pi^5 N_A n^4 R^6}, \tag{1.1}$$

where, κ^2 is orientational factor, k_r is donor radiative rate [s^{-1}], N_A is Avogadro's number, n is medium refractive index and R is interchromophore distance [nm]. The Förster overlap (J_F) [L mol^{-1} cm^{-1} nm^4] is the overlap between area normalized donor emission $F_D(\lambda)$ and extinction coefficient spectrum of acceptor $\varepsilon_A(\lambda)$:

$$J_{\mathrm{F}} = \int F_{\mathrm{D}}(\lambda)\varepsilon_{\mathrm{A}}(\lambda)\,\lambda^4\,d\lambda\,. \tag{1.2}$$

FRET rate is highly sensitive to distance between donor and acceptor ($k_{\mathrm{FRET}} \sim 1/R^6$) and relative orientation and of transition dipole moment vectors.[131] In a similar manner to excitonic coupling, head-to-tail orientation gives higher FRET rate than side-by-side, while FRET rate is zero for perpendicular dipoles (Figure 1.10).

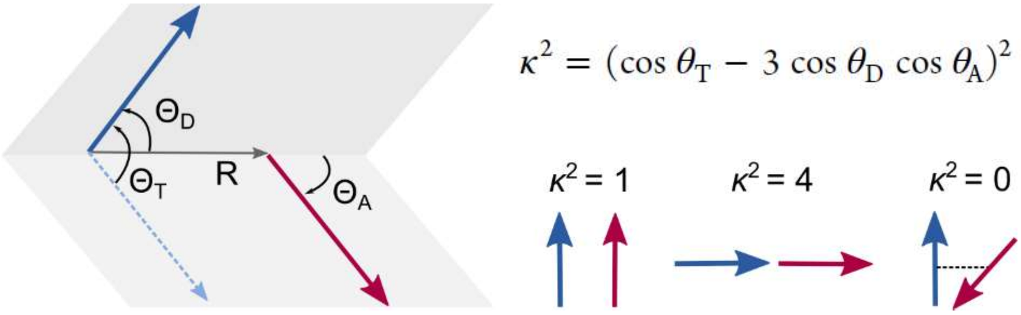

Figure 1.10. Evaluation of orientational factor κ^2 between donor and acceptor transition dipole moments.

Förster theory is successful at predicting energy transfer rates between donor and acceptor species that show weak excitonic coupling with the surrounding media. A good example of such media is amorphous organic film with randomly oriented and well-spaced chromophores. However, in highly ordered crystalline media, excitonic coupling between chromophores is inevitable. This requires a generalized solution for Förster theory that also includes the coherent effects appearing due to resonant interactions between chromophores.[5,6] As the collective effects of excitonic coupling change the total dipole moment of an aggregate, this should also be reflected in calculation of energy transfer rate. For example, if $N_{\mathrm{coh}} \sim 2$ chromophores in linear J-aggregate show coherent enhancement of radiative rate, the energy transfer rate should be accelerated accordingly. In this case, as the exciton is still localized on two chromophores due to strong vibronic coupling the hopping motion occurs between excitonically bound pairs (Figure 1.11). Furthermore, the outcome of generalized Förster theory is that energy transport is significantly faster in J-type than in H-type aggregates.[109,132]

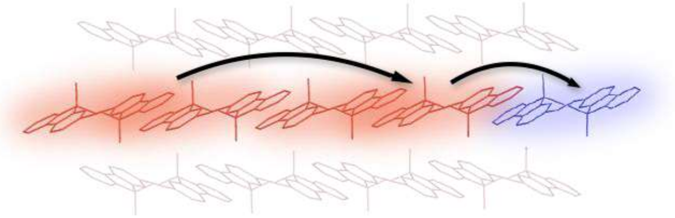

Figure 1.11. Illustration of partly coherent transport in molecular aggregates.

The temperature dependence of the energy transfer rate in conventional Förster theory is brought by thermal broadening of the absorption and emission spectra. Larger Förster overlap at increasing temperatures leads to temperature activated hoping.[45] Highly disordered (amorphous) materials show weak temperature dependence of exciton diffusion due to large inhomogeneous broadening. In contrast, introduction of excitonic coupling in ordered molecular aggregates complicates temperature dependence as coherent function is highly sensitive to thermal scattering. Therefore, temperature dependence of radiative rate can be used to determine the regime of exciton transport. If the radiative rate is enhanced at low temperatures as in J-aggregates, larger coherence number leads to enhancement of exciton transport rate. Such partly coherent exciton transport was observed for anthracene single crystals by several experimental techniques.[133,134] On the other hand, most of the oligo phenylene-thiophene crystals that can be associated with weak H-type excitonic coupling showed temperature activated energy transport.[100,135,136]

Concluding remarks

Despite many technological advances toward creating materials for laser applications, organic lasers have yet not attracted as much interest as other optoelectronic devices (OLED, photovoltaics or transistors) due to lack of stable devices. This leads to many phenomena occurring at high intensity charge-light interaction within organic matter remain unexplored. However, it is clear that design strategies used in conventional organic light emitting devices are not sufficient for production of current-driven organic lasers. Recent upsurge in research of coherent phenomena in molecular aggregates and crystals is highly promising for new generation of materials and device architectures, where strong intermolecular interactions would be harnessed and not avoided.

2 EXPERIMENTAL METHODS

2.1 Photoluminescence spectroscopy

Photoluminescence spectroscopy in essential for determining emission spectral features, quantum yields and temporal characteristics of organic laser materials. One of the main characteristics used to evaluate emission characteristics of any light emitting material is its radiative (k_r) and non-radiative (k_r) rates:

$$k_r = \Phi_{PL}/\tau \qquad \text{and} \qquad k_{nr} = (1 - \Phi_{PL})/\tau\,, \tag{2.1}$$

where τ is emission lifetime and Φ_{PL} photoluminescence quantum yield that is described as a ratio of the rates:

$$\mathit{\Phi}_{PL} = \frac{k_r}{k_r + k_{nr}}\ . \tag{2.2}$$

To obtain the Φ_{PL} and τ parameters experimentally, steady-state and time-resolved emission measurements were performed. Steady-state PL spectra were measured using a back-thinned CCD spectrometer PMA-11 (Hamamatsu) and a xenon lamp coupled to a monochromator (FWHM<10 meV) as an excitation source. PL quantum yields (PLQY) were estimated from a ratio of absorbed and emitted photons using the integrating sphere method.[137] Quinine sulfate 0.1 M H_2SO_4 solution was used as a calibrating sample ($\Phi_{PL} = 54 \pm 5\%$) in integrating sphere (SphereOptics) coupled to the CCD spectrometer via optical fiber. Reabsorption effects in solution samples were minimized by reducing concentration down to 5 x 10^{-6} M. Alternatively, for highly absorbing thin films and crystals reabsorption was corrected by comparing emission recorded inside and outside of the integrating sphere.

To measure time-resolved photoluminescence (TRPL) spectra a streak camera setup was used. The pump laser source for the TRPL measurements was wavelength-tunable optical parametric amplifier (Orpheus, Light Conversion) pumped by pulsed 190 fs laser (Pharos-SP, Light Conversion). Laser repetition rate was adjusted in the 1-100 kHz range using in-built pulse picker. TRPL spectra were detected with streak scope detector (C10627, Hamamatsu) coupled to spectrograph (Acton SP2300, Princeton Instruments). The time resolution of approximately 20 ps was achieved.

Temperature controlled studies were performed in closed-cycle helium cryostat (Cryo Industries 204N) or in nitrogen cryostat (OptistatDN, Oxford instruments).

2.2 Steady-state absorption spectroscopy

The absorption of light in a material is governed by Beer-Lambert's law, which states that the transmission corresponding to intensity ratio of transmitted (I) and incident (I_0) light intensity follows power law:

$$T = \frac{I}{I_0} = 10^{-\epsilon c d} \ . \tag{2.3}$$

Where ϵ is the extinction coefficient of absorbers [$M^{-1}cm^{-1}$], c is the concentration of absorbers [M], and d is sample thickness [cm]. Absorbance (A) allows to describe previous equation in linear fashion:

$$A = -\log_{10}\left(\frac{I}{I_0}\right) = \epsilon c d \ . \tag{2.4}$$

For strongly absorbing crystal samples it is also useful to introduce the quantity of absorption length (μ) [μm] that corresponds to distance intensity falls to 1/e and is reciprocal to absorption coefficient ($\mu = 1/\alpha$). Then equation (2.3) can be rewritten as:

$$T = \frac{I}{I_0} = e^{-\alpha d} \ . \tag{2.5}$$

Absorption spectra of sample solutions and thin films were recorded on a UV−vis−NIR spectrophotometer Lambda 950 (Perkin-Elmer). Absorption measurements of single crystals were limited by resolution of the spectrometer due to their large absorbance ($A > 4$). One of the solutions to measure crystal absorption spectra was to use polarizer setting light to minimum absorption in highly anisotropic crystals. Other solution was to measure transmittance of a wavelength-tunable laser beam. Transmission anisotropy in crystals was determined either by rotating laser polarization with a waveplate or by rotating crystal mounted in homebuilt sample holder.

2.3 Transient absorption spectroscopy

Transient absorption (TA), also known as pump-probe, spectroscopy allows to measure differential absorption signal with high temporal resolution.[138] Its concept relies on sample interaction with two short pulses: intense “pump” creates excitation and less intense “probe” pulse monitors change in transmission (Figure 2.1). Initially both pump and probe pulses originate from the same laser source, where transmission signal difference is created by synchronized chopper limiting the amount of pump pulses. The delay between pulses is varied mechanically by moving retroreflector at a distance ΔL from the point where the light path for both probe and pump pulses is equal (referred to as time-zero point, $\Delta t = 0$), thereby causing the delay $\Delta t = 2\Delta L/c$, where c is the speed of light. Therefore, time resolution of TA experiment is determined by the pulse duration as well as precision of retroreflector motion.

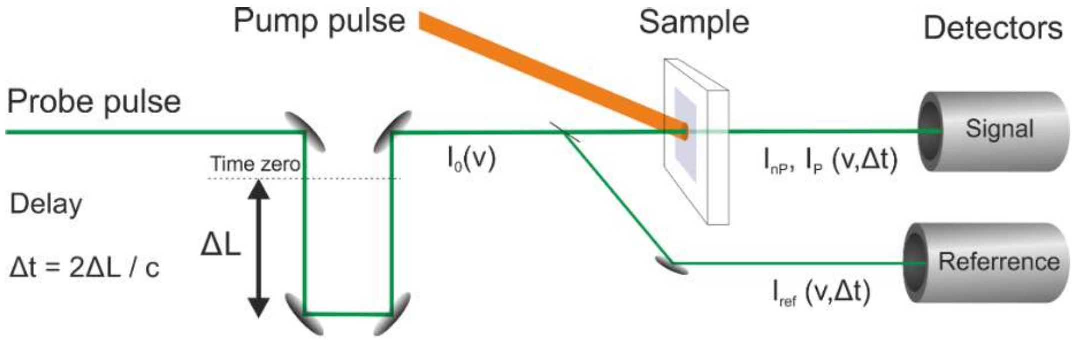

Figure 2.1. A simplified scheme of pump-probe setup, where pump and probe pulses are focused on a sample.

Sub-picosecond resolution is made available by femtosecond laser pulses. What appears contradictory to Heisenberg’s uncertainty principle is that time resolution and frequency resolution are not related.[139] However, limitations imposed by Heisenberg’s principle become important when using femtosecond pulses lead to broad excitation pulse bandwidth that covers a broad band of vibrational states. This opens possibilities for observation of coherent phenomenon.

The changes in the absorption of the sample induced by the pump pulse can be analyzed as change of transmitted probe intensity without excitation (*I*) and with excitation (I^*), which is referred to as differential absorption signal:

$$\Delta A = A^* - A = log\left(\frac{I^*}{I_0}\right) - log\left(\frac{I}{I_0}\right) = log\left(\frac{I^*}{I}\right) \qquad 2.6$$

The need for the reference pulse intensity is eliminated in the differential absorption measurement, however, can be used to compensate for pulse intensity variation.

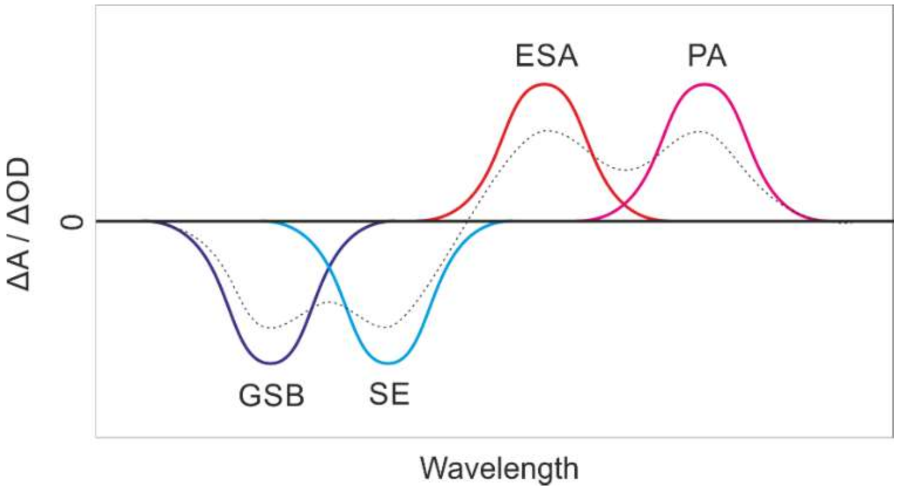

Figure 2.2. Examples of contributions to ΔA signal: ground-state bleach (GSB), stimulated emission (SE), excited-state absorption (ESA), product absorption (PA) and sum of these contributions (dashed line).

TA is considered to be a fundamental spectroscopic technique as it contains information about the population of excited states and unlike photoluminescence-based time-resolved techniques, can detect signal of dark states such as triplets. The typical TA signal shown in Figure 2.2 contains different information:

- Ground state bleach (GSB) spectra corresponds to the reduced sample absorbance due to large excited state population, therefore negative GSB signal mimics absorption. Other signals are specific to a given excited states.

- The negative stimulated emission (SE) signal corresponds to stimulated transitions from excited states induced by probe pulse. Its intensity depends directly on stimulated emission cross-section (σ_{SE})
- Excited-state emission (ESA) signal corresponds to transitions from excited states to higher excited states, which results in a positive differential absorption signal.
- The product absorption (PA) of these transient states will appear as a positive signal in the differential absorption spectra. In some cases, excitation of the sample can lead to photochemical reaction that will occur through transient states of the molecules.

The dataset obtained from TA measurements also contains artifacts that must be corrected prior to data analysis. A temporal chirp of the probe beam is caused by group velocity dispersion in the medium. It is reflected in 2D TA spectra as red side of the spectra arriving prior to blue. Another artifact is cross-phase modulation (XPM) occurring when pump and probe beams overlap in time and space. XPM refers to the situation when strong pump pulse modulates the refractive index of the medium (quartz cuvette or glass substrate of the sample) and induces spectral changes of probe pulse in a time dependent fashion. Although XPM is difficult to correct, it is important not to confuse it with coherent phenomena occurring due to excited state dynamics.

Femtosecond transient absorption (TA) measurements were carried out using commercial pump-probe spectrometer (Harpia, Light Conversion) pumped with pulsed femtosecond laser and parametric amplifier system (Orpheus and Pharos, Light Conversion). Probe source was white light continuum (WLC) pulses generated by focusing the fundamental 1030 nm harmonic onto the sapphire crystal. To extend the probe in 2.6 – 3.2 eV region WLC was generated in purified water flowing inside quartz cuvette coupled to home-built flow system. The probe light was recorded using the linear CCD sensor (Hamamatsu). Global analysis of TA data was performed by data analysis software “CarpetView” (Light Conversion).

2.4 Light induced transient grating spectroscopy

Light-induced transient grating spectroscopy (LITG) is a variation of pump-probe technique, where the absorption of two time-coincident coherent pulses form an interference pattern of the photoexcited states, which is then probed by the third time-delayed pulse.[140] LITG measurements presented in this work were performed by dr. P. Ščajev, while the detailed description of the experimental setup is provided elsewhere.[141]

Figure 2.3 illustrates the principal scheme of the LIGT experiment. The angle Θ between two pump beams and wavelength of the pump beam λ_p determine the period Λ of the resulting interference field: $\Lambda = \lambda_p/(2\sin(\Theta/2))$. The spatially periodic photoexcitation of the sample results in variation of refractive index, thus part of the probe beam is diffracted if the Bragg condition is met. The diffraction efficiency η is measured as a function of delay time between pump and probe pulses.

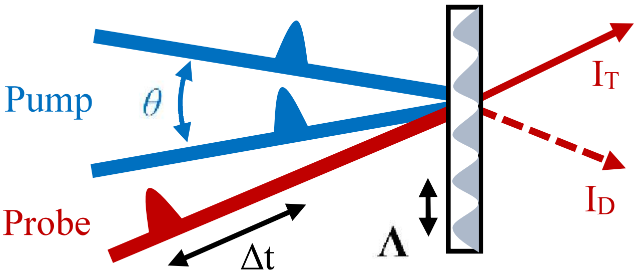

Figure 2.3. Principle scheme of LITG experiment.

The diffraction efficiency signal is produced by the periodic variation of complex refractive index ($\mathbf{n} = n + iK$). Generation of the excited states results in change of both real and imaginary parts of the refractive index.[142] The change in the in the real part of the refractive index ($\Delta n(\lambda)$) is caused by the difference in the optical dispersion between grating peaks and nulls at the probe wavelength. This induces phase gratings, which are related to phonon wave generation (via rapid nonradiative relaxation or electrostriction mechanisms). In contrast, the change of the imaginary part of the refractive index ($\Delta K(\lambda)$) is related to the peak-null absorption difference at the probe wavelength, resulting in an amplitude grating. As most organic materials exhibit strong excited state absorption in the region of visible light, diffraction signal is formed due to amplitude grating, *i.e.* spatial variation in the optical density.[143] The measured signal to excitation intensity dependence of BF-p crystal for LITG and differential transmission (DT) techniques is displayed in Figure 2.4a. In the case of DT the slope of 0.96 showed that differential absorption signal is directly proportional to the excitation density. Whereas in the LITG case, the slope of diffraction efficiency signal is proportional to the square of the excitation density. This indicates that diffraction efficiency signal is due to an amplitude grating (*i.e.* change of absorption coefficient (ΔK) for the probe pulse between grating peaks and nulls).[141,142]

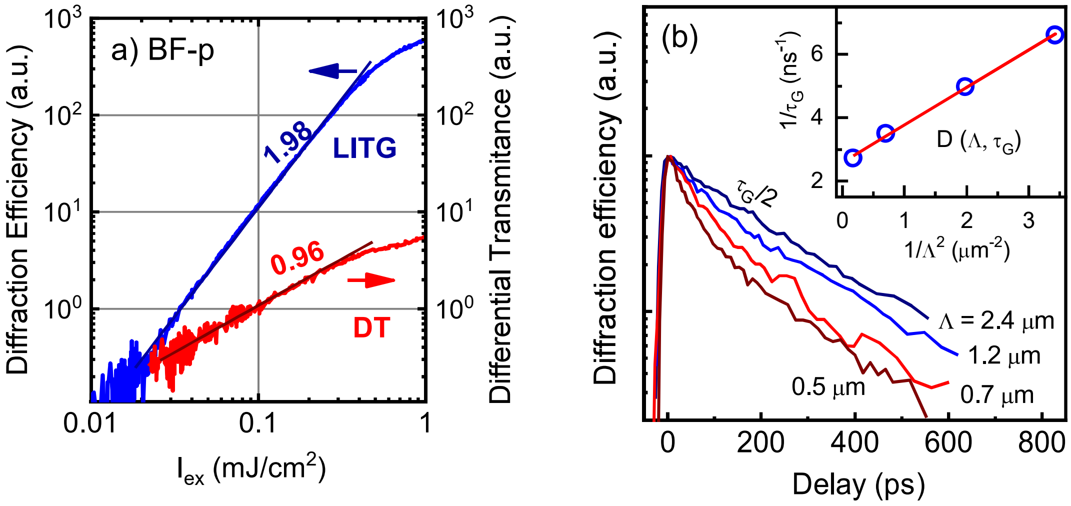

Figure 2.4. LITG measurements of the BF-p crystal. (a) Excitation density dependence of LITG and DT signals and the corresponding slope coefficients. (b) Example of LITG decays recorded at different grating periods.Inset shows the linear fit of the grating decay rates, where slope corresponds to the diffusion coefficient.

The decay of the diffraction efficiency in time is governed by two processes: amplitude of the grating peaks is reduced due to exciton recombination rate $1/\tau_R$, while grating peak broadening is caused by the diffusion along the grating axis with rate $1/\tau_D$. The observed diffraction efficiency signal decays exponentially at a rate:

$$\frac{1}{\tau_G} = \frac{1}{\tau_R} + \frac{1}{\tau_D} = \frac{1}{\tau_R} + \frac{4\pi^2 D}{\Lambda^2}\ . \qquad 2.7$$

It is possible to determine diffusion coefficient D and lifetime τ_R by recording a set of LITG transients for various grating periods Λ. In Figure 2.4b more rapid signal decay at smaller diffraction gratings indicates a measurable impact of exciton diffusion in BF-p crystal.

2.5 Amplified spontaneous emission measurements

Optically excited ASE characteristics were measured employing thin excitation stripe technique.[72] The technique is based on the excitation of slab waveguide samples with a laser stripe and registration of emission spectra from a sample edge (Figure 2.5a). Spontaneous emission travelling along the excitation stripe is amplified due to the stimulated transitions resulting in directional emission emerging at the sample edge.

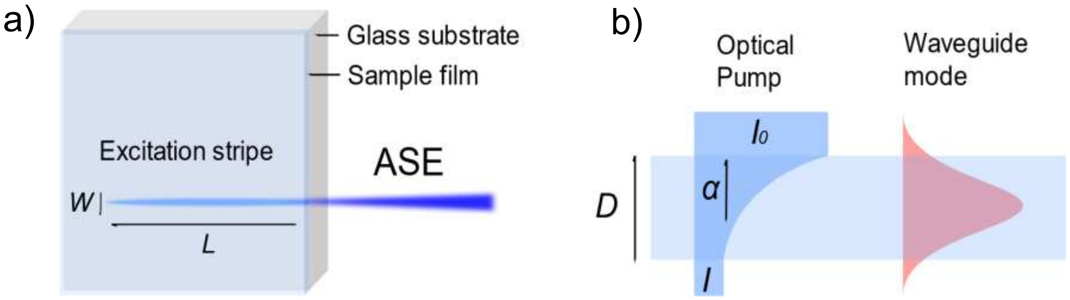

Figure 2.5. (a) Schematic representation of thin stripe excitation method. (b) the excitation population and waveguide mode profiles within the sample thickness *D*.

The edge emission spectra are recorded as a function of excitation density. The spectral narrowing of the emission above the certain pump intensity is referred to as ASE threshold (I_{th}^{ASE}). Due to stimulated transitions occurring at emission energy bearing the highest gain (usually coinciding with 0-1 vibronic peak) emission intensity versus excitation density dependence undergoes change from linear to superlinear above I_{th}^{ASE}. It is observed when modal gain overcomes absorption losses (α) resulting in positive net gain:

$$g = \sigma_{SE}\Delta N - \alpha \,, \qquad 2.8$$

where σ_{SE} is stimulated emission cross-section [cm^2] and ΔN is population inversion [cm^{-3}]. If the gain saturation is neglected, the ASE intensity is related to stripe length (L) as follows:

$$I_{ASE} = \frac{I_{spont}}{g}\left[\exp(gL) - 1\right], \qquad 2.9$$

where I_{spont} is the seeding term related to power density of spontaneous emission within the stripe length. It is obvious that at long excitation path geometry ASE exhibits exponentially higher intensity. Figure 2.5b illustrates another issue that often limits observation of low ASE threshold in highly absorbing samples. Reduced overlap between non-uniform pump population and waveguiding modes (pump-mode overlap) within sample thickness can lead to significant waveguide losses.[144,145]

In this work, ASE measurements were performed using two different excitation sources and stripe parameters:

- For papers I-IV excitation source was a wavelength tunable optical parametric amplifier pumped by nanosecond Nd:YAG laser (repetition rate 10 Hz, pulse duration 5 ns). Laser stripe (width – 40-50 μm, length – 5 mm) was focused on the sample surface near the edge by using a cylindrical lens. Measurements were performed by Dr. G. Kreiza.
- For paper V excitation was carried out with a wavelength-tunable optical parametric amplifier (Orpheus, Light Conversion) pumped by 190 fs pulsed laser (Pharos-SP, Light Conversion). Laser excitation frequency was adjusted in 1-100 kHz range with built-in pulse picker. ASE measurements were performed in two geometries: 300 μm excitation spot focused far from sample edge and 2800 x 200 μm excitation stripe focused at the sample edge.

Relative pulse duration (t_{pulse}) in respect to emission lifetime (τ_{PL}) is important when determining ASE threshold.[72,88] In most cases, ASE measurements are performed using short excitation pulses ($t_{\mathrm{pulse}} << \tau_{\mathrm{PL}}$), which corresponds to instantaneous excitation of gain medium, and I_{th}^{ASE} is expressed in μJ/cm^2. If excitation pulse is comparable or longer than lifetime ($t_{\mathrm{pulse}} \geq \tau_{\mathrm{PL}}$) excitation regime approaches quasi continuous-wave (q-CW), and I_{th}^{ASE} is expressed in W/cm^2. Although evaluation of ASE threshold at CW excitation conditions is more practical considering device applications, it is rarely evaluated due to poor photostability of organic materials.[49] ASE threshold at CW excitation is enhanced due to influence of non-radiative decay channels (*e.g.* accumulation of triplets).

2.6 Samples under study

Molecular compounds

General design criteria for molecular compounds investigated in this work was small linear structures containing fluorene units substituted with alkyl chains. All investigated fluorene oligomers are presented in Figure 2.6. Fluorene unit was selected for its emission properties and success in low gain laser materials.[23] Linear oligomer structures allow to achieve extended conjugation, which is essential for high oscillator strength. Furthermore, linear structures also favor crystal formation.[91] Finally, molecular packing can be controlled by length of alkyl chains. Long chains as in FFF lead to large intermolecular distances and random orientation in amorphous films. Short chains as in BF series lead to high tendency to crystalize and specific molecular orientation in crystal lattice.

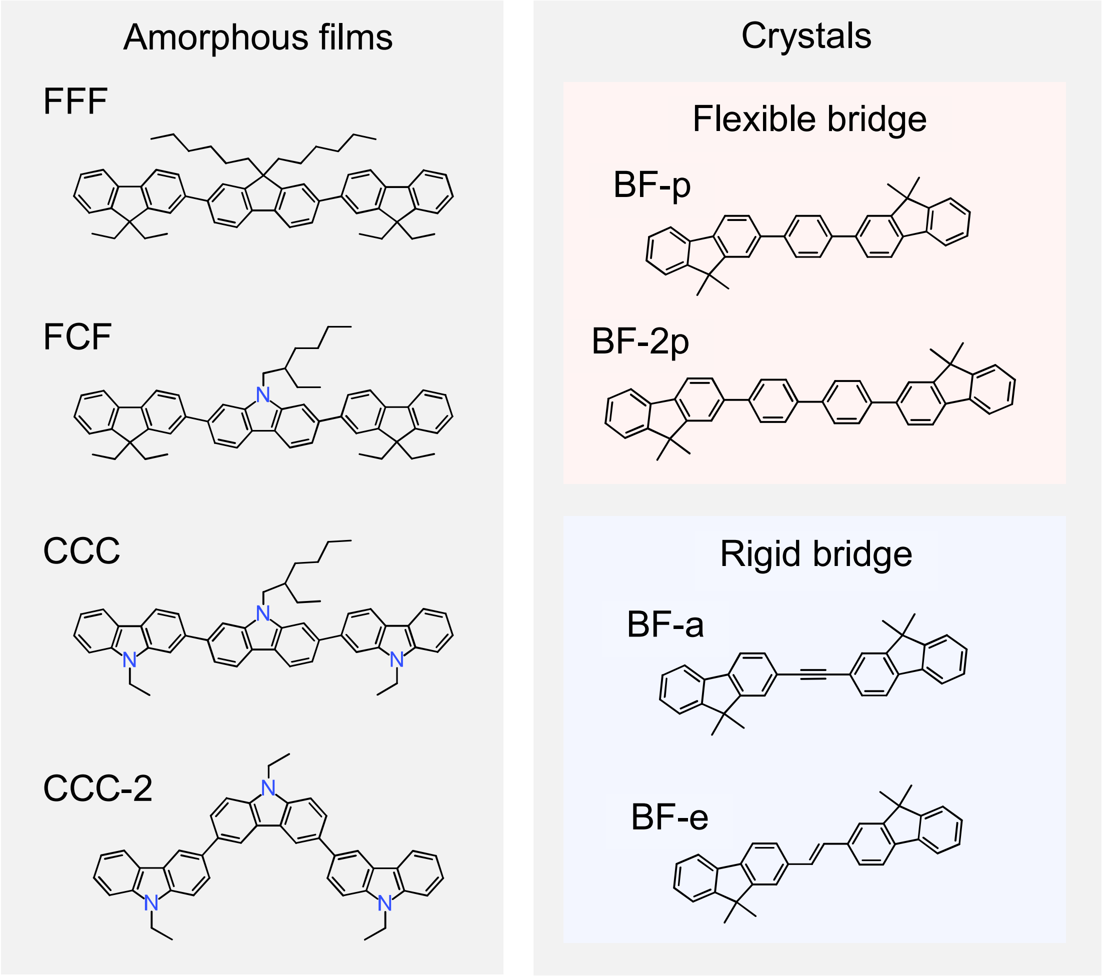

Figure 2.6. Molecular structures of fluorene oligomers.

Fluorene triads (FFF, FCF, CCC and CCC-2) for study in amorphous films form a basis for Paper I. Bifluorenes for crystals were subdivided to reflect the type of bridge unit: flexible phenyl containing (BF-p and BF-2p) and rigid acetylene or ethylene bridge (BF-a and BF-e). Synthesis route of BF-p and BF-2p was reported in Paper II and synthesis of BF-a and BF-e was reported in Paper III.

Solution and film preparation

Solutions of all fluorene oligomers were prepared in spectroscopic grade tetrahydrofuran (THF) solvent by dissolving material at low concentration ($<10^{-5}$ M) to avoid aggregation. Amorphous films were prepared by drop-casting on a ozone cleaned glass substrates. For production of neat films concentrated solutions (10^{-3} M) were used. Polymer films doped at various concentrations were produced from dissolved mixture of studied compound and polystyrene (PS) at appropriate mass ratio in toluene solution. For ASE measurements thin films (~1μm) were produced by spin-coating method to obtain a higher quality waveguide.

Crystal growth and characterization

Aiming for high waveguide quality, single crystals were grown by physical vapor transport (PVT) technique.[95] Figure 2.7 shows a schematic representation of horizontal tube-based sublimation system DSU-20 (CreaPhys). Starting materials in powder form were heated up to temperatures 10 - 30 K below their melting points to achieve evaporation without melting of the initial powder. Crystal growth temperature was set to be like material crystallization temperature obtained by means of differential scanning calorimetry (DSC). Pure nitrogen was used as a carrier gas with a gas flow of 10 mL/min. Sublimation chamber pressure was varied from 0.1 to 1 bar by utilizing vacuum pump system. Crystal growth process usually took from 12 to 24 hours, after which thin (up to 10 μm) plate-like single crystals with lateral dimensions up to 1 cm were obtained. Crystals were placed on pre-cleaned glass substrates for spectroscopic and microscopic analysis. Doped crystals were produced sublimating 100:5 w.t. host:dopant powder mixture at 230 °C. The temperature gradient from 230 °C to 170 °C created in the crystallization zone resulted in plate-like crystals with various degrees of doping concentrations. Ultrapure BF-a micro-crystals were produced by sublimation at 150 °C in high vacuum on cleaned quartz substrate. Crystal growth experiments were performed by Dr. G. Kreiza.

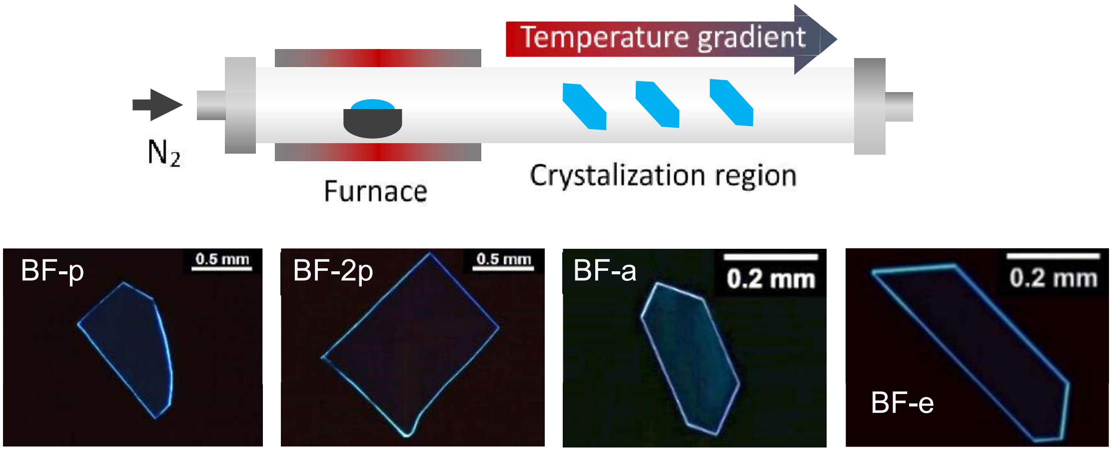

Figure 2.7. Scheme of crystal growth employing vapor transport deposition technique.

2.7 Crystal structure

Crystal structures of BF-p, BF-a and BF-e were determined employing single-crystal X-ray diffraction (SC-XRD) analysis, which was performed by dr. G. Kreiza. Suitable crystals were selected and analyzed on a XtaLAB Synergy, Dualflex, HyPix 6000-HE diffractometer using PhotonJet X-ray source with CuKα (λ = 1.54184 nm) radiation. Data collection was performed at 100.0(10) K using CrysAlisPro software. Crystallographic data of BF-a and BF-e were deposited at the Cambridge Crystallographic Data Centre (CCDC 1942503-1942504). Crystal parameters are summarized in Table 2.1. Cell volume allowed to calculate molecular density in a crystal ($1.7x10^{21}$ cm^{-3}), which was used to estimate dopant densities in doped crystals.

Table 2.1. Crystallographic data from XRD analysis.

Compound	**BF-p**	**BF-a**	**BF-e**
Formula weight/(g/mol)	518.7	410.5	412.5
Crystal system	monoclinic		
Space group	$P 2_1/c$	$P2_1/c$	$P2_1/c$
a/Å	14.5	8.5	8.5
b/Å	5.9	9.7	10.1
c/Å	16.0	27.9	26.4
Volume/Å^3	1290	2313	2260

The 2-theta XRD analysis of doped and non-doped crystals was performed by dr. S. Stanionytė. XRD patterns by were collected using SmartLab (Rigaku) diffractometer with a 9 kW Cu rotating anode x-ray tube. For measurement of XRD curves from (002) planes Ge(400) × 2 monochromator and scintillation detector SC-70 were used.

Unit cells of bifluorene crystals in respect to large crystal plane are displayed in Figure 2.8. All bifluorene crystals exhibited similar molecular packing. Molecular layers were formed parallel to main crystal facet, with interlayer distance of approximately 14 Å. Intralayer molecular arrangement showed herringbone (HB) type packing. Single layer showed highly directional alignment of dipoles pointing towards direction of inclination.

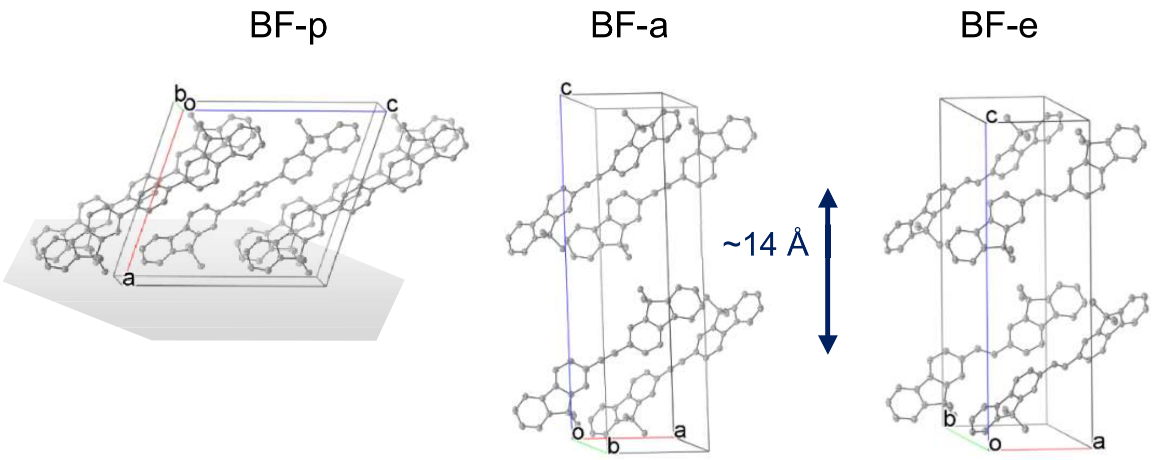

Intralayer herringbone packing

Closest neighbors in the direction of inclination

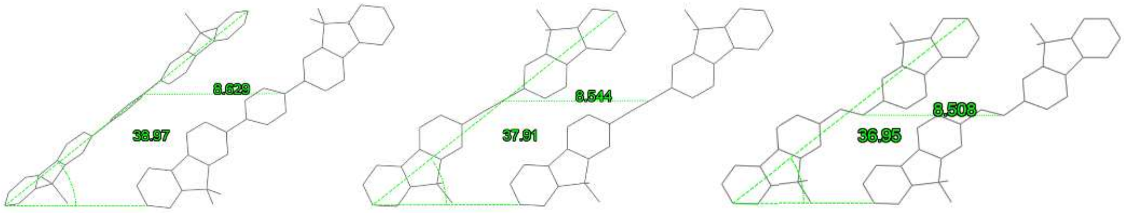

Figure 2.8. Molecular packing in bifluorene crystals. (top) crystal unit cells. (middle) view of single molecular layer from the short molecular axis. (bottom) relative orientation of two molecules in a unit cell with indicated intramolecular distance and inclination angle.

3 RESULTS AND DISCUSSION

3.1 Light amplification in fluorene-based amorphous films

The lasing properties of organic molecules are highly sensitive to selection of aromatic fragments and their linking position in multi-chromophoric systems.[23] Two of the most exploited aromatic units constituting the multichromophoric systems are fluorene and carbazole, which, in fact, by proper substitution are capable of delivering multifunctional properties. For instance, fluorenes are known for their high fluorescence efficiency, high laser gain as well as excellent thermal and oxidative stability.[23,73,76–79,146] Meanwhile, carbazole is just fluorene substituted with nitrogen heteroatom, which makes it a superior hole transporter.[83,147] Functionalization of carbazole or fluorene units *via* 2,7-positions have demonstrated great potential for light-emitting device applications by yielding extended conjugation, enhanced emission efficiency, and, in some cases, bipolar charge carrier transport with electron and hole mobilities as high as 10^{-3} $cm^2/(V\cdot s)$.[148,149] More symmetrical, linear-shaped molecules with the emitting dipoles oriented in the plane of the active layer were found to be beneficial for enhanced light outcoupling from an OLED structure as well as for reduced ASE threshold.[150] On the other hand, substitution *via* 3,6-positions creates a twisted molecular structure, which in turn results in lower fluorescence efficiency due to higher ISC to triplets and degraded charge transport properties compared to 2,7-position.[151–153]

To this end, aiming for compounds with efficient light amplification, the impact of linking topology of a series of fluorene-carbazole triads on ASE threshold as well as on emission quantum yield, concentration quenching of emission and radiative decay rate was studied. Chemical structures of fluorene triads are displayed in Figure 3.1. In the study, the triads **FFF**, **FCF** and **CCC** bearing 2,7- substitution pattern were mainly utilized as favoring extended π-conjugation, linear molecular shape (for controllable orientation), and thus, highly promising for efficient emission, charge transport, and consequently, for organic laser applications. A compound **CCC-2** utilizing 3,6- substitution patterns was also investigated for comparison. The fluorene-carbazole triads were also designed to possess various alkyl chains substituted at 9th position for investigating molecular packing effects on the concentration quenching.

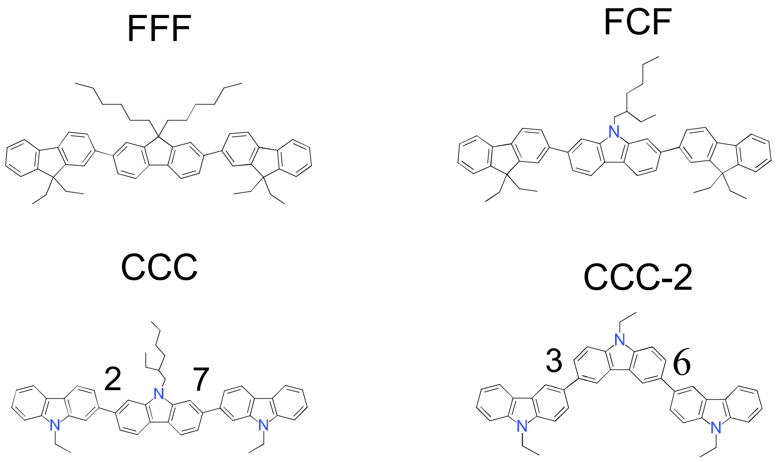

Figure 3.1. Chemical structures of differently-linked fluorene triads.

To investigate the effects of emitter concentration on photophysical properties, carbazole/fluorene triads were compared in highly diluted media and neat amorphous films. For diluted media 10^{-5} M THF solutions and polystyrene (PS) matrices were chosen to verify any excited state torsional dynamics of singly bonded triads. PS matrices doped at various (0.1-10% wt.) concentrations showed a transition from monomer to aggregate photophysical properties. Pure aggregate properties were achieved in glassy amorphous films. The glass-forming capability of the compounds as evaluated by differential scanning calorimetry (DSC) is presented elsewhere.[154] Generally, all the fluorene-carbazole triads were capable of glass formation at room temperature with glass transition temperatures (T_g) ranging from 60 to 143 °C. The triads containing only carbazole units, i.e. **CCC** and **CCC-2**, showed higher T_g as compared to those based on fluorene only or fluorene and carbazole units. Moreover, the compound **CCC-2** exhibited the highest T_g (143 °C) among the studied triads most likely resulting from the angular molecular conformation associated with its 3,6- substitution pattern. It is worth noting that high T_g of the fluorene-carbazole triads is beneficial for good morphological stability of optoelectronic devices (including organic lasers). It also ensures homogeneous glassy films, which are critical in evading optical losses due to scattering of directional amplified emission by aggregates or other inhomogeneities.[155] Moreover, amorphous nature of the films permits deposition on a variety of substrates, and therefore, provides almost effortless integration possibilities.

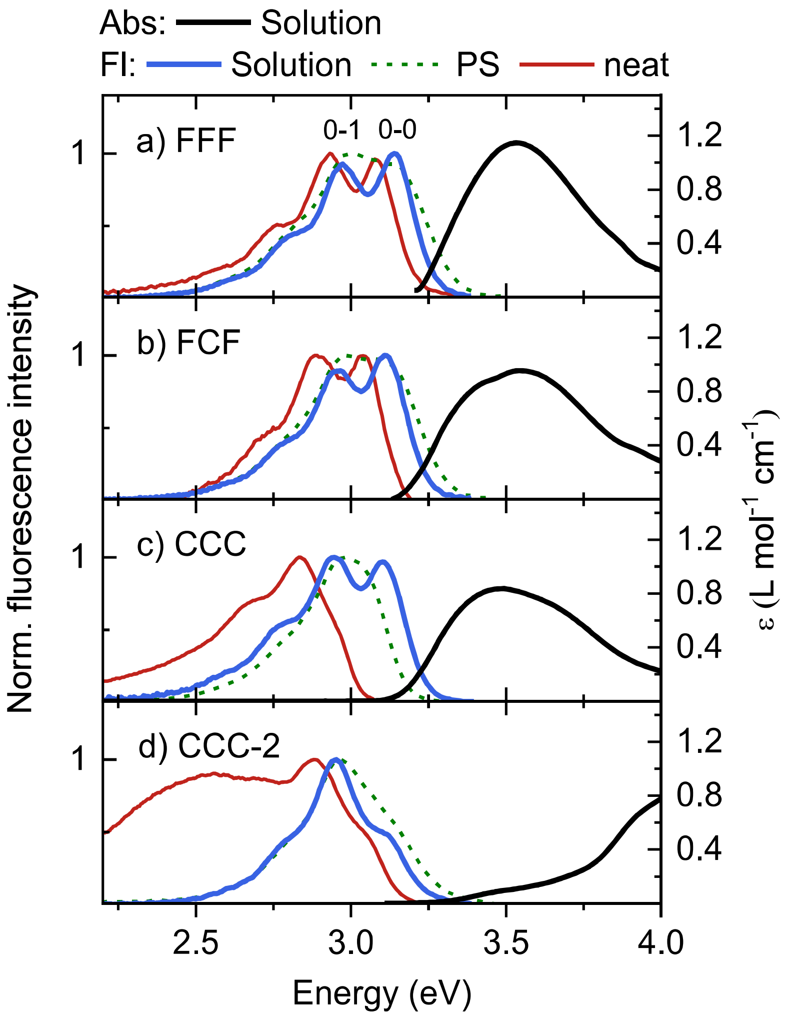

Figure 3.2. Absorption and fluorescence spectra of fluorene-carbazole triads in 10^{-5} M THF solutions (solid thick line), neat films (thin solid line) and PS matrices at 0.1% wt concentration (dashed line).

Optical properties

Absorption and fluorescence spectra of the studied fluorene-carbazole triads in dilute THF solutions, PS matrices, and neat films are shown in Figure 3.2. Broad absorption spectra with barely visible vibronic structure were likely caused by the differently twisted conformers formed due to the low-energy-barrier intramolecular twisting.[156] The largest extinction coefficient (up to ~1.2×10^5 $\mathrm{l\cdot mol^{-1}\cdot cm^{-1}}$) was found in the 2,7-substituted fluorene triad **FFF**, whereas the triad **CCC-2** featuring 3,6- substitution pattern expressed significantly smaller extinction, down to ~9×10^3 $\mathrm{l\cdot mol^{-1}\cdot cm^{-1}}$. The large extinction obtained for the 2,7-substituted triads indicates high molecular oscillator strength, which translates to lower optical pumping needed to attain ASE threshold.

Dilute solutions of the triads exhibited blue-UV emission with clearly resolved vibronic bands (Figure 3.2). Irrespectively of the substitution pattern, all the compounds displayed similar 0-0 vibronic peak energies (3.11 – 3.17 eV). The significantly lower 0-0/0-1 vibronic band ratio was observed for the carbazole-based compounds **CCC** and **CCC-2** signifing enhanced electron-vibronic coupling, which was particularly well pronounced in the compound featuring 3,6- (or angular) linking topology. Fluorescence spectra of the fluorene-carbazole triads embedded in rigid PS matrices at low concentrations (0.5 wt %) were found to be similar to the solution spectra, although with less distinct vibronic structure. This can be associated with restricted torsional planarization of molecular structures in rigid PS matrix.[157] Meanwhile the emission spectra of the neat films were apparently shifted to lower energies due to the enhanced intermolecular interaction. The triad **CCC-2** featuring the shortest alkyl (ethyl) moieties expressed additional broad structureless band peaking at ~2.6 eV, which was likely caused by excimer formation.[118]

The dilute solutions of all the fluorene-containing triads (**FFF** and **FCF**) exhibited high emission quantum yield of up to 0.95, whereas Φ_F for the carbazole-only triads (**CCC** and **CCC-2**) were considerably lower 0.22 – 0.56 (Table 3.1). Φ_F of the triads dispersed in PS matrices were estimated to be close to those of their dilute solutions with an exception of compound **CCC-2** displaying nearly 3-fold lower quantum yield ($\Phi_F = 0.08$) in the PS. This reduction of Φ_F could be explained by the suppressed intramolecular planarization of the molecules incorporated into rigid PS films. Bearing twisted geometry and angular linking topology the triad **CCC-2** (upon excitation in a solution) can exhibit geometry changes towards planarization, followed by increased conjugation and thus enhanced emission quantum yield [158–160]. Since intramolecular twisting is restricted in solid matrices, excited state planarization is unable to occur.

Reduction of Φ_F down to 4 times as compared to that in PS matrix was observed in the neat films of fluorene-carbazole triads (Table 3.1). Obviously, the reduced emission efficiency in the neat films originated from enhanced intermolecular coupling facilitating exciton migration to some quenching sites, *i.e.*, poorly-emissive aggregate or excimer species, intrinsic defects, etc. For the neat films of fluorene-containing compounds Φ_F varied from 0.32 to 0.59, whereas for the films of carbazole-only compounds it altered from 0.06 to 0.18. Note that the lowest Φ_F of 0.06 was determined for the film of **CCC-2** expressing broad unstructured and redshifted band due to excimers, which are commonly associated with non-emissive states.[118] Excimers may readily be formed in the films with tighter molecular packing, which is the case of triad **CCC-2** bearing the smallest alkyls at periphery.

Table 3.1. Fluorescence quantum yields, lifetimes and excited-state decay rates of fluorene-carbazole triads in 10^{-5} M THF solutions, 0.1 wt % PS matrices and neat films.

	THF solution				PS matrix (0.1 wt %)		Neat film	
Comp.	Φ_F [a]	τ (ns) [b]	k_r (ns^{-1}) [c]	k_{nr} (ns^{-1}) [d]	Φ_F [a]	τ (ns) [b]	Φ_F [a]	τ (ns) [b]
FFF	0.95	0.71	1.33	0.07	0.92	0.8 [100%]	0.45	0.55 [93%] 0.98 [7%]
FCF	0.9	1.26	0.66	0.07	0.86	1.3 [100%]	0.32	0.70 [90%] 1.48 [10%]
CCC	0.56	0.97	0.57	0.46	0.82	1.3 [100%]	0.18	0.14 [64%] 0.64 [32%] 3.23 [5%]
CCC-2	0.22	5.75	0.04	0.14	0.08	0.8 [14%] 7.5 [82%] 35.4 [5%]	0.06	0.24 [26%] 1.42 [66%] 5.85 [8%]

[a] Fluorescence quantum yield. [b] Fluorescence lifetime measured at band maximum. Fractional intensities of each fluorescence decay component are indicated in brackets. [c] Radiative decay rate. [d] Nonradiative decay rate.

Measurements of fluorescence transients were fitted with multi-exponential decays yielding excited state lifetimes (τ) (Figure 3.3). Fits revealed mono-exponential decay profile of the fluorene-carbazole triads in dilute THF solution with spanning the range of 0.71 – 1.26 ns excluding the compound **CCC-2**, which exhibited roughly 6-fold longer τ of 5.75 ns (Table 3.1). The substantially prolonged τ was evidently determined by the 3,6-linking topology of **CCC-2** implying reduced π-conjugation and diminished excited state relaxation rates. The lifetimes of the triads dispersed in PS matrices were found to be similar to those in dilute solution with exception of **CCC-2** expressing several additional τ components associated with different conformers. Conversely to the mono-exponential decay transients measured in the compound solutions, fluorescence decay profiles in the neat films showed highly non-exponential behavior. This behavior accompanied by the red shifted fluorescence bands in the neat amorphous films indicated dispersive exciton hopping through the localized states in disordered medium.[161] The major decay components (with fractional intensity >50%) extracted by fitting the transients with two- or three-component exponential decay models were significantly shortened as compared to τ obtained for the compounds in PS films (see Table 3.1). The shortened τ in the neat films nicely correlated with the reduced Φ_F, which was previously assigned to enhanced excitation migration to nonradiative traps.

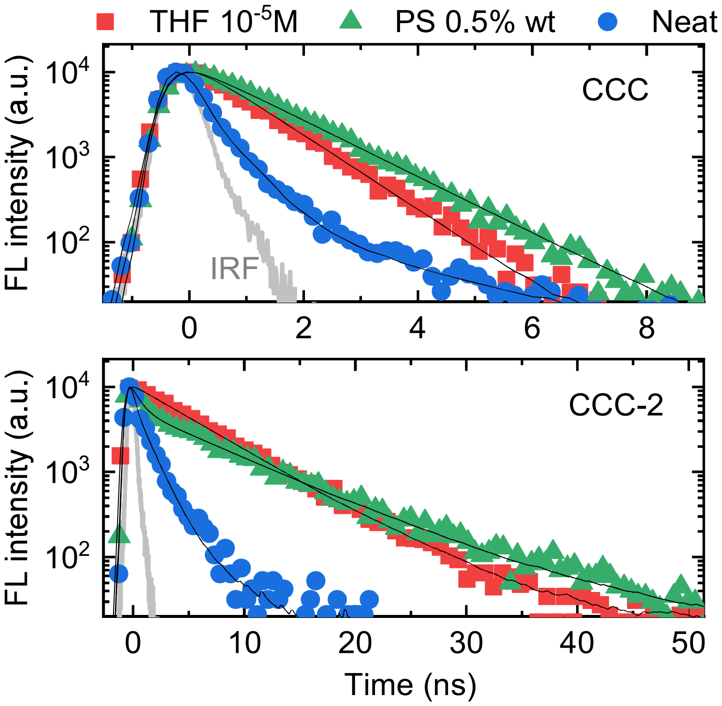

Figure 3.3. Fluorescence transients and corresponding exponential fits of carbazole triads in 10^{-5} M THF solutions (red squares), PS matrices at 0.5% wt concentration (green triangles) and neat films (blue circles). Transients were measured at the maximum of Fl spectra. Instrument response function is indicated.

The calculated radiative (k_r) and non-radiative (k_{nr}) decay rates are listed in Table 3.1. Generally, k_r values in the 2,7-substituted triads were found to be very high (up to 1.33×10^9 s^{-1}) and comparable to the best performing compounds for organic lasers.[76,82] Whereas more than one order of magnitude lower k_r was estimated for the **CCC-2** triad featuring 3,6- linking topology. Markedly lower k_{nr} as compared to k_r obtained for fluorene-containing triads evidenced domination of radiative processes, which are essential for light amplification. Large k_r was shown to benefit in attaining low ASE threshold in lasing materials.[82]

Higher k_{nr} values for carbazole containing triads can be justified by enhanced ISC losses to triplets appearing due to different alignment of triplet levels. Triplet state energies (E_{Ph}) of the fluorene-carbazole triads were evaluated from the phosphorescence spectra measured at 20 K (Figure 3.4). Clear evidence of the increasing triplet energy with the increased number of carbazole moieties in the triads was observed. All-fluorene containing compound **FFF** exhibited the lowest E_{Ph}. Whereas for all-carbazole containing 3,6- substituted triad **CCC-2** highest E_{Ph}. It is well-known that the exchange energy, and thus the position of the triplet state energy in respect to the singlet, strongly depends on the electron wave function overlap in the highest occupied molecular orbital (HOMO) and lowest unoccupied molecular orbital (LUMO).[151] The smaller overlap, and therefore the higher E_{Ph}. Additionally, the overlap can be reduced by the introduction of heteroatom as in carbazole unit, which creates perpendicularly orientated non-bonding orbitals and localizes LUMO closer to nitrogen atom. The similar reduction of exchange energy for 3,6-substituted carbazoles due to the angular linking topology was also recently reported.[163,164]

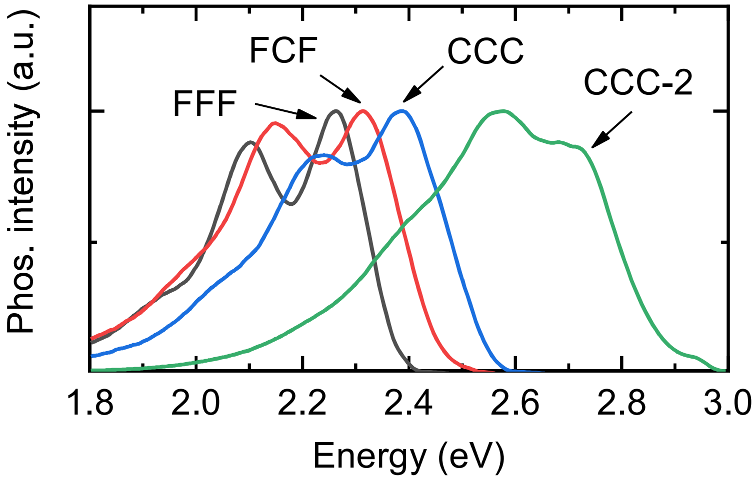

Figure 3.4. Normalized phosphorescence spectra of the fluorene-carbazole triads dispersed in PMMA matrix at a concentration of 4.0 wt %.

Concentration quenching

In addition to intramolecular emission quenching mechanisms discussed previously, intermolecular emission quenching followed by increasing chromophore concentration is a serious issue limiting utilization of highly emissive compounds in the neat form for light-emitting device applications. Realization of efficient laser requires low ASE threshold, and hence high k_r and Φ_F to be maintained at high chromophore concentration.[72,155] Strong intermolecular interactions between closely packed chromophores can lead to reduced k_r or formation of weakly emissive CT or excimer states that act as excitation traps.[109]

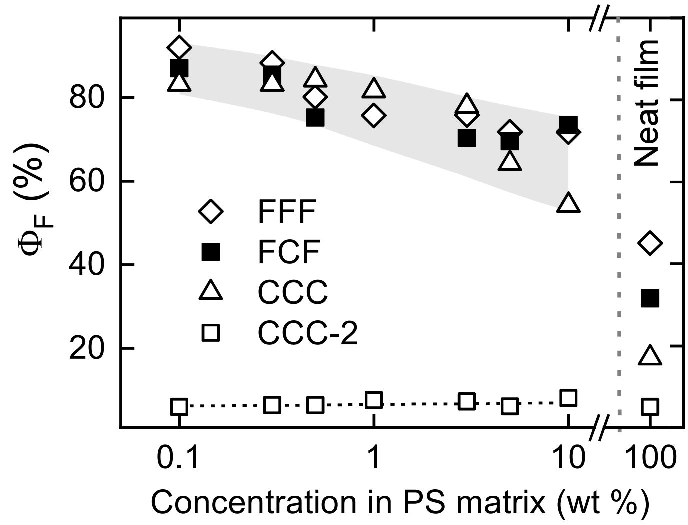

Figure 3.5. Fluorescence quantum yields of the fluorene-carbazole triads as a function of their concentration in PS matrix.

Concentration quenching in fluorene-carbazole triads was investigated by dispersing them in a rigid polystyrene matrix and estimating Φ_F changes as a function of compound concentration in the range of 0.06-100 wt % (Figure 3.5). At low concentrations Φ_F values approached those of non-interacting molecules of the triads in dilute solutions (see Table 3.1). Importantly, increasing the chromophore concentration up to 10 wt % revealed relatively weak quenching effect resulting in a less than 20% reduction of the initial Φ_F values. The smaller drop in efficiency, thus weaker concentration quenching was experienced by **FFF** and **FCF** bearing the bulky dihexyl and ethylhexyl groups linked to the 9th position of central unit. This was particularly clearly seen from the Φ_F values of the compound neat films, *i.e.* when compound concentration was 100%. Meanwhile carbazole triads **CCC** and **CCC-2** showed more pronounced quenching as can be evidenced from rapid decay of strongly non-exponential fluorescence transients of neat films (see Figure 3.3 and Table 3.1) and appearance of low energy band in emission spectra (see Figure 3.2). This is associated with formation of low energy CT and excimer states due to stronger orbital overlap of heteroatom containing carbazole units. Interestingly, k_r values were found to be similar for aggregates in amorphous neat films to the ones of monomers dispersed in solid PS matrix indicating weak excitonic coupling.[165] Although ASE properties are mostly determined by k_r, aggregates formed in neat films can act as emission scattering centers preventing light amplification in a nonhomogeneous waveguide.[155]

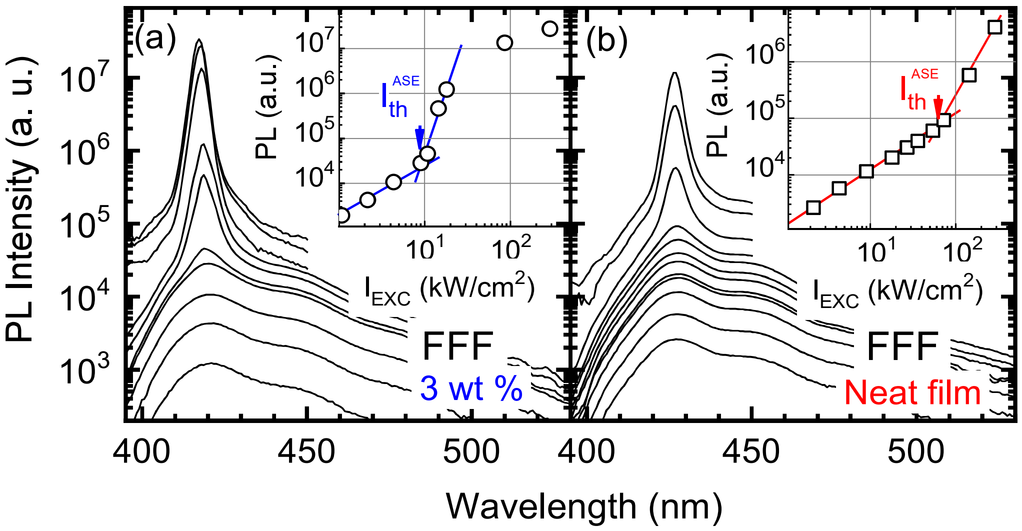

Figure 3.6. Excitation power dependence of the edge emission spectra of **FFF** triad molecularly dispersed in PS matrix at 3 wt % concentration (a) and the neat film (b). Insets show emission peak intensity *vs* excitation power density (I_{exc}). Excitation was set to 355 nm (3.55 eV).

Amplified spontaneous emission

ASE properties of the triads were examined in a PS matrix at different compound concentrations to reveal the concentration effects on the ASE performance. All the triads showed ASE behavior above the threshold pump density except for the triad **CCC-2**, for which ASE could not be attained even at the highest pumps due to very low k_r (see Table 3.1) in addition to the low absorption at the excitation wavelength (355 nm). Figure 3.6 shows edge emission spectra of **FFF** in PS matrix and neat film for nanosecond (5ns) pump pulse excitation at different fluence. The dynamics are presented for the optimal compound concentration (3 wt %), for which minimal I_{th}^{ASE} value was obtained. It is worth noting that ASE was also attained in the neat films of most triads, though at somewhat higher I_{th}^{ASE}. At low excitation power densities all the triads demonstrate spontaneous emission spectra reabsorbed at the high energy side due to long excitation path though the sample. An increase in the excitation power density resulted in the emission band narrowing indicating an onset of the ASE. The ASE band emerged roughly at the spectral position of the first (0-1) vibronic transition (or at the maximum of the reabsorbed edge-emission band), which is typical for a quasi-four-level vibronic system.[166] The sudden emission band narrowing with the increasing pump was followed by an abrupt change in the slope of emission intensity from linear to superlinear at I_{th}^{ASE} (see insets of Figure 3.6). The details of the ASE properties for the fluorene-carbazole triads are summarized in Table 3.2.

Table 3.2. ASE properties of the fluorene-carbazole triads molecularly dispersed in PS matrix at their optimal concentration.

Compound	c_{opt} [a] (wt %)	λ_{ASE} [b] (nm)	I_{th}^{ASE} (kW/cm^2)	FWHM [c] (nm)	k_r [d] (ns^{-1})
FFF	3	419	9	5	1.1
FCF	3	421	15	5	0.6
CCC	0.5	424	13	6	0.7
CCC-2	ASE has not been attained				0.01

Concentration dependences of I_{th}^{ASE} for the triads **FFF**, **FCF** and **CCC** dispersed in PS matrix are illustrated in Figure 3.7. The determination of I_{th}^{ASE} describes the feasibility of the material to be employed as an active medium in organic lasers. Additionally, these investigations are indispensable for determination of the optimal compound concentration (c_{opt}) for laser operation,[156,167] since intermolecular coupling is known to crucially affect Φ_F, k_r and I_{th}^{ASE}.[91]

Essentially, the ASE performance of the fluorene-carbazole triads was found to be rather sensitive to their concentration in PS matrix. At low concentrations I_{th}^{ASE} decreased with increasing concentration, whereas at high concentrations it increased clearly indicating an optimal compound concentration for which I_{th}^{ASE} is the lowest. The c_{opt} range for the studied triads was found to vary between 0.5 and 3 wt % (Table 3.2). Increasing compound concentration up to 0.5 – 3 wt % reduced intermolecular separation causing higher absorption coefficient, and thus lowering of the I_{th}^{ASE}. However, further increasing concentration resulted in the enlarged I_{th}^{ASE} (see Figure 3.7) likely due to the concentration quenching effects, commonly associated with non-emissive molecular aggregates, excimer species, intrinsic defects or other "dark" states. Fluorescence microscopy measurements of the fluorene-carbazole triads (except for **CCC-2** with the smallest alkyls at periphery) performed at the highest compound concentrations in PS matrix indicated homogeneous amorphous films. This ruled out the presence of aggregates (at least bigger ones with sizes >10^2 nm) and associated optical losses due to aggregate absorption/scattering. However, the lowest c_{opt} of 0.5 wt % obtained for the triad **CCC** signified its increased tendency for aggregation.

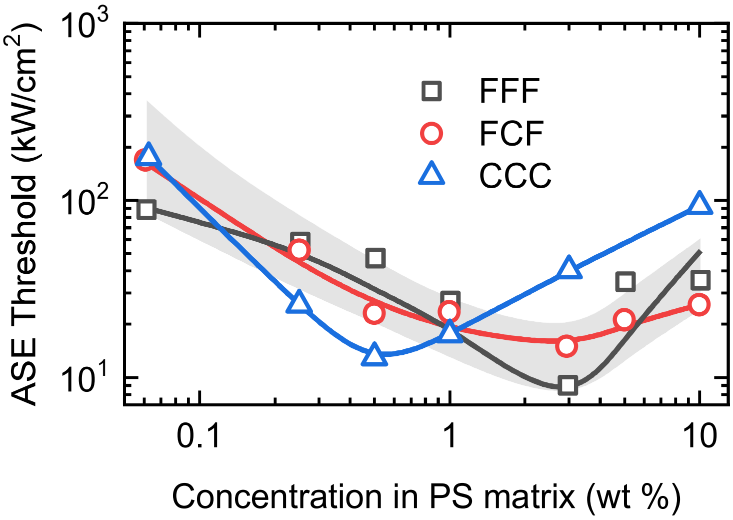

Figure 3.7. ASE threshold as a function of compound concentration in a PS matrix. Lines are guides for the eye.

The I_{th}^{ASE} values estimated at c_{opt} varied in the range of 9 - 17 kW/cm^2. All-fluorene containing triad **FFF** demonstrated the lowest I_{th}^{ASE} (9 kW/cm^2) among the studied fluorene-carbazole triads, which could be justified by the largest k_r. The calculated k_r values of the triads dispersed in PS matrix at c_{opt} concentration are presented in Table 3.2. Obviously, a clear anticorrelation between radiative decay rate and ASE threshold was evidenced, *i.e.*, larger k_r values cause reduction of I_{th}^{ASE} in the compounds. This can be explained by the direct relation of k_r and stimulated emission cross-section. I_{th}^{ASE} value of 9 kW/cm^2 (45 μJ/cm^2) achieved for the wet-casted **FFF** film in air was found to be comparable to that reported for various oligofluorenes[78,168] and polyfluorenes.[169,170] Generally, ASE thresholds for the **FCF** and **CCC** triads differed by less than 2-fold signifying the importance of the central position of fluorene moiety in the triad. Furthermore, the study revealed a huge advantage of 2,7- substitution pattern over 3,6- pattern for the triads in terms of ASE performance. In this regard 2,7-substituted fluorene-carbazole triads were found to be far more superior for lasing application.

The stability of the triads was evaluated in terms of photostability lifetime defined as the number of pump pulses resulting in a decrease of ASE intensity to half its initial value. For this, ASE intensity was monitored as a function of the number of pump pulses at the pump density twice as high as the ASE threshold at c_{opt}. The estimated photostability lifetime was found to be slightly above 1×10^4 pump pulses (excitation pulse duration – 5 ns, laser frequency – 10 Hz) for all ASE-expressing fluorene-carbazole triads and was comparable to the lifetimes of other fluorene-based organic compounds tested under similar conditions.[155,171]

Aiming for practical applications in optical communication carbazole-fluorene triads were tested for production of random lasers based on electrospun light-emitting polymer fibers.[172,173]

Highlights

- Blue-emitting fluorene-carbazole triads with different linking topologies were evaluated as potential compounds for light amplification.
- The twisted molecular structure and bulky peripheral moieties in the compounds ensured formation of stable amorphous films.
- High emission quantum yields (0.8 – 0.9) and large radiative decay rates (~10^9 s^{-1}) accompanied by weak concentration quenching of emission enabled to attain rather low amplified emission thresholds (down to 9 kW/cm^2) for compound concentrations up to 3 wt % in polymer matrix.
- Incorporation of nitrogen heteroatoms (carbazole moiety) in triads was found to influence higher intramolecular non-radiative losses due to enhanced intersystem crossing to triplets as well as more pronounced intermolecular interactions leading to formation of non-radiative trap states.
- 2,7- linking topology of triads were determined to be far superior for lasing application as compared to 3,6- topology.

3.2 Effects of molecular torsion in crystals

To this day, the best performing organic gain media for light amplification are thin amorphous films exhibiting low ASE thresholds in the range of 100 W/cm^2 (1 μJ/cm^2).[23,76,83,174,175] Meanwhile, an order of magnitude higher ASE thresholds for organic crystals are caused by losses associated with strong intermolecular coupling.[91] Although ASE in the crystals with both H- and J-type excitonic coupling was observed, the strong coupling for both types possesses serious drawbacks such as reduced radiative decay in the H-aggregates or enhanced reabsorption and exciton annihilation in J-aggregates. Thereby, weak excitonic coupling in crystals would allow to retain monomer-like photophysical properties as in amorphous films, while still taking advantage of densely packed and highly aligned emitters. The resonance condition for excitonic coupling between neighboring chromophores in crystal lattice is disturbed by introduction of energetic disorder.[109] This can be readily achieved in molecules incorporated with single-bonded phenyl rings bearing torsional degrees of freedom.[176] Furthermore, enhanced electron-vibronic coupling (Huang-Rhys factor) on the intramolecular level contribute to higher Stokes shift, and thus lower reabsorption losses. Taking all this into account, molecules exhibiting strong electron-vibronic coupling yet capable to form crystals with weak excitonic coupling hold great potential for light amplification.

To this end, two bifluorene compounds featuring non-rigid twisted structure composed of singly bonded phenyl core and out-of-plane twisted dimethyl moieties attached at the fluorene end-groups (for increased intermolecular spacing) were designed (see Figure 3.8). The compounds **BF-p** and **BF-2p** contain either single phenyl or biphenyl core to reveal the effects of conjugation length (that is directly related to radiative rate) on ASE properties. Ground-state geometry optimization of the bifluorene compounds revealed twisted molecular backbone with dihedral angles of approximately 36° between all the neighboring fragments.[177] As expected, dimethyl moieties attached to the fluorene end-groups were oriented perpendicularly to the plane of fluorene units, providing increased intermolecular separation and particular molecular packing in the crystalline phase (see Figure 2.8).

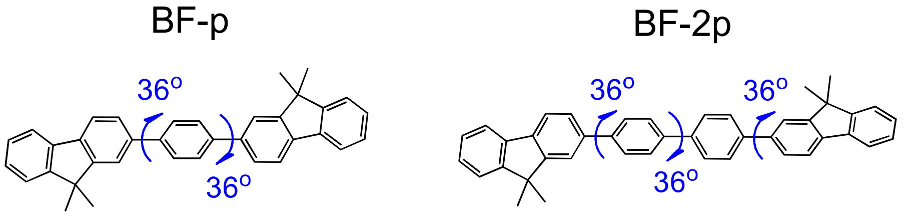

Figure 3.8. Optimized geometry of bifluorene compounds **BF-p** and **BF-2p**.

To distinguish intra- and intermolecular contributions on photophysical properties, bifluorene compounds were investigated in diluted cyclohexane (CH) solutions, at low concentrations in polystyrene (PS) matrix as well as in single crystals grown by PVT method. Liquid media of viscous and non-polar CH solutions allows to probe the torsional excited state dynamics of phenyl containing bifluorene monomers. Meanwhile, increased rigidity of inert PS matrix should restrict torsional motion without affecting the electronic properties of the non-interacting monomers. In contrast, close molecular packing in crystalline structure is often thought to eliminate torsional degrees of freedom due to Van der Walls interactions. Furthermore, comparing photophysical properties of monomers in diluted media and molecular aggregates in crystals is a straightforward approach to evaluate the type and magnitude of excitonic coupling.

Vibronic and excitonic coupling in crystals

The characteristic features of vibronic and excitonic coupling are encoded in absorption and photoluminescence spectra.[109] Figure 3.9 displays UV-Vis spectral bands of the bifluorene compounds in various media. CH solutions of both bifluorene compounds were found to exhibit strong absorption bands in the UV range extinction coefficients of well over 10^4 M^{-1} cm^{-1}. Higher extinction coefficient and slightly lower optical transition energy of **BF-2p** compared to shorter **BF-p** derivative is associated with enhanced oscillator strength and extended conjugation length. Broad and structureless absorption bands of the compounds indicated presence of variety of conformers in the ground state. On the other hand, well-resolved vibronic progression in the PL spectra of CH solutions most likely signified only the emissive conformers. Planarization of highly twisted conformers in the excited state is a typical feature of singly bonded phenylene and fluorene oligomers.[176,178] Broader emission peaks recorder in the rigid PS matrix indicates emission from twisted conformers due to restricted planarization. A comparable intensity of 0-0 and

0-1 vibronic bands indicating Huang-Rhys (HR) factor of $\lambda^2 = 0.9$ and the large Stokes shift of 0.5 eV confirmed an enhanced electron-vibronic coupling feasible for molecules with flexible backbone.

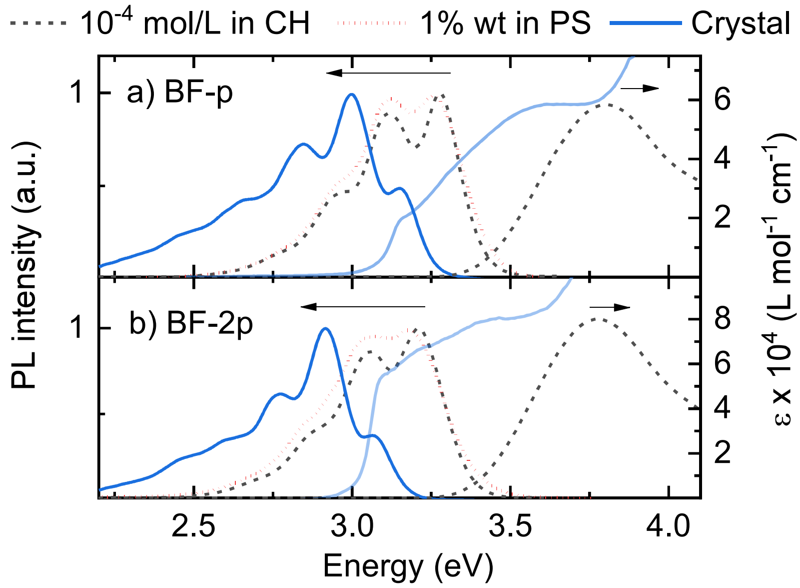

Figure 3.9. Absorption and photoluminescence spectra of **BF-p** and **BF-2p** CH solutions, PS films and single crystals. Molar extinction coefficient of **BF-p** crystal was normalized to that of a solution.

The intermolecular interactions appearing between closely packed molecules in crystals are signified by significantly reduced optical transition energy. More than 100 meV shift to lower energies was observed for crystal PL spectra of both bifluorene derivatives compared to monomer spectra recorded in diluted media (Figure 3.9). Such shift typically appears due to dispersive interactions between chromophores.[4,109] Some indications of excitonic coupling can be obtained from change of HR factor of crystal PL spectra. Significantly increased HR factor ($\lambda^2 > 2$) compared to that of a monomer suggest H-type excitonic coupling in crystals. However, at this point strong reabsorption effects cannot be excluded, which may distort 0-0 intensity in highly absorbing crystals. Reabsorption may be caused by low energy absorption features at 3.15 eV and 3.10 eV for **BF-p** and **BF-2p** crystals, respectively, overlapping with 0-0 peak of crystal emission. These low energy features may originate from CT interactions between neighboring chromophores or from large amount of impurities in crystals. Interestingly, absorption spectra of **BF-p** crystal at energies above low energy band exhibited lack of vibronic features similar to that of monomer in diluted CH solution (Figure 3.9). This implied some torsional disorder despite enhanced intermolecular interactions in crystal.

Another reliable indicator of excitonic coupling in crystals is the change of radiative rate of aggregates compared to monomers. Figure 3.10a shows spectrally-integrated excited state relaxation dynamics of bifluorene compounds dispersed in 1 wt% PS films as well as of their single crystals. The summarized optical properties are presented in Table 3.3. In PS films the bifluorene compounds exhibited single exponential decay profiles with decay time constants (τ_{PL}) of 0.67 ns and 0.58 ns for **BF-p** and **BF-2p**, respectively. High fluorescence quantum yields (Φ_{PL} ~0.9) estimated for the compounds in PS films confirmed the radiative decay to be the major excited state relaxation pathway. Estimated substantial radiative decay rates ($k_r = \Phi_{PL}/\tau_{PL}$) of **BF-p** (1.30 ns^{-1}) and **BF-2p** (1.55 ns^{-1}) and nearly an order of magnitude lower nonradiative rate ($k_{nr} = [1-\Phi_{PL}]/\tau_{PL}$) hint the superiority of compounds for light amplification.

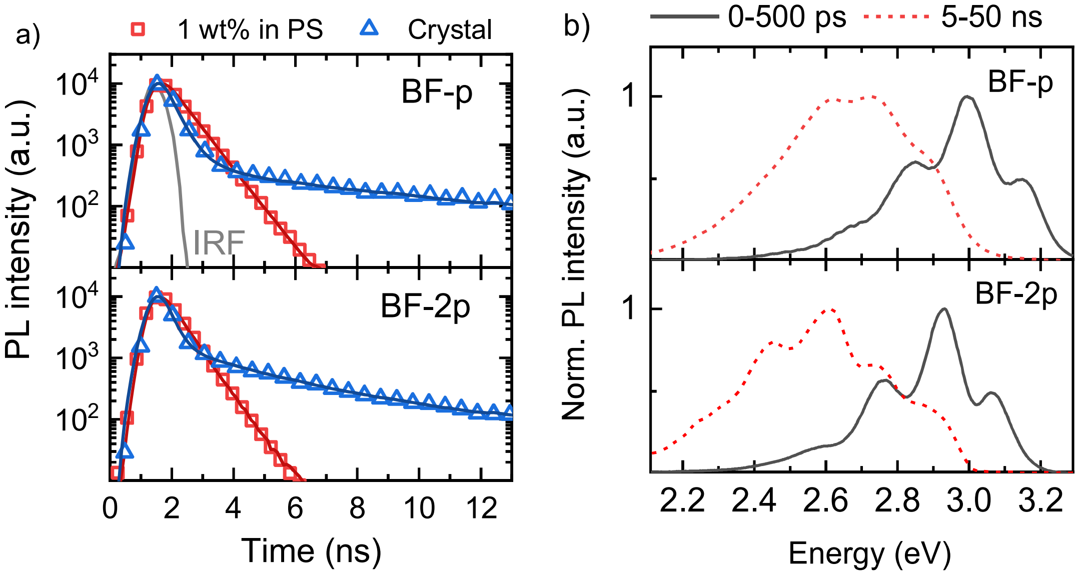

Figure 3.10. (a) Spectrally-integrated photoluminescence decay transients in 1 wt% PS films and single crystals. Solid lines indicate exponential decay fits of the transients and instrument response function (IRF). (b) Time resolved PL spectra of the bifluorene single crystals obtained by integrating over 0-500 ps and 5–50 ns time windows.

Interestingly, PL transients of bifluorene single crystals displayed multi-exponential behavior with the dominant decay component (with fractional intensity >50%) 2-fold shorter as compared to τ_{PL} determined in PS films. The transients additionally contained long-lived decay component (τ_{PL} ~10 ns), which was associated with different excited state. To reveal the spectral features associated with short- and long-lived decay components in bifluorene single crystals PL spectra were time-integrated over the initial 500 ps after the laser pulse and 5 – 50 ns, respectively (Figure 3.10b). The PL spectra corresponding to short-lived decay component showed clear vibronic features. On the other hand, long-lived PL components were found to be much broader and considerably shifted to the lower energies. The onset of long-lived emission at around 3.0 eV coincided with the low energy absorption feature present in both bifluorene crystals (see Figure 3.9). The low radiative rate ($k_r \approx 0.02$ ns^{-1}) of the long component suggested that its origin may be associated with CT or excimer type transition.[109] Such transitions become possible when intermolecular distances become close enough to produce orbital overlap. Another possibility is the formation of keto defects at 9th position of the fluorene leading to weakly emissive fluorenone, which shows similar k_r values.[179–181] Generally, the long-lived states are unimportant to amplification process and does not affect pulsed excitation ASE threshold since stimulated optical transitions occur from short-lived states (bearing high radiative rate) prior to energy transfer to trap states. However, considering continuous wave excitation conditions, long-lived trap states can become a considerable loss channel.

Table 3.3. Fluorescence lifetime, decay rates and fluorescence quantum yield of bifluorene compounds in 1 wt% PS films and single crystals.

	1 wt% PS film				Single crystal		
Comp.	Φ_{PL}[a)]	τ_{PL} (ns)[b)]	k_r (ns^{-1})[c)]	k_{nr} (ns^{-1})[d)]	Φ_{PL}[a)]	τ_{PL} (ns)[b)]	k_r (ns^{-1})[c)]
BF-p	0.87	0.67	1.30	0.19	0.61	0.35 [69%] 8.9 [31%]	1.20
BF-2p	0.90	0.58	1.55	0.17	0.65	0.25 [53%] 10.0 [47%]	1.38

[a)]Photoluminescence quantum yield; [b)] Photoluminescence decay time. Numbers in brackets show fractional intensity; [c)]Radiative decay rate; [d)]Nonradiative decay rate.

The effects of excitonic coupling in crystals can be evaluated by the relative change of radiative rate of the fast component compared to that of a monomer. Considering that fraction of the fast component of the spectrally integrated transients presented in Table 3.3 represents its relative emission efficiency, the k_r values of 1.20 ns^{-1} and 1.38 ns^{-1} were estimated for **BF-p** and **BF-2p** single crystals, respectively. These radiative rates of aggregate states in crystals were only slightly below those recorded for monomers in diluted PS matrix implying weak excitonic coupling in the bifluorene-based single crystals. One of the possible explanations for weak excitonic coupling is that intermolecular arrangement in the single crystals is close to the point where inversion from H-type to J-type aggregates occurs (see Figure 1.7).[91] Such arrangement was confirmed by XRD measurements of **BF-p** single crystal (displayed in Figure 2.8) and is most likely is imposed by dimethyl moieties on the fluorene end-groups. On the other hand, torsional disorder imposed by rotation of central phenyl fragments can also inhibit exitonic coupling between neighboring molecules in the crystal lattice.

Torsional dynamics

The excited state conformational reorganization of single bonded fluorene oligomers typically occurs within tens of picoseconds.[157] Torsional relaxation dynamics are observed in highly viscous media, where in rigid media such as PS matrix or crystals torsional motion is often considered to be restricted. To resolve ultrafast excited state dynamics of bifluorene derivatives femtosecond transient absorption technique was employed.

Transient absorption spectra of **BF-p** and **BF-2p** in diluted CH solutions are displayed in Figure 3.11a-b. Typically to other fluorene-based compounds the measured excited state absorption spectra (ESA) correspond to the Franck-Condon transitions from S_1 ($1B_u$) to S_n (mA_g) with the major bands peaking in the 1.6-1.8 eV range (Figure 3.11c).[182,183] The absorption cross section of the dominant features agreed well with the one measured for fluorene triads.[182] Interestingly, ESA spectra of **BF-2p** indicated higher HR factor compared to **BF-p** suggesting stronger vibronic coupling of double phenyl core bifluorene molecule. However, this was not reflected in the PL spectra (see Figure 3.9). Furthermore, TA measurements revealed that ESA features of both bifluorene derivatives do not reach maximum intensity until approximately 20 ps after excitation. The risetime clearly indicates some conformational dynamics occurring within picosecond timescale, which can be controlled with optical excitation energy or viscosity of the surrounding media. Figure 3.11d shows transients of the 1.75 eV ESA feature recorded for **BF-p** in CH solution and

PS matrix with excitation photon energy set at the absorption maximum (3.75 eV) and below (3.44 eV). Excitation with higher energy quanta results in absorption of conformers with higher twist angles, therefore fast excited state conformational relaxation is more pronounced than for lower energy excitation. In contrast, no risetime was observed in rigid PS matrix indicating restricted conformational relaxation. Restricted planarization in rigid media compared to viscous solution agrees with broader vibronic features observed in the PL spectra (see Figure 3.9). Similar ultrafast torsional relaxation (planarization) in solution was previously observed for fluorene oligomers.[157]

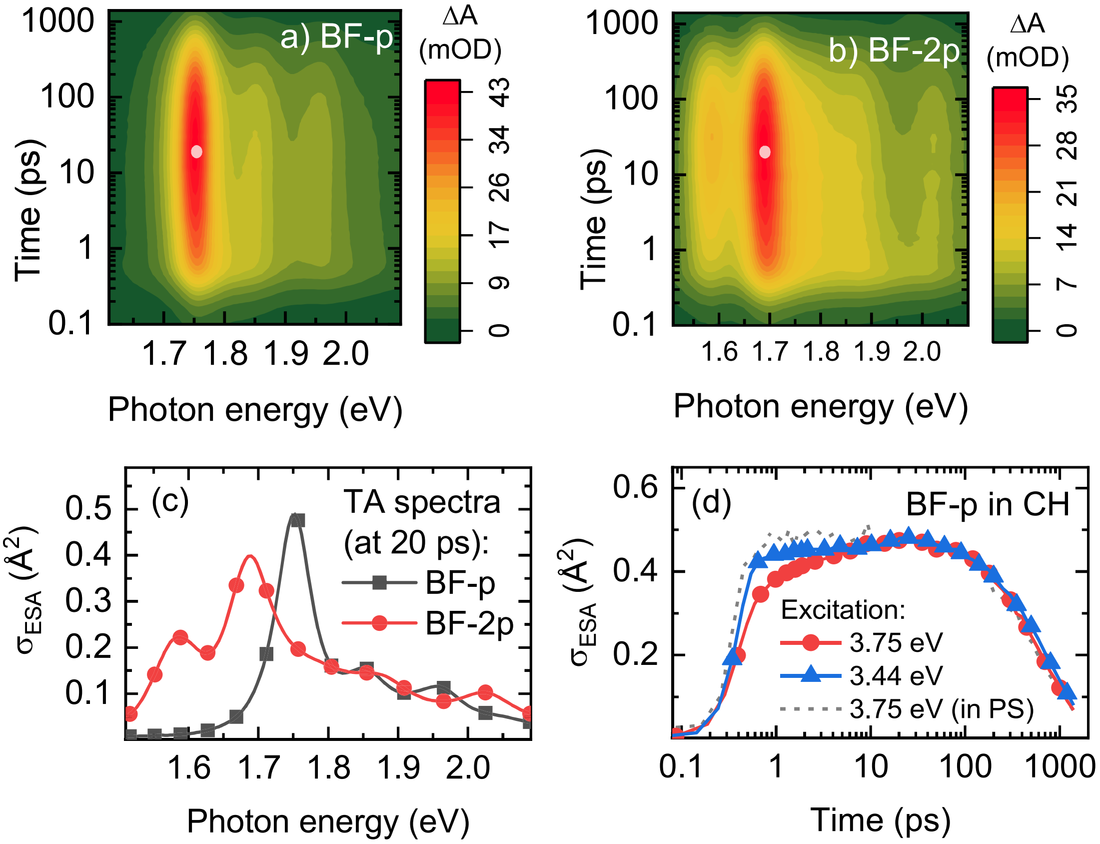

Figure 3.11. Transient absorption maps of (a) **BF-p** and (b) **BF-2p** in 10^{-4} M^{-1} CH solutions. Excitation photon energy was set at absorption band maximum (3.75 eV). (c) Transient absorption spectra at 20 ps delay time. (d) Transients of 1.75eV ESA feature recorded in **BF-p** CH solution with different excitation photon energy. Transients recorded for **BF-p** in rigid PS matrix are given in dashed line.

Despite stronger intermolecular interactions restricting conformational dynamics in the crystalline medium, some evidence of torsional motion can still be obtained by means of ultrafast spectroscopy. The low energy of torsional modes are in the 100 cm^{-1} (~0.01 eV) range, which enables to coherently excite a manifold of vibrational levels with energetically broad femtosecond pulses.[5,184,185] This creates a wave packet oscillating in the vibrational potential with the oscillation period corresponding to the energy of the torsional mode. Figure 3.12a shows the transient absorption spectra recorded for **BF-p** single crystal. Global fit of the transient absorption data with single exponential decay resulted in residual signal showing oscillatory behavior in the early times after excitation (Figure 3.12b). The observed oscillation period of 420 fs corresponds to 80 cm^{-1} vibrational mode that can be associated with torsional motion of the central phenyl ring. The 180° phase shift is in accordance with the torsional motion leading to a minimum in the excited potential energy surface, where maximum amplitude is observed at the edge of the potential energy surface (Figure 3.12c).[185] Interestingly, oscillatory behavior was not observed for **BF-2p** crystal suggesting that synchronized torsional motion of two phenyl rings moving at opposite phase cancel out the absorption signal.

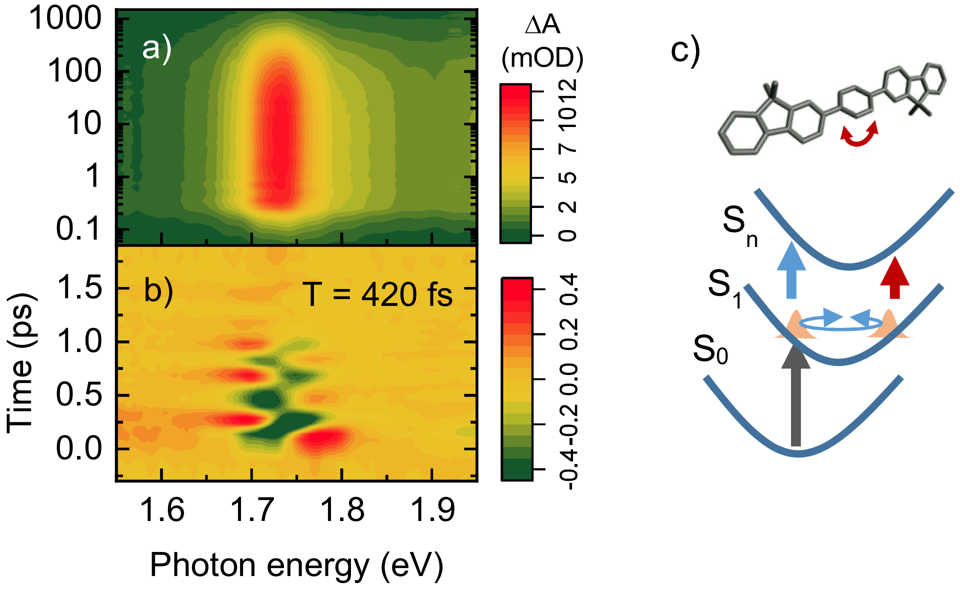

Figure 3.12. (a) Transient absorption map of **BF-p** crystal excited with 3.75 eV 200 fs laser pulse. (b) Map of residuals from global fit of the transient absorption data with single exponential (τ=350 ps) decay profile. Oscillation period is indicated. (c) Scheme illustrating coherent wave packet dynamics, explaining how torsional modes create the observed oscillations.

Excitonic coupling

The observation of low energy torsional modes in **BF-p** crystal clearly indicates that stronger intermolecular interactions between closely packed chromophores do not suppress torsional motion of the central ring. The low energy of torsional modes allows to populate them at room temperature ($k_B T \approx$ 25 meV) creating a conformational disorder in the crystal. In turn this inhibits excitonic coupling between neighboring chromophores.[109] Absorption and PL spectra of **BF-p** crystal measured at different temperatures are displayed in Figure 3.13. Upon lowering of the temperature vibronic features of the absorption spectra become apparent due to reduced dynamic disorder. The reduced broadening of absorption spectra determines lower overlap with PL spectra, and thus weaker reabsorption, which results in slight recovery of 0-0 PL peak intensity. Except that, the ratio of the 0-0 and 0-1 PL peaks remains almost constant throughout the temperature range signaling weak excitonic coupling in **BF-p** crystal.[109]

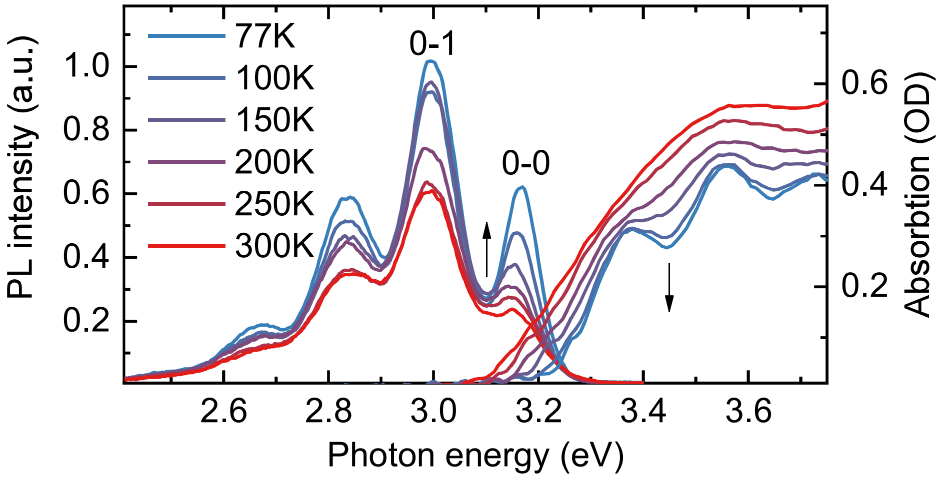

Figure 3.13. Temperature dependent time-integrated PL and absorption spectra of **BF-p** crystal measured in 77 – 300 K range. Arrows indicate the trend with reduced temperature.

The overall increase of the time-integrated PL intensity of **BF-p** crystal displayed in Figure 3.13 signals the enhanced PL quantum yield at low temperatures. This can be explained by temperature-dependent Forster energy transfer to the non-radiative defects. The temperature activated behavior of energy transport in **BF-p** crystal is evident from the enhanced overlap between absorption and emission at room temperature (Figure 3.13). At low temperatures overlap becomes negligible, therefore energy transfer to non-radiative trap states should be suppressed. Figure 3.14a illustrates the transients of **BF-p** single crystal measured at 0-0 vibronic peak (~3.15 eV) as a function of temperature. Evidently, lowering temperature suppresses non-radiative losses, which slows down PL decay resulting in the increased τ_{PL}.

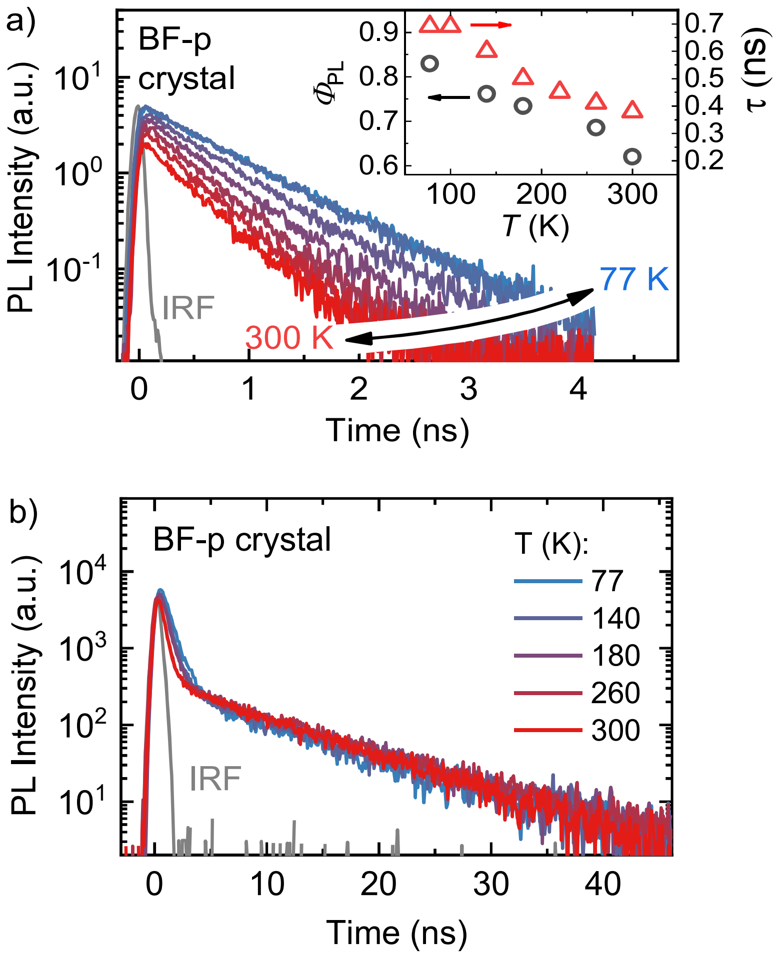

Figure 3.14. (a) PL decay transients of **BF-p** single crystal measured at 0-0 vibronic peak at different temperatures. Inset shows Φ_{PL} and τ_{PL} as a function of temperature. (b) Spectrally integrated transients including the long-lived component.

The corresponding enhancement of Φ_{PL} with decreasing temperature was also observed (Figure 3.13). Interestingly, PL transients show enhancement of PL intensity at initial times upon reduction of temperature. In this case, enhancement of Φ_{PL} at low temperatures cannot be fully explained by suppression of non-radiative losses and may also be related to enhancement of radiative rate or reduced reabsorption losses. Importantly, at temperatures below 100 K, fluorescence lifetime and PL quantum yield in the single crystal reaches the values of 0.69 ns and 0.83, respectively, which are very close to those of single molecules dispersed in PS matrix (see Table 3.3). This is yet another indication of weak excitonic coupling in **BF-p** crystals.

Furthermore, the temperature resolved transients of the long-lived component revealed no change upon reduction of temperature (Figure 3.14b). This suggested that long-lived weakly emissive states observed in Figure 3.10 were not populated via short-lived states. Similar temperature dependent dynamics were also recorded for **BF-2p** single crystals (not shown here) implying the temperature activated energy transfer to non-radiative trap states.

It was found that conformational disorder induced by torsional motion of phenyl ring is present in solutions as well as single crystals of both phenyl-cored bifluorene compounds. Here, disorder in crystalline medium plays an important role as it prevents strong resonant excitonic coupling between. Weak excitonic coupling accompanied with moderate vibronic coupling (higher Huang-Rhys factor) are desirable in crystals aiming for lower reabsorption losses and superior amplified emission properties.

Amplified spontaneous emission

Amplified spontaneous emission properties of **BF-p** and **BF-2p** were investigated by using thin excitation stripe technique. ASE properties of the bifluorene compounds were examined in PS matrix as well as in single crystals. Figure 3.15a shows typical excitation power dependence of the edge emission spectra of **BF-2p** dispersed in PS film at a concentration of 1 wt%, whereas such dependence for **BF-2p** single crystal is displayed in Figure 3.15b.

Generally, broad spontaneous emission bands at low pump density transform to spectrally narrower bands with the increasing pump intensity above the onset of ASE. The ASE bands of the single crystals are narrower as compared to those of compounds in PS films due to significantly diminished inhomogeneous broadening in highly ordered crystalline phase. The ASE peaks emerge at the 0-1 vibronic replica due to the reabsorption of higher-energy slope of edge emission spectra. The emission band narrowing with increasing pump is followed by an abrupt change in the emission intensity profile from linear to superlinear at I_{th}^{ASE} (see insets of Figure 3.15). I_{th}^{ASE} values of **BF-p** and **BF-2p** in PS matrix and single crystals are presented in Table 3.4.

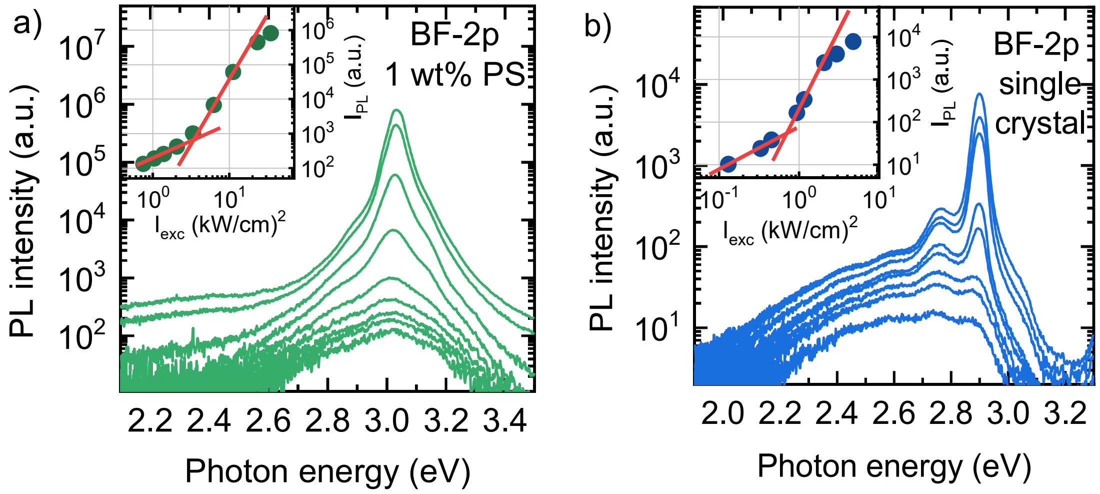

Figure 3.15. Excitation power dependence of the edge emission spectra of **BF-2p** in a) 1 wt% PS film and b) single crystal**.** Insets show emission peak intensity *vs.* excitation power density ($I_{exc.}$). Excitation was set to 3.55 eV.

Table 3.4. ASE thresholds and radiative rates of the bifluorenes in PS matrix and single crystals.

Comp.	1 wt% PS film		Single crystal	
	I_{th}^{ASE} (kW/cm^2)	k_r (ns^{-1})	I_{th}^{ASE} (kW/cm^2)	k_r (ns^{-1})
BF-p	4.8	1.30	1.8	1.20
BF-2p	3.3	1.55	0.7	1.38

An increase of compound concentration above 1 wt% in PS matrix caused steep increase of the threshold values due to emission scattering induced by formation of microcrystals in the polymer matrix.[177] On the other hand, single crystals as highly ordered and homogeneous media offer an attractive solution in minimizing scattering losses while simultaneously allowing to maintain high exciton density required for low I_{th}^{ASE}. Furthermore, sublimation-grown plate-like single crystals showed bright emission at the crystal edges indicating excellent waveguiding properties of the crystals. In contrast to concentrated PS films, significantly lower I_{th}^{ASE} were obtained for **BF-p** and **BF-2p** single crystals, i.e. 1.8 kW/cm^2 (9.2 μJ/cm^2) and 0.7 kW/cm^2 (3.5 μJ/cm^2), respectively. Note somewhat lower I_{th}^{ASE} for **BF-2p** as compared to that for **BF-p** is due to the larger k_r. Importantly, the ASE threshold of

700 W/cm^2 estimated in the single crystals of bifluorene compound **BF-2p** is among the lowest achieved in organic crystalline material.[23,91,93,112,186–188]

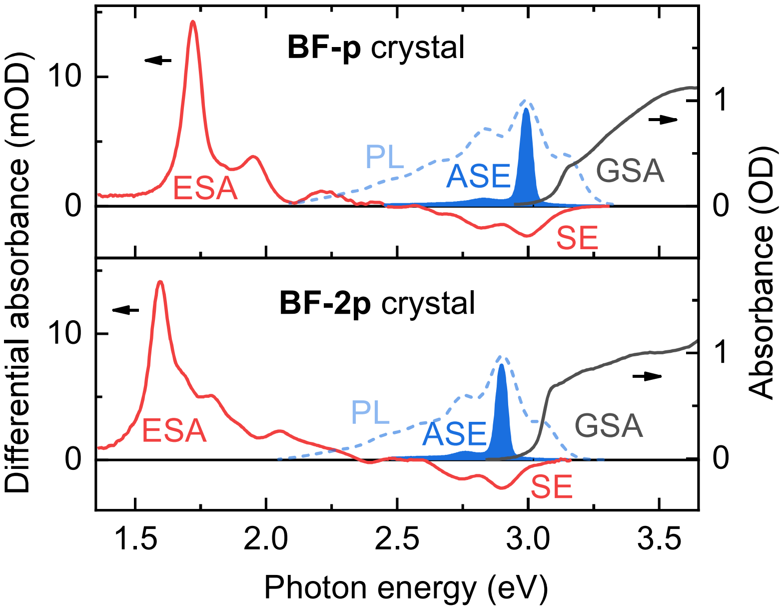

Figure 3.16. Ground state absorption (GSA), excited state absorption (ESA), stimulated emission (SE), PL and ASE spectra of the **BF-p** and **BF-2p** single crystals. Differential absorption spectra were at 2 ps delay time.

While internal conversion, intersystem crossing to triplet states, trapping, polaron absorption or exciton annihilation are not so critical for attaining light amplification in molecular crystals, photoinduced absorption to the excited states $S_1 \rightarrow S_n$ extending towards the gain region can be a decisive factor for gain properties.[91] Hence losses related to excited-state absorption (ESA) in the bifluorene single crystals were evaluated. Figure 3.16 illustrates differential absorption spectra of the **BF-p** and **BF-2p** crystals along with the ground-state absorption (GSA), PL and ASE spectra. High-energy slope of the ESA spectra of bifluorene single crystals extends up to ~2.3 eV, which is far below their gain region. At higher energies (from 2.6 eV to 3.2 eV) stimulated emission dominates over ESA, that is evident from the negative differential absorption values. Moreover, the shape of stimulated emission spectra was found to be similar to that of PL spectra indicating minor role of ESA at the ASE position. On the other hand, a noticeable overlap of GSA and PL spectra implies that some reabsorption losses are induced by low energy trap state.

Highlights

- The bifluorene compounds were designed to possess twisted molecular structure comprising of singly-bonded phenyl and fluorene chromophores with out-of-plane sticking dimethyl moieties for reduced intermolecular coupling, and thus for enhanced fluorescence and ASE properties in the solid state
- The flexible molecular backbone also facilitated increased vibronic coupling to torsional modes implying large Stokes shift (0.5 eV) and thereby reduced reabsorption of emission
- Coherently excited low energy vibrational modes (~80 cm^{-1}) observed in transient absorption measurements were assigned to torsional motion of phenyl ring in crystals
- Enhanced vibronic coupling imposed by torsional modes of central phenyl fragments lead to conformational disorder, which in turn disabled resonant excitonic coupling between chromophores in crystalline medium
- The bifluorene compounds showed great potential in light amplification expressing low ASE thresholds (down to 700 $\mathrm{W/cm}^2$) in single-crystalline phase.

Key finding A

- Enhanced electron-vibronic coupling and conformational disorder of phenyl and biphenyl bridged bifluorene molecules reduces excitonic coupling strength in single crystals, hence improving ASE performance.

Research opportunities

- Explore the relation between strong vibronic coupling and non-radiative losses in laser materials

3.3 Effects of excitonic coupling in crystals

Conformational disorder set by flexible molecular structure can suppress excitonic coupling in crystal leading to weak reabsorption and monomer like radiative rate, that are highly desirable for lasing applications. Another strategy that allows to avoid effects of excitonic coupling is excitation energy transfer to low concentration of highly emissive dopants via FRET mechanism.[72,83,189] It is often employed to boost the ASE performance of amorphous films, however, due to slow exciton diffusion in amorphous films high doping concentrations (5-10%) are required to achieve rapid population inversion.[83] Significantly higher energy transfer rates can be achieved in well-ordered crystalline media with low conformational disorder.[45,190] In doped crystals ultrafast host-dopant energy transfer rate dominates over other radiative and non-radiative processes.[189]

In this Chapter, series of new bifluorene compounds featuring acetylene and ethylene bridging groups that ensure torsional rigidity of molecular structure were investigated. Reduced vibronic coupling reduced dynamic disorder and promoted resonant excitonic coupling in crystals. Although degraded ASE performance due to stronger reabsorption was expected, thorough characterization of sublimation-grown crystals revealed the significant differences in ASE performance of both rigid bifluorene derivatives. Improved ASE performance was later justified by ultrafast energy transfer to minute amount of highly emissive self-dopant in crystals. This creates an opportunity to engineer byproducts from the chemical synthesis to be employed as emissive self-dopants saving production steps needed to synthesize dopant separately.[191]

Chemical structures of bifluorene compounds with different acetylene (**BF-a**) and ethylene (**BF-e**) bridging groups are displayed in Figure 3.17. **BF-a** was synthesized by cross-coupling 2-ethynyl-9,9-dimethylfluorene with 2-bromo-9,9-dimethylfluorene according to procedure reported in literature.[192] **BF-e** derivative was prepared from **BF-a** by its hydrolysis, reduction and dehydration as displayed in Figure 3.17.

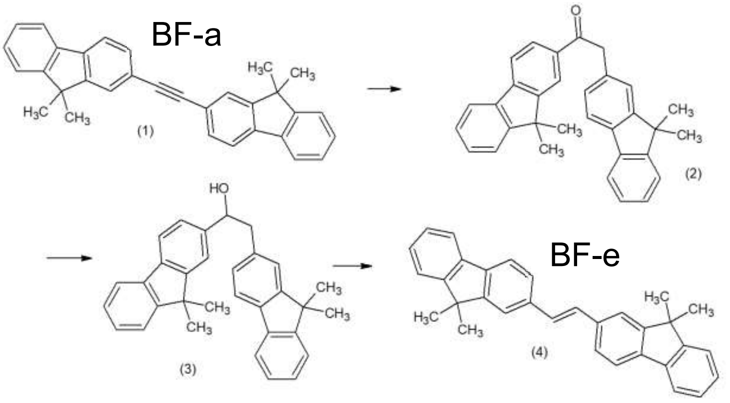

Figure 3.17. Synthesis route displaying production of **BF-e** derivative using **BF-a** as a precursor.

Optical properties

Absorption and photoluminescence (PL) spectra of the bifluorene compounds in dilute solution indicated 0.21 eV shift to lower energies for ethylene-bridged **BF-e** as compared to that possessing acetylene linkage (**BF-a**) (Figure 3.18). Note that the absorption as well as emission spectra of rigid bifluorene derivatives in solution exhibit nicely resolved vibronic structure. On the other hand, somewhat enhanced vibronic coupling was evident from ethylene-bridged **BF-e** emission spectrum showing Huang-Rhys factor of $\lambda^2 = 1.15$ compared to $\lambda^2 = 0.80$ recorded for **BF-e** monomer. This suggests that some torsional degrees of freedom are maintained with ethylene bridge providing a larger Stokes shift between emission and absorption. Thermal population of torsional modes was previously investigated for similar ethylene-bridged oligo-phenylene-vinylenes.[193]

Emission spectra of polycrystalline neat films and PVT grown single crystals showed a typical shift to lower energies as compared to the spectra of isolated molecules in solution (see Figure 3.18). Energy shift is an attribute of intermolecular interaction between closely packed molecules. Generally, the positions of vibronic peaks of the polycrystalline films match those of the crystals, however their intensity distribution is different due to effects of stronger reabsorption of waveguided light in the bulk of single crystals. This was exactly the case for **BF-e** neat film and crystal. In contrast, weaker reabsorption was observed for **BF-a** crystal. Moreover, 0-0 vibronic peaks of **BF-a** polycrystalline film and single crystal were recorded at 3.30 eV and 3.00 eV, respectively. Almost 300 meV energy difference could not be accounted for reabsorption and most likely indicates distinct emitting species.

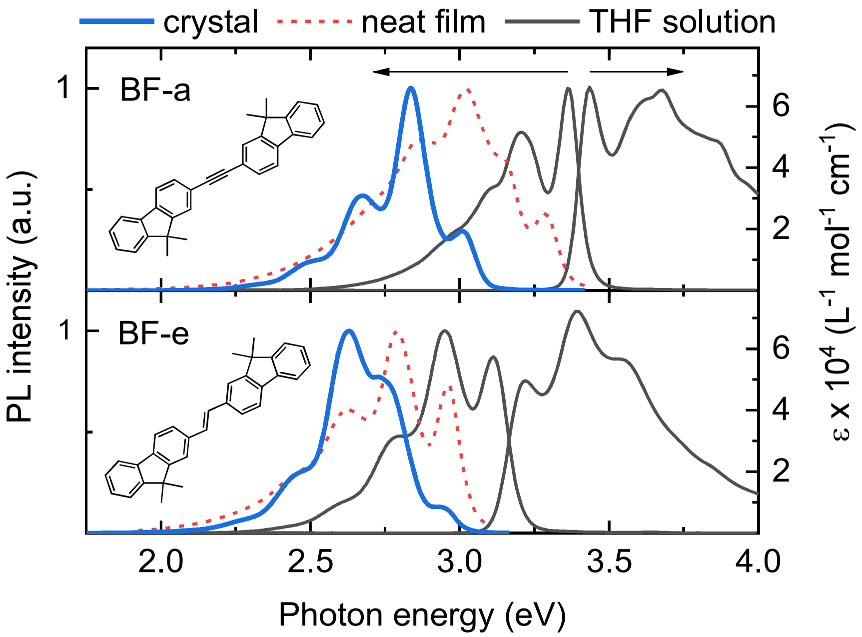

Figure 3.18. Absorption and fluorescence spectra of bifluorene compounds **BF-a** and **BF-e** in 10^{-5} M THF solutions along with fluorescence spectra of neat films and PVT grown crystals.

Unintentional self-doping in crystals

Important differences were revealed in the crystal absorption and emission spectra of both bifluorene compounds (Figure 3.19**)**. **BF-e** crystal exhibited small Stokes shift (~50 meV) between absorption and PL leading to strong emission reabsorption. In contrast, the anomalously large energy difference between the dominant absorption band of **BF-a** crystal at 3.30 eV and 0-0 PL band at 3.00 eV indicated some intermediate state involved in emission. Indeed, detailed investigation revealed a weak additional absorption band at 3.05 eV (Figure 3.19a). As this absorption band coincides with onset of **BF-a** PL spectrum, the origin of PL may be attributed to unintentional self-dopant and not the **BF-a** host crystal states. The comparison of absorption intensities of dopant (A_1^D) and host (A_1^H) peaks gave a rough estimate of dopant concentration ($C_D \approx 1\%$). It is obvious, that low dopant concentration allowed to significantly reduce reabsorption in **BF-a** crystal.

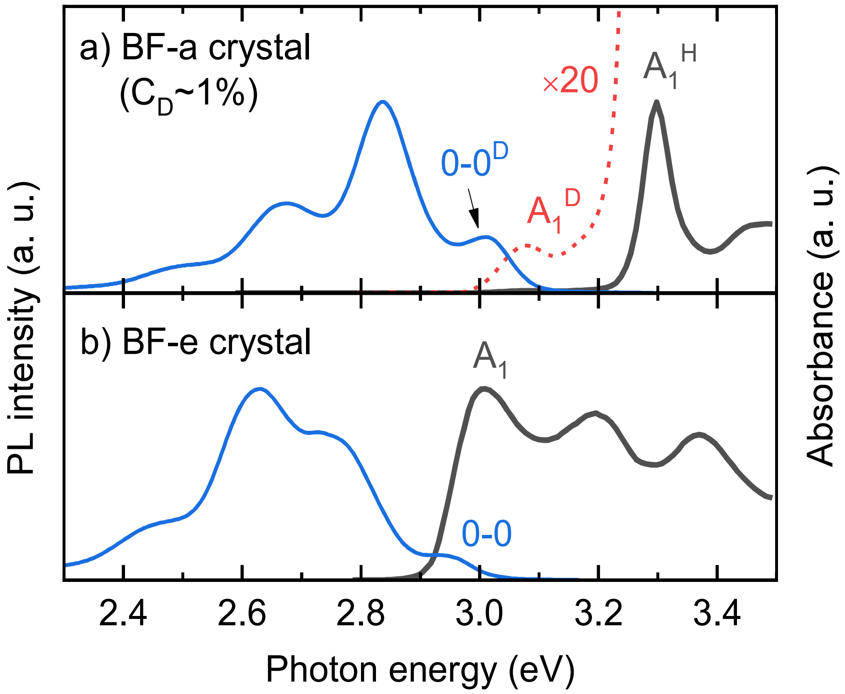

Figure 3.19. Absorption (black solid lines) and fluorescence (blue solid lines) spectra of a) self-doped **BF-a** and b) **BF-e** crystals. Dashed line corresponds to **BF-a** crystal absorption spectrum multiplied by a factor of 20.

Crystals with significantly lower doping concentrations ($C_D < 0.1\%$) were produced from the same **BF-a** powder by lowering PVT zone temperature from 230 °C (used for the initial crystal growth) to 175 °C. Notable differences in the time resolved emission spectra of crystals with reduced doping concentration are displayed in Figure 3.20. At early delay times, PL spectrum with 0-0 vibronic peak located at around 3.30 eV was observed indicating host emission, which is in agreement with dominant $A_1{}^H$ absorption peak of BF-a crystal (see Figure 3.19a). At later times, PL spectrum evolves to show 0-0 emission at 3.01 eV. This exemplifies the typical Förster resonant energy transfer dynamics between host and dopant states, when the energy transfer efficiency low. In contrast, time-resolved spectra of ~1% self-doped crystals showed no evidence of the host emission suggesting enhanced excitation energy transfer rate.

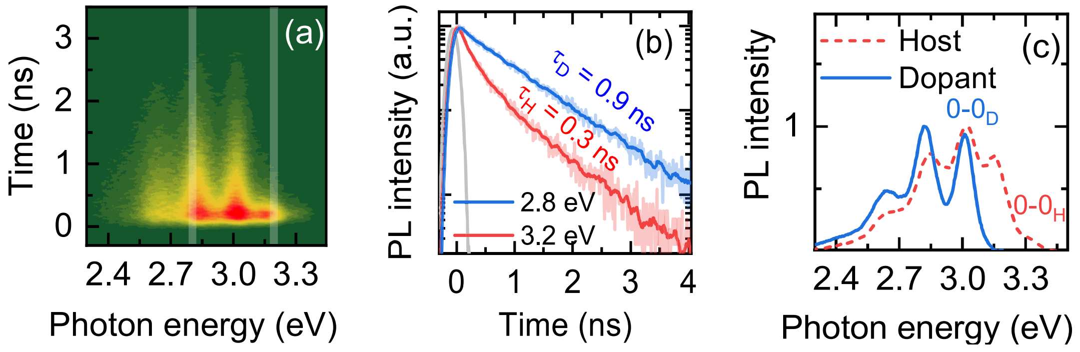

Figure 3.20. Time-resolved PL spectra of weakly doped ($C_D < 0.1\%$) BF-a crystal. (a) PL spectral map showing change of spectral composition with time, (b) PL transients at indicated photon energies and (c) decomposed spectral features of host and dopant components.

To visualize the ultrafast energy transfer in ~1% self-doped **BF-a** crystals we performed femtosecond transient absorption studies (Figure 3.21a). Recorded narrow bands at 1.82 eV and 1.60 eV corresponded to host and dopant excited state absorption, respectively. The energy transfer from host to dopant occurred within tens of picoseconds after initial excitation. In contrast, **BF-a** crystals with significantly lower doping concentration ($C_D < 0.1\%$) showed only the dominant host excited state absorption at 1.82 eV (Figure 3.21b). Such high energy transfer rate enables fast population inversion at relatively low doping concentrations signaling a long-range energy transport in single crystal. This may be a result of low energetic disorder of rigid **BF-a** molecules creating conditions for resonant energy transfer between neighboring molecules.

It is important to point out that excited state absorption signal of pure **BF-e** crystal was exactly at 1.60 eV (see Figure 3.21c), which perfectly coincided with self-dopant ESA signal. This suggests that highly emissive self-dopant embedded in **BF-a** crystals may be the similar ethylene-bridged **BF-e** derivative. Unintentional doping could have occurred as small quantity of impurities produced during synthesis were embedded in the host crystal structure a result of zone refining during the crystal growth by PVT method.[194] However, production of **BF-e** impurities during initial synthesis of **BF-a** was highly unlikely considering the absence of oxidation and reduction reactions (see Figure 3.17). This was supported by no detectable spectral signatures of **BF-e** in PL or absorption spectra of **BF-a** powder diluted in solution. On the other hand, self-dopant concentration in PVT grown crystals was found to be directly dependent on zone temperature, where higher self-dopant concentration was achieved at 230 °C than at 170 °C. Interestingly, evaporation of **BF-a** powder on quartz substrate at 150 °C in high vacuum resulted in micrometer sized microcrystals with no detectable self-dopant emission. Therefore, dopant production may be related to temperature as well as other impurities (e.g. H_2O) in powder or type of carrier gas (e.g. N_2) in PVT experiment, that may create the conditions for oxidation and reduction reactions. While it is still unclear what conditions led to formation of self-dopant, it must be noted that self-doping experiments were successfully repeated to exclude possibility for accidental contamination.

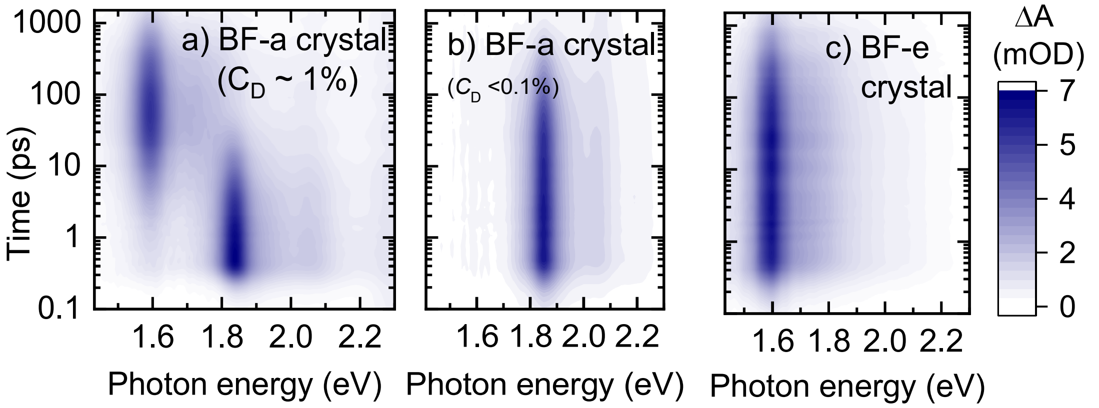

Figure 3.21. Transient absorption spectral maps of PVT grown (a) BF-a ($C_D \approx 1\%$), (b) pure BF-e crystal and (c) BF-a ($C_D < 0.1\%$) crystal. Crystals were excited with photon energy set to 3.30 eV.

Excitonic coupling

The detailed optical properties of the studied bifluorene derivatives are summarized in Table 3.5. Typically to other fluorene-based molecules PL quantum yield of both bifluorene compounds in dilute solutions were estimated to be very high ($\Phi_{PL} > 0.8$), which accompanied by rather short fluorescence lifetimes (τ < 1 ns) resulted in high radiative decay rates (k_r ~1 ns^{-1}). The superior radiative properties were also maintained in the molecular crystals. High radiative rate of 0.91 ns^{-1} and low non-radiative rate of 0.20 ns^{-1} recorded for **BF-e** crystal were almost identical to values of a monomer in solution. This is indicative of weak intermolecular coupling and low concentration of non-radiative defects.

The presence of highly emissive self-dopant in **BF-a** crystals complicated the evaluation of radiative properties of host crystal. At low doping concentrations ($C_D < 0.1\%$) reduced emission quantum yield was observed together with shorter decay lifetime compared to **BF-a** monomer in solution. This either suggested reduced radiative recombination rate due to H-type excitonic coupling or enhanced pathway for non-radiative recombination at the defects. Nevertheless, **BF-a** crystals with higher self-dopant concentration ($C_D \sim 1\%$) exhibited significantly improved emission properties with quantum yield of 0.75 and radiative rate of 0.86 ns^{-1}. Comparable radiative rate is yet another indication that self-dopant in **BF-a** crystal is probably a **BF-e** monomer. It is worth noting that lower energy dopant should not be excitonically coupled to a surrounding molecules in a crystal.

Table 3.5. Optical properties of the bifluorene compounds in THF solutions, neat films and SCs.

Compd.	Form[a]	E_{abs}[b] (eV)	E_{PL}[c] (eV)	Φ_{PL}	τ (ns)	k_r (ns^{-1})	k_{nr} (ns^{-1})
BF-a	THF	3.43	3.36	0.83	0.68	1.22	0.25
($C_D \approx 1\%$)	SC	**3.30**	**3.01**	0.78	1.01	0.86	0.22
($C_D < 0.1\%$)	SC	**3.30**	**3.29**	0.29	0.30[50%] 0.95[50%]		
BF-e	THF	3.22	3.12	0.88	0.99	0.89	0.12
	SC	3.01	2.95	0.82	0.90	0.91	0.20

[a] Compounds were investigated in 10^{-5} mol/l THF solutions and sublimation-grown SCs, C_D indicates approximate concentration of self-dopant; [b] Energy of first absorption peak; [c] Energy of 0-0 PL peak.

Weak excitonic coupling of the dopant with the surrounding crystal medium was also confirmed by temperature resolved emission of self-doped crystal (Figure 3.22). Temperature independent PL emission spectral structure, quantum yield and emission lifetime indicated that radiative and non-radiative rates were constant in the temperature range. Considering that exciton transport within host crystal prior to capture at the dopant usually shows strong temperature dependence, temperature independent PLQY suggests the whole host-dopant energy transfer process is 100% efficient.

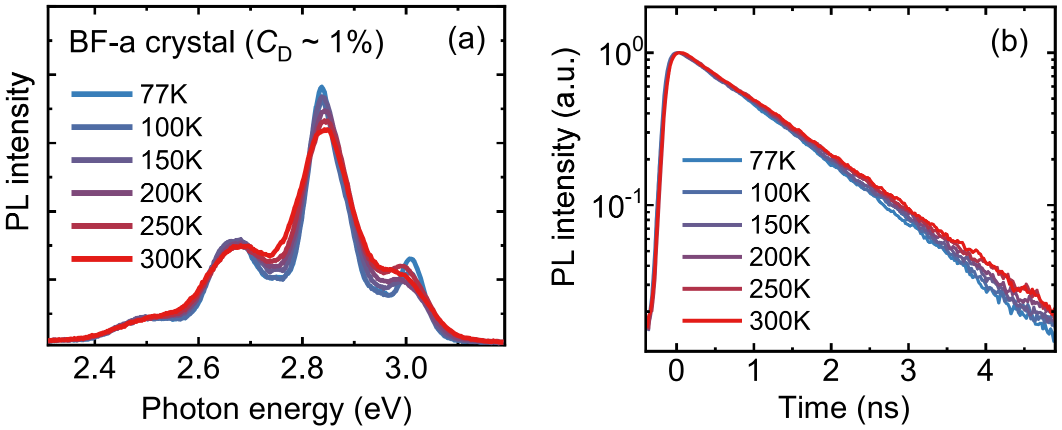

Figure 3.22. Photoluminescence (a) time-integrated spectra and (b) spectrally integrated transients of **BF-a** single crystal as a function of temperature. Pump photon energy was set to 3.54 eV.

The emission spectra of non-coupled dopant in the crystal matrix provides a unique opportunity to extract the energy of excitonic coupling. Usually, contribution of resonant excitonic shift to the overall shift of energy level is difficult to evaluate by comparing just monomer and aggregate spectra.[109] In the case of the dopant, most of the energy shift is caused dispersive interactions with surrounding media due to Van der Walls attraction. Therefore, if dopant embedded in host crystal is only affected by dispersive interactions, the energy shift compared to a monomer in solution allows to evaluate magnitude of dispersive shift (ΔE_D). Then, resonant coupling energy (ΔE_R) can be obtained from further shift observed in isoenergetic crystalline medium. Figure 3.23a shows the low temperature emission spectra of **BF-e** monomer diluted in inert polymer matrix, as dopant in **BF-a** crystal and single crystal. The observed 89 meV resonant shift of **BF-e** crystal to the lower energies indicates J-type excitonic coupling.[109] Furthermore, this also agrees with enhancement of first absorption peak in crystal compared to a monomer (see Figure 3.18 and Figure 3.19). No enhancement of radiative rate in **BF-e** crystal at room temperature could be explained by thermal scattering of exciton coherence. However, at low temperatures, superradiant behavior is suggested by intense 0-0 emission (Figure 3.23a) as well as reduced recombination lifetime (from 0.90 ns at 300 K to 0.67 at 77 K) (Figure 3.23b).

Interestingly, evident increase of 0-0 emission peak intensity was observed for dopant at 10 K temperature (Figure 3.23a) compared to room temperature PL spectra (Figure 3.22a). This may be caused by reduced reabsorption at low temperatures, which is associated with thermal broadening of absorption spectrum. Otherwise it would suggest that lower energy dopant can be excitonically coupled to a surrounding medium, which results in superradiance observed at 0-0 peak position at low temperatures.

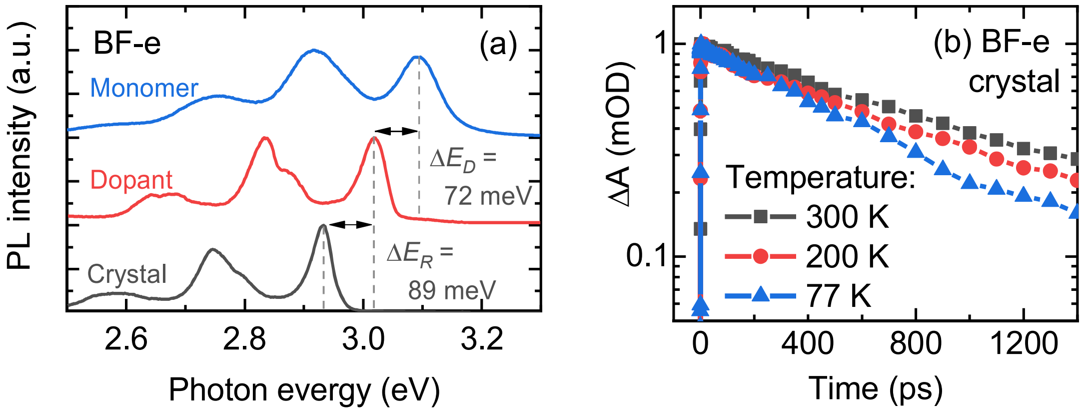

Figure 3.23. (a) Pholuminescence spectra of **BF-e** in diluted 0.1% wt. polymer (Zeonex) matrix recorded at 77 K temperature (blue line), in ~1% self-doped crystal recorded at 10 K (red line) and pure single crystal recorded at 10 K (black line). (b) Temperature dependent transient absorption kinetics of **BF-e** crystal recorded at dopant excited state absorption maximum (1.60 eV).

The observed weak-to-intermediate J-type excitonic coupling in **BF-e** crystal most probably originates from slip-stacked packing (see Figure 2.8) of molecular dipoles and low structural disorder provided by rigid molecular structures.[91] Although J-aggregates are known to possess coherently enhanced oscillator strength (and radiative rate) owing to collective interactions of dipole moments, at room temperature superradiance is rarely observed due to thermal scattering.[109] Therefore, only strong J-type excitonic coupling ($\Delta E_R > E_{vibr}$) would improve the stimulated emission properties of single crystals. On the other hand, intensity enhancement of the first absorption peak and reduced Stokes shift are the properties of the J-aggregates causing strong reabsorption in crystals.[109] Therefore, J-type excitonic coupling is known to degrade ASE properties in organic crystals.[91] Here, one of the best strategies to avoid reabsorption effects in crystals is to utilize ultrafast energy transfer to the emissive dopant, which was observed in self-doped **BF-a** crystals.

Amplified spontaneous emission

To reveal the potential of bifluorene crystals for lasing applications their ASE properties were explored by utilizing thin excitation stripe technique.

Excitation power dynamics of the edge emission spectra of **BF-e** and self-doped **BF-a** crystals is displayed in Figure 3.24. Broad spontaneous emission bands observed at low excitation density become narrower with the increasing pump density above the onset of stimulated optical transitions. The ASE peaks emerge at the 0-1 and lower vibronic replicas, while the highest energy 0-0 vibronic band of both samples is reabsorbed in the bulk of the crystal. Evidently, much stronger reabsorption was observed for **BF-e** crystal, where ASE at the 0-2 peak position was also observed. Stronger reabsorption also lead to relatively high ASE threshold for **BF-e** crystal (I_{th}^{ASE} = 3.4 kW/cm^2) (see inset of Figure 3.24a). In contrast, emission from low concentration of dopants lead to almost order of magnitude reduced I_{th}^{ASE} (0.4 kW/cm^2) for self-doped **BF-a** crystal. Obviously, the emissive traps play a crucial role in achieving extremely low I_{th}^{ASE} in **BF-a** crystals implying the essential difference from the other studied bifluorene SCs.

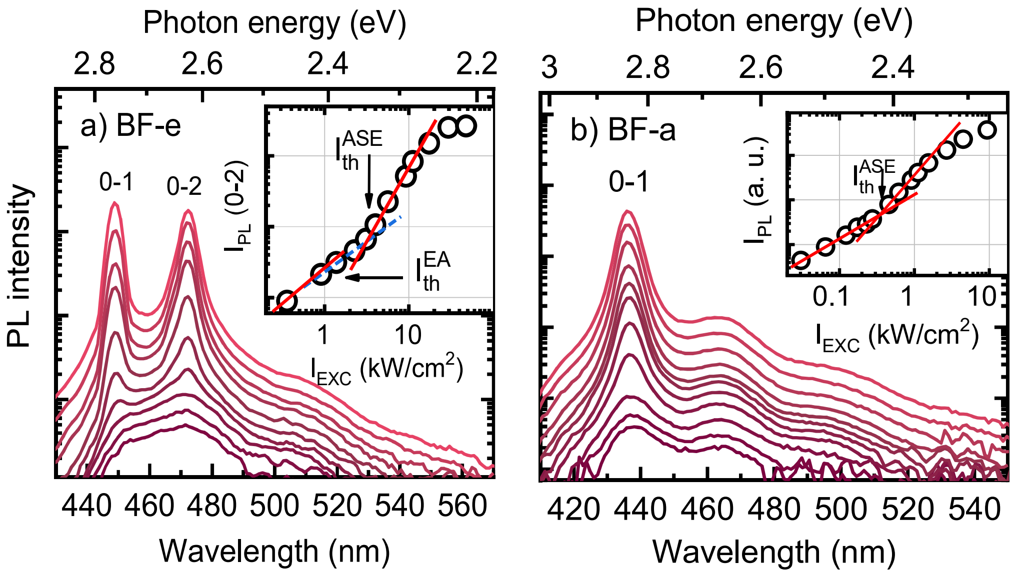

Figure 3.24. Edge emission spectra at different excitation power densities for bifluorene **BF-e** and self-doped **BF-a** crystals. Insets show emission peak intensity *vs.* excitation power density ($I_{\mathrm{exc.}}$). I^{EA} indicates threshold for observable exciton annihilation.

Exciton annihilation is another mechanism that could play a remarkable role at high excitation densities by significantly reducing exciton concentration, and thus preventing population inversion. Furthermore, previously observed J-type excitonic character of aggregates in **BF-e** crystal suggest enhanced exciton transport (and exciton annihilation).[132] The signs of annihilation could be traced by the deviation from linear PL intensity dependence vs excitation power density before the onset of ASE. Exactly this was observed for **BF-e** crystal (see insets of Figure 3.24a), proving that the impact of exciton annihilation to I_{th}^{ASE} cannot be disregarded. In contrast, trapping excitation at the dopant (as in **BF-a** crystal) allows to avoid annihilation. If the doping concentration is higher than excitation density onset for annihilation events excitation gets captured prior to exciton-exciton interaction.

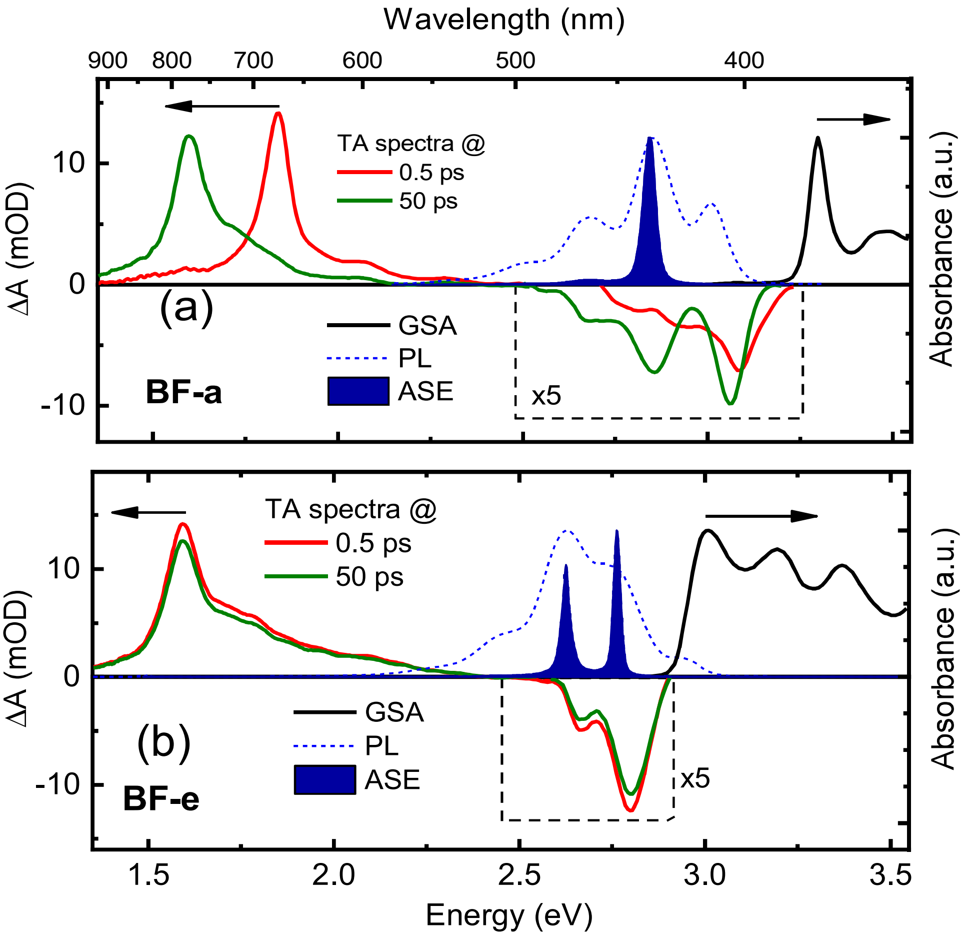

Figure 3.25. Ground state absorption (black solid line), transient absorption at 0.5 ps (red solid line) and 50 ps (green solid line) delay, PL (dashed blue) and ASE (blue) spectra of a) **BF-a** and b) **BF-e** SCs. Pump wavelength was set to 375 nm (3.30 eV).

Finally, to prove that ASE in **BF-a** crystal originates from low concentration of self-dopant broad-spectrum transient absorption was performed on both bifluorene crystals. Figure 3.25 illustrates transient absorption (TA) spectra of the **BF-a** and **BF-e** crystals along with the ground-state absorption (GSA), PL and ASE spectra. Excited state absorption bands are located in the range of 1.4 – 2.3 eV, whereas at higher energies (in the range of 2.5 - 3.1 eV) stimulated emission is evidenced by the negative values of differential absorption. In the case of **BF-a**, the interplay between two states was revealed in the time-domain of tens of picoseconds, whereas the **BF-e** expressed typical single state dynamics. The additional lower-energy band was observed in the excited state and stimulated emission regions at the delay of 50 ps as compared to the initially excited states probed at 0.5 ps (Figure 3.25a). The higher energy band appearing at 0.5 ps is associated with the host crystal states, while the lower energy band emerging within the first 50 ps is related to the self-dopant states. The dominant negative stimulated emission peak at around 2.8 eV indicated the highest probability for stimulated transitions agreeing with ASE position. While the later peak at 3.05 eV was even higher in intensity, it was overlapped with dopant ground state bleach signal related to reabsorption.

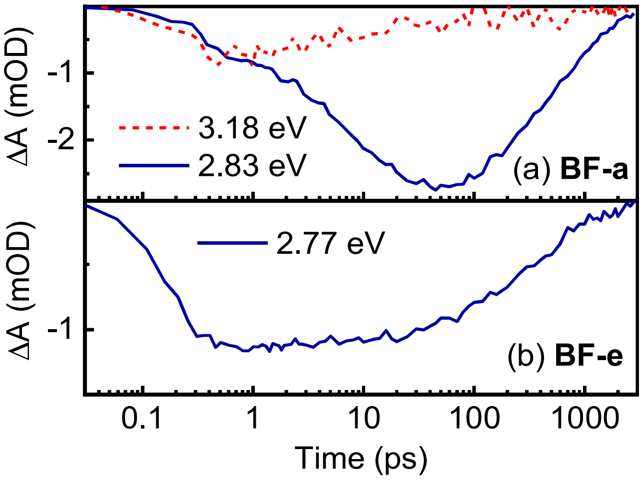

Figure 3.26. Differential absorption transients of a) **BF-a** and b) **BF-e** crystals at different probe energies in the stimulated emission region.

The temporal evolution of stimulated emission features is presented in Figure 3.26. The most important result here is that maximum population of emissive states in self-doped **BF-a** crystal is reached within 50 ps after the initial excitation. The accumulation of population lasts much longer than typical excited state thermalization, which occurs within less than 0.5 ps (rise time in **BF-e** crystal). Thus, it is related with excitation migration via thermalized excitonic states until it is trapped by low density of self-dopants. Such long migration time implies hundreds of exciton hop events towards trap states taking into account time for the single hop of approximately 100 fs.[195] This signifies that long-range transport in crystalline organic materials makes them superior for host-guest laser system compared to amorphous counterparts.

Highlights

- The bifluorene compounds investigated in this chapter were designed to possess molecular structure comprising of rigid ethylene and acetylene bridging moieties for reduced vibronic coupling.
- Low conformational disorder of rigid molecular structures lead to enhanced resonant excitonic coupling in crystals. Negative effects of weak vibronic and intermediate excitonic coupling were revealed as strong reabsorption and exciton annihilation losses causing relatively high ASE threshold (3.4 kW/cm^2).
- Loss mechanisms associated with strong coupling were overcome in self-doped BF-a crystals, where excitation energy transfer to low concentration of highly emissive self-dopants states resulted in almost order of magnitude lower ASE threshold of 400 W/cm^2.
- To the best knowledge self-doping occurred as oxidation and reduction reactions during vapor phase crystal growth lead to change of acetylene bond to vinylene bond in bifluorene molecule.
- Strong indications of J-type resonant coupling were observed for rigid bifluorene crystals, which lead to highly efficient energy transfer to self-dopant

Key finding B

- Self-doping of molecular crystals via acetylene-ethylene bond modification in bifluorenes is a promising cost-saving strategy to obtain highly emissive and low ASE threshold doped crystals.

Research opportunities

- In depth study of self-doping mechanism via acetylene-ethylene link modification in other molecular compounds

3.4 Anisotropic long-range energy transport in crystals

Exciton transport undoubtedly plays a crucial role in determining the performance of organic semiconductors used in state-of-the-art devices.[45,196] While the efficiency of organic solar cells is known to directly benefit from long-range exciton diffusion,[197,198] advantages for light emitting devices are debatable. Generally, high excitation densities promote exciton annihilation, a diffusion mediated process, which is detrimental to the device performance.[40,88,199,200] Particularly, this scenario is anticipated for organic lasers requiring high exciton concentrations to achieve population inversion, and subsequently, light amplification. On the other hand, for a host-guest emitter system, large exciton diffusion can be advantageous for it may enable excitons generated in the host to be transferred to the emitter on the ultrafast time-scale.[123,189,201,202]

Typically, singlet exciton diffusion length (L_D) rarely exceeds 10 nm in amorphous media of small molecules or polymer fragments.[45,197] According to Förster resonant energy transfer (FRET) theory, random transition dipole moments orientation and large intermolecular distances limit energy transfer time to several picoseconds, which is often represented as an incoherent hopping process.[6,126] In contrast, long-range exciton transport ($L_D > 100$ nm) was observed in highly aligned and densely packed molecular aggregates.[128,129] Strong intermolecular interactions in crystalline media lead to short energy transfer times (< 100 fs) that become comparable to vibrational modes suggesting a partly coherent energy transport.[5] Therefore, it is thus obvious that evaluation of exciton diffusion, especially for crystals, is of prime importance.

Most methods employed to date to evaluate exciton diffusion in organic media are based on excitation quenching techniques, which require special sample preparation (e.g. in the case of surface or volume quenching)[45,203] or prior knowledge of exciton diffusion model (e.g. exciton-exciton annihilation)[204–206]. Moreover, these widely used techniques provide limited information about the direction of energy transfer, thus making observation of spatial distribution of excitons in anisotropic crystals practically impossible. To fill the gap, recently rather complex transient microscopy techniques have been employed to visualize singlet and triplet exciton dynamics in crystals with sub-micrometer resolution.[207,208] An alternative way to directly probe direction-dependent exciton diffusion in anisotropic materials is to use light induced transient grating (LITG) technique.[140,142] Although the technique was not extensively exploited for investigation of organic materials due to their small diffusion lengths, it was proved to be fully applicable for studying exciton and charge dynamics in crystalline media, where diffusion lengths are considerably longer.[141,209,210]

Here, LITG method was exploited to evaluate singlet exciton diffusion coefficients and directionality in highly anisotropic bifluorene single crystals. Complementary studies of exciton-exciton annihilation were performed to verify the values obtained from LITG experiments. The main emphasis was put on determining the effects of conformational disorder in crystals appearing due to different rigidity of **BF-e** and **BF-p** bifluorene derivatives presented in Figure 3.27. As was shown in previous chapter, specific molecular packing together with reduced conformational disorder of rigid structures lead to moderate J-type excitonic coupling, which is known to promote energy transport rate between chromophores in crystal.[109]

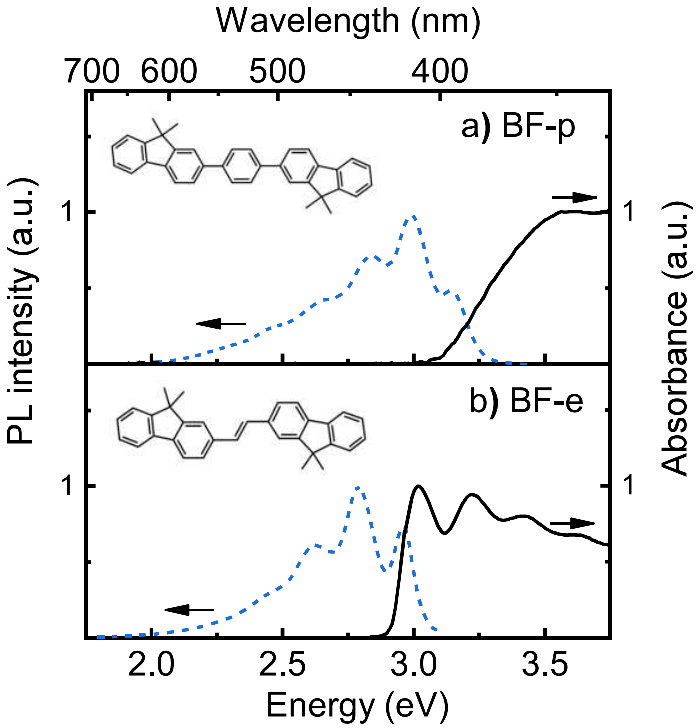

Figure 3.27. Absorption and PL spectra of (a) BF-p and (b) BF-e crystals. PL spectra were measured in polycrystalline films to avoid the effects of reabsorption. Insets show chemical structures of bifluorene compounds.

Absorption and PL spectra of the bifluorene crystals are displayed in Figure 3.27. Conformational disorder appearing due to torsional degrees of freedom in **BF-p** crystals is evidenced by featureless absorption. In contrast,

BF-e crystals expressed clear vibronic structure of absorption spectrum suggesting lower conformational disorder. Despite significant differences in ground state geometry, the structured PL emission spectral shape of both bifluorene derivatives reflected a planar molecular configuration. The effects of additional vibrational coupling to torsional modes of **BF-p** were evident on reduced overlap between PL and absorption spectra. Nevertheless, considerable overlap as well as high radiative relaxation rates of 1.3 ns^{-1} and 0.9 ns^{-1} for **BF-p** and **BF-e**, respectively, signify the high FRET rate due to dipole-dipole interaction. Theoretical estimation of FRET rate will be presented later in this chapter.

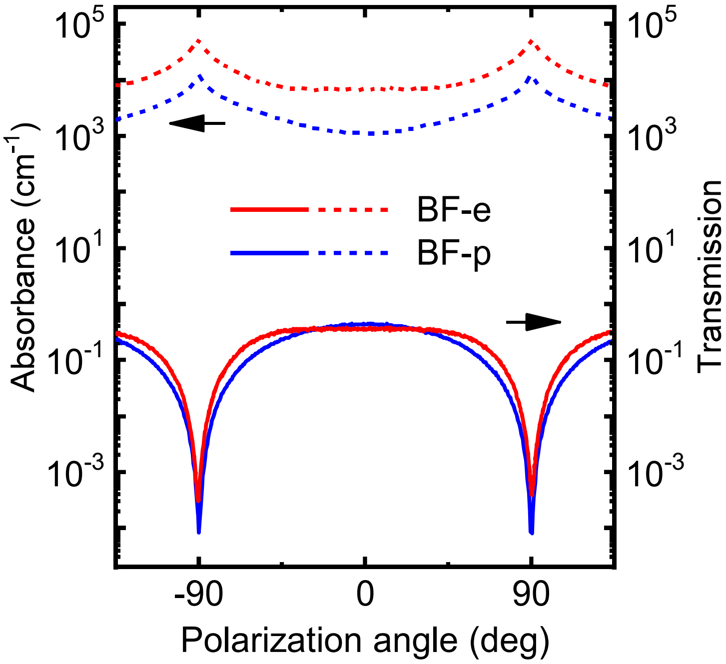

Figure 3.28. Transmission and absorption coefficient dependence on angle of the light polarization of BF-p and BF-e crystals measured at 350 nm. Laser light was perpendicular to the crystal surface, where light polarization angle of 90 degree corresponded to *a* (BF-e) and *c* (BF-e) crystal directions. Crystal thickness was 1.5 and 7.8 µm for BF-e and BF-p, respectively.

Angle resolved absorption polarization measurements of bifluorene crystals are presented in Figure 3.28. Both bifluorene crystals exhibited strong absorption and emission anisotropy (r ~ 1) implying highly ordered molecular orientation in the crystal. Polarization of strongest absorption coincided with *a* and *c* crystal directions of **BF-e** and **BF-p** crystals, respectively (see Figure 2.8). Somewhat higher polarization contrast was observed in **BF-p** crystal suggesting a better alignment of molecular dipoles, which agreed with crystallographic data. However, the most surprising finding was more than five-fold higher absorption coefficient of **BF-e** compared to **BF-p** crystal at 3.54 eV photon energy. This was not related to different crystal thickness as it was later confirmed for other crystals and it could not be explained by more dense molecular packing as both crystals exhibited similar crystal structure (see Figure 2.8). For all the later experiments excitation polarization was set to minimum absorption to achieve homogeneous excitation density profile.

LITG measurements

To determine exciton diffusion coefficient directly from spatial exciton distribution in a crystal LITG technique was employed. See chapter 2.4 for more information on LITG measurements. The diffraction signal in bifluorene crystals was produced by an amplitude grating due to a change in the imaginary part of refractive index, which corresponds to the change of absorption coefficient (ΔK) for the probe pulse.[143] Figure 3.29a shows diffraction efficiency transients at different grating periods (Λ). Here, the grating erasure lifetime (τ_G) at largest grating period corresponded to an intrinsic exciton recombination lifetime (τ_R) as relatively slow exciton diffusion in organics is unlikely to be observed at such large grating separations. At reduced Λ grating lifetime became faster showing measurable impact of grating broadening due to exciton diffusion. Diffusion coefficient (D) was estimated as a slope of grating decay rate versus grating period (inset of Figure 2.4b).

Figure 3.29 depicts LITG measurements of both bifluorene single crystals performed at two grating vector orientations positioned parallel and perpendicular to the molecular dipole moments in the crystal. The corresponding diffusion directions are indicated in the schematic illustrations of the single crystals (see insets of Figure 3.29). Substantial difference between grating decay transients at different grating periods indicates exciton diffusion along direction parallel to the molecular dipole moments. In contrast, measurements at perpendicular direction showed no observable difference of decay transients at various grating periods. The direction of the high exciton diffusion in bifluorene crystals was found to coincide with *c* (**BF-p**) and *a* (**BF-e**) crystallographic directions, in which J-type excitonic coupling of molecular dipole moments is expected (see Figure 2.8).

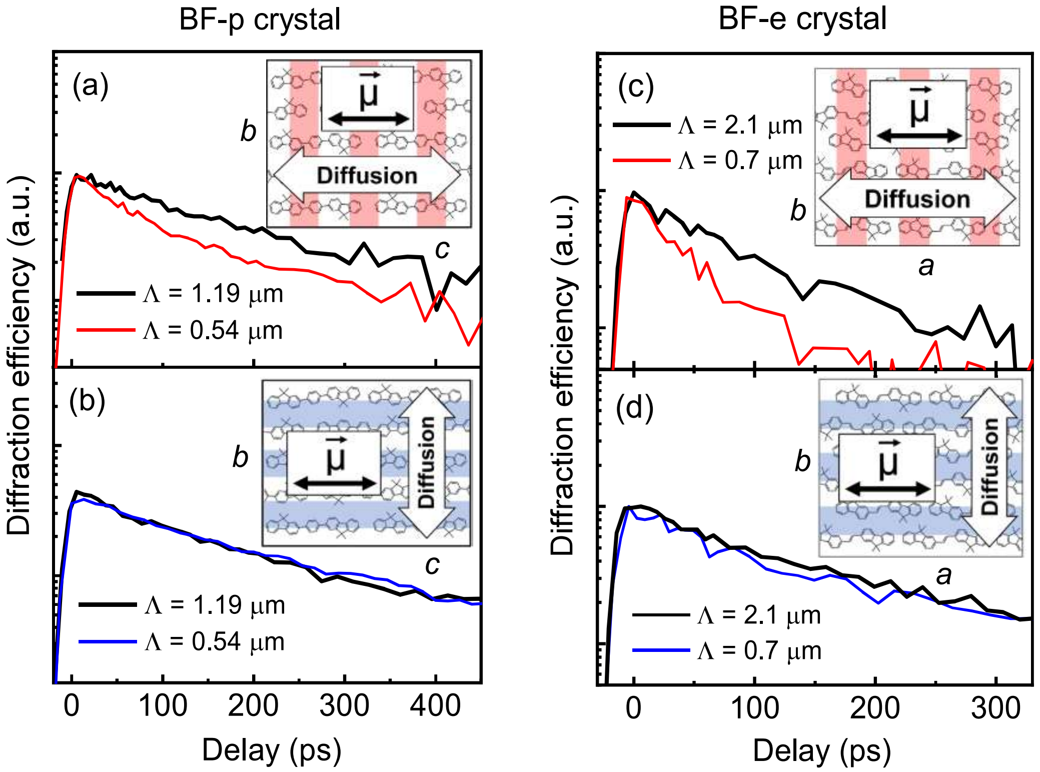

Figure 3.29. LITG decays of BF-p and BF-e crystals recorded at (a, c) parallel and (b, d) perpendicular direction of grating vector (corresponding to measured diffusion direction) in respect to the dipole moment (μ) of molecules in a crystal. Insets show a schematic representation of gratings on the crystal surface. Grating periods are indicated. Excitation fluence was set to 0.15 mJ/cm^2 and 0.04 mJ/cm^2 for BF-p and BF-e crystals, respectively.

Table 3.6. The measured parameters of BF-p and BF-e single crystals.

Sample	$\tau_R$$^{a)}$, ps	$D_{\|}$$^{b)}$, cm^2/s	$D_{\perp}$$^{b)}$, cm^2/s	$L_{D\|}$$^{c)}$, nm	$\gamma$$^{d)}$, 10^{-9} cm^3/s
BF-p	500	0.24 ± 0.03	< 0.01	110 ± 7	7.1 ± 1.1
BF-e	950	0.96 ± 0.10	< 0.01	302 ± 15	31.2 ± 2.6

$^{a)}$ exciton relaxation lifetime; $^{b)}$ diffusion coefficient measured parallel (||) and perpendicular (⊥) to the molecular dipole moments in the crystal; $^{c)}$ Estimated diffusion lengths at parallel (||) direction. $^{d)}$ annihilation rate coefficient.

Summarized results of exciton dynamics of bifluorene crystals are presented in Table 3.6. The almost 5-fold larger *D* in the direction of strongest dipole interaction was estimated for **BF-e** crystal (0.96 cm^2/s) as compared to

BF-p (0.24 cm^2/s). While exciton diffusion could not be observed in the perpendicular direction, considering short exciton relaxation lifetimes (τ_R < 1 ns) and the smallest diffraction grating period possible by LITG setup (Λ = 0.5 μm), the limit for *D* measurement was approximately 0.01 cm^2/s. The exciton diffusion length was estimated from the relation $L_D = \sqrt{D\tau_R}$.[211] Exciton diffusion lengths in the *c* (**BF-p**) and *a* (**BF-e**) crystal directions were 110 nm and 300 nm, respectively. Generally, the *D* values of incoherent exciton transfer found for the bifluorene single crystals (up to ~1 cm^2/s at room temperature) signifies rather strong singlet exciton transfer. Such high *D* and L_D values recorded for bifluorene crystals were comparable to values reported for highly anisotropic aggregates.[128,204,212]

Anisotropic exciton transport was previously measured with exciton quenching techniques and confirmed by theoretical modeling for anthracene crystal, which resulted in exciton diffusion coefficients of 8.7 × 10^{-3} cm^2/s (L_D = 130 nm) in *b* crystal direction and 1.7 × 10^{-3} cm^2/s (L_D = 60 nm) in *a* direction.[213] It is worth nothing, that *b* direction of the strongest diffusion in oligoacene crystals corresponds to J-type excitonic coupling between chromophores.[109,117] Room temperature LITG measurements of exciton diffusion in either *a* or *b* direction of anthracene crystals reported no observable diffusion assuming the lower detection limit for *D* of 5 × 10^{-4} cm^2/s.[214] On the other hand, low temperature LITG measurements of anthracene crystals yielded *D* of 0.8 cm^2/s at 20 K and 10 cm^2/s at 2.8 K along *a* direction.[210] Such inverse temperature dependence lead to debates on coherent exciton transport of excitons in molecular crystals.[134]

While LITG experiments did not prove useful for many organic materials due to lower limit of diffusion coefficient, measurable impact was observed for organic crystals. Another matter of concern about LITG measurements was possibility of long-range radiative transport by means of reabsorption of the emitted light in anthracene crystals, however it was later proven improbable due to small reabsorption integral.[214] Exciton diffusion coefficient values obtained by low temperature LITG experiments on anthracene crystals were found to be considerably higher than ones obtained by exciton quenching techniques, which raised a question about the appropriateness of the later experiments to determine exciton transport parameters.[215] This was associated with capture-limited nature of exciton annihilation and quenching experiments. Nevertheless, both later experiments have practical implications allowing to determine exciton diffusion related parameters that will be relevant in device applications.

Exciton-exciton annihilation

Singlet-singlet annihilation (SSA) is a complementary method to study exciton diffusion dynamics in organic materials.[206,216] Figure 3.30 shows the differential absorption transients of main ESA band recorded at different excitation densities for BF-p and BF-e crystals. At the lowest exciton densities annihilation is negligible and exciton population decays exponentially with relaxation time τ_R. At higher excitation densities mean distances between excitons become comparable or smaller than exciton diffusion length, hence the probability for exciton-exciton interaction and consequent non-radiative losses become larger.

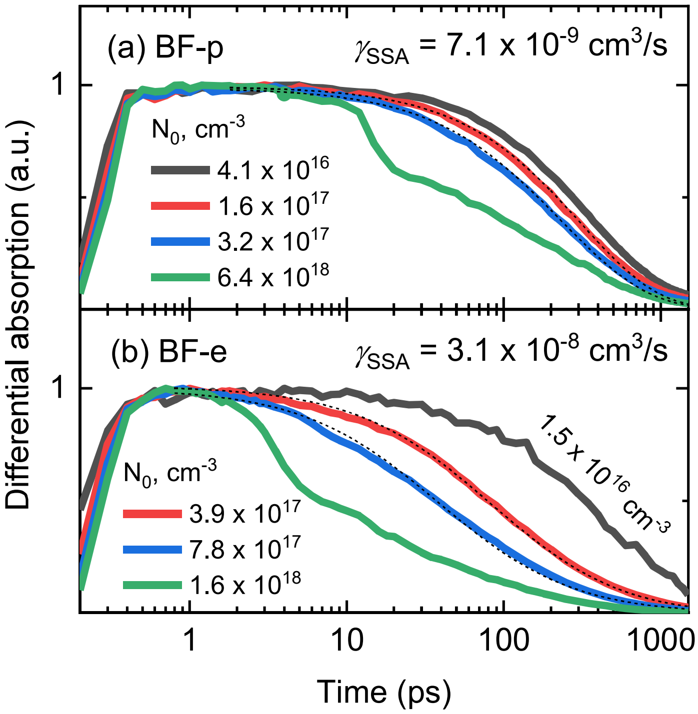

Figure 3.30. Excitation density dependent differential absorption transients for (a) BF-p and (b) BF-e single crystals recorded at the ESA band maxima of 1.72 eV and 1.60 eV, respectively. Initial exciton densities are indicated. Black lines are fits of exciton annihilation model.

In this case, exciton dynamics $N(t)$ is described by $dN(t)/dt = -N(t)/\tau_R - \gamma N(t)^2$, where annihilation coefficient γ is a function of diffusion coefficient D and effective exciton annihilation radius R_a, and in the time-independent form is expressed as $\gamma = 4\pi D R_a$.[206] Exciton population dynamics are described as $N(t)=[N_0\cdot\exp(-t/\tau_R)]/\{1+\gamma\cdot\tau_R\cdot N_0[1-\exp(-t/\tau_R)]\}$. Here, N_0 is the initial average exciton density calculated as $N_0 = (I_0/(dh\nu))\cdot(1\text{-}\exp(-\alpha d))$, where I_0 is excitation flux [μJ/cm^{-2}], hv is photon energy and α is absorption coefficient [cm^{-1}]. Fits of the SSA model are shown in Figure 3.30, while the extracted γ values are given in Table 3.6. In support to diffusion parameters determined by LITG, 5-fold higher annihilation rate was estimated for **BF-e** crystal (7.1×10^{-9} cm^3/s) compared to **BF-p** (3.1×10^{-8} cm^3/s). Furthermore, higher annihilation rate may have also been responsible for higher onset of ASE due to stimulated transitions, which were evidenced in transients as instantaneous population decay at highest excitation densities (Figure 3.30). Interestingly, onset of ASE in **BF-p** crystals occurred later in time (>10 ps) compared to **BF-e** (>3 ps), which might indicate longer thermalization time related to torsional motion of the central phenyl fragment.

Based on obtained annihilation rates and assuming typical annihilation radius for both crystals was equal to intermolecular distance in the crystal ($R_a \sim 0.85$ nm), diffusion coefficients for **BF-p** and **BF-e** crystals were 0.6×10^{-2} cm^2/s and 2.9×10^{-2} cm^2/s, respectively. More than an order of magnitude lower D were estimated from exciton annihilation rates compared to parameters determined by LITG method (see Table 3.6). It must be noted, that values were obtained using three-dimensional (3D) exciton annihilation model, while organic single crystals generally feature anisotropic exciton diffusion.[208,213] In the case of strictly one-dimensional (1D) diffusion, model employing time-dependent $\gamma(t)$ is employed to determine D in polymers or other highly anisotropic aggregates.[204,205,217] For example, in highly aligned β-phase polyfluorene time-dependent annihilation rate was observed in the initial 10 ps, which indicated that excitons were slowing down due to localization.[218] Nevertheless, no reasonable fit of the SSA transient displayed in Figure 3.30 was obtained employing the proposed 1D model.

Moreover, in the general case of isotropic energy transport time constant for single exciton hop (t_{hop}) can be approximated from diffusion coefficient following relation $D = R^2/(6 \cdot t_{\mathrm{hop}})$, where R is average intermolecular spacing.[219] Based on D values obtained from exciton annihilation studies and $R \approx 0.85$ nm, hopping time was 170 fs and 40 fs for **BF-p** and **BF-e**, respectively. Although these values are among the shortest recorded for organic crystals,[219] similar t_{hop} was observed in photosynthetic aggregates, where non-radiative Förster type energy transfer is enhanced by excitonic interactions between neighboring chromophores.[6]

FRET rate calculations

To clarify the energy transport differences in crystals of various bifluorene derivatives bearing flexible and rigid core units, Förster energy transfer was estimated according to procedures provided in the literature.[6] As FRET rate is directly related to magnitude of interacting dipoles, BF-a compound with rigid acetylene core and high radiative rate was also included considering its potential for rapid energy transport.

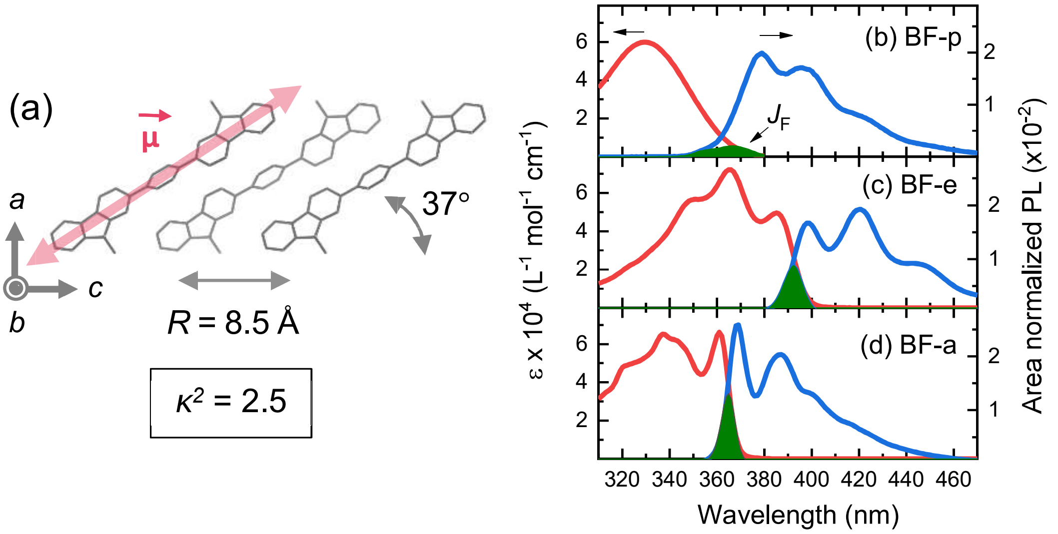

Figure 3.31. (a) View of molecular packing in single layer from *b* direction of BF-p crystal. Packing angle, intermolecular distance and estimated orientational factor are indicated. Molecular transition dipole moment is illustrated with pink arrow. Absorption and emission spectra of (b) BF-p, (c) BF-e and (d) BF-a in THF solutions. Green area indicates Förster overlap.

FRET rate was calculated using equations (1.1) and (1.2) presented in the Section 1.5. Calculation parameters are presented in Table 3.7. Highest orientational factor $\kappa^2 \approx 2.5$ was estimated in the direction of molecular inclination for all bifluorene crystals (see Figure 3.31a), which also coincided with the direction of the highest exciton diffusion coefficient previously determined by LITG experiments. As energy transfer is highly sensitive to intermolecular distance ($k_{\mathrm{FRET}} \sim 1/R^6$), hopping between molecular layers can be neglected due to large interlayer distance ~1.4 nm (see Figure 2.8).

Table 3.7. Parameters for FRET calculations.

	k_{rad} [a] (ns^{-1})	κ^2 [b]	R [c] (nm)	J_F x 10^{16} [d] (cm^2 mol^{-1} nm^4)	t_{hop} [e] (fs)
BF-p	1.3	2.5	0.85	1.8	495
BF-e	0.9	2.5	0.85	7.8	166
BF-a	1.2	2.5	0.85	8.8	108

[a] radiative rate; [b] orientational factor; [c] intermolecular distance; [d] Förster overlap integral; [e] hopping time estimated by FRET calculations ($k_{\text{FRET}} = 1/t_{\text{hop}}$).

Similar molecular packing in all bifluorene crystals meant that energy transfer was determined by differences in the radiative rates and spectral overlap integral (J_F). Lowest overlap integral was estimated for **BF-p** (Figure 3.31b) owing to conformational disorder presented by torsional motion of central phenyl ring. In contrast, up to five times larger J_F was observed for rigid **BF-e** and **BF-a** derivatives. These differences were reflected in calculated hopping times of 495 fs (**BF-p**), 166 fs (**BF-e**) and 108 fs (**BF-a**). It is worth noting, that for FRET calculation radiative rate and spectral overlap was obtained for bifluorene monomers, which allowed to exclude the effects or resonant (excitonic) interactions between molecules in the crystal. Intriguingly, noticeably shorter t_{hop} previously obtained from LITG and SSA experiments suggest that exciton transport in bifluorene crystals might be enhanced by excitonic interactions. This would imply J-type excitonic coupling in the direction of molecular inclination leading to highly anisotropic exciton transport.[109] While no indications of excitonic coupling were observed for **BF-p** derivative (see Chapter 3.2), **BF-e** crystals showed evidences of coherent enhancement of dipole moments as in J-aggregates (see Chapter 3.3). Furthermore, highest radiative rate and largest Förster overlap of **BF-a** indicates the possibility for fastest energy transport in crystals and signifies its potential for efficient host-dopant organic laser systems.

Highlights

- LITG technique was applied to study exciton diffusion in principal crystallographic axis organic crystals
- At least two orders of magnitude larger diffusion coefficient (up to 0.96 cm^2/s) bifluorene crystals in the direction of the strongest dipole coupling as compared to that estimated for the perpendicular direction ($D < 0.01$ cm^2/s)
- The long singlet exciton diffusion length (up to 300 nm) in the direction of strongest molecular dipole coupling suggested that exciton transport is enhanced by excitonic interactions
- Crystals of phenyl-bridged bifluorene derivative showed five times lower exciton diffusion coefficient compared to crystals of ethylene-bridged derivatives, which is associated with conformational disorder presented by torsional flexibility
- The exciton annihilation studies confirmed the differences of exciton transport rate in both crystals of flexible and rigid bifluorenes and revealed high annihilation coefficient, which must be considered for laser devices operating at high excitation densities

Key finding C

- Highly anisotropic singlet exciton transport with diffusion coefficients of up to 1 cm^2/s in bifluorene single crystals is enabled by J-type excitonic coupling. Reduced conformational disorder in crystals containing rigid acetylene and ethylene linked bifluorene derivatives leads to coherent enhancement of exciton transport as evidenced by inverse temperature dependence of energy transfer rate

Research opportunities

- Low temperature LITG measurements to investigate exciton coherence effects on transport
- Quantum chemical analysis for the computation of the exciton diffusion and its anisotropy

3.5 Effects of enhanced energy transfer in doped crystals

Host-dopant systems are a straightforward approach to combine charge transport and light-emitting properties by employing Förster resonant energy transfer from host to lower concentration of highly emissive dopants.[101,191,201] This allows to significantly reduce reabsorption losses by shifting laser emission line to lower energies simultaneously enabling wide emission color tunability.[122,189,220–223]

For practical applications of host-dopant systems in lasers FRET to low concentration of dopants must occur within picosecond timescale to sustain population inversion.[72,166] Hence it is important to consider exciton transport within host as a factor limiting FRET efficiency.[123] In this regard, taking an advantage of enhanced exciton motion in J-aggregates can lead to extremely efficient host-dopant energy transfer. Despite multiple reports on long-range exciton transport in molecular aggregates[126,128,224], this phenomenon has not been extensively explored for use in laser applications.

Production of high-quality doped crystals

Efficient host-dopant energy transfer in doped crystals is ensured by a two-step process involving energy (exciton) transport within host crystal states followed by transfer to the dopant. Both energy transfer stages are controlled by spectral overlap, host photoluminescence (PL) quantum yield and dipole-dipole orientation factor.[128,131,225] Foremost challenge for efficient FRET in doped crystals is to achieve considerable spectral overlap between host PL and dopant absorption, while maintaining almost identical molecular structure to avoid defects in a host crystal lattice.[226] Moreover, to have low ASE threshold for laser applications, linear dopant molecules with high radiative rate are desirable.[91] Therefore, rigid linear molecules packed in J-type aggregates appear as ideal candidates for host-dopant crystals.

Following our previous studies, for production of doped crystals we selected fluorene-based small molecules, where BF-a (host) and BF-e (dopant) differed only by modification of acetylene and ethylene bridging groups, respectively (Figure 3.32). Here, bridging groups performed several functions required for efficient host-dopant systems: (i) bridge rigidity minimized torsional disorder in crystal and reduced exciton-vibronic coupling; (ii) almost identical host and dopant molecular structures inhibited lattice defect formation and (iii) host-dopant energy gap difference provided sufficient spectral overlap for FRET.

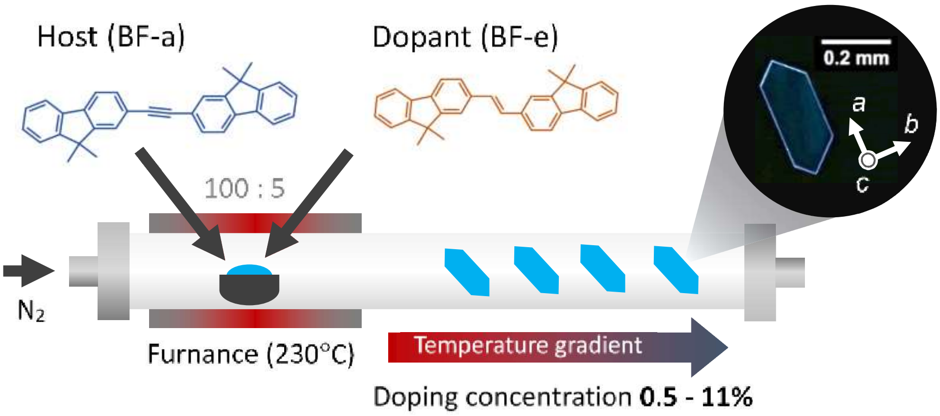

Figure 3.32. Scheme of crystal doping employing physical vapor transport technique. Weight ratio of host and dopant is indicated. Temperature gradient from 230 °C to 170 °C created in the crystallization zone resulted in crystals with various degrees of doping. Micrograph of crystal shows crystallographic axis in respect to crystal orientation.

Doped crystals were produced by physical vapor transport (PVT) technique as shown in Figure 3.32.[101,123] Temperature gradient created in crystallization zone resulted in crystals containing different doping concentrations (C_D). C_D was quantified by dissolving crystals in THF solutions and measuring their absorption spectra (see Figure 3.33). Distinct feature at 3.2 eV allowed to estimate the BF-e (dopant) content in crystals to be in a range of 0.5 – 11.0%. Here, 0.5% doped crystal was selected from a batch of previously grown self-doped BF-a crystals discussed in Chapter 3.3. Intermediate doping concentrations were estimated by evaluating absorption coefficient of the dopant absorption band at 3.1 eV in actual crystals without dissolving them.

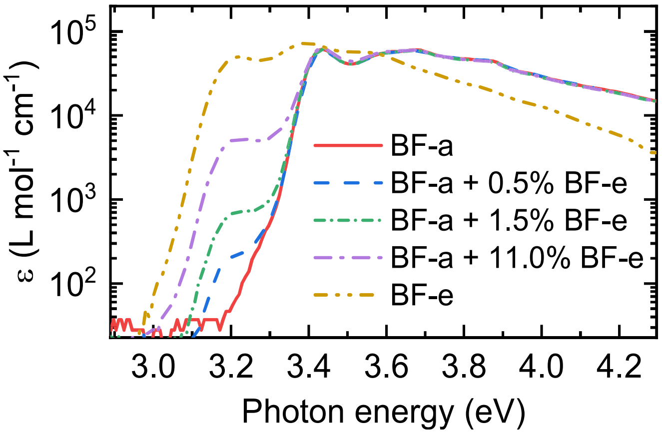

Figure 3.33. Absorption spectra of pure BF-a and BF-e compounds and PVT grown doped single crystals dissolved in 10^{-3} M/l THF solution.

Dopant alignment in host crystal was confirmed by strongly polarized absorption and emission (Figure 3.34). Although, at higher C_D somewhat reduced absorption polarization contrast of host matrix indicated somewhat disturbed host crystal lattice, the relative host and dopant dipole orientation was maintained. It is worth noting that host and dopant transition dipole alignment is critical for efficient FRET in doped crystals, where perpendicular dopant dipoles (as in most oligoacenes) result in two orders of magnitude lower orientational factor, and thus low energy transfer rates.[131]

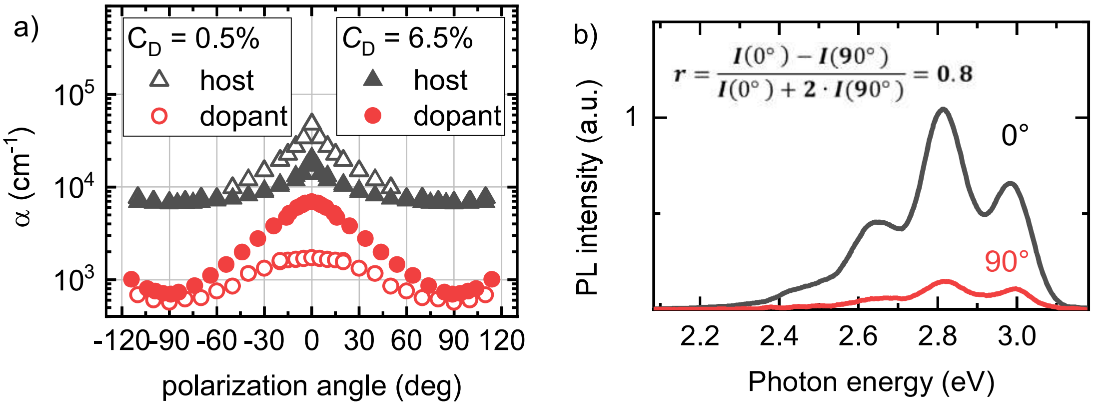

Figure 3.34. (a) absorption polarization measurement of doped crystals. To selectively observe absorption polarization of host and dopant states 3.40 eV (365 nm) and 3.05 eV (405 nm) linearly polarized laser light was used, respectively. Laser beam was set perpendicular to the crystal plane, crystals were rotated around the centered laser excitation spot. (b) PL anisotropy of 0.5% doped crystal measured with the laser excitation polarization fixed to 0° and recording dopant PL spectra through polarizer perpendicular to crystal surface at 0° and 90°, estimated anisotropy value is indicated.

To determine whether introduction of dopants lead to changes of crystalline structure XRD measurements were performed in non-doped and doped co-crystals (Figure 3.35). The observed signal in 002 plane measurements confirmed that molecular layers are parallel to the large crystal facet. The estimated d-spacing values were 27.57 Å and 26.39 Å for **BF-a** and **BF-e** single crystals, respectively, which was in good agreement with *c* direction lattice parameters obtained from single crystal XRD (Table 2.1). The results proved that by introducing BF-e dopant into BF-a crystal, crystalline lattice is not significantly disturbed as only slight peak shift was observed for the 6.5% doped crystals. The linewidth was also found to be equal for doped and non-doped BF-a crystals suggesting that no disorder was created by doping. Furthermore, no signal at BF-e crystal position was observed when measuring doped crystals, which indicates that no clusters of dopant phase were forming in host crystal. Homogeneous distribution of dopants is crucial for efficient hos-dopant energy transfer. Importance of matching lattice constants of host and dopant was previously manifested for production of high-quality tetracene/pentacene doped distyrylbenzene crystals.[226]

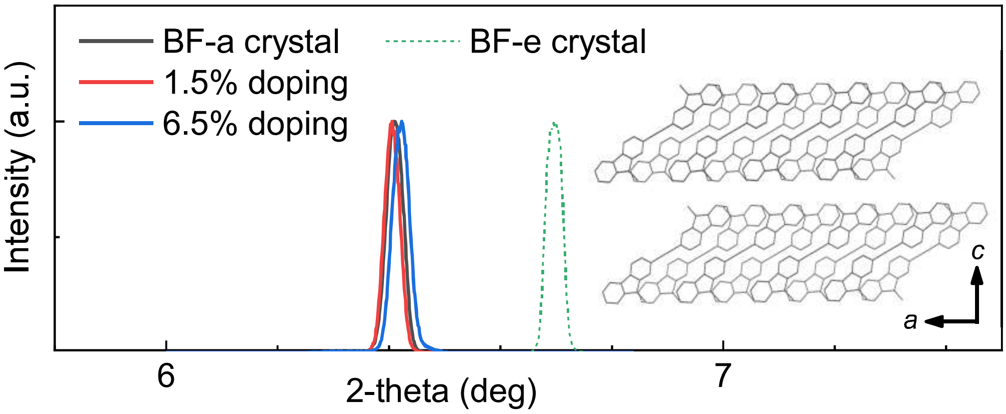

Figure 3.35. XRD patterns of 002 diffraction peak in pure BF-a, BF-e doped BF-a and pure BF-e single crystals. Inset shows view of layered molecular packing in *ac* plane of non-doped BF-a crystal.

The molecular packing of host crystals obtained from single-crystal XRD analysis is presented in the inset of Figure 3.35. The typical layered crystal structure was revealed, where 2D molecular layers were formed in *c* direction with interlayer distance of approximately 14 Å. Molecules within layer are slip stacked at 32° pitch angle in respect to *ab* crystal plane. The intralayer molecular arrangement was assigned to herringbone-type (HB), with 4 Å distance and 62° angle between π-conjugated planes (Figure 2.8). Such intralayer molecular packing leading to reduced π-π overlap is ensured by dimethyl side chains on fluorene units. Moreover, as transition dipole moment of elongated molecules containing several bridged fluorene, phenylene or thiophene units coincide with long molecular axis, intralayer slip-stack packing results in constructive interference, and thus enhancement of oscillator strength.[55,91] Analogous packing properties resulting in spectral features associated with J-type excitonic coupling were observed for modified distyrylbenzene aggregates.[115,227]

Initial assessment of excitonic coupling in host crystals can be made from absorption and PL spectral features.[109] Figure 3.36 shows strong first absorption peak at 3.30 eV and narrow Stokes shift observed for host crystal, that are prominent spectral signatures of J-aggregates.[228] It is evident that these features lead to strong reabsorption of host PL spectrum. Strength of excitonic coupling can be estimated by comparing spectral features of host (**BF-a**) crystal to a monomer (for monomer spectra see Figure 3.18 in Chapter 3.3). First absorption peak of host crystal exhibits 113 meV shift to the lower energies together with 2.7-fold increase of the oscillator strength compared to monomer. This signals weak-to-intermediate resonant J-type coupling strength considering substantial non-resonant (solution-to-aggregate) shift.

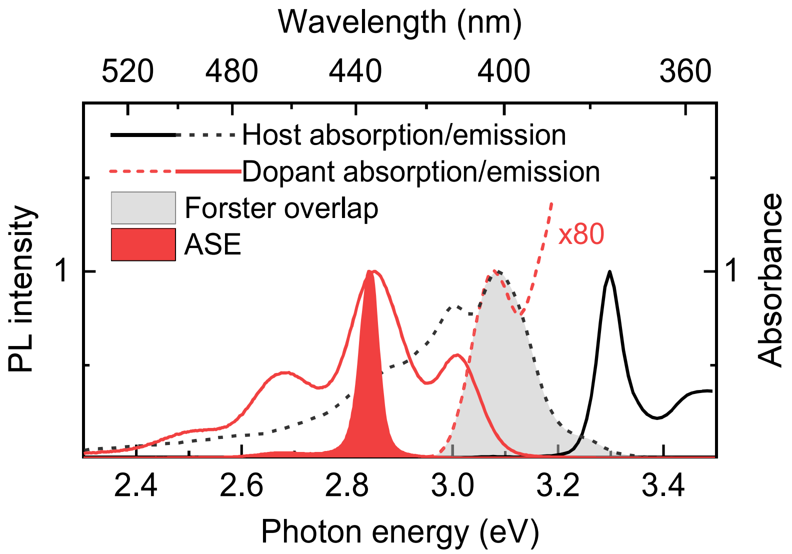

Figure 3.36. Absorption and PL of 0.5% doped crystal, where weak absorption of dopant state is shown by magnifying absorption spectra 80 times. PL spectra of host crystal was measured for crystals grown on quartz at 170 °C in high vacuum to reduce possibility for self-doping. Spectral Förster overlap and ASE spectra are shown as colored areas.

The possibility for efficient FRET in doped crystals is signified by overlap between dopant absorption and host PL spectra presented in Figure 3.36. Here, weak absorption peak centered at 3.1 eV corresponds to dopant absorption. Pronounced Förster spectral overlap allowed to estimate host-dopant FRET time constant of 15 fs (according to procedures provided in Chapter 3.4). Such high FRET rate guarantees that energy transfer process is significantly faster than hopping motion between host chromophores. Moreover, similarly to self-doped crystals presented in Chapter 3.3, intentionally doped crystals showed high $\Phi_{PL} \sim 0.8$ and $k_r \sim 0.9$ ns^{-1}. Close resemblance of k_r values for doped crystal and dopant diluted in solution suggested that, despite excitonic coupling in host crystal, dopants retain monomer-like radiative properties.

Energy transport in doped crystals

J-type exciton coupling in the host crystal is particularly important aiming for fast energy transport to the dopants. As it was shown in the Chapter 3.4 slip-stacked packing of rigid bifluorene derivatives resulted in anisotropic long-range exciton diffusion. Here, molecular rigidity plays an important role as it reduces conformational disorder and increases probability for resonant coupling. In such way coherence between dipoles can lead to further enhancement of energy transfer rate beyond Förster model.[6]

Among multiple methods proposed to determine exciton transport in organic materials, bulk excitation quenching technique is one of the most frequently used allowing to compare transport parameters obtained for various amorphous and crystalline organic semiconductors.[45,198,219] Exciton dynamics in the material are simply determined by the time it takes for host excitation to be transferred to a known concentration of quenchers, and thus exciton transport parameters can be evaluated from the change in host lifetime. Here, quenching in doped bifluorene crystals is ensured by efficient host-dopant FRET.

Excitation quenching dynamics in 0.5%, 1.5% and 6.5% doped crystals visualized by femtosecond transient absorption measurements are displayed in Figure 3.37a. Here, excited state absorption (ESA) appears as positive differential absorption (ΔA) signal. For ease of reference specific ESA spectral features at 1.85 eV and 1.60 eV were associated with the corresponding host and dopant singlet states, respectively. Evident decrease of host lifetime with increasing doping concentration indicated was observed. Global analysis of the transient absorption data was performed to obtain host and dopant decay lifetimes.[229] Simple model of energy transfer between two compartments was fitted with mono-exponential functions convoluted with 200 fs instrumental function. Figure 3.37b shows globally fitted temporal population dynamics between host and dopant states at various doping concentrations. Interestingly, the complete energy transfer from host to dopant states was achieved at doping concentrations as low as 0.5%, while energy transfer efficiency began to degrade at lower doping concentrations (~0.1%) given the larger distance exciton must travel to the dopant. In contrast, observation of energy transfer time at concentrations above 3.5% became limited by 200 fs transient absorption resolution.

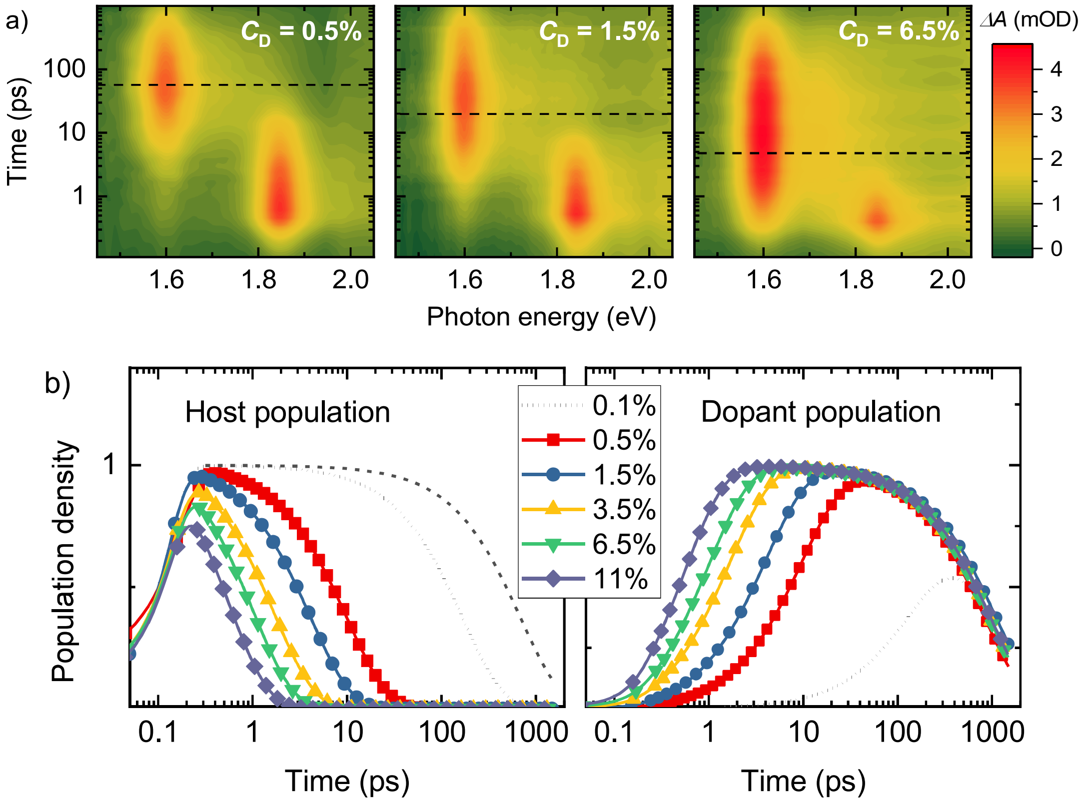

Figure 3.37. (a) Transient absorption maps of 0.5%, 1.5% and 6.5% doped crystals. Host excitation density was set to $N_0=1\mathrm{x}10^{17}$ cm^{-3} for all crystals. Dashed lines indicate the delay time at which maximum dopant population is reached. (b) Globally fitted temporal population dynamics of host and dopant compartments. Initial host population is normalized, however ultrafast host decay in highly doped crystal was limited by the 200 fs instrument response function. Grey dashed line shows non-doped host decay.

As an approximation to determine exciton transport parameters excitation quenching model described in the literature was employed.[219] It follows that host lifetime depends on number of quenching sites (i.e. dopant concentration), thus exciton transport within the host crystal is directly related to the effective energy transfer rate (k_{eff}). In this case, ratio between decay lifetimes of host without and with dopant is linearly related to doping concentration: $\tau_{\mathrm{h0}}/\tau_{\mathrm{h}} = 1 + k_{eff}C_D$, where host crystal lifetime $\tau_{\mathrm{h0}} = 700$ ps was approximated from transient absorption kinetics of non-doped host crystals. The effective energy transfer rate corresponds to average number of hops during the lifetime of non-doped host, therefore hopping time can be expressed as $t_{\mathrm{hop}} = \tau_{h0}/k_{\mathrm{eff}}$. However, if the reduction host lifetime due to quenching is significant ($\tau_{\mathrm{h}} << \tau_{\mathrm{h0}}$), then hopping time is simply approximated as $t_{\mathrm{hop}} \approx \tau_h/C_{\mathrm{D}}$. The calculated energy transport parameters are summarized in

Table 3.8. No significant variation of $k_{eff} \approx 10^4$ with doping concentration suggests that dopants were well dispersed in host crystal even at high C_D. This was not the case for tetracene-doped anthracene crystals, where reduction of k_{eff} was observed above $C_D \sim 10^{-3}$ indicating the effects of clustering.[219]

Table 3.8. Energy transfer parameters obtained from quenching experiments.

C_D[a)]	τ_h[b)] (ps)	k_{eff}[c)], × 10^4	t_{hop}[d)] (fs)	D[e)] (cm^2/s)
0.5%	13.0	1.1	66	2.3 x10^{-2}
1.5%	4.3	1.1	65	1.8 x10^{-2}
2.0%	2.7	1.3	54	2.1 x10^{-2}
3.5%	1.7	1.2	60	1.9 x10^{-2}
4.5%	1.3	1.2	59	2.0 x10^{-2}
6.5%	0.9	1.1	61	1.9 x10^{-2}
11.0%	0.5	1.3	55	2.1x10^{-2}

a) dopant concentration in host crystal b) host lifetime in doped crystals obtained from global analysis of the transient absorption data; c) effective energy transfer rate; d) apparent hopping time $t_{hop} = \tau_{h0}/k_{eff}$; e) apparent diffusion coefficient.

In the most general isotropic energy transport scenario the exciton diffusion coefficient can be approximated as $D = R^2/(6 \cdot t_{hop})$, where R is the spacing between adjacent host molecules in crystal.[219] The rough estimate of average intermolecular spacing from crystallographic data was $c = 0.85$ nm given the 4 molecules in 2.31 nm^3 volume of unit cell (Table 2.1). The calculated diffusion coefficient obtained for doped crystals was averaged to $D = 1.9 \pm 0.14 \times 10^{-2}$ cm^2/s. This approach allowed to compare exciton transport parameters to other doped organic crystals reported in full-scale review on exciton transfer by Powel and Soos.[219] Doped bifluorene crystals investigated in this work stood out for their high apparent diffusion coefficient. However, the assumption of isotropic energy transport model may be inaccurate considering that a long-range order of transition dipole moments in crystals should result in anisotropic exciton motion.[230]

It is important to point out, that estimated hopping time of 6x10^{-14} s is faster than 10^{-13} – 10^{-12} s predicted for other organic systems.[219] It is also almost two times faster than one previously predicted for aligned **BF-a** dimer by FRET calculations (see Table 3.7). Within such ultrafast timescales exciton hopping time becomes comparable to molecular vibrations, therefore the incoherent exciton hopping model becomes inaccurate to describe energy transport, hence partly coherent exciton motion must be considered.[126] Evolution of initially delocalized excitons into hopping motion is governed by scattering due to static and dynamic (thermal) disorder, which limit coherence size.[109] While dynamic disorder in bifluorene crystals is minimized owing to reduced torsional degrees of freedom in rigid molecular structures, strong coupling to molecular vibrations (i.e. exciton-phonon coupling) may completely suppress coherent exciton motion at room temperature.

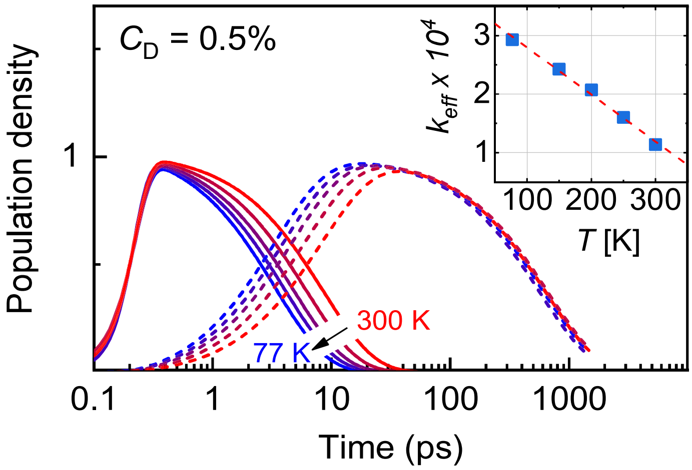

Figure 3.38. The host (solid lines) and dopant (dashed lines) dynamics in 0.5% doped crystal as a function of temperature. Transients were obtained from global analysis of transient absorption data. Temperature dependence of effective host-dopant energy transfer rate is displayed in the inset.

To investigate how thermal energy influences host-dopant excitation energy transport, we performed measurements of is betransient absorption as a function of temperature (Figure 3.38). The crystal with low doping concentration (C_D = 0.5%) was selected for prolonged exciton transport time within host crystal states meaning that an excitation is not immediately trapped at the dopant. Transient absorption measurements revealed a 3-fold enhancement of k_{eff} at 77 K compared to room (see inset of Figure 3.38). A similar feature of enhanced exciton transport at low temperatures has been previously reported by Braun et al. for tetracene-doped anthracene crystals showing inverse linear temperature dependence of energy transport rate below 300 K.[133] Likewise, immediate increase in energy transport rate at temperatures below 300 K signifies that some coherent character of exciton motion within host crystal states might be retained even at room temperature.

Room temperature exciton coherence has been previously reported for highly anisotropic 1D and 2D J-aggregates.[128,224,231]

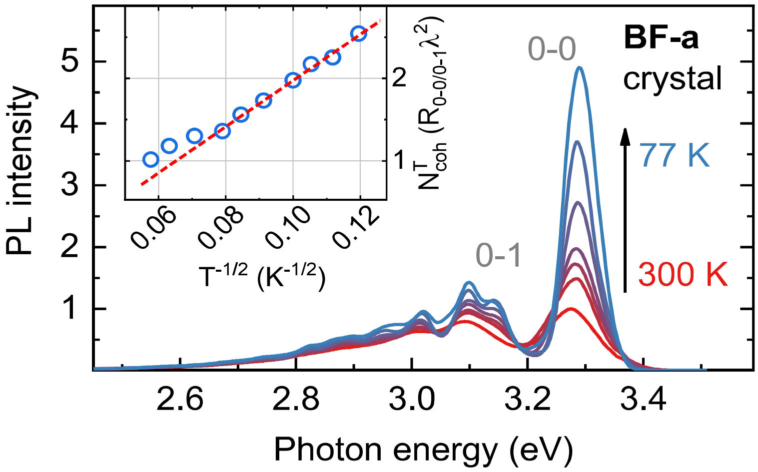

Figure 3.39. Reabsorption corrected PL spectra of pure host recorded at different temperatures. Inset shows calculated coherence length as a function of inverse square temperature.

Further evidence of enhanced exciton transport associated with J-type excitonic coupling can be obtained from temperature dependent PL spectra, which was measured in dopant-free host crystals (Figure 3.39). PL spectra were corrected for strong reabsorption of the 0-0 peak, taking into account the thermal broadening of the absorption line (the procedure is explained in detail in the Supporting Information of Paper V).[232] As coherent nature of 0-0 PL transition is highly sensitive to exciton-phonon coupling, recovery of its intensity upon reduction of temperature compared to lower energy vibronic bands is a characteristic feature of superradiance in J-aggregates.[109,224] Exciton coherent size can therefore be determined using a generalized PL ratio rule $R_{PL} \approx N_{coh}/\lambda^2$, where R_{PL} is the PL ratio of 0-0 and 0-1 vibronic bands, N_{coh} is the exciton coherence number and λ^2 is the Huang-Rhys (HR) factor indicating strength of nuclear relaxation energy. The observed $N_{coh} \sim T^{-1/2}$ temperature dependence and $N_{coh} \approx 2.7$ at low temperatures ($T = 70$ K) implies partial exciton delocalization over several host molecules. The crystallographic data suggests that excitonic coupling is strongest between closest neighbors in *a*-direction (Figure 2.8). Similar temperature dependencies were previously observed for defect-free polydiacetylene chains (a model material for linear J-aggregate)[233] as well as tetracene crystals.[117]

The observed inverse temperature dependence of exciton transport rate may also be an attribute of rigid molecular structures, which lead to lower torsional disorder in crystal. Opposite behavior showing temperature activated energy transport was previously observed in bifluorene (Figure 3.13 in the Chapter 3.2) and thiophene–phenylene co-oligomer single crystals featuring similar molecular packing.[177,191] Evidently, linkers between fragments enabling torsional degrees of freedom contributed to broad distribution of states evidenced by the featureless ground state absorption in the crystals. Hence, coherent excitonic coupling between neighboring molecules in crystal was disrupted by static (torsional) as well as dynamic (thermal) disorder. Although the underlying mechanism of partly coherent exciton transport presented in this section is not definite, it must be pointed out that excitonic coupling in the host crystal contributes to an enhanced host-dopant energy transfer rate in doped crystals. This will have an impact on processes dependent on exciton density including exciton annihilation and amplified spontaneous emission.

Exciton-exciton annihilation

High excitation densities required to sustain population inversion lead to inevitable exciton annihilation processes in organic lasers.[72] As annihilation is an exciton diffusion mediated process, for long-range energy transport materials exciton annihilation may result in substantial excitation losses and material degradation. To demonstrate the effectiveness of crystal doping to suppress annihilation losses in gain material, exciton dynamics were investigated as a function of excitation density and doping concentration.

To determine the SSA rate with and without presence of dopants we measured transient absorption of the pure host crystal versus excitation density (Figure 3.40a). Excitation above 1 x 10^{17} cm^{-3} resulted in a rapid increase of decay rate indicating an onset of SSA in pure host crystal. Transients were fitted according to exciton annihilation model described in Chapter 3.4, which yielded an average annihilation constant of $\gamma = 2.7 \times 10^{-8}$ cm^3/s. Similar annihilation constant has been previously shown to induce strong enough bimolecular recombination to have negative effects on lasing threshold in *para*-sexiphenyl crystals.[88,135] Importantly, the diffusion constant of $D = 2.5 \times 10^{-2}$ cm^2/s estimated from annihilation rate agreed with the one obtained from quenching experiments (Table 3.8).

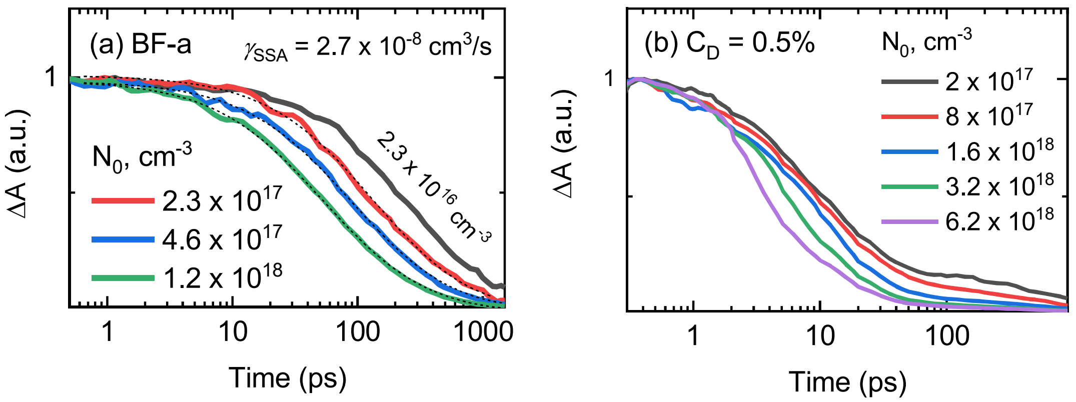

Figure 3.40. Excited state absorption transients of (a) pure host and (b) 0.5% doped crystals as a function of excitation density. Transients were recorded at 1.85 eV, i.e. host excited state absorption maxima. Crystals were excited with 3.26 eV laser pulses, excitation densities are indicated. Fitted curves of annihilation model are included for (a), estimated annihilation constant is indicated.

However, SSA was significantly suppressed with introduction of dopants that acted as energy traps (Figure 3.40b). An order of magnitude higher SSA onset for doped crystals was observed at excitation densities above 10^{18} cm^{-3}. Considering the dopant density in host crystals is approximately $N_D = 8 \times 10^{18}$ cm^{-3} in 0.5% doped crystals, the excitation density must be on the same order of magnitude to initiate SSA. For 6.5% doped crystal ($N_D = 1.2 \times 10^{20}$ cm^{-3}) SSA was not observed at significantly higher excitation due to even faster exciton trapping. Importantly, early onset of SSA in crystals with lower doping concentrations can lead to non-radiative losses before ASE threshold is reached.

The effects of SSA on ASE properties were assessed by investigating transient absorption signal of dopant population as a function of excitation density in 0.5% and 6.5% doped crystals (Figure 3.41). Here, dopant ΔA signal is directly related to population density at any given time. At excitation densities above ASE threshold a fast decay component appearing within picoseconds after energy transfer reflected rapid stimulated transitions from the dopant excited state. At later times it was followed by slow decay indicating spontaneous transitions when excitation density has settled below ASE threshold.

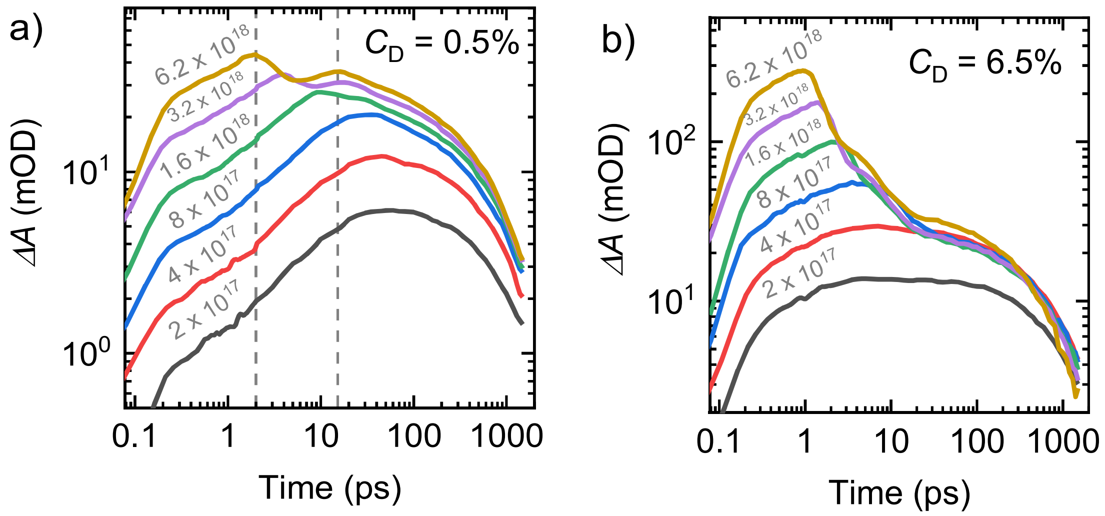

Figure 3.41. Dopant population dynamics as a function of excitation density and dopant concentration. The transient absorption signal of (a) 0.5% and (b) 6.5% doped crystals was recorded at 1.60 eV of dopant excited state absorption. Crystals were excited with 3.26 eV laser pulses. Initial host state excitation density in cm^{-3} is indicated above transients.

Interestingly, as depopulation rate due to ASE became faster than repopulation rate via FRET, two temporal ASE processes were observed for the 0.5% doped crystal (Figure 3.41a). Above $N_0 = 8 \times 10^{17}$ cm^{-3} a step function at 15 ps was observed signifying ASE threshold, while at higher excitation densities another temporal step appears at 2 ps resulting in second ASE burst from dopant states. Similarly, ASE dynamics have been previously reported for doped DCM-Alq$_3$ neat films.[234] On the other hand, oscillatory behavior of dopant population was less pronounced in the 6.5% doped crystal owing to a significantly increased host-dopant energy transfer rate (Figure 3.41b). Approximately 2-fold lower ASE threshold density of $N_0 = 4 \times 10^{17}$ cm^{-3} was recorded for the 6.5% doped crystal compared to the 0.5% doped one.

Higher annihilation losses in 0.5% doped crystals were evidenced by saturation of maximum *ΔA* signal, indicating lower dopant population at high excitation densities compared to 6.5% doped crystal (Figure 3.41). Essentially, improvements of ASE threshold may be justified by enhanced excitation trapping rate. For practical laser applications, low exciton annihilation rate is highly desirable as annihilation events lead to inevitable degradation of organic compounds.[43,235] In particular, singlet-singlet annihilation was shown to generate long-lived polarons due to autoionization in *para*-sexiphenyl crystals.[69]

Amplified spontaneous emission

Although suppressed exciton annihilation losses in doped crystals benefit the ASE performance, the increasing doping concentration should eventually reintroduce reabsorption by the dopant species. This implies that the lowest ASE threshold in host-dopant systems is achieved at the optimal doping concentration.

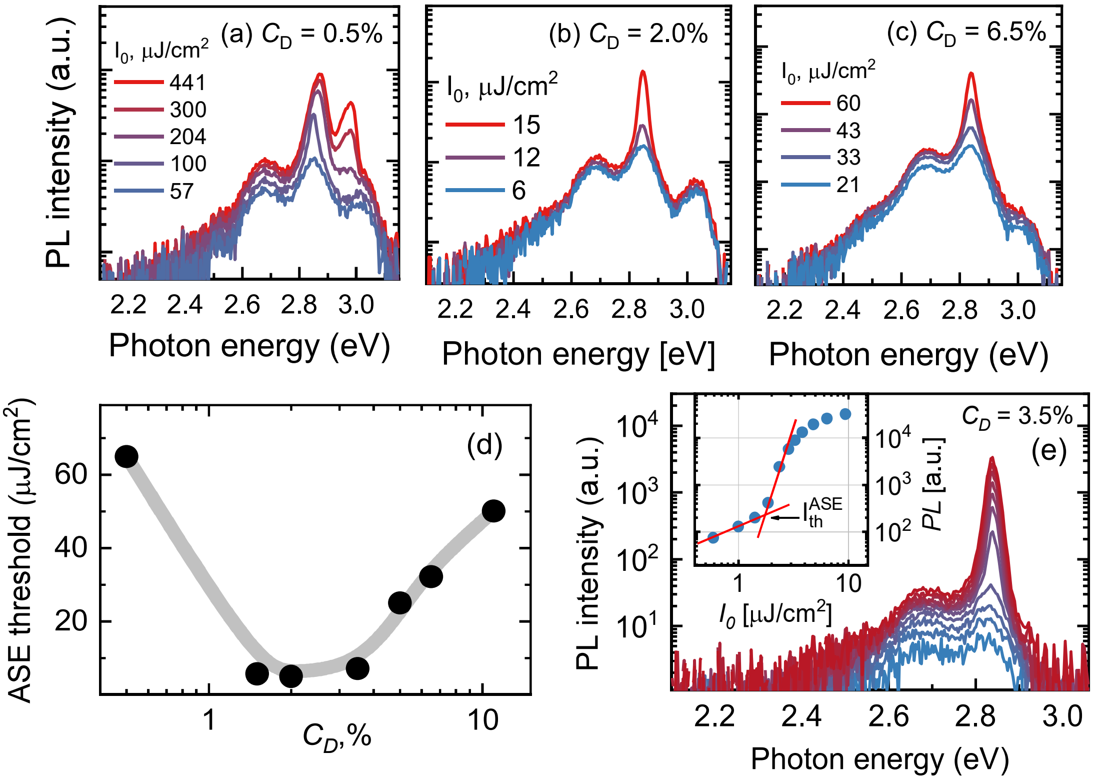

Figure 3.42. ASE properties as a function of doping concentration. (a-c) PL spectra of 0.5%, 2.0% and 6.5% doped crystals recorded at different excitation fluence. Excitation spot diameter was set to 300 µm. (d) ASE threshold values recorded at spot excitation geometry as a function of doping concentration. (e) PL spectra of 3.5% doped crystal versus excitation fluence recorded in thin stripe (200 x 2400 µm) excitation geometry. Inset shows PL intensity at 2.85 eV as a function of excitation fluence. For all ASE measurements laser excitation (photon energy – 3.31 eV, repetition rate - 10 kHz, pulse duration - 200 fs) was used.

To compare ASE performance in crystals with different doping concentrations we measured PL intensity as a function of excitation fluence in crystals with C_D ranging from 0.5 to 11.0%. The characteristic excitation dependent PL spectra of low (0.5%), medium (2.0%) and high (6.5%) doped crystals are presented in Figure 3.42(a, b and c). The evident spectral narrowing at 2.85 eV above a certain pump intensity (ASE threshold, I_{th}^{ASE}), is induced by spontaneous emission travelling along the excited region getting amplified by the stimulated transitions. Interestingly, PL spectra of 0.5% doped crystal showed a second ASE peak appearing at 2.97 eV for excitation above 200 μJ/cm^2, which may be associated with emission from 0-2 vibronic peak of the host. This is supported by step function observed in host transients at 6.2 x 10^{18} cm^{-3} excitation density (see Figure 3.40b), indicating that rate of stimulated emission from host states becomes faster than energy transfer to host states.[189] In contrast, host ASE was not observed in crystals with higher doping concentrations owing to enhanced energy transfer rate. However, at doping concentrations >3.5% reabsorption at 3.0 eV edge of the PL spectra became evident (Figure 3.42c).

I_{th}^{ASE} plotted as a function of crystal doping concentration presented in Figure 4d shows a clear trend of lowest ASE threshold values (down to 5.1 μJ/cm^2) achieved at optimal 1.5 – 3.5% doping range (Figure 3.42d). This implies that different loss mechanisms dominate low- and high-end of doping. As it was shown in the previous section, SSA losses in low doping crystals suppress efficient population of the dopant, while increasing reabsorption losses lead to almost order of magnitude enhanced ASE threshold at high doping concentrations.

It must be noted that I_{th}^{ASE} values presented in Figure 3.42d were measured using 300 μm diameter spot excitation geometry, where light amplified in the short path was scattered by imperfections of the crystal surface. The ASE threshold can be significantly improved in long excitation path and edge emission geometry provided by thin excitation stripe measurements.[72] Thin stripe excitation method is highly sensitive to waveguiding properties and edge quality of the crystal, complicating the comparison of the samples due to varying thickness, size or shape of PVT grown crystals. Nevertheless, by employing thin stripe excitation I_{th}^{ASE} as low as 1.9 μJ/cm^2 was achieved for 3.5% doped crystal (Figure 3.42d). Similar values of 2.1 μJ/cm^2 and 3.0 μJ/cm^2 were also recorded for 2.0% and 1.5% doped crystals, respectively. ASE thresholds recorded for doped bifluorene crystals is among the lowest reported for organic crystalline materials.[91,112] However, ASE threshold in doped crystals are still above 0.3 μJ/cm^2 recorded for best performing amorphous CBP:BSBCz 6 wt% blend films.[83]

The observed variation of recorded ASE threshold values in 1.5 - 3.5% doped crystals was most likely caused by differing crystal thickness (in the range of 0.8-5 μm). The reduced overlap between pump population and waveguide modes (see Figure 2.5 in the Experimental Methods) has been shown to have detrimental effects on ASE threshold in thick films with short absorption length ($\mu < 1$ μm).[76,144] For example, extremely low ASE threshold (down to 0.09 μJ/cm^2) was recorded in $d = 260$ nm Octafluorene neat amorphous films.[76] Considering high absorption coefficients of bifluorene crystals, thinner crystals should exhibit significantly lower ASE threshold values in excitation fluence units. Therefore, demonstration of low ASE threshold in most single crystals is probably limited by nonoptimal crystal thickness and size ratio for thin stripe excitation measurements.

Strong sample thickness dependence of I_{th}^{ASE} due to pump-mode overlap signifies the importance to also express ASE threshold value in excitation density units N_{th}^{ASE}[cm^{-3}] for volume excitation conditions ($\mu \geq d$). For lowest absorption at 3.40 eV excitation ($\mu \approx 1.8$ μm) N_{th}^{ASE} of 4 x 10^{16} cm^{-3} was obtained in 3.5% doped crystal. Furthermore, considering 1 ns PL lifetime of doped crystals, ASE exciton density for continuous-wave (CW) laser operation would be in the range of 5x10^{25} cm^{-3}/s, which in ideal device would allow to reach lasing threshold at relatively low charge carrier densities of ~50 A/cm^2 (see Figure 1.2 in Chapter 1.1). However, in real organic laser device CW operation leads multiple quenching mechanisms associated with build-up of charges or triplet excited states, that initiate annihilation and degradation processes often inhibiting lasing altogether.[18,35,40,43,49]

Triplet accumulation in doped crystals

One of the possible loss mechanisms affecting organic lasers at CW excitation is overlap of emission with triplet excited state absorption.[59,71] To clarify effects of triplets transient absorption studies at pulsed and quasi-CW excitation conditions were performed. Figure 3.43a shows that triplet accumulation can be achieved if the time between excitation pulses is significantly shorter than triplet lifetime, which for organic materials is in the order or microseconds.[151] Therefore, in transient absorption measurements performed at 100 kHz excitation frequency, accumulated triplet signal appears as constant excited state absorption at 2.3 eV during the measured delay times (Figure 3.43b).

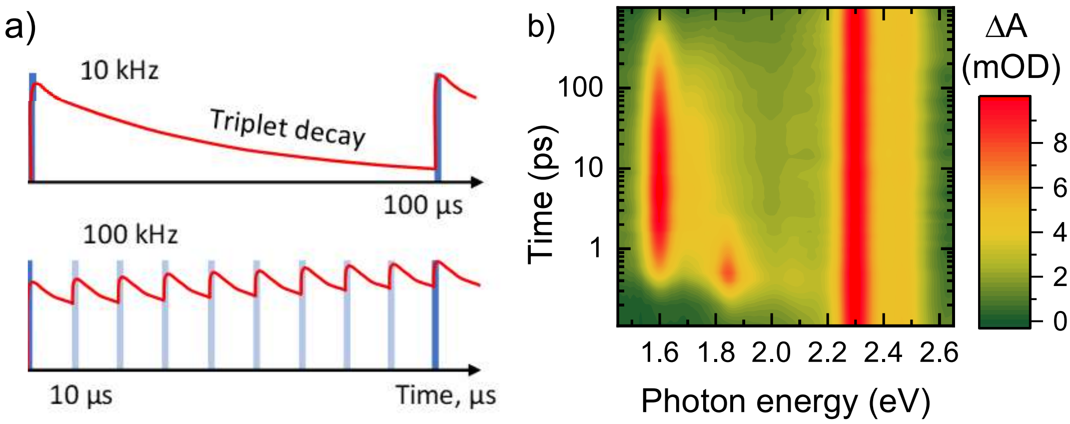

Figure 3.43. (a) Scheme explaining triplet accumulation at 10 and 100 kHz excitation frequency. Triplet transient is indicated with red line. (b) Transient absorption map of 6.5% doped crystal recorded at 100 kHz excitation frequency.

To demonstrate how triplet accumulation affects stimulated emission properties, broad-band transient absorption spectra were recorded at 1, 10 and 100 kHz excitation frequencies (Figure 3.44a). Evidently, at increasing excitation frequency rise of triplet ESA at 2.3 eV was associated with decrease of dopant singlet ESA at 1.6 eV. This gave a rough estimate of triplet lifetime to be in the range of 50 µs. Considering at 100 kHz excitation triplet lifetime is already longer than time between pulses excitation, further increase of laser repetition rate should not result in significantly larger triplet population, thus quasi-CW excitation conditions can be assumed. Similar saturation of triplet buildup with true CW excitation has been previously shown to result in two ASE thresholds for pulsed and CW excitations.[49]

The quasi-CW excitation conditions also lead to reduction of stimulated emission (SE) peak intensity at 2.82 eV (Figure 3.44a). Negligible overlap with weak triplet absorption tail could not explain such large difference. Therefore, it was related to triplet buildup saturating available states and thus effectively reducing singlet population. Thin stripe excitation measurements performed at 100 kHz excitation frequency confirmed a negative impact of triplet buildup, which resulted in approximately 1.5-fold increase of I_{th}^{ASE} for all doped crystals.

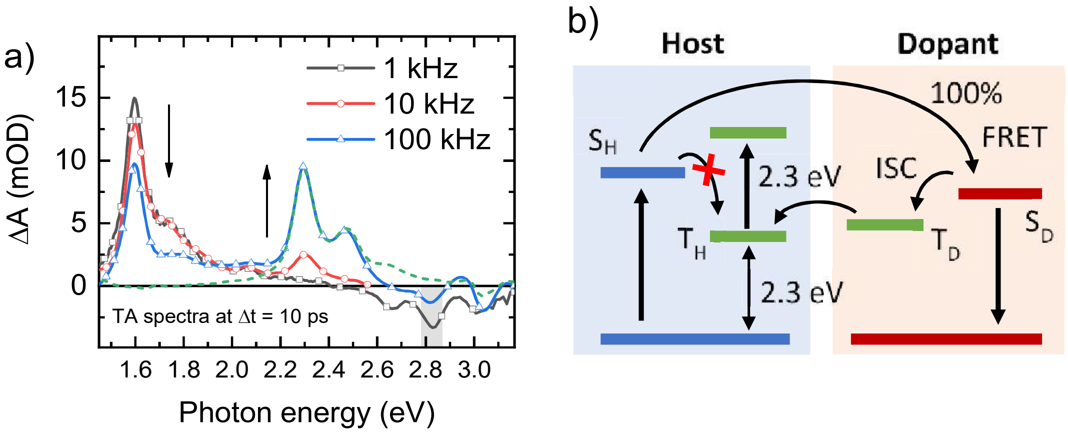

Figure 3.44. (a) Transient absorption signal of 6.5% doped crystal recorded at 10 ps delay time as a function of 1, 10 and 100 kHz laser repetition rate. Excitation was set at 3.26 eV and density of $I_0 = 8$ μJ/cm^2 ($N_0 \sim 10^{17}$ cm^{-3}). Dashed line shows triplet absorption signal at -5 ps delay time. (b) Scheme illustrating singlet and triplet population dynamics in host-dopant crystal.

The negative SE feature at 2.82 eV coincided with spectral position of the ASE peak (see Figure 3.42). The SE cross-section was estimated according to relation:[182] $\sigma_{SE} = -1/(d \cdot N_0 \cdot \ln(10^{-\Delta A}))$, where ΔA is differential absorption signal intensity; d is sample thickness; N_0 – initial excitation density. Calculated stimulated emission cross-section at 1kHz excitation frequency was $\sigma_{SE} = 1.5\text{x}10^{-16}$ cm^2, that is in agreement with other characteristic high-performance organic laser gain materials.[236,237]

It is important to point out that triplet build-up also lead to reduction of host singlet ESA signal at 1.82 eV (not displayed here) indicating that triplets excitations reside at host. To illustrate the origin of triplet signal in doped crystals a diagram was devised (Figure 3.44b). Direct host triplet formation via intersystem crossing (ISC) in doped crystals was highly unlikely considering low ISC rate compared to high FRET rate, which led to 100% energy transfer to dopant states. As a matter of fact, identical triplet signal was observed selectively exciting dopants at 3.05 eV, suggesting that triplet generation via ISC may occur from dopant singlet. However, pure dopant (BF-e) crystals showed no triplet ESA signal at 2.3 eV, which was only observed for pure host (BF-a) crystals. These findings prove that triplets must be transferred back to host via Dexter transfer mechanism. The low triplet level of host (BF-a) is most likely associated with acetylene bond.[238] Low temperature (10 K) phosphorescence measurements revealed low lying triplet of BF-a (host) films at 2.34 eV, while no phosphorescence was detected for BF-e (dopant) films measured in same conditions. Interestingly, in agreement with scheme of exciton dynamics presented in Figure 3.44b, triplet accumulation was found to be independent of energy transfer rate, and thus doping concentration. Interestingly, this together with weak overlap between ASE peak and triplet absorption (Figure 3.44a) would suggest that triplet states might not have strong influence on photostability of doped crystals.

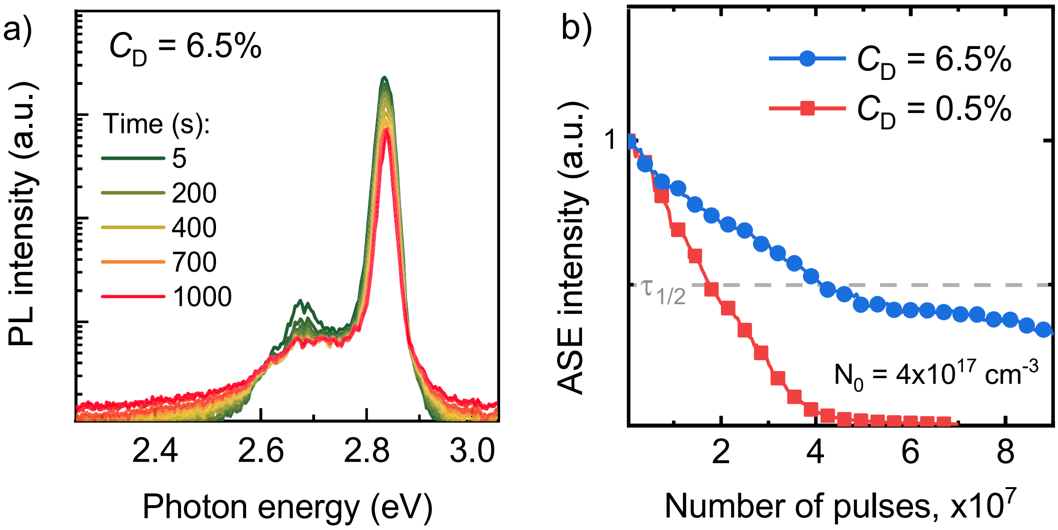

Figure 3.45. (a) PL photodegradation measurements of 6.5% doped crystal recorded in thin stripe excitation geometry. (b) PL peak intensity at 2.82 eV as a function of number of excitation pulses absorbed in 0.5% and 6.5% doped crystals. For all ASE measurements laser excitation (photon energy – 3.31 eV, repetition rate - 100 kHz, pulse duration - 200 fs) was used. Excitation density was set above ASE threshold at 4 x 10^{17} cm^{-3}.

ASE photostability measurements of 0.5% and 6.5% doped crystals under continuous 100kHz excitation above ASE threshold are presented in Figure 3.45. Significantly faster photodegradation of 0.5% doped crystal may be associated with more pronounced exciton annihilation processes. While in Figure 3.40 it was shown that singlet exciton annihilation losses at 4 x 10^{17} cm^{-3} were barely observable for 0.5% doped crystal, other annihilation mechanisms between singlet and triplet may be occurring at quasi-CW excitation. It is known that triplet photodissociation is associated with singlet-triplet annihilation (STA) that is induced by absorption of singlet energy high to the triplet excited state manifold approaching ionization potential.[239]

To minimize losses associated with triplets multiple strategies based on triplet quenching have been proposed.[43,48,49,240] More advanced strategies utilize triplet-singlet up conversion via reverse intersystem crossing[41] or employing phosphorescent complexes as triplet sensitizers for triplet-singlet guest-host systems.[241,242] However, these methods are difficult to implement in single crystals while maintaining defect-free crystal structure. In this case, a straightforward solution would be to have a host material showing high triplet-triplet annihilation rate, which would allow to convert triplets to singlets at high excitation densities. TTA was previously observed in polyfluorene films, where delayed emission due to recycled triplets contributed to one third of efficiency in fluorescent OLEDs.[243,244] Furthermore, BF-a host already shows the overlap between triplet emission and triplet excited state absorption, which is one of the conditions for efficient TTA process. For that reason, triplet related processes in host-dopant crystals will remain an area for further investigation.

Highlights

- It was demonstrated that differently linked bifluorene molecules can serve as an energy transporting host and an emitting dopant in a well-ordered crystal structure with high doping levels
- Control of picosecond host-dopant energy transfer times was made possible by varying dopant concentration (0.5 – 11.0%) as close to 100% energy transfer efficiency was achieved even at low doping concentrations
- Direct monitoring of the energy transfer process by femtosecond transient absorption revealed a significantly enhanced exciton transport rate at low temperatures suggesting partly coherent transport
- Crystal doping was proved to be a successful strategy to substantially reduce reabsorption losses in gain media and suppress exciton annihilation losses at optimized doping concentrations
- The lowest achieved ASE threshold of 1.1 $\mu J/cm^2$ (1×10^{16} cm^{-3}) in 3.5% doped crystal was comparable to the best performing amorphous organic solid-state gain materials

Key finding D

- Long-range exciton transport in doped bifluorene crystals mediates ultrafast exciton transfer to highly emissive dopants allowing to significantly reduce reabsorption and exciton annihilation losses at optimal doping concentration, and thus improved ASE performance and photostability can be achieved

Research opportunities

- Photodegradation studies as a function of doping concentration to investigate the influence of exciton annihilation suppression
- Study of triplet-triplet annihilation process as a possible triplet scavenging mechanism

SANTRAUKA

Įvadas

Organinių puslaidininkinių medžiagų atradimas yra svarbus naujos kartos elektronikos prietaisų kūrimui, nes šie prietaisai būtų lankstūs, pigūs ir pritaikomi biologinėmis sistemomis.[1,2] Organinės medžiagos suderina plastikui būdingas mechanines ir chemines savybes bei pasižymi puslaidininkiams būdingomis savybėmis, kas leidžia atlikti tokias funkcijas kaip šviesos sugertis ir spinduliavimas arba elektrinis laidumas. Šiuo metu praktiškai visuose elektronikos prietaisuose įprastai naudojami neorganinių puslaidininkių kristalai, reikalaujantys sudėtingų aukštatemperatūrių gamybos procesų bei retai žemėje sutinkamų cheminių elementų. Skirtingai, organiniai puslaidininkiai yra sudaryti iš vieno dažniausiai žemėje sutinkamų elementų – anglies, o organinių medžiagų savybės įgalina tokius gamybos procesus kaip didelio ploto prietaisų gamyba tiesiog liejant iš tirpalo.[3] Tai yra viena iš priežasčių, kodėl trapių kristalinių neorganinių puslaidininkių eroje organiniai puslaidininkiai buvo praminti minkštomis netvarkiomis medžiagomis, o siekiant aprašyti jose vykstančius fizikinius procesus reikėjo sukurti naujas teorijas.[4] Nors šiuo metu naudojant sąlyginai pigias organines medžiagas yra bandoma atkartoti tradicinių puslaidininkių funkcionalumą tokiuose prietaisuose kaip saulės celės, šviestukai ar kompiuterių tranzistoriai, tikimasi, kad netolimoje ateityje dėl fenomenalių fizikinių savybių naujos medžiagos gali pasiūlyti unikalių technologijų.

Viena iš neįprastų organinių medžiagų savybių – jų funkciją apibrėžia tiek tvarka, tiek netvarka. Visų pirma, anglies bei kitų atomų tvarka organinėje molekulėje lemia visas jų chemines ir fizikines savybes sutalpintas į nanometro (viena milijardinė metro dalis) dydžio struktūrą. Pavyzdžiui, tam tikras atomų išsidėstymas leidžia stiprią sąveiką su šviesa ir tai lemia spalvas (ir jų suvokimą) gamtoje sutinkamose organinėse molekulėse. Antra vertus, netvarką molekuliniame lygmenyje nusako sąlyginai silpni ryšiai laikantys anglies atomus kartu, kas leidžia molekulių struktūrai virpėti, suirti ir sudaryti naujus junginius, bei sudaro organinės chemijos pagrindą.[5] Ryšys tarp tvarkios ir netvarkios struktūros taip pat yra svarbus, kai glaudžiai supakuotos mikroskopinės molekulės sudaro makroskopinius objektus, skirtus tam tikrai funkcijai atlikti, kaip tai atsitinka augalų ir gyvūnų ląstelėse. Tokių molekulinių darinių sužadinimas šviesa sukuria kvazidalelę vadinamą eksitonu, kuris yra atsakingas už energijos dinamiką tiek natūraliose fotosintezę vykdančiose sistemose, tiek dirbtiniuose elektronikos prietaisuose.[6,7] Šiuo atveju tvarka, kuria molekulės yra išsidėsčiusios tarpusavyje, gali turėti dramatiškų efektų lemiančių tam tikras fizikines savybes. Net turėdama ribotus „žinių" ir medžiagų išteklius (palyginti su tuo, ką šiuo metu taiko žmogus savo kuriamiems prietaisams) per daugelį metų gamta sugebėjo sukurti efektyvią struktūrą versti šviesos energiją kitomis energijos rūšimis augaluose. Tuo tarpu neseniai atrastas elektros laidumas ypatingą struktūrą turinčiose kabelinėse bakterijose buvo palyginamas su laidumu stebėtu geriausiuose dirbtiniuose organiniuose puslaidininkiuose.[8] Deja, net moderniausios organinių puslaidininkių technologijos šiuo metu neišnaudoja molekulinės tvarkos potencialo, todėl tokiuose rinkoje esančiuose prietaisuose kaip organiniai šviestukai ar saulės elementai, naudojami daugiausia netvarkūs (amorfiniai) molekuliniai sluoksniai.

Vienas iš būdų pagerinti elektronikos prietaisų efektyvumą yra tvarkių organinių sistemų panaudojimas siekiant spartesnės eksitonų pernašos ir geresnio elektrinio laidumo. Pavyzdžiui, tai ypač svarbu naujos kartos plastikiniams tranzistoriams, kur neseniai įvykusi gamybos technologijų pažanga greitu metu leis integruoti organines kristalines medžiagas žymiai nekeičiant gamybos kainos bei neaukojant prietaisų mechaninių lankstumo savybių.[9] Pastaraisiais metais organinėms saulės celėms pasiekus naujus efektyvumo rekordus (virš 16%) buvo akcentuota valdomos morfologijos (t.y. ryšio tarp kristalinės tvarkos ir netvarkos) svarba.[10–13] Taip pat, pritaikius eksitonų skilimo fenomeną, vykstantį išskirtinai organiniuose kristaluose, buvo žymiai padidintas plačiai naudojamų neorganinių silicio saulės celių efektyvumas (nuo 29% iki 35%), kas galbūt netolimoje ateityje leis ekonomiškesnę elektros energijos gamybą.[14,15] Molekulinės tvarkos nauda neaplenkė ir organinių šviestukų (*angl.*, OLED, *Organic Light-Emitting Diode*), kuriuose šviečiančių molekulių orientavimas leido pasiekti 30% viršijančius išorinius kvantinius našumus dėl geresnės šviesos ištrūkos lyginant su netvarkių molekulių sluoksniais.[16] Tai yra tik keli pavyzdžiai, parodantys, kaip valdoma molekulinė tvarka leido sukurti našesnius organinės elektronikos prietaisus.

Kai dauguma šiuolaikinės elektronikos komponentų jau yra atkurti naudojant organines medžiagas ir netrukus pakeis mūsų elektronikos suvokimą, elektra kaupinami organiniai lazeriai yra tik pradiniuose vystymo etapuose. 2019 metais, išsprendus pagrindines problemas susijusias su stipriu organinių medžiagų sužadinimu, buvo pademonstruoti pirmieji veikiantys organinio lazerio prototipai.[17–19] Neįprasta tai, kad nuo pat lazerio sukūrimo

1960-taisiais metais organiniai junginiai buvo naudojami kaip aktyvi terpė taip vadinamuose dažų lazeriuose, kurie tuo metu net pranoko neorganinių lazerių technologijas, dėl plačiai derinamos emisijos spalvos ir galimybės formuoti ultratrumpus impulsus.[20] Vėliau išvystyta kompaktiškų elektra kaupinamų neorganinių lazerių technologija iš rinkos išstūmė didelių matmenų neefektyvius dažų lazerius. Tolimesnis lazerių technologijų vystymas 2019 metais atvėrė 14 mlrd. dolerių rinką taikymams medžiagų apdirbimo, komunikacijos, medicinos ir kitose srityse.[21] Nors šiuo metu poreikis lazerių technologijoms yra ypač didelis, lazerių taikymą plataus naudojimo elektronikai riboja tiek didelė jų gamybos kaina, tiek universalumo stoka. Žvelgiant į organinių puslaidininkinių medžiagų perspektyvą, dabartinė OLED vaizduoklių rinkos vertė siekia 31 mlrd. dolerių.[22] Numatomas tolimesnis OLED rinkos augimas taip pat reiškia ir didėjančią organinių medžiagų svarbą ateities elektronikai bei galimą proveržį organinių lazerių technologijose.

Trapi organinių medžiagų struktūra niekada neleis sukurti patikimų didelio galingumo lazerių, kuriuos šiuo metu galima gaminti naudojant neorganinius puslaidininkius, tačiau jau dabar yra svajojama apie unikalias organinių lazerių technologijas. Galimybė naudojant organines medžiagas sukurti sudėtingas mikro- ar nano- lazerių sistemas domina mokslininkus, kuriančius prototipus taikymams biologijoje ar kompiuterijoje.[23–25] Optiškai kaupinami organiniai lazeriai jau yra išbandomi didelės raiškos biologinių procesų vizualizavimui gyvų ląstelių viduje arba implantuojamų sveikatos priežiūros priemonių kūrimui.[26–28] Kitas analogo neturintis organinių lazerių taikymas yra kvantinė kompiuterija, kur organiniai puslaidininkiai puikiai tinka sukurti egzotišką kvazidalelę – poliaritoną, kuri atsiranda esant ypač stipriai šviesos sąveikai su eksitonais.[29] Garsaus kompiuterių gamintojo IBM mokslininkai 2019 metais įrodė, kad poliaritoniniai lazeriai, pagaminti naudojant organines medžiagas, yra „proveržio technologija" optiniams tranzistoriams.[29–31] Taigi, šios technologijos žada šviesią ateitį organinių medžiagų panaudojimui lazeriuose, ir belieka sulaukti kol gamybos technologijos įgalins kurti nanoskalės dydžio sistemas.

Prisiminkime, kad anglies pagrindu sukurtos molekulės evoliucionavo į sudėtingas, savarankiškai surenkamas molekulines mašinas, kaip fotosintetinė sistema arba DNR replikavimo mechanizmas.[6,32] Šiuo metu, net turint prieigą prie visų įmanomų išteklių, mokslo pastangos siekiant atkartoti šias sistemas vis dar neprilygsta tam, ką sukūrė gamta per 4,5 milijardo metų. Viena iš sričių žadanti didelius proveržius šiuo klausimu yra supramolekulinė chemija, kuri leistų panaudoti paprastas organines molekules apjungiant jas į sudėtingas dirbtines sistemas, skirtas atlikti elektronikos prietaisų funkcijas.[33] Nauji evoliucinės chemijos metodai, paremti biologinio dizaino principais (idėja laimėjusi Nobelio premiją 2018 metais), netolimoje ateityje padės išplėsti organinės sintezės įrankius skirtus kurti nano-medžiagoms.[34] Nors šiuo metu tokios idėjos atrodo neįtikėtinos, ateityje atotrūkis tarp biologinių sistemų ir elektronikos prietaisų gali sparčiai sumažėti.

Disertacijos tikslas

Šios disertacijos tikslas buvo pasiekti žemus sustiprintos savaiminės spinduliuotės (SSS) sleksčius organiniuose kristaluose, užaugintuose naudojant fluoreno tipo molekules, ir taip parodyti jų potencialą organiniams lazeriams. Šiam tikslui pasiekti buvo suformuotos užduotys:

- Charakterizuoti serijos cheminių junginių, kurių pagrindą sudaro fluoreno fragmentai, fotofizikines savybes amorfiniuose ir kristaliniuose būviuose.
- Įvertinti eksitoninės sąveikos efektus organiniuose kristaluose, kai yra keičiamas molekulinės struktūros standumas, bei jų įtaką SSS savybėms.
- Nustatyti eksitonų pernašos kryptį ir spartą bifluoreno kristaluose keliomis skirtingomis metodikomis.
- Ištirti sparčios eksitonų pernašos panaudojimo galimybes efektyviai energijos pernašai legiruotuose kristaluose.
- Įvertinti sugerties ir eksitonų anihiliacijos nuostolius legiruotuose kristaluose bei rasti optimalius legiravimo parametrus siekiant žemiausio SSS slenksčio.

Naujumas ir svarba

- Stipri eksitoninė sąveika organiniuose kristaluose lemia nuostolius, didinančius SSS slenkstį, todėl šiuo metu geriausi rezultatai pasiekiami amorfinėse stiprinimo terpėse, kuriose dėl didelės netvarkos eksitoniniai efektai yra nestebimi. Šiame darbe buvo pademonstruota, kad modifikuojant bifluoreno molekulių struktūros kietumą galima valdyti tiek elektron-vibroninę sąveiką molekulėse, tiek eksitoninę sveiką kristaluose. Silpnos eksitoninės ir stiprios vibroninės sąveikos atveju, kai buvo naudojamos minkštos molekulinės struktūros, kristalai pasižymėjo pavienių molekulių savybėmis ir tai leido pasiekti žemą SSS slenkstį.

- Buvo parodyta, kad silpna vibroninė sąveika ir vidutinio stiprumo eksitoninė sąveika lėmė spartų eksitonų transportą kristaluose, sudarytuose iš kietų bifluorene molekulių. Naudojant unikalią foto-indukuotų gardelių metodiką buvo nustatyta stipri eksitonų difuzijos anizotropija susijusi su specifiniu molekulių pakavimusi kristaluose. Molekulinių J-agregatų kryptimi kristaluose difuzijos koeficientai siekė net 1 cm^2/s (įvertintas difuzijos nuotolis ~300 nm). Stebėta anomali atvirkštinė eksitonų transporto priklausomybė nuo temperatūros indikavo dalinai koherentinę eksitonų pernašą, kuri greičiausiai buvo susijusi su maža netvarka kietų molekulių kristaluose.
- Vidutinio stiprumo J-tipo eksitoninė sąveika kietų molekulių kristaluose lėmė aukštas SSS slenksčio vertes dėl didelių sugerties nuostolių ir stiprios eksitonų anihiliacijos, kuri yra tiesiogiai susijusi su eksitonų pernašos sparta. Tačiau, buvo parodyta, kad legiruojant šiuos kristalus nedideliu kiekiu emiterių turinčių panašią molekulinę struktūrą galima eliminuoti nuostolius nespinduliniu būdu perduodant sužadinimo energiją į spinduolius. Ultrasparti energijos pernaša iš kristalo į priemaišą, kurią lėmė sparti eksitonų pernaša J-tipo aggregatuose, leido susilpninti eksitonų anihiliaciją esant dideliems sužadinimo tankiams reikalingiems stiprinimui pasiekti. Optimizavus legiruotų kristalų sistemą buvo pasiektas ypač žemas SSS slenkstis ir geras lazerio veikos stabilumas, pasiekti parametrai palyginami su geriausiomis amorfinių sluoksnių sistemomis.

Ginamieji teiginiai

A. Sustiprinta elektron-vibroninė sąveika ir konformacinė netvarka stebėta fenilo tiltelį turinčiuose bifluorene junginiuose lėmė silpną eksitoninę sąveiką kristaluose, kas leido pasiekti žemus SSS slenksčius.

B. Molekulinių kristalų savaiminis legiravimas pasitelkiant acetileno-etileno jungties modifikaciją bifluoreno molekulėse yra perspektyvi metodika siekiant gaminti aukšto kvantinio našumo bei žemo SSS slenksčio kristalus.
C. J-tipo eksitoninė sąveika bifluoreno kristaluose lėmė stipriai anizotropinę singuletinių eksitonų pernašą su eksitonų difuzijos koeficientu siekiančiu 1 cm^2/s. Sumažinta dinaminė konformacinė netvarka kristaluose sudarytuose iš bifluoreno junginių, kuriuose naudojamas kietas acitileno arba etileno tiltelis, lėmė koherentiškai sustiprintą eksitonų pernašą.
D. Ilgo nuotolio eksitonų transportas bifluoreno kristaluose lemia sparčią sužadinimo pernašą į spindulinius centrus legiruotuose kristaluose, kas leidžia eliminuoti sugerties ir anihiliacijos nuostolius esant optimaliai legiravimo koncentracijai bei taip pasiekti žemas SSS vertes ir padidinti fotostabilumą.

Teorinis įvadas

Viena pagrindinių problemų su kuria susiduriama vystant organinius lazerius yra organinių medžiagų degradacija esant dideliems sužadinimo tankiams. Degradacija pasireiškia dėl įvairių eksitonų anihiliacijos vyksmų medžiagoje, kurie ne tik lemia dalies molekulių suardymą, bet ir sunaikina dalį naudingų sužadinimų. Kadangi eksitonų anihiliacijos sparta tiesiogiai priklauso nuo sužadinimo tankio, siekiant sumažinti anihiliacijos vyksmų įtaką yra ypač svarbu užtiktinti lazerio veiką prie kuo žemesnio sužadinimo slenksčio.

Pagrindinius bet kurio lazerio komponentus sudaro žadinimo šaltinis, optinis rezonatorius ir aktyvioji stiprinimo terpė.[23,72] Dėl papildomų problemų, su kuriomis susiduriama organines medžiagas žadinant elektriškai, dauguma organinių lazerių šiuo metu yra tiriami naudojant optinį žadinimą kitais galingais šviesos šaltiniais.[23] Optinis rezonatorius suteikia grįžtamąjį ryši ir taip lemia didelį stimuliuotų šuolių intensyvumą aktyvioje terpėje, o jo kokybės rodiklis nustato lazerio veikos slenkstį.[72] Tačiau fundamentinė lazerio slenksčio vertė yra apribota stiprinimo ir nuostolių koeficientais organinėje terpėje. Nuostolius gali lemti tiek tiesiniai sugerties vyksmai, tiek netiesiniai eksitonų anihiliacijos vyksmai. Šiuo atveju, sustiprintos savaiminės spinduliuotės (SSS) procesas, kurio metu spontaniškai spinduliuojami fotonai yra stiprinami stimuliuotų šuolių sužadintoje medžiagoje, yra dažnai naudojamas siekiant nustatyti stiprinimo ir nuostolių įtaką nepriklausomai nuo optinio rezonatoriaus kokybės. Šiuo metu vienos žemiausių SSS slenksčio verčių organinių medžiagų sluoksniams siekia 100 W/cm^2 (arba 0.1 μJ/cm^2).[23,43,76] SSS slenksčiui nustatyti dažiausiai pasitelkiama juostelės žadinimo metodika, kurios metu bandinys yra žadinamas optiškai siaura juostele, stebint sustiprintą emisiją iš bandinio krašto.[72] Tuo tarpu pagrindinis mikroskopinis parametras lemiantis žemas SSS slenksčio vertes yra molekulių spindulinė sparta, kuri tiesiogiai atspindi molekulės osciliatoriaus stiprį.[72] Geriausių organinių medžiagų dabar naudojamų lazeriams spindulinė sparta yra 1-2 ns^{-1} ruože.[23,83]

Šiuo metu geriausios SSS slenksčio vertės yra pasiekiamos netvarkiuose amorfiniuose sluoksniuose, o organiniai kristalai dažniausiai pasižymi maždaug eile didesnėmis SSS vertėmis.[91,112] Viena pagrindinių to priežasčių – eksitoninės sąveikos efektai, kurie lemia didesnius sugerties arba anihiliacijos nuostolius ar sumažėjusią spindulinę spartą molekulėms kristaluose.[91] Tarpmolekulinei eksitoninei sąveikai įtakos turi tokie vidujmolekuliniai veiksniai kaip molekulių dipolių stipris ir elektron-vibroninės sąveikos stipris (molekulės kietumas), bei išoriniai veiksniai tokie kaip molekulinių dipolių tarpusavio orientacija ar atstumas.[109] Dėl eksitoninės sąveikos molekuliniai lygmenys suskyla į tiek lygmenų, kiek yra sąveikaujančių molekulių agregate, pavyzdžiui, stiprios sąveikos atveju gali susidaryti energijos juosta. Pagal supaprastintą Kaša modelį eksitoninė sąveika molekuliniuose agregatuose ir kristaluose yra klasifikuojama į H- ir J-tipo pagal dipolių tarpusavio orientaciją. Šiuo atveju H-tipo agregatuose molekuliniai dipoliai yra lygiagretūs ir tai lemia, kad žemiausio lygmens osciliatoriaus stipris yra silpninamas, o aukščiausio lygmens - stiprinamas. Kadangi spinduliniai šuoliai visada vyksta iš žemiausio lygmens, H-agregatų atveju sumažėjęs osciliatoriaus stipris lemia ir mažą spindulinę spartą, kas yra neparanku organinių lazerių taikymams. Tuo tarpu J-agregatai susidaro, kai molekulinių dipolių kryptis rodo viena į kitą, taip koherentiškai stiprinant žemiausio eksitoninio lygmens osciliatoriaus stiprį. Nors J-tipo agregatuose išauga spindulinių sparta, taip pat išauga ir žemiausio lygmens sugertis, todėl dėl striprios nuosavosios sugerties kristaluose išauga nuostoliai neleidžiantys pasiekti žemų SSS verčių. Taip pat J-agregatuose stebima koherentiškai stiprinama eksitonų pernaša, kuri lemia spartesnę eksitonų anihiliaciją ir didesniu netiesinius nuostolius. Taigi siekiant optimalių SSS parametrų lazeriams yra dažnai siekiama sumažinti eksitoninės sąveikos efektus kristaluose.

Eksitoninės sąveikos efektus galima sumažinti valdant tarpmolekulines ir vidujmolekulines savybes. Tarpmolekulinės savybės priklauso nuo molekulių pakavimosi kristale ir yra valdomos keičiant tarpmolekulinius atstumus arba tarpusavio orientaciją. Pavyzdžiui, prie molekulių prijungiant erdvinius pakaitus dėl sterinės sąveikos padidėja atstumai, o eksitoninės sąveikos stipris ypač stipriai priklauso nuo atstumo ($\sim 1/R^6$). Tačiau tokiu atveju kristalinės struktūros morfologija tampa sunkiai kontroliuojama, išauga defektų tikimybė, o siekiant elektriškai kaupinti kristalus suprastėja ir krūvio pernašos savybės. Taigi, eksitoninę sąveiką yra geriau valdyti modifikuojant molekulių struktūrą nedideliais steriniais pakaitais taip, kad molekulinių dipolių orientacija kristale būtų tarpinėje padėtyje tarp H- ir J-tipo agregatų, o molekulių osciliatoriaus stipris kristale būtų panašus į pavienių molekulių. Panašų rezultatą galima pasiekti ir keičiant vidujmolekulinės elektron-vibroninės sąveikos stiprį. Pavyzdžiui, į molekulinę struktūrą įvedant labilius fragmentus, kurie padinina vibroninę sąveiką dėl žemos energijos sukamųjų virpesių modų, ir taip sumažina rezonansinės tarpmolekulinės sąveikos tikimybę. Dėl didesnės vibroninės sąveikos stiprio taip pat sumažėja sanklota tarp sugerties ir emisijos spektrų, todėl stebimi mažesni sugerties nuostoliai lazeriams, o lėtesnė eksitonų pernaša lemia mažesnius anihiliacijos nuostolius. Kitu atveju, stiprios rezonansinės sąveikos efektų J-tipo agregatuose galima išvengti panaudojant ypač sparčią eksitonų pernašą į priemaišas pasižyminčias didele spinduline sparta. Šiuo atveju sužadinimo energija kristale yra sparčiai pernešama į nedidelį kiekį molekulių, kurių spinduliuojami mažesnės energijos fotonai yra nesugeriami kristalo tūryje, taip išvengiant nuosavosios sugerties nuostolių. Šis energijos pernašos metodas yra dažnai naudojamas ir amorfinėms organinių lazerių sistemoms, leidžiantis gerokai sumažinti SSS slenkstį.[72,83]

Eksperimentiniai metodai

Bandiniai

Pagrindiniai šiame darbe tirtų molekulių dizaino kriterijai buvo tiesinės mažų molekulių struktūros, kurių pagrindą sudarė fluoreno fragmentai su alkilo pakaitais. Visi tirti junginiai yra pavaizduoti Pav. 1. Fluoreno fragmentai buvo pasirinkti dėl gerai žinomų emisinių savybių bei panaudojimo kuriant medžiagas organiniams lazeriams.[23] Tiesinės struktūros lemia ištęstą molekulės konjugaciją (didelį osciliatoriaus stiprį) bei palankų molekulių pakavimąsi kristale.[91] Inertiški alkilo pakaitai leidžia kontroliuoti molekulių pakavimąsi nekeičiant optinių savybių – ilgi pakaitai, kaip fluoreno triados (FFF) junginyje, neleidžia molekulėms glaudžiai pakuotis, trumpi, kaip bifluoreno (BF) serijoje, lemia specifinę molekulių orientaciją kristale. BF serijos junginiai buvo modifikuojami keičiant jungiamąjį tiltelį iš „minkšto“, kurį sudarė galintys besisukti fenilo fragmentai, arba „kieto“, kurį sudarė standūs acetileno ir etileno fragmentai. Molekulių sintezė yra plačiau aprašyta I-III publikacijose.[154,177,194]

Siekiant ištirti pavienių molekulių savybes jos buvo ištirpinamos stipriai atskiestame ($<10^{-5}$ M) tetrahidrofurano (THF) tirpale. Polimero plėvelės su tam tikru tiriamų molekulių masės kiekiu buvo ruošiamos sumaišant medžiagos tirpalus su polistirenu (PS) ir liejant mišinį ant nuvalyto stiklo padėklo. Grynos medžiagos amorfinės plėvelės buvo paruoštos liejant koncentruotus tirpalus ant nuvalytų stiklo padėklų.

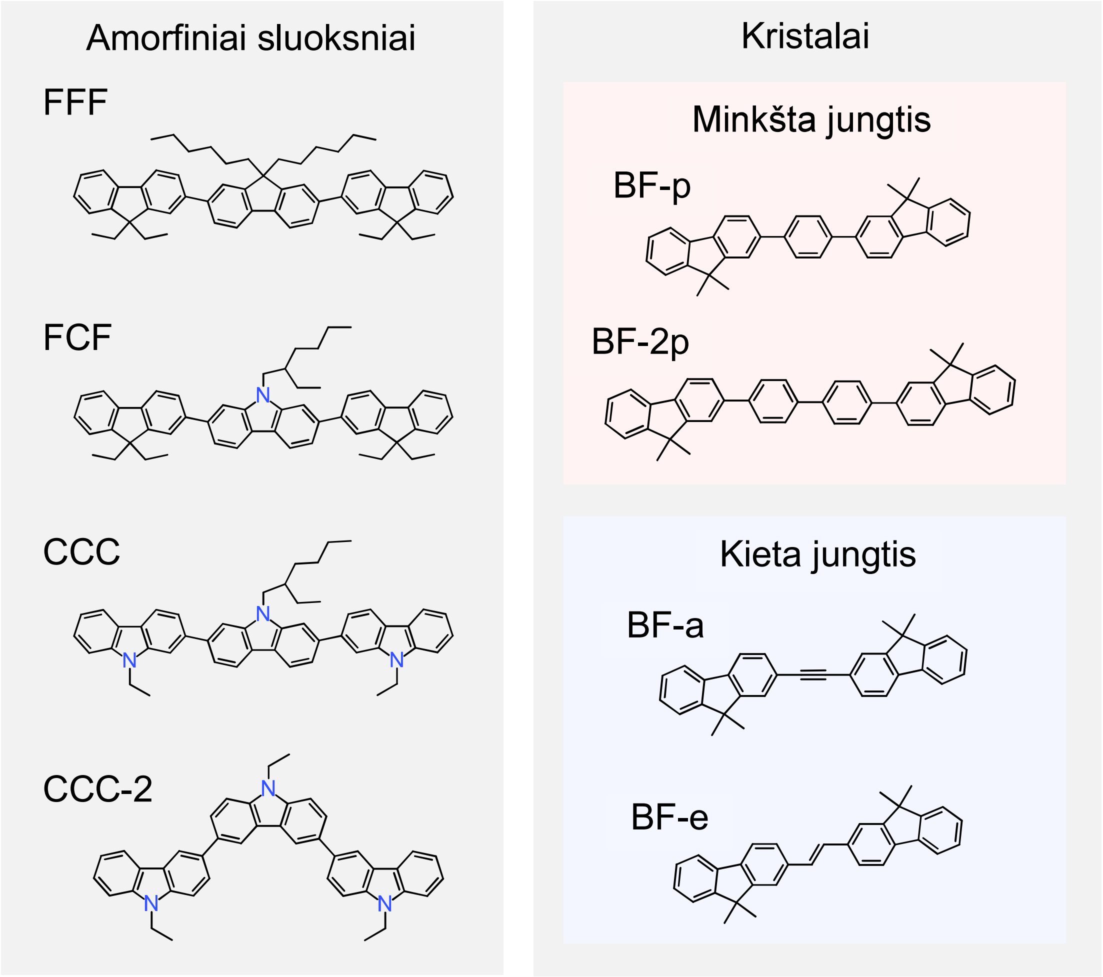

Pav. 1. Fluoreno oligomerų molekulinės struktūros.

BF serijos kristalai buvo auginami pasitelkiant auginimo iš garų fazes metodą (Pav. 2). Auginimui buvo naudojama komercinė sublimacijos sistema DSU-20 (CreaPhys). Išgrynintos azoto dujos buvo naudojamos kaip nešančios dujos. Auginimo metu susidariusių plokščių kristalų dydis svyravo nuo 0.1 iki 10 mm, o storis buvo 1-10 µm. Tolimesnei analizei kristalai buvo uždedami ant ozono garais nuvalytų kvarco padėklų. Legiruoti kristalai buvo gaminami sumaišant aktyvios matricos ir priemaišos medžiagas masės santykiu 100:5. Kristalizacijos regione sukurtas temperatūros gradientas leido pasiekti skirtingas legiravimo koncentracijas dėl skirtingų molekulių gardelių konstantų. Ypač švarūs (be nuosavojo legiravimo) BF-a kristalai buvo gauti garinant medžiagą vakuume 150 °C temperatūroje ant švarių kvarco padėklų.

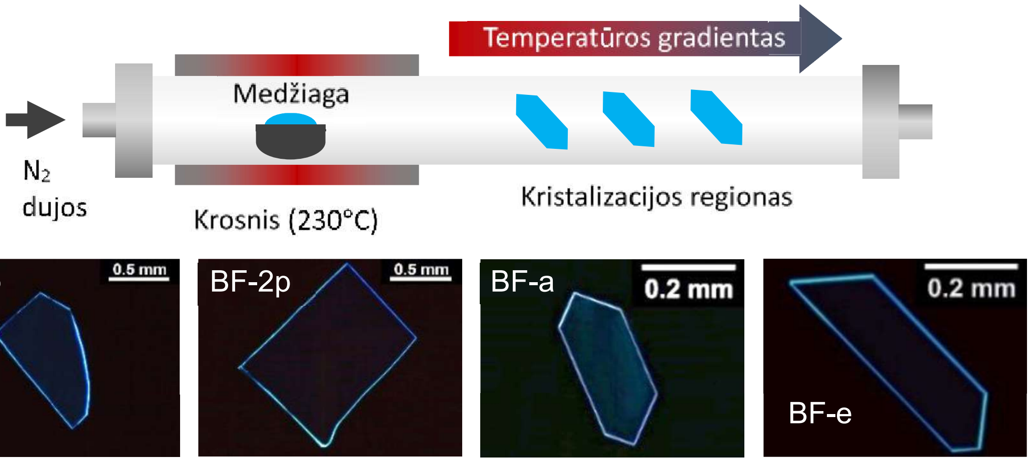

Pav. 2. Kristalų auginimo iš garų fazės schema ir kristalų pavyzdžiai.

BF-p, BF-a ir BF-e kristalų struktūros buvo nustatytos naudojant pavienių kristalų rentgeno spindulių difrakcijos analizę difraktometru XtaLAB Synergy (Rigaku). Kristalografinės analizės rezultatai buvo patalpinti į Cambridge kristalografinių duomenų bazę (CCDC 1942503-1942504). Legiruotų kristalų kokybė buvo nustatyta atliekant 2-teta rentgeno spindulių difrakcijos analizę. Bifluoreno serijos kristalų vienetinės celės iliustruotos Pav. 3. Visuose bifluoreno kristaluose buvo stebėtas panašus molekulių pakavimasis, kur molekuliniai sluoksniai formavosi statmenai didžiajai kristalo plokštumai (atstumas tarp sluoksnių ~14 Å). Sluoksnyje ilgoji molekulės ašis buvo palinkusi apie 37° į kristalo plokštumą.

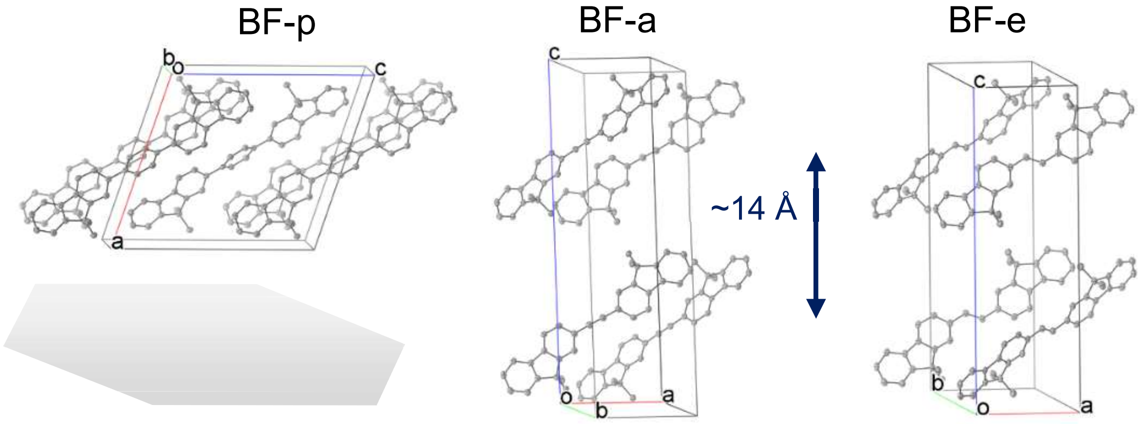

Pav. 3. Bifluoreno kristalų vienetinės celės nustatytos rentgeno difrakcijos metodu. Kristalo didžioji plokštuma atvaizduota vienetinių celių atžvilgiu. Rodyklė žymi atstumą tarp molekulinių sluoksnių.

Spektroskopiniai metodai

Fotoliuminescencijos spektroskopijos metodai buvo pasitelkti siekiant nustatyti emisijos spektrinius skirtinius, kvantinius našumus (Φ_F) ir gesimo trukmes (τ). Naudojantis nustatytais parametrais buvo įvertintos spindulinė ($k_s = \Phi_F/\tau$) ir nespindulinė ($k_{ns} = [1\text{-}\Phi_F]/\tau$) spartos. Emisijos spektrai buvo išmatuoti CCD spektrometru (PMA-11, Hamamatsu) žadinant medžiagas monochromatoriumi parinkto bangos ilgio šviesa iš ksenono lempos. Emisijos kvantinis našumas buvo nustatytas integruojančios sferos (SphereOptics) metodu.[137] Laikinės emisijos charakteristikos buvo nustatomos STREAK detektoriumi (C10627, Hamamatsu), medžiagas žadinant trumpais (~200 fs) parenkamo bangos ilgio lazerio (Pharos+Orpheus, Light Conversion) impulsais parenkant žadinimo dažnį 1-100 kHz ruože. Kontroliuojamos temperatūros matavimai buvo atlikti helio (204N, Cryo Industries) arba azoto (OptistatDN, Oxford instruments) kriostatuose.

Sustiprintos savaiminės spinduliuotės matavimai buvo atlikti pasitelkiant žadinimo siaura juostele metodą.[72] Cilindriniu lešiu suformuota siaura žadinimo juostelė buvo sufokusuojama prie bandinio krašto, spontaninė emisija sustiprinta dėl stimuliuotų šuolių buvo stebima CCD detektoriumi. Žadinimo tankis, virš kurio stebimas emisijos juostos siaurėjimas buvo laikomas SSS slenksčiu (I^{SSS}). Matavimai buvo atliekami naudojant du impulsinius lazerinio žadinimo šaltinius su skirtingomis impulse trukmėmis: keičiamo bangos ilgio nanosekundinį Nd:YAG lazerį (pakartojimų dažnis 10 Hz, impulse trukmė 5 ns); ir keičiamo bangos ilgio femtosekundinę lazerinę sistemą (Pharos+Orpheus, Light Conversion) (pakartojimų dažnis 1-100 kHz, impulse trukmė 200 fs)).

Nuostovios sugerties matavimai tirpaluose ir plonose plėvelėse buvo atlikti komerciniu UV−vis−NIR spektrometru (Lambda 950, Perkin-Elmer). Sugertis kristaluose buvo nustatoma matuojant poliarizuotos lazerio spinduliuotės pralaidumą dėl didelių kristalų sugerties koeficientų ($A > 4$).

Skirtuminės sugerties matavimai leido nustatyti ypač sparčius (<1 ps) vykstančius procesus stebint sugerties pokyčius taip vadinama žadinimo-zondavimo metodika.[138] Metodo esmė – plataus spektro (350 – 1030 nm) baltos šviesos zondo pralaidumo pokytis, kai bandinys yra sužadintas. Tiek zondo tiek žadiinimo spinduliai yra gaunami padalinant 1030 nm femtosekundinio lazerio spinduliuotę (Pharos, Light Conversion), tačiau mechaniškai ilginant zondo spindulio kelią gaunamas vėlinimas žadinimo atžvilgiu bei laikinė skiriamoji geba. Plataus spektro zondo šviesa buvo generuojama terpėje (safyras arba vanduo) sufokusuojant 1030 nm spinduliuotę, tuo tarpu keičiamo bangos ilgio žadinimo spinduliuotė generuojama optiniame parametriniame stiprintuve (Orpheus, Light Conversion). Žadinimo-zondavimo matavimai ir jų analizė buvo atlikti naudojant komercinę įrangą (Harpia, Light Conversion).

Šviesa indukuotų dinaminių difrakcinių gardelių metodas buvo pritaikytas tiriant eksitonų difucijos dinamiką bifluoreno kristaluose. ŠIDDG metodika lyginant su kitomis difuzijos nustatymo metodikomis yra unikali tuo, kad leidžia tiksliai nustatyti eksitonų pernašos kryptį kristale.[140] Metodo esmė yra ta, kad dviejų trumpų impulsų (trumpesnių už eksitono gyvavimo trukmę) interferencijos sukuriamas gardelių sužadinimo profilis bandinyje nyksta tiek dėl eksitonų difucijos trukmės (τ_D), tiek dėl eksitonų rekombinacijos trukmės (τ_R). Tokiu atveju trečiu zondo spinduliu stebint nuo laiko priklausantį difrakcijos efektyvumą galima nustatyti gardelių išsitrynimo laiką (τ_G), kuriame atspindimos eksitonų difuzijos ir rekombinacijos trukmės ($1/\tau_G = 1/\tau_D + 1/\tau_R$). Keičiant gardelių periodą (Λ) ŠIDDG metodu galima tiksliai įvertinti eksitonų difuzijos koeficientą ($D = \Lambda^2/[4\pi^2 \tau_D]$). Matavimai buvo atlikti įranga, kurios aprašas pateiktas literatūroje.[141]

1 Skyrius: Šviesos stiprinimas amorfinėse fluoreno junginių plėvelėse

Siekiant žemų SSS slenksčių amorfinėje fazėje buvo sukurta fluoreno ir karbazolo triadų serija (žiūrėti Pav. 1). Junginiai **FFF**, **FCF** ir **CCC** pasižymėjo 2,7-jungimo pozicija, kuri yra pranašesnė dėl tiesinės molekulės struktūros, didelio osciliatoriaus stiprio ir sparčios spindulinės rekombinacijos. Junginys **CCC-2** su 3,6-jungimu buvo pasirinktas tam, kad būtų pademonstruotos silpnos spindulinės savybės, kurias lemia stipriai susisukusios molekulinių fragmentų konformacijos. Ilgos alifatinės heksil grandinės prijungtos prie centrinio fragmento 9-pozicijoje **FFF**, **FCF** ir **CCC** triadose lėmė didesnius tarpmolekulinius atstumus grynoje amorfinėje medžiagos fazėje, o dėl silpnesnės tarpmolekulinės sąveikos buvo stebimas silpnesnis koncentracinis gesinimas. 2,7-pozicijoje sujungtos triados pasižymėjo aukštais foto-liuminescencijos kvantiniais našumais (Φ_F ~ 80-90%) ir sparčia spinduline rekombinacija (k_R ~ 1 ns^{-1}). Svarbu paminėti, kad azoto heteroatomai karbozolo grupėse lėmė sumažėjusią spindulinę spartą triadose bei padidėjusius nespindulinius nuostolius dėl interkombinacinės konversijos iš singuletinių į tripletines būsenas. Tačiau 3,6-pozicijoje sujungtos triados spindulinė sparta buvo daugiau nei eile mažesnė (k_R ~ 0.04 ns^{-1}). Taigi, optimaliausi spindulinės rekombinacijos parametrai siekiant žemo stiprinimo slenksčio buvo nustatyti **FFF** triadai.

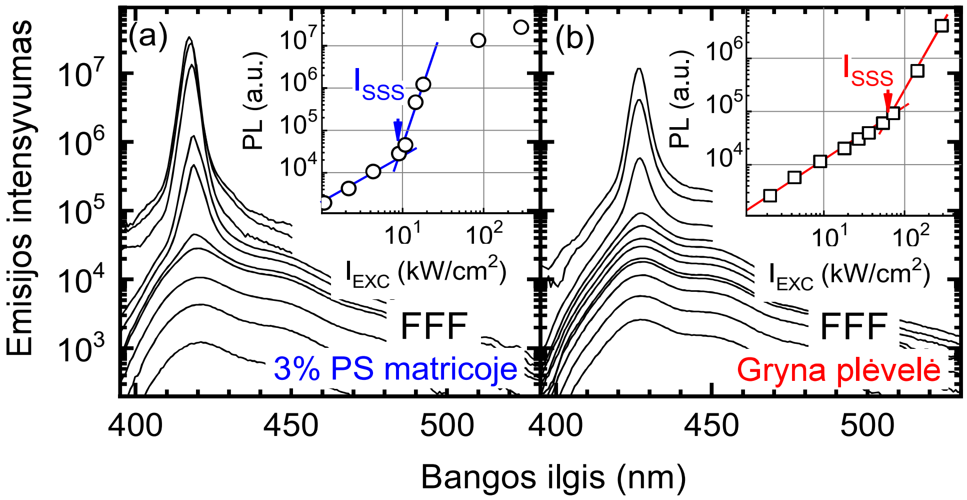

Pav. 4. Emisijos spektrų priklausomybė nuo sužadinimo galios FFF junginio 3% PS plėvelėje (a) ir gryname amorfiniame sluoksnyje (b). SSS emisijos piko intensyvumo nuo galios priklausomybė nurodyta.

Sustiprintos savaiminės spinduliuotės matavimai plonos juostelės žadinimo metodu buvo atlikti plonose amorfinėse plėvelėse, kuriose tiriamųjų triadų koncentracija buvo keičiama nuo 0.1% iki 10% inertiškoje polistireno (PS) matricoje, o 100% plėveles atitiko grynos medžiagos sluoksniai. Emisijos priklausomybė nuo žadinimo galios pavaizduota Pav. 4. SSS parametrai apibendrinti 1 lentelėje. Optimali SSS slenksčio vertė **FFF** junginiui buvo nustatyta ties 3% masės koncentracija PS matricoje, tuo tarpu didesnes SSS vertes didesnės koncentracijos plėvelėse lėmė koncentracinio gesinimo ir emisijos sklaidos efektai. Panašūs rezultatai buvo gauti **FCF** ir **CCC** triadoms, tačiau karbazolo grupės šiuo atveju lėmė didesnius SSS slenksčius, kuriuos galima būtų pagrįsti mažesnėmis spindulinėmis spartomis. **CCC-2** triados amorfiniams ir PS matricos sluoksniams SSS nebuvo stebėta.

Lentelė 1. Optimalūs SSS parametrai fluoreno ir karbazolo triadoms amorfinėse polimero matricos plėvelėse.

Junginys	c_{opt} (%)	λ_{SSS} (nm)	I_{SSS} (kW/cm^2)	k_s (ns^{-1})
FFF	3	419	9	1.1
FCF	3	421	15	0.6
CCC	0.5	424	13	0.7
CCC-2	SSS nestebėta			0.01

Tyrimais buvo įrodyta, kad siekiant optimalių SSS parametrų amorfinėse plėvelėse 2,7-pozicijoje triadose sujungti fluoreno fragmentai leidžia pasiekti geriausias spindulines savybes. Tuo tarpu žemiausios SSS slenksčio vertės buvo nustatytos spinduolio molekulėms esant atskiestose (~3%) polimero matricose, kai tarpmolekulinė sąveika yra negalima.

2 Skyrius: Molekulės virpesių įtaka stiprinimo savybėms kristaluose

Stipri tarpmolekulinė eksitoninė sąveika organiniuose kristaluose dažnai lemia stiprius sugerties nuostolius, todėl SSS parametrai yra palyginti prastesni nei amorfinėse plėvelėse.[91] Tačiau eksitoninės sąveikos stipris gali būti silpninamas esant stipriai elektron-vibroninei sąveikai, kurią lemia atomų virpesiai molekulėse. Šiuo atveju siekiant stiprios vibroninės sąveikos buvo sukurta bifluoreno molekulių serija, kur fluoreno fragmentai 2,7-pozicijoje buvo sujungti fenilo tilteliais, kurie lėmė sukamųjų virpesių laisvę (žiūrėti Pav. 5 kairėje). Sukamųjų virpesių laisvę ir jų nulemtą konformacinę netvarką pagrindinėje būsenose indikavo platūs bestruktūriai sugerties spektrai tiek molekulėms esant tirpale, tiek kristalinėje struktūroje. Tuo tarpu sužadintoje būsenoje buvo stebima molekulinės struktūros planarizacija, nes emisija pasižymėjo aiškia vibronine seka. Toks molekulinės struktūros plokštėjimas sužadintoje būsenoje yra būdingas fluoreno oligomerams ir leidžia sumažinti savi-sugerties nuostolius, kuriuos lemia sugerties ir emisijos spektrų sanklota. Tai leidžia pasiekti ypač žemus SSS slenksčius panašiose sistemose.[76]

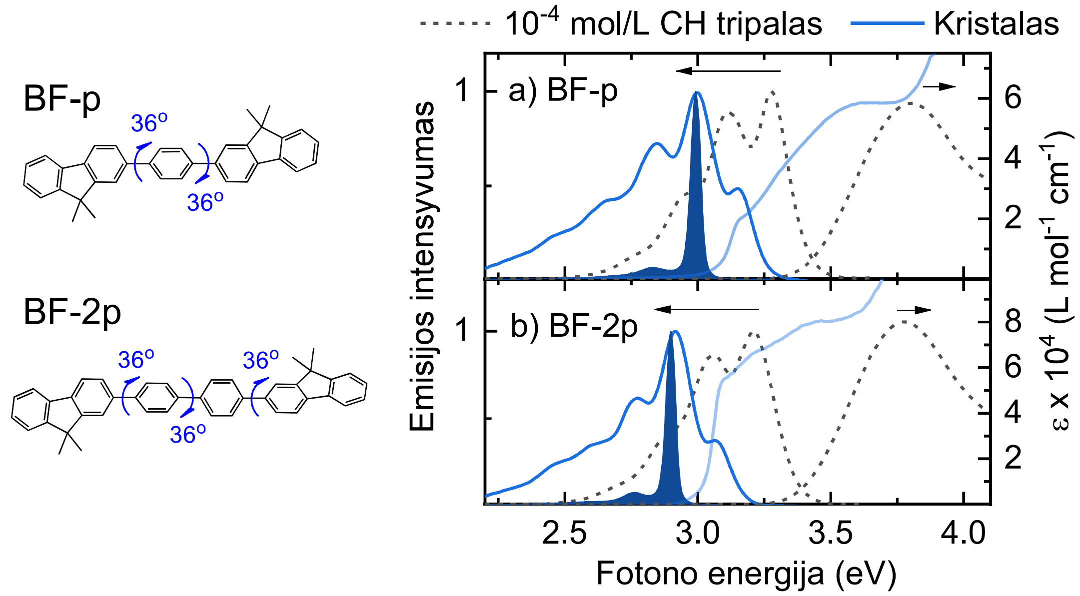

Pav. 5. Bifluoreno molekulių struktūros (kairėje). Sugerties ir emisijos spektrai molekulėms ištirpintos cikloheksano (CH) tirpale ir kristale. Tamsiai mėlynos sritys rodo SSS spektrus abiejų junginių kristalams.

Siekiant palyginti SSS vertes bifluoreno kristaluose ir amorfiniuose sluoksniuose buvo atlikti matavimai plonos juostelės metodu (žiūrėti 2 lentelę). Šiuo atveju optimalios SSS vertės polistireno matricos amorfiniams sluoksniams buvo pasiektos esant 1% emiterių koncentracijai, nes aukštesnėse koncentracijose buvo stebimas mikrokristalų formavimasis lemiantis sklaidos nuostolius. Įdomu tai, kad sumažinus sklaidos nuostolius didelių matmenų kristaluose, kurie pasižymėjo puikiomis bangolaidinėmis savybėmis, abiejų molekulių atveju buvo nustatyti žemesni SSS slenksčiai nei amorfinėse PS plėvelėse. Tuo tarpu žemesnis SSS slenkstis **BF-2p** kristale buvo nulemtas didesnio osciliatoriaus stiprio ilgesnėje molekulėje bei spartesnės spindulinės rekombinacijos.

Lentelė 2. SSS slekščiai ir spindulinės spartos bifluoreno polistireno plėvelėms ir kristalams.

Junginys	1% PS plėvelė		Kristalas	
	I_{SSS} (kW/cm^2)	k_s (ns^{-1})	I_{SSS} (kW/cm^2)	k_s (ns^{-1})
BF-p	4.8	1.30	1.8	1.20
BF-2p	3.3	1.55	0.7	1.38

Svarbu tai, kad spindulinė sparta praktiškai nepriklausė nuo skirtingos tarpmolekulinės sąveikos atskiestoje PS matricoje ar tankiame kristale, kas yra vienas iš silpnos eksitoninės sąveikos požymių (žiūrėti Lentelė 2 lentelę). Šiuo atveju eksitoninę sąveiką galėjo silpninti molekuliniai virpesiai, kurie panaikina rezonansinę sąveiką tarp greta esančių molekulinių dipolių kristale. Kadangi žemos energijos sukamieji virpesiai gali būti pildomi termiškai, siekiant įvertinti eksitoninės sąveikos stiprį buvo atlikti emisijos ir sugerties matavimai nuo temperatūros **BF-p** kristale (Pav. 6). Didėjantis emisijos intenyvumas žemose temperatūrose buvo nulemtas nespindulinių nuostolių susijusių su molekuliniais virpesiais mažėjimo. Tuo tarpu emisijos vibroninių pikų 0-0 ir 0-1 santykis visame temperatūrų regione praktiškai nekito, tai yra vienas iš pagrindinių silpnos eksitoninės sąveikos indikatorių.[109] Įdomu tai, kad žemose temperatūrose išryškėjo sugerties vibroniniai pakartojimai, kas rodė, kad kambario temperatūroje mažos energijos virpesinės modos yra pildomos dėl terminės energijos.

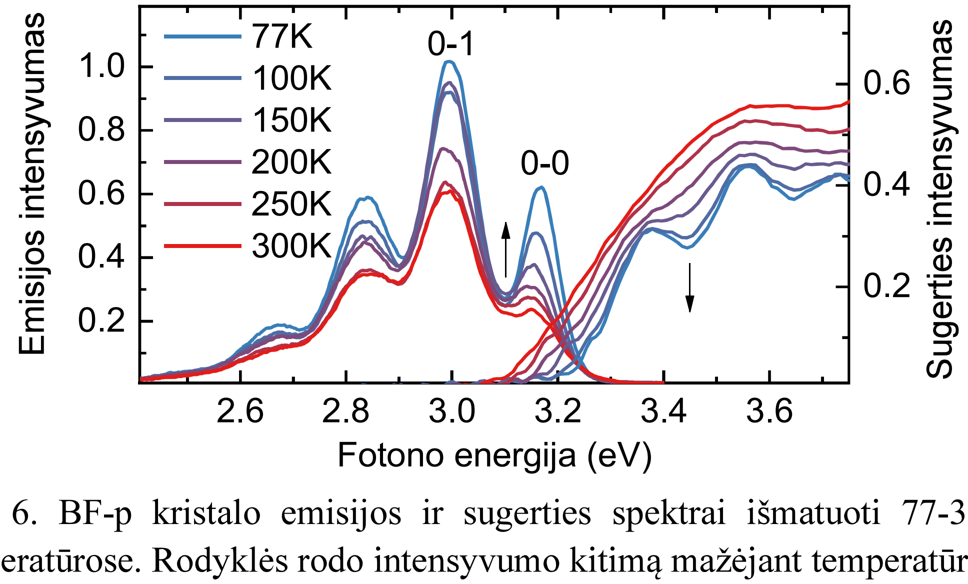

Pav. 6. BF-p kristalo emisijos ir sugerties spektrai išmatuoti 77-300 K temperatūrose. Rodyklės rodo intensyvumo kitimą mažėjant temperatūrai.

Maža sukamųjų virpesių energija leido juos koherentiškai sužadinti ypač trumpais impulsais skirtuminės sugerties matavimo metodika. Pav. 7

matomos bangų paketo osciliacijos sužadintos būsenos potenciale buvo nulemtos mažos energijos virpesių koherentinio sužadinimo. Šiuo atveju osciliacijos periodas leido nustatyti virpesių energiją, kuri BF-p molekulės atveju buvo apie 80 cm^{-1} ir puikiai atitiko fenilo sukamųjų virpesių energiją kitose sistemose.[109] Šių virpesių stebėjimas kristale reiškė, kad net esant ypač glaudžiam molekulių pakavimuisi, sukamieji fenilo virpesiai lemia dinaminę netvarką stebėtą sugerties spektruose ir taip neleidžia atsirasti eksitoninei sąveikai.

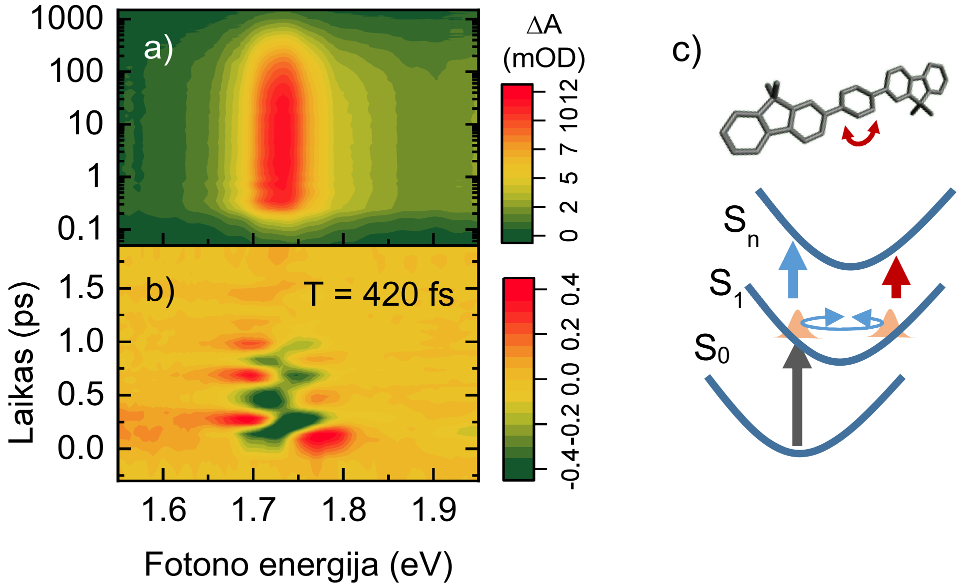

Pav. 7. (a) Skirtuminės sugerties kitimas nuo laiko BF-p kristale. Žadinimo impulso energija buvo 3.75 eV, trukmė - 200 fs. (b) Likutinių verčių žemėlapis atlikus skirtuminės surgerties globalią analizę naudojant vienos eksponentės ($\tau = 350$ ps) gesimo funkciją. Osciliacijų periodas nurodytas. (c) Schema iliustruojanti korehentinio bangų paketo, kurį moduliuoja sukamieji fenilo virpesiai, dinamiką sužadintos būsenos potenciale.

Bifluoreno molekulių, pasižyminčių stipria elektron-vibronine sąveika, kurią lėmė centrinio fenilo fragmento sukamieji virpesiai, tyrimai leido nustatyti silpną eksitoninę sąveiką šių junginių kristaluose. Dėl abiejų šių sąveikų nulemtų mažų sugerties nuostolių bei didelės spindulinės spartos bifluoreno kristalams buvo stebėti vieni žemiausių SSS slenksčių, kokie yra užfiksuoti organiniams kristalams.[177]

3 Skyrius: Eksitoninės sąveikos įtaka striprinimo savybėms kristaluose

Silpna elektron-vibroninė sąveika kietose molekulinėse struktūrose gali lemti stipresnius eksitoninės sąveikos efektus molekuliniuose agregatuose.[109] Siekiant sumažinti vibroninę sąveiką bifluoreno molekulėje buvo panaudotos acetileno (**BF-a**) ir etileno (**BF-e**) jungtys apribojančios sukamuosius virpesius. Pav. 8 pavaizduoti emisijos ir sugerties išmatuoti abiejų bifluoreno junginių THF tirpaluose rodė veidrodinę simetriją, kur tiek sugerties, tiek emisijos spektrai pasižymėjo aiškia vibronine struktūra. Abi kietais tilteliais modifikuotos molekulės THF tirpaluose pasižymėjo aukštais kvantiniais našumais ($\Phi_F \sim$ 80-90%) ir sparčia spinduline rekombinacija ($k_R \sim 1$ ns^{-1}).

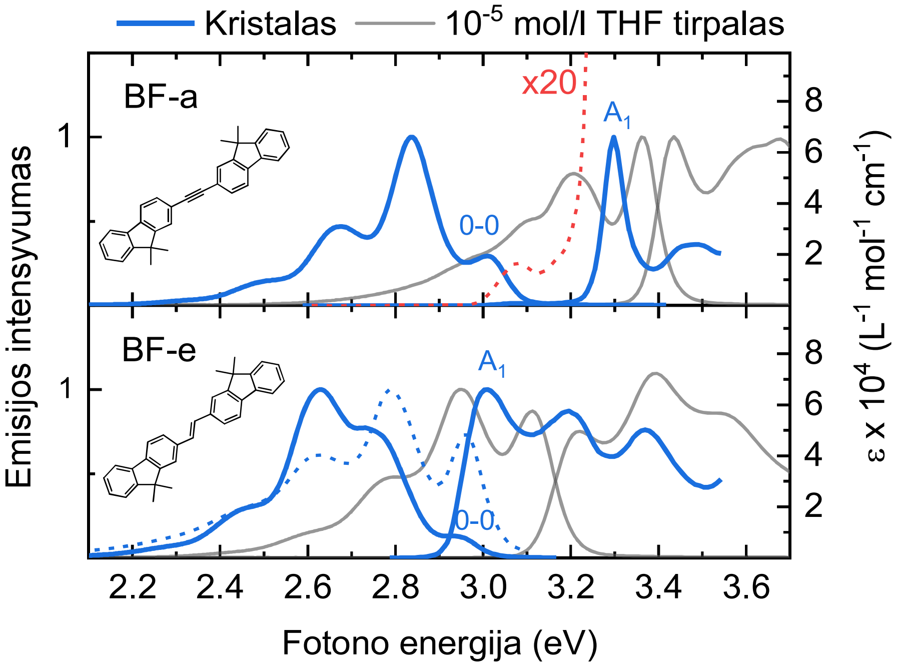

Pav. 8. Bifluoreno junginių emisijos ir sugerties spektrai išmatuoti 10^{-5} M THF tirpaluose ir kristaluose. BF-a kristalo sugerties spektras padidintas 20 kartų pavaizduotas raudona punktyrinė linija. BF-e mikrokristalų spektras pavaizduotas mėlyna punktyrine linija.

Silpna elektron-vibroninė sąveika **BF-a** ir **BF-e** junginiuose lėmė eksitoninės sąveikos efektus kristaluose, kurie buvo matomi iš sugerties spektrų (žiūrėti Pav. 8). Žemiausio sugerties šuolio (ties 3.3 eV ir 3.0 eV atitinkamai **BF-a** ir **BF-e**) poslinkis į žemesnes energijas bei išaugęs intensyvumas kristaluose, lyginant su monomerais tirpaluose, indikavo J-tipo eksitoninę sąveiką.[109] Nedidelis Stokso poslinkis tarp **BF-e** kristalo žemiausios sugerties smailės (A_1) ir didžiausios energijos emisijos smailės (0-0) lėmė ypač stiprią emisijos nuosavąją sugertį dideliuose kristaluose.

Sumažinti nuosavosios sugerties efektai buvo stebėti mikrokristalų emisijos spektruose, kuriuose spektrų vibroninių pikų intensyvumų santykis buvo panašus į monomerų tirpale. Tokia stipri nuosavoji sugertis **BF-e** kristale lemia didelius sugerties nuostolius stimuliuotai emisijai. Įdomu tai, kad silpna savi-sugertis buvo stebėta **BF-a** kristale dėl anomalaus 300 meV skirtumo tarp sugerties A_1 ir emisijos 0-0 smailių. Detaliau išnagrinėjus sugerties spektrus buvo nustatyta, kad emisija **BF-a** kristale vyksta iš žemos energijos priemaišos būsenos ties 3.05 eV, kurios sugerties intensyvumas yra keliasdešimt kartų mažesnis už pagrindinių kristalinių būsenų.

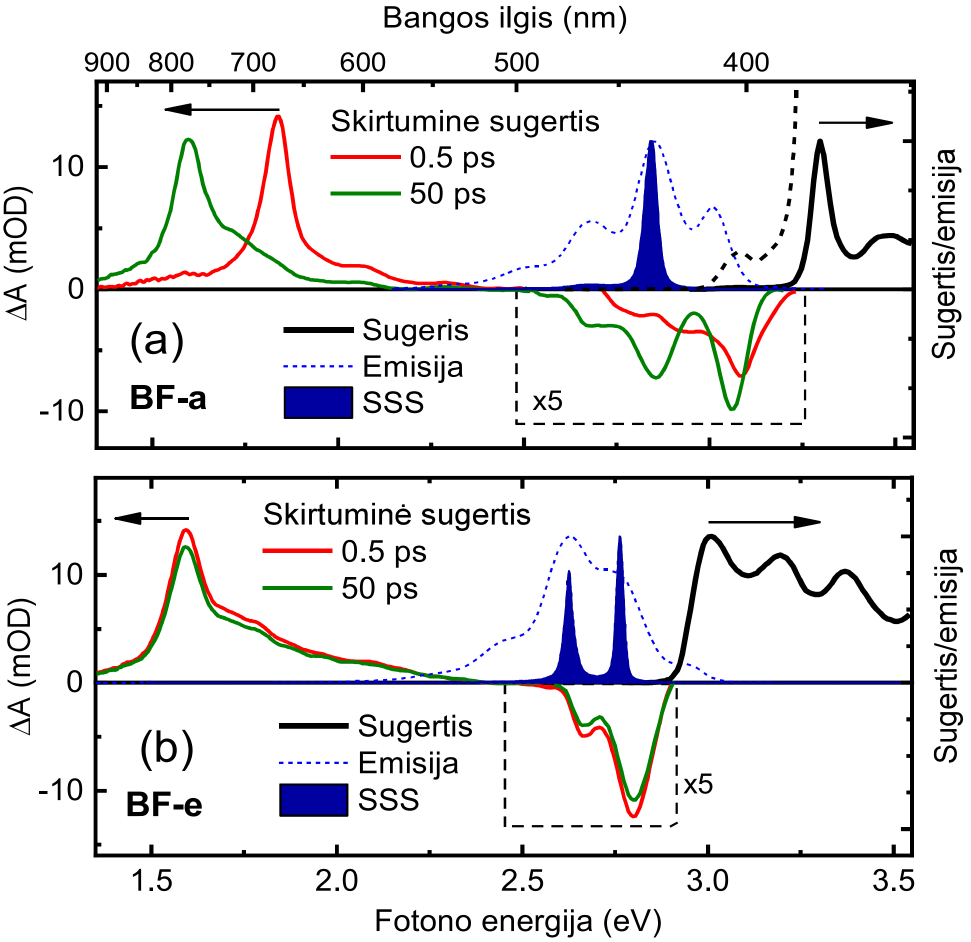

Pav. 9. BF-a ir BF-e kristalų sugerties, skirtuminės sugerties, emisijos ir sustiprintos savaiminės spinduliuotės spektrais. Skirtuminės sugerties spektrai buvo užfiksuoti ties 0.5 ps ir 50 ps vėlinimo laikais. Žadinimo bangos ilgis - 375 nm (3.30 eV).

Siekiant detaliau išnagrinėti nuosavosios priemaišos kilmę **BF-a** kristale buvo atlikti skirtuminės sugerties matavimai su femtosekundine laiko skyra.

Pav. 9(a) matoma, kad skirtinguose vėlinimo laikuose buvo stebima kristalinių (0.5 ps) ir priemaišos (50 ps) būsenų skirtuminė sugertis dėl ypač sparčios sužadinimo prenašos iš kristalo į priemaišą. Svarbu tai, kad priemaišos indukuotos sugerties siganlas ties 1.6 eV sutapo su **BF-e** kristalo indukuota sugertimi (Pav. 9b). Tai indikavo, kad nuosavosios priemaišos galėjo susidaryti dėl acetileno-etileno jungties modifikacijos kristalų auginimo sublimacijos metodu metu.

Sužadinimo pernaša į mažą kiekį (~1%) priemaišų **BF-a** kristale lėmė mažesnius sugerties nuostolius. Atlikus SSS tyrimus plonos juostelės metodu, buvo nustatyta, kad legiruoto **BF-a** kristalo SSS slenkstis buvo 0.4 kW/cm^2. Tuo tarpu eile didesnis SSS slenkstis (4 kW/cm^2) nustatytas **BF-e** kristalams buvo nulemtas didelių nuosavosios sugerties nuostolių atsiradusių dėl silpnos vibroninės ir vidutinio stiprumo eksitoninės sąveikų.

4 Skyrius: Eksitonų difuzija kristaluose

Eksitonų transportas organinėse medžiagose yra ypač svarbus taikymams optoelektronikoje.[45,196] Organiniams lazeriams sparti eksitonų difuzija kristaluose galėtų būti naudinga siekiant ultrasparčios energijos pernašos į spindulines priemaišas, taip efektyviai sukuriant sąlygas populiacijos inversijai. Siekiant nustatyti eksitonų difuziją bifluorene kristaluose buvo pasitelkta unikali šviesa indukuotų dinaminių difrakcinių gardelų metodika, leidžianti ne tik tiesiogiai nustatyti eksitonų difuzijos koeficientą, bet ir difuzijos kryptį, ko neleidžia dauguma kitų metodikų.[198,210]

Atlikus ŠIDDG matavimus dvejomis pagrindinėmis **BF-p** ir **BF-a** kristalų kryptimis, eksitonų difuzija abiejų kristalų atveju buvo stebėta tik molekulių šuolio dipolinių momentų kryptimi kristale (Pav. 10). Tokia kryptis atitinka J-tipo agregatų kryptį ir numato koherentinį eksitonų pernašos stiprinimą.[109] Statmena kryptimi eksitonų difuzija nebuvo stebėta dėl ŠIDDG eksperimento skiriamosios gebos ribojimo. Įdomu tai, kad nustatyti difuzijos koeficientai palankia eksitonų difuzijai kryptimi buvo net 5 kartu didesni **BF-e** kristale lyginant su **BF-p** kristalu (Lentelė 3).

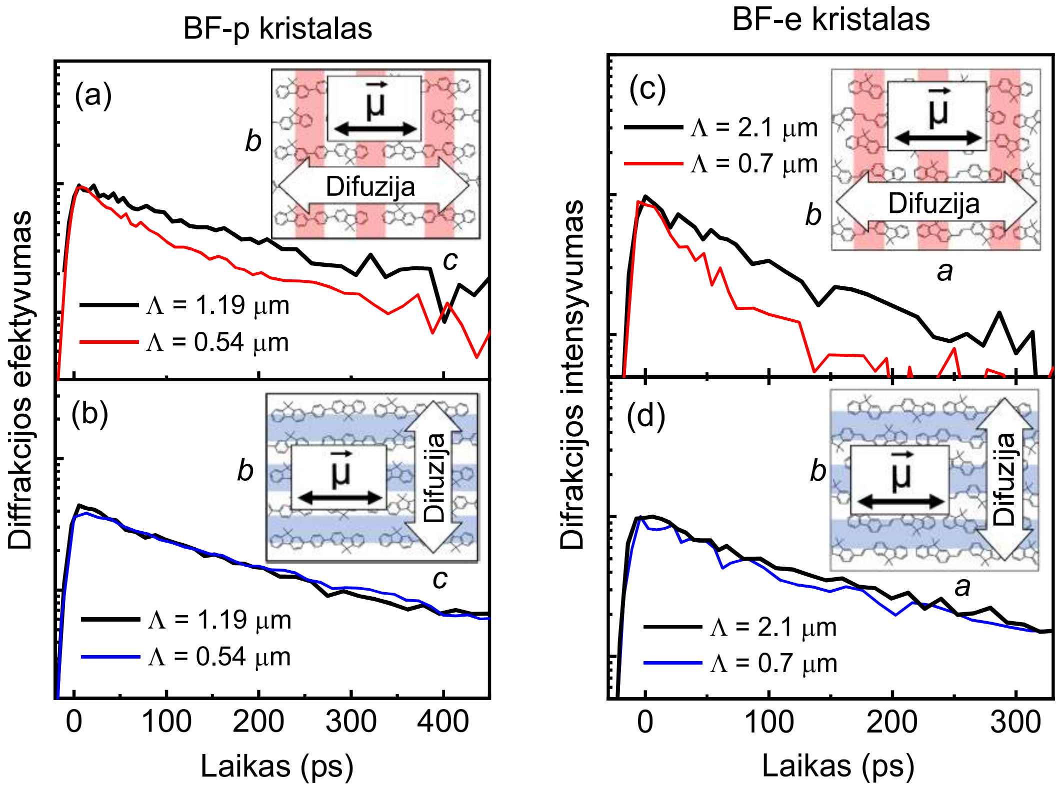

Pav. 10. ŠIDDG gesimo kinetikos išmatuotos BF-p ir BF-e kristaluose paralelia (a, c) ir statmena (b, d) gardelių vektorių kryptimis (difuzijos kryptimis) lyginant su molekulių šuolio dipoliniu momentu (μ) kristale. Matavimai atlikti dviem gardelių periodams (Λ).

Lentelė 3. ŠIDDG metodu išmatuoti eksitonų transporto parametrai.

Sample	$\tau_R$$^{a)}$, ps	$D_{\parallel}$$^{b)}$, cm^2/s	$D_{\perp}$$^{b)}$, cm^2/s	$L_{D\parallel}$$^{c)}$, nm	$\gamma$$^{d)}$, 10^{-9} cm^3/s
BF-p	500	0.24 ± 0.03	< 0.01	110 ± 7	7.1 ± 1.1
BF-e	950	0.96 ± 0.10	< 0.01	302 ± 15	31.2 ± 2.6

$^{a)}$ eksitonų relaksacijos laikas; $^{b)}$ difuzijos koeficientas paraleliai (||) ir statmentai (⊥) molekulių dipoliniam momentui kristale; $^{c)}$ difuzijos atstumas (||) kryptimi. $^{d)}$ anihiliacijos koeficientas.

Siekiant palyginti eksitonų difuzijos koeficientus, buvo atliktas papildomas eksitonų anihiliacijos spartos tyrimas abiejuose kristaluose. Šiuo atveju eksitonų anihiliacijos koeficientas (γ) tiesiogiai priklausė nuo eksitonų difuzijos spartos kristaluose. Gautas 5 kartus didesnis anihiliacijos koeficientas **BF-e** kristalui patvirtino spartesnę eksitonų pernašą, kuri buvo susijusi su kietesne molekulių struktūra bei dėl J-tipo eksitoninės sąveikos koherentiškai stiprinamais eksitonų šuoliais. Tuo tarpu anksčiau nustatyta dinaminė netvarka **BF-p** kristaluose lėmė lėtesnį eksitonų šokavimą netvarkiuose kristaluose.

5 Skyrius: Sparti sužadinimo pernaša legiruotuose kristaluose

Aktyvios matricos kristalų legiravimo strategija leidžia gauti aukštą liuminescencijos našumą ir žemą SSS slenkstį organiniuose kristaluose.[201] Aktyvi matrica veikia kaip energiją sugerianti terpė (arba krūvio pernašos ir eksitonų sudarymo terpė), iš kurios sužadinimo energija perduodama į tolygiai pasiskirsčiusias priemaišas, kurie pasižymi geromis emisijos savybėmis, taip išvengiant rezonansinės sąveikos tarp priemaišos ir kristalo matricos. Šiai strategijai įgyvendinti buvo pasirinkta bifluoreno sistema keičiant tik centrinį jungimo fragmentą, atitinkamai, acetileno (**BF-a**) ir etileno (**BF-e**) (žiūrėti Pav. 11). Čia centrinis fragmentas atliko kelias svarbias funkcijas: (i) vienodos molekulinės struktūros sumažino kristalo struktūrinių defektų tikimybę prie didelių legiravimo koncentracijų; (ii) skirtinga konjugacija lėmė energijos tarpų skirtumą energijos pernašai iš matricos į spindulines priemaišas; (iii) plokščios molekulių struktūros sumažino energetinę netvarką kristale bei lėmė spartesnę energijos pernašą iki priemaišos. Siekiant kontroliuoti energijos pernašos spartą kristalų auginimo iš garų fazės būdu buvo pagaminta serija kristalų su skirtingomis legiravimo koncentracijomis (0.5-11%). Rentgeno spindulių difrakcijos metodu atlikta atskirų **BF-e** ir **BF-a** kristalų bei legiruotų kristalų struktūrinė analizė (žiūrėti Pav. 3) parodė, kad dėl labai panašios matricos ir priemaišos molekulių struktūros jų pakavimasis kristale iš esmės nesiskiria.

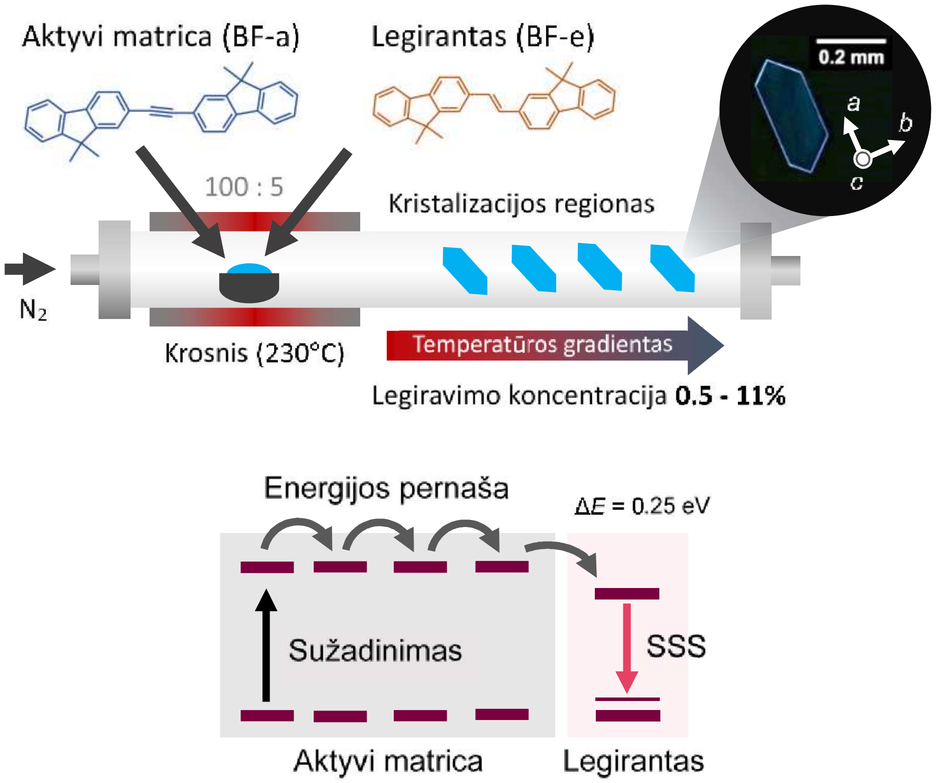

Pav. 11. Molekulių struktūros ir kristalų legiravimo garų fazės metodu schema (viršuje). Energijos pernašos legiruotame kristale schema, kai aktyvi matrica yra sužadinama optiškai (apačioje). Energijos tarpų skirtumas tarp matricos ir priemaišos nurodytas.

Tam, kad vyktų efektyvi energijos pernaša nuo sužadinimo matricoje į priemaišą, turėjo būti užtikrinti du pernašos etapai: sparti energijos pernaša aktyvioje matricoje ir pernaša iš matricos į priemaišas (schema apačioje Pav. 11). Pirmąjį spartaus eksitonų transporto etapą lėmė tiek kietos molekulių struktūros sumažinusios energetinę netvarką kristale, tiek tam tikra molekulinių dipolių orientacija (molekulės sluoksnyje palinkusios *a* kristalografinėje kryptyje) lėmusi rezonansinę dipolių sąveiką. Tuo tarpu antrąjį pernašos etapą užtikrino žemesnis priemaišų energijos lygmuo bei žymus sanklotos integralas tarp matricos emisijos ir priemaišų sugerties. Taigi dėl efektyvios pernašos optiškai žadinant aktyvią matricą buvo stebima tik priemaišų emisija, o esant dideliam sužadinimo tankiui, dėl stimuliuotų šuolių buvo stebima sustiprinta savaiminė emisija.

Siekiant įrodyti sparčią energijos pernašą iš aktyvios matricos į priemaišas buvo pasitelktas žadinimo-zondavimo metodas su femtosekundine skiriamąja geba. Buvo nustatyta, kad esant sąlyginai nedideliam priemaišų tankiui (~1%) pilna energijos pernaša įvykdavo iki dešimties pikosekundžių (Pav. 12a).

Energijos pernaša (populiacijos inversija) legiruotame bifluoreno kristale yra žymiai spartesnė negu analogiškose legiruotose amorfinėse sistemose. Legiravimo koncentracija leido valdyti populiacijos inversijos spartą.

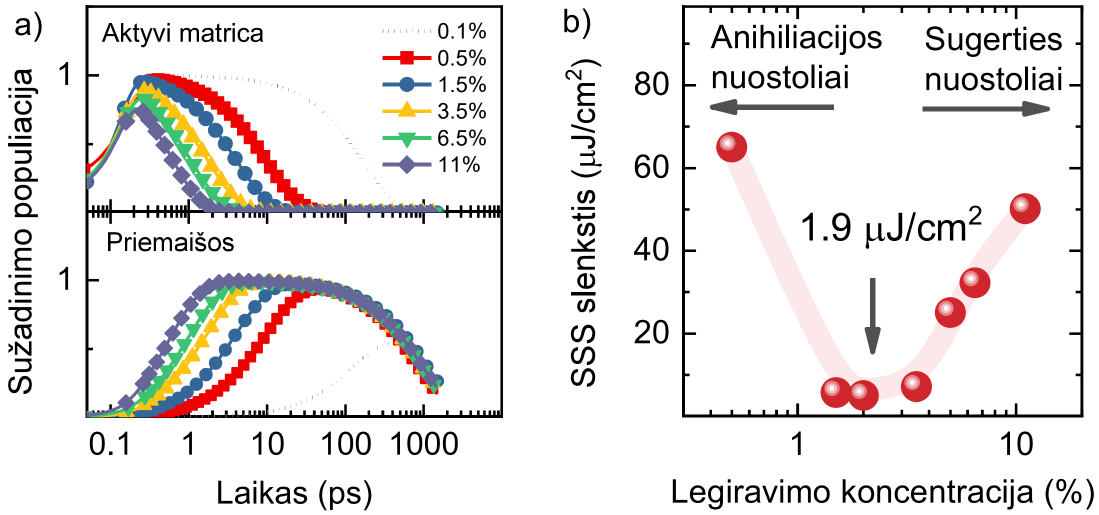

Pav. 12. Nuo laiko priklausanti energijos pernaša nustatyta žadinimo zondavimo metodu kristaluose su skirtinga legiravimo koncentracija (kairėje). SSS slenksčio vertės prie skirtingų kristalų legiravimo koncentracijų (dešinėje). Žemiausia pasiekta SSS vertė nurodyta.

Tačiau sparti energijos pernaša aktyvioje matricoje turi ir neigiamą efektą – esant dideliems sužadinimo tankiams vyksta eksitonų anihiliacija, kuri efektyviai mažina populiaciją. Šiuo atveju didesnė legiravimo koncentracija padeda išvengti anihiliacijos nuostolių, nes sužadinimai yra sparčiai lokalizuojami sekliuose priemaišų lygmenyse. Tačiau siekiant žemiausio SSS slenksčio organinių lazerių taikymams, didelė legiravimo koncentracija lemia nuostolius dėl nuosavosios sugerties priemaišose. Atlikus SSS tyrimus siauros juostelės žadinimo metodu, buvo nustatyta, kad optimali legiravimo koncentracija bifluoreno kristalų sistemai yra 1.5–3.5% ruože (grafikas dešinėje Pav. 12). Tuo tarpu gauta SSS slenksčio vertė (1.9 μJ/cm^2) buvo tarp geriausių verčių nustatytų organiniams kristalams pateiktų literatūroje.

Išvados

- 2,7-pozicijoje sujungti fluoreno oligomerai pasižymi aukštais fluorescencijos kvantiniais našumais (80 – 90%) ir sparčia spinduline rekombinacija (~1 ns^{-1}), kas lemia puikias stimuliuotos emisijos savybes.
- Bifluoreno kristaluose eksitoninės ir vibroninės sąveikos stipriai buvo valdomi keičiant molekulių jungiamųjų tiltelius, kurie lemia skirtingą sukamųjų virpesių laisvę.
- Bifluoreno junginiai su fenilo tilteliais pasižymėjo stipria vibronine sąveika dėl sukamųjų fenilo virpesių, kurie kristaluose lėmė dinaminę netvarką ir silpną eksitoninę sąveiką.
- Silpnos eksitoninės sąveikos ir stiprios vibroninės sąveikos efektai lėmė mažus sugerties nuostolius, o sparti spindulinė rekombinacija lėmė didelį stimuliuotų šuolių skerspjūvį, todėl kristalams sudarytiems iš bifluoreno junginių su fenilo tilteliais buvo stebimi žemi SSS slenksčiai.
- Bifluoreno junginiai su kietais acetileno ir etileno tiltaliais pasižymėjo silpna vibronine sąveika, o dėl mažos dinaminės netvarkos buvo stebima J-tipo eksitoninė sąveika kristaluose.
- J-tipo eksitoninės sąveikos efektai, tokie kaip stipri nuosavoji sugertis ir sparti eksitonų anihiliacija kristaluose lėmė aukštus SSS slenksčius.
- Nuosavasis legiravimas dėl atsitiktinės acetileno-etileno jungies modifikacijos leido išvengti eksitoninės sąveikos efektų ir pasiekti ypač žemus SSS slenksčius legiruotuose kristaluose.
- Sparčią sužadinimo pernašą į priemaišas aktyvioje kristalo matricoje lėmė J-tipo eksitoninė sąveika. Stipriai anizotropinės eksitonų difuzijos kryptis sutapo su J-agregato kryptimi (išilgai molekulinių šuolio dipolinių momentų).
- Siekiant išvengti anihiliacijos ir sugerties nuostolių kristaluose buvo atlikta legiruotų kristalų optimizacija. Optimalios legiravimo koncentracijos ties 1.5 - 3.5% leido pasiekti vieną žemiausių SSS slenksčio verčių nustatytų organiniams kristalams (1.9 $\mu J/cm^2$).

BIBLIOGRAPHY

1. Köhler, A. & Bässler, H. The Electronic Structure of Organic Semiconductors. in *Electronic Processes in Organic Semiconductors* 1–86 (John Wiley & Sons, Ltd, 2015). doi:10.1002/9783527685172.ch1.
2. Lanzani, G. Molecular Exciton. in *The Photophysics behind Photovoltaics and Photonics* 35–52 (John Wiley & Sons, Ltd, 2012). doi:10.1002/9783527645138.ch3.
3. Handbook of Flexible Organic Electronics. in *Handbook of Flexible Organic Electronics* (ed. Logothetidis, S.) iii (Woodhead Publishing, 2015). doi:10.1016/B978-1-78242-035-4.01001-0.
4. Pope, Martin & Swenberg Charles E. *Electronic Processes in Organic Crystals and Polymers*. (Oxford University Press, 1999).
5. Scholes, G. D. *et al.* Using coherence to enhance function in chemical and biophysical systems. *Nature* **543**, 647–656 (2017).
6. Mirkovic, T. *et al.* Light Absorption and Energy Transfer in the Antenna Complexes of Photosynthetic Organisms. *Chem. Rev.* **117**, 249–293 (2017).
7. Ostroverkhova, O. Organic Optoelectronic Materials: Mechanisms and Applications. *Chem. Rev.* **116**, 13279–13412 (2016).
8. Bonné, R. *et al.* Cable bacteria as long-range biological semiconductors. *ArXiv191206224 Cond-Mat Physicsphysics* (2019).
9. Wang, Y. *et al.* Organic crystalline materials in flexible electronics. *Chem Soc Rev* **48**, 1492–1530 (2019).
10. New record: Over 16 percent efficiency for single-junction organic solar cells. *EurekAlert!* https://www.eurekalert.org/pub_releases/2019-03/scp-nro031819.php.
11. Fan, B. *et al.* Achieving over 16% efficiency for single-junction organic solar cells. *Sci. China Chem.* **62**, 746–752 (2019).
12. Liu, Y. *et al.* Aggregation and morphology control enables multiple cases of high-efficiency polymer solar cells. *Nat. Commun.* **5**, 5293 (2014).
13. Inganäs, O. Organic Photovoltaics over Three Decades. *Adv. Mater.* **30**, 1800388 (2018).
14. Einzinger, M. *et al.* Sensitization of silicon by singlet exciton fission in tetracene. *Nature* **571**, 90–94 (2019).
15. Congreve, D. N. *et al.* External Quantum Efficiency Above 100% in a Singlet-Exciton-Fission–Based Organic Photovoltaic Cell. *Science* **340**, 334–337 (2013).
16. Kim, K.-H. & Kim, J.-J. Origin and Control of Orientation of Phosphorescent and TADF Dyes for High-Efficiency OLEDs. *Adv. Mater.* **30**, 1705600 (2018).

17. Organic laser diodes move from dream to reality. *EurekAlert!* https://www.eurekalert.org/pub_releases/2019-05/ku-old052419.php.
18. Sandanayaka, A. S. D. *et al.* Indication of current-injection lasing from an organic semiconductor. *Appl. Phys. Express* **12**, 061010 (2019).
19. Kanagasekaran, T. *et al.* Towards electrically driven organic semiconductor laser with field-effective transistor structure. *ArXiv190308869 Phys.* (2019).
20. Schafer, F. P. Dye lasers. (1990).
21. Annual Laser Market Review & Forecast 2019: What goes up... | Laser Focus World. https://www.laserfocusworld.com/lasers-sources/article/16556290/annual-laser-market-review-forecast-2019-what-goes-up.
22. DSCC: the OLED market will grow 19% in 2019 to reach $31 billion in revenues | OLED-Info. https://www.oled-info.com/dscc-oled-market-will-grow-19-2019-reach-31-billion-revenues.
23. Kuehne, A. J. C. & Gather, M. C. Organic Lasers: Recent Developments on Materials, Device Geometries, and Fabrication Techniques. *Chem. Rev.* **116**, 12823–12864 (2016).
24. Hill, M. T. & Gather, M. C. Advances in small lasers. *Nat. Photonics* **8**, 908–918 (2014).
25. Zhang, W., Yao, J. & Zhao, Y. S. Organic Micro/Nanoscale Lasers. *Acc. Chem. Res.* **49**, 1691–1700 (2016).
26. Gather, M. C. & Yun, S. H. Single-cell biological lasers. *Nat. Photonics* **5**, 406–410 (2011).
27. Humar, M. & Hyun Yun, S. Intracellular microlasers. *Nat. Photonics* **9**, 572–576 (2015).
28. Lee, G.-H. *et al.* Multifunctional materials for implantable and wearable photonic healthcare devices. *Nat. Rev. Mater.* (2020) doi:10.1038/s41578-019-0167-3.
29. Sanvitto, D. & Kéna-Cohen, S. The road towards polaritonic devices. *Nat. Mater.* **15**, 1061 (2016).
30. World’s First Ultrafast All-Optical Room Temperature Transistor. https://www.photonicsviews.com/worlds-first-ultrafast-all-optical-room-temperature-transistor/.
31. Zasedatelev, A. V. *et al.* A room-temperature organic polariton transistor. *Nat. Photonics* **13**, 378–383 (2019).
32. BROWNE, W. R. & FERINGA, B. L. Making molecular machines work. in *Nanoscience and Technology* 79–89 doi:10.1142/9789814287005_0009.
33. Mattia, E. & Otto, S. Supramolecular systems chemistry. *Nat. Nanotechnol.* **10**, 111–119 (2015).
34. Chen, K. & Arnold, F. H. Engineering new catalytic activities in enzymes. *Nat. Catal.* (2020) doi:10.1038/s41929-019-0385-5.

35. Murawski, C., Leo, K. & Gather, M. C. Efficiency Roll-Off in Organic Light-Emitting Diodes. *Adv. Mater.* **25**, 6801–6827 (2013).
36. Uoyama, H., Goushi, K., Shizu, K., Nomura, H. & Adachi, C. Highly efficient organic light-emitting diodes from delayed fluorescence. *Nature* **492**, 234–238 (2012).
37. Baldo, M. A., O'Brien, D. F., Thompson, M. E. & Forrest, S. R. Excitonic singlet-triplet ratio in a semiconducting organic thin film. *Phys Rev B* **60**, 14422–14428 (1999).
38. Hirata, S. *et al.* Efficient Persistent Room Temperature Phosphorescence in Organic Amorphous Materials under Ambient Conditions. *Adv. Funct. Mater.* **23**, 3386–3397 (2013).
39. Adachi, C., Baldo, M. A., Thompson, M. E. & Forrest, S. R. Nearly 100% internal phosphorescence efficiency in an organic light-emitting device. *J. Appl. Phys.* **90**, 5048–5051 (2001).
40. Baldo, M. A., Holmes, R. J. & Forrest, S. R. Prospects for electrically pumped organic lasers. *Phys Rev B* **66**, 035321 (2002).
41. Nakanotani, H., Furukawa, T. & Adachi, C. Light Amplification in an Organic Solid-State Film with the Aid of Triplet-to-Singlet Upconversion. *Adv. Opt. Mater.* **3**, 1381–1388 (2015).
42. Kim, D.-H. *et al.* High-efficiency electroluminescence and amplified spontaneous emission from a thermally activated delayed fluorescent near-infrared emitter. *Nat. Photonics* **12**, 98–104 (2018).
43. Matsushima, T. *et al.* Degradation Mechanism and Stability Improvement Strategy for an Organic Laser Gain Material 4,4′-Bis[(*N* -carbazole)styryl]biphenyl (BSBCz). *Adv. Funct. Mater.* **29**, 1807148 (2019).
44. Tyagi, P., Srivastava, R., Giri, L. I., Tuli, S. & Lee, C. Degradation of organic light emitting diode: Heat related issues and solutions. *Synth. Met.* **216**, 40–50 (2016).
45. Mikhnenko, O. V., Blom, P. W. M. & Nguyen, T.-Q. Exciton diffusion in organic semiconductors. *Energy Env. Sci* **8**, 1867–1888 (2015).
46. Salehi, A. *et al.* Realization of high-efficiency fluorescent organic light-emitting diodes with low driving voltage. *Nat. Commun.* **10**, 1–9 (2019).
47. Lee, J.-H. *et al.* Blue organic light-emitting diodes: current status, challenges, and future outlook. *J. Mater. Chem. C* **7**, 5874–5888 (2019).
48. Sandanayaka, A. S. D. *et al.* Improvement of the quasi-continuous-wave lasing properties in organic semiconductor lasers using oxygen as triplet quencher. *Appl. Phys. Lett.* **108**, 223301 (2016).
49. Zhang, Y. & Forrest, S. R. Existence of continuous-wave threshold for organic semiconductor lasers. *Phys. Rev. B* **84**, 241301 (2011).
50. Meister, S., Brückner, R., Sudzius, M., Fröb, H. & Leo, K. Optically pumped lasing of an electrically active hybrid OLED-microcavity. *Appl. Phys. Lett.* **112**, 113301 (2018).

51. Capelli, R. *et al.* Organic light-emitting transistors with an efficiency that outperforms the equivalent light-emitting diodes. *Nat. Mater.* **9**, 496–503 (2010).
52. M. Muccini, S. T. Organic Light-Emitting Transistors. in *Organic Light-Emitting Transistors* 45–85 (John Wiley & Sons, Ltd, 2016). doi:10.1002/9781119189978.ch3.
53. Liu, C.-F., Liu, X., Lai, W.-Y. & Huang, W. Organic Light-Emitting Field-Effect Transistors: Device Geometries and Fabrication Techniques. *Adv. Mater.* **30**, 1802466 (2018).
54. Hotta, S., Yamao, T., Bisri, S. Z., Takenobu, T. & Iwasa, Y. Organic single-crystal light-emitting field-effect transistors. *J Mater Chem C* **2**, 965–980 (2014).
55. Zhang, X., Dong, H. & Hu, W. Organic Semiconductor Single Crystals for Electronics and Photonics. *Adv. Mater.* **30**, 1801048 (2018).
56. Wang, C., Dong, H., Jiang, L. & Hu, W. Organic semiconductor crystals. *Chem. Soc. Rev.* **47**, 422–500 (2018).
57. Kanagasekaran, T., Shimotani, H., Shimizu, R., Hitosugi, T. & Tanigaki, K. A new electrode design for ambipolar injection in organic semiconductors. *Nat. Commun.* **8**, 999 (2017).
58. Brückner, R. *et al.* Phase-locked coherent modes in a patterned metal–organic microcavity. *Nat. Photonics* **6**, 322–326 (2012).
59. Sandanayaka, A. S. D. *et al.* Quasi-Continuous-Wave Organic Thin-Film Distributed Feedback Laser. *Adv. Opt. Mater.* **4**, 834–839 (2016).
60. Tsutsumi, N., Kawahira, T. & Sakai, W. Amplified spontaneous emission and distributed feedback lasing from a conjugated compound in various polymer matrices. *Appl. Phys. Lett.* **83**, 2533–2535 (2003).
61. Karnutsch, C. *et al.* Improved organic semiconductor lasers based on a mixed-order distributed feedback resonator design. *Appl. Phys. Lett.* **90**, (2007).
62. Fang, H.-H. *et al.* Distributed Feedback Lasers Based on Thiophene/Phenylene Co-Oligomer Single Crystals. *Adv. Funct. Mater.* **22**, 33–38 (2012).
63. Wei, G.-Q., Wang, X.-D. & Liao, L.-S. Recent Advances in 1D Organic Solid-State Lasers. *Adv. Funct. Mater.* **0**, 1902981 (2019).
64. Wei, C. *et al.* Organic Janus Microspheres: A General Approach to All-Color Dual-Wavelength Microlasers. *J. Am. Chem. Soc.* **141**, 5116–5120 (2019).
65. Zhuang, X., Ouyang, Y., Wang, X. & Pan, A. Multicolor Semiconductor Lasers. *Adv. Opt. Mater.* 1900071 (2019) doi:10.1002/adom.201900071.
66. Zhang, C. *et al.* Dual-color single-mode lasing in axially coupled organic nanowire resonators. *Sci. Adv.* **3**, e1700225 (2017).

67. Ou, C.-J. *et al.* Dimerization effect of fluorene-based semiconductors on conformational planarization for microcrystal lasing. *J. Mater. Chem. C* **5**, 5345–5355 (2017).
68. Drexhage, K. H. Structure and Properties of Laser Dyes. in *Dye Lasers* (ed. Schäfer, F. P.) 144–193 (Springer Berlin Heidelberg, 1973). doi:10.1007/978-3-662-11579-4_4.
69. Cordella, F. *et al.* Optical Gain Performance of Epitaxially Grown para-Sexiphenyl Films. *Adv. Mater.* **19**, 2252–2256 (2007).
70. Varghese, S. *et al.* Polymorphism and Amplified Spontaneous Emission in a Dicyano-Distyrylbenzene Derivative with Multiple Trifluoromethyl Substituents: Intermolecular Interactions in Play. *Adv. Funct. Mater.* **26**, 2349–2356 (2016).
71. Sandanayaka, A. S. *et al.* Toward continuous-wave operation of organic semiconductor lasers. *Sci. Adv.* **3**, e1602570 (2017).
72. Forget, S. & Chénais, S. Fundamentals of Organic Lasers. in *Organic Solid-State Lasers* (eds. Forget, S. & Chénais, S.) 13–73 (Springer Berlin Heidelberg, 2013). doi:10.1007/978-3-642-36705-2_2.
73. Qian, Y. *et al.* H-Shaped Oligofluorenes for Highly Air-Stable and Low-Threshold Non-Doped Deep Blue Lasing. *Adv. Mater.* **26**, 2937–2942 (2014).
74. Mowatt, C. *et al.* Comparison of the performance of photonic band-edge liquid crystal lasers using different dyes as the gain medium. *J. Appl. Phys.* **107**, 043101 (2010).
75. Kozlov, V. G., Bulović, V., Burrows, P. E. & Forrest, S. R. Laser action in organic semiconductor waveguide and double-heterostructure devices. *Nature* **389**, 362–364 (1997).
76. Kim, D.-H. *et al.* Extremely low amplified spontaneous emission threshold and blue electroluminescence from a spin-coated octafluorene neat film. *Appl. Phys. Lett.* **110**, 023303 (2017).
77. Wei, Q. *et al.* A High Performance Deep Blue Organic Laser Gain Material. *Adv. Opt. Mater.* **5**, 1601003 (2017).
78. Choi, E. Y. *et al.* Photophysical, amplified spontaneous emission and charge transport properties of oligofluorene derivatives in thin films. *Phys Chem Chem Phys* **16**, 16941–16956 (2014).
79. Yap, B. K., Xia, R., Campoy-Quiles, M., Stavrinou, P. N. & Bradley, D. D. C. Simultaneous optimization of charge-carrier mobility and optical gain in semiconducting polymer films. *Nat Mater* **7**, 376–380 (2008).
80. Nakanotani, H. *et al.* Extremely Low-Threshold Amplified Spontaneous Emission of 9,9′-Spirobifluorene Derivatives and Electroluminescence from Field-Effect Transistor Structure. *Adv. Funct. Mater.* **17**, 2328–2335 (2007).
81. Ruan, S.-B. *et al.* A spirofluorene-end-capped bis-stilbene derivative with a low amplified spontaneous emission threshold and balanced hole and electron mobilities. *Opt. Mater.* **100**, 109636 (2020).

82. Aimono, T. *et al.* 100% fluorescence efficiency of 4,4′-bis[(N-carbazole)styryl]biphenyl in a solid film and the very low amplified spontaneous emission threshold. *Appl. Phys. Lett.* **86**, 071110 (2005).
83. Mamada, M., Fukunaga, T., Bencheikh, F., Sandanayaka, A. S. D. & Adachi, C. Low Amplified Spontaneous Emission Threshold from Organic Dyes Based on Bis-stilbene. *Adv. Funct. Mater.* **28**, 1802130 (2018).
84. Oyama, Y. *et al.* Design Strategy for Robust Organic Semiconductor Laser Dyes. *ACS Mater. Lett.* 161–167 (2020) doi:10.1021/acsmaterialslett.9b00536.
85. Dong, H., Fu, X., Liu, J., Wang, Z. & Hu, W. 25th Anniversary Article: Key Points for High-Mobility Organic Field-Effect Transistors. *Adv. Mater.* **25**, 6158–6183 (2013).
86. Kölle, P., Schnappinger, T. & Vivie-Riedle, R. de. Deactivation pathways of thiophene and oligothiophenes: internal conversion versus intersystem crossing. *Phys. Chem. Chem. Phys.* **18**, 7903–7915 (2016).
87. Fichou, D., Delysse, S. & Nunzi, J.-M. First evidence of stimulated emission from a monolithic organic single crystal: α-Octithiophene. *Adv. Mater.* **9**, 1178–1181 (1997).
88. Losio, P. A., Hunziker, C. & Günter, P. Amplified spontaneous emission in *para* -sexiphenyl bulk single crystals. *Appl. Phys. Lett.* **90**, 241103 (2007).
89. Quochi, F., Saba, M., Mura, A. & Bongiovanni, G. Excited-State Dynamics and Laser Action in Epitaxial Organic Nanofibers. in *Small Organic Molecules on Surfaces: Fundamentals and Applications* (eds. Sitter, H., Draxl, C. & Ramsey, M.) 231–249 (Springer Berlin Heidelberg, 2013). doi:10.1007/978-3-642-33848-9_9.
90. Andreev, A. *et al.* Coherent random lasing in the deep blue from self-assembled organic nanofibers. *J. Appl. Phys.* **99**, 034305 (2006).
91. Gierschner, J., Varghese, S. & Park, S. Y. Organic Single Crystal Lasers: A Materials View. *Adv. Opt. Mater.* **4**, 348–364 (2016).
92. Nakanotani, H., Saito, M., Nakamura, H. & Adachi, C. Highly balanced ambipolar mobilities with intense electroluminescence in field-effect transistors based on organic single crystal oligo(p-phenylenevinylene) derivatives. *Appl. Phys. Lett.* **95**, 033308 (2009).
93. Kabe, R., Nakanotani, H., Sakanoue, T., Yahiro, M. & Adachi, C. Effect of Molecular Morphology on Amplified Spontaneous Emission of Bis-Styrylbenzene Derivatives. *Adv. Mater.* **21**, 4034–4038 (2009).
94. Varghese, S. *et al.* Orthogonal Resonator Modes and Low Lasing Threshold in Highly Emissive Distyrylbenzene-Based Molecular Crystals. *Adv. Opt. Mater.* **2**, 542–548 (2014).
95. Fang, H.-H. *et al.* Functional organic single crystals for solid-state laser applications: Organic laser crystals. *Laser Photonics Rev.* **8**, 687–715 (2014).

96. Hotta, S. & Yamao, T. The thiophene/phenylene co-oligomers: exotic molecular semiconductors integrating high-performance electronic and optical functionalities. *J. Mater. Chem.* **21**, 1295–1304 (2011).
97. Hotta, S. Optically and electrically excited emissions from organic semiconducting oligomer crystals. *Polym. Int.* **66**, 223–236 (2017).
98. Bisri, S. Z. *et al.* High Mobility and Luminescent Efficiency in Organic Single-Crystal Light-Emitting Transistors. *Adv. Funct. Mater.* **19**, 1728–1735 (2009).
99. Ichikawa, M. *et al.* Photopumped laser oscillation and charge-injected luminescence from organic semiconductor single crystals of a thiophene/phenylene co-oligomer. *Appl. Phys. Lett.* **87**, 221113 (2005).
100. Kanazawa, S., Ichikawa, M., Koyama, T. & Taniguchi, Y. Self-Waveguided Photoemission and Lasing of Organic Crystalline Wires Obtained by an Improved Expitaxial Growth Method. *ChemPhysChem* **7**, 1881–1884 (2006).
101. Nakanotani, H. & Adachi, C. Amplified Spontaneous Emission and Electroluminescence from Thiophene/Phenylene Co-Oligomer-Doped *p* -bis(*p* -Styrylstyryl)Benzene Crystals. *Adv. Opt. Mater.* **1**, 422–427 (2013).
102. Sawabe, K. *et al.* High current densities in a highly photoluminescent organic single-crystal light-emitting transistor. *Appl. Phys. Lett.* **97**, 043307 (2010).
103. Komori, T., Nakanotani, H., Yasuda, T. & Adachi, C. Light-emitting organic field-effect transistors based on highly luminescent single crystals of thiophene/phenylene co-oligomers. *J. Mater. Chem. C* **2**, 4918 (2014).
104. Sirringhaus, H. 25th Anniversary Article: Organic Field-Effect Transistors: The Path Beyond Amorphous Silicon. *Adv. Mater.* **26**, 1319–1335 (2014).
105. Fratini, S., Ciuchi, S., Mayou, D., de Laissardière, G. T. & Troisi, A. A map of high-mobility molecular semiconductors. *Nat. Mater.* **16**, 998–1002 (2017).
106. Oberhofer, H., Reuter, K. & Blumberger, J. Charge Transport in Molecular Materials: An Assessment of Computational Methods. *Chem. Rev.* **117**, 10319–10357 (2017).
107. Hestand, N. J. & Spano, F. C. Molecular Aggregate Photophysics beyond the Kasha Model: Novel Design Principles for Organic Materials. *Acc. Chem. Res.* **50**, 341–350 (2017).
108. Kasha, M., Rawls, H. R. & Ashraf El-Bayoumi, M. The exciton model in molecular spectroscopy. *Pure Appl. Chem.* **11**, 371–392 (1965).
109. Hestand, N. J. & Spano, F. C. Expanded Theory of H- and J-Molecular Aggregates: The Effects of Vibronic Coupling and Intermolecular Charge Transfer. *Chem. Rev.* **118**, 7069–7163 (2018).

110. Camposeo, A. *et al.* Polarized superradiance from delocalized exciton transitions in tetracene single crystals. *Phys. Rev. B* **81**, (2010).
111. Eisfeld, A., Marquardt, C., Paulheim, A. & Sokolowski, M. Superradiance from Two Dimensional Brick-Wall Aggregates of Dye Molecules: The Role of Size and Shape for the Temperature Dependence. *Phys. Rev. Lett.* **119**, 097402 (2017).
112. Ding, R., An, M.-H., Feng, J. & Sun, H.-B. Organic Single-Crystalline Semiconductors for Light-Emitting Applications: Recent Advances and Developments. *Laser Photonics Rev.* **13**, 1900009 (2019).
113. Hotta, S. *et al.* Crystal Structures of Thiophene/Phenylene Co-Oligomers with Different Molecular Shapes. *Chem. Mater.* **16**, 237–241 (2004).
114. Varghese, S. *et al.* Stimulated Emission Properties of Sterically Modified Distyrylbenzene-Based H-Aggregate Single Crystals. *J. Phys. Chem. Lett.* **4**, 1597–1602 (2013).
115. Varghese, S. *et al.* Stimulated Resonance Raman Scattering and Laser Oscillation in Highly Emissive Distyrylbenzene-Based Molecular Crystals. *Adv. Mater.* **24**, 6473–6478 (2012).
116. Lécuiller, R. *et al.* Fluorescence yield and lifetime of isolated polydiacetylene chains: Evidence for a one-dimensional exciton band in a conjugated polymer. *Phys. Rev. B* **66**, 125205 (2002).
117. Lim, S.-H., Bjorklund, T. G., Spano, F. C. & Bardeen, C. J. Exciton Delocalization and Superradiance in Tetracene Thin Films and Nanoaggregates. *Phys. Rev. Lett.* **92**, (2004).
118. Birks, J. B. Excimers. *Rep. Prog. Phys.* **38**, 903–974 (1975).
119. Yamagata, H., Pochas, C. M. & Spano, F. C. Designing J- and H-Aggregates through Wave Function Overlap Engineering: Applications to Poly(3-hexylthiophene). *J. Phys. Chem. B* **116**, 14494–14503 (2012).
120. *Organic lasers: fundamentals, developments, and applications*. (Pan Stanford Publishing, 2018).
121. *Highly Efficient OLEDs: Materials Based on Thermally Activated Delayed Fluorescence*. (Wiley-VCH Verlag GmbH & Co. KGaA, 2018). doi:10.1002/9783527691722.
122. Ding, R. *et al.* Clarification of the Molecular Doping Mechanism in Organic Single-Crystalline Semiconductors and their Application in Color-Tunable Light-Emitting Devices. *Adv. Mater.* **30**, 1801078 (2018).
123. Mannanov, A. A. *et al.* Long-range exciton transport in brightly fluorescent furan/phenylene co-oligomer crystals. *J. Mater. Chem. C* **7**, 60–68 (2019).
124. Ding, R. *et al.* Highly Efficient Three Primary Color Organic Single-Crystal Light-Emitting Devices with Balanced Carrier Injection and Transport. *Adv. Funct. Mater.* **27**, 1604659 (2017).

125. Nakanotani, H., Saito, M., Nakamura, H. & Adachi, C. Emission Color Tuning in Ambipolar Organic Single-Crystal Field-Effect Transistors by Dye-Doping. *Adv. Funct. Mater.* **20**, 1610–1615 (2010).
126. Brixner, T., Hildner, R., Köhler, J., Lambert, C. & Würthner, F. Exciton Transport in Molecular Aggregates – From Natural Antennas to Synthetic Chromophore Systems. *Adv. Energy Mater.* **7**, 1700236 (2017).
127. Bardeen, C. J. The Structure and Dynamics of Molecular Excitons. *Annu. Rev. Phys. Chem.* **65**, 127–148 (2014).
128. Jin, X.-H. *et al.* Long-range exciton transport in conjugated polymer nanofibers prepared by seeded growth. *Science* **360**, 897–900 (2018).
129. Haedler, A. T. *et al.* Long-range energy transport in single supramolecular nanofibres at room temperature. *Nature* **523**, 196–199 (2015).
130. Forster, Th. Energiewanderung und Fluoreszenz. *Naturwissenschaften* **33**, 166–175 (1946).
131. Wang, H. *et al.* Controlled transition dipole alignment of energy donor and energy acceptor molecules in doped organic crystals, and the effect on intermolecular Förster energy transfer. *Phys. Chem. Chem. Phys.* **15**, 3527 (2013).
132. Tempelaar, R., Jansen, T. L. C. & Knoester, J. Exciton–Exciton Annihilation Is Coherently Suppressed in H-Aggregates, but Not in J-Aggregates. *J. Phys. Chem. Lett.* **8**, 6113–6117 (2017).
133. Braun, A., Mayer, U., Auweter, H., Wolf, H. C. & Schmid, D. Singlet-Exciton Energy Transfer in Tetracene-doped Anthracene Crystals as Studied by Time-Resolved Spectroscopy. *Z. Für Naturforschung A* **37a**, 1013 (1982).
134. Kenkre, V. M. & Schmid, D. Coherence in singlet-exciton motion in anthracene crystals. *Phys. Rev. B* **31**, 2430–2436 (1985).
135. Quochi, F. *et al.* Temperature Tuning of Nonlinear Exciton Processes in Self-Assembled Oligophenyl Nanofibers under Laser Action. *Adv. Mater.* **20**, 3017–3021 (2008).
136. Clark, J., Silva, C., Friend, R. H. & Spano, F. C. Role of Intermolecular Coupling in the Photophysics of Disordered Organic Semiconductors: Aggregate Emission in Regioregular Polythiophene. *Phys. Rev. Lett.* **98**, 206406 (2007).
137. de Mello, J. C., Wittmann, H. F. & Friend, R. H. An improved experimental determination of external photoluminescence quantum efficiency. *Adv. Mater.* **9**, 230–232 (1997).
138. Berera, R., van Grondelle, R. & Kennis, J. T. M. Ultrafast transient absorption spectroscopy: Principles and application to photosynthetic systems. *Photosynth. Res.* **101**, 105–118 (2009).

139. Pollard, W. T. & Mathies, R. A. Analysis of Femtosecond Dynamic Absorption Spectra of Nonstationary States. *Annu. Rev. Phys. Chem.* **43**, 497–523 (1992).
140. Eichler, H. J., Günter, P. & Pohl, D. W. *Laser-Induced Dynamic Gratings*. vol. 50 (Springer Berlin Heidelberg, 1986).
141. Ščajev, P. *et al.* Two Regimes of Carrier Diffusion in Vapor-Deposited Lead-Halide Perovskites. *J. Phys. Chem. C* **121**, 21600–21609 (2017).
142. Fayer, M. D. Dynamics of molecules in condensed phases: picosecond holographic grating experiments. *Annu. Rev. Phys. Chem.* **33**, 63–87 (1982).
143. Nelson, K. A., Casalegno, R., Miller, R. J. D. & Fayer, M. D. Laser-induced excited state and ultrasonic wave gratings: Amplitude and phase grating contributions to diffraction. *J. Chem. Phys.* **77**, 1144–1152 (1982).
144. Calzado, E. M., Ramírez, M. G., Boj, P. G. & García, M. A. D. Thickness dependence of amplified spontaneous emission in low-absorbing organic waveguides. *Appl Opt* **51**, 3287–3293 (2012).
145. Anni, M., Perulli, A. & Monti, G. Thickness dependence of the amplified spontaneous emission threshold and operational stability in poly(9,9-dioctylfluorene) active waveguides. *J. Appl. Phys.* **111**, 093109 (2012).
146. Scherf, U. & List, E. J. W. Semiconducting Polyfluorenes—Towards Reliable Structure–Property Relationships. *Adv. Mater.* **14**, 477–487 (2002).
147. Tomkeviciene, A. *et al.* Impact of Linking Topology on the Properties of Carbazole Trimers and Dimers. *J. Phys. Chem. C* **115**, 4887–4897 (2011).
148. Chua, L.-L. *et al.* General observation of n-type field-effect behaviour in organic semiconductors. *Nature* **434**, 194–199 (2005).
149. Wu, C. *et al.* Unusual Nondispersive Ambipolar Carrier Transport and High Electron Mobility in Amorphous Ter(9,9-diarylfluorene)s. *J. Am. Chem. Soc.* **125**, 3710–3711 (2003).
150. Yokoyama, D., Sakaguchi, A., Suzuki, M. & Adachi, C. Horizontal orientation of linear-shaped organic molecules having bulky substituents in neat and doped vacuum-deposited amorphous films. *Org. Electron.* **10**, 127–137 (2009).
151. Köhler, A. & Bässler, H. Triplet states in organic semiconductors. *Mater. Sci. Eng. R Rep.* **66**, 71–109 (2009).
152. Li, W. *et al.* 3,6-Carbazole vs 2,7-carbazole: A comparative study of hole-transporting polymeric materials for inorganic–organic hybrid perovskite solar cells. *Beilstein J. Org. Chem.* **12**, 1401–1409 (2016).
153. Shen, J.-Y. *et al.* Ambipolar Conductive 2,7-Carbazole Derivatives for Electroluminescent Devices. *Adv. Funct. Mater.* **17**, 983–995 (2007).

154. Baronas, P. *et al.* Differently linked fluorene-carbazole triads for light amplification. *Dyes Pigments* **123**, 370–379 (2015).
155. Kazlauskas, K. *et al.* Concentration effects on spontaneous and amplified emission in benzo[c]fluorenes. *Phys. Chem. Chem. Phys.* **17**, 12935–12948 (2015).
156. Krotkus, S. *et al.* Pyrenyl-Functionalized Fluorene and Carbazole Derivatives as Blue Light Emitters. *J. Phys. Chem. C* **116**, 7561–7572 (2012).
157. Clark, J., Nelson, T., Tretiak, S., Cirmi, G. & Lanzani, G. Femtosecond torsional relaxation. *Nat. Phys.* **8**, 225–231 (2012).
158. Belletete, M., Bedard, M., Leclerc, M. & Durocher, G. Absorption and emission properties of carbazole-based dyads studied from experimental and theoretical investigations. *Synth. Met.* **146**, 99–108 (2004).
159. Karpicz, R. *et al.* Impact of intramolecular twisting and exciton migration on emission efficiency of multifunctional fluorene-benzothiadiazole-carbazole compounds. *J. Chem. Phys.* **134**, 204508–204516 (2011).
160. Cekaviciute, M. *et al.* Structure–Properties Relationship of Phenylethenyl-Substituted Triphenylamines. *J. Phys. Chem. C* **117**, 7973–7980 (2013).
161. Kersting, R. *et al.* Femtosecond site-selective probing of energy relaxing excitons in poly(phenylenevinylene): Luminescence dynamics and lifetime spectra. *J. Chem. Phys.* **106**, 2850–2864 (1997).
162. Aimono, T. *et al.* 100% fluorescence efficiency of 4,4′-bis[(N-carbazole)styryl]biphenyl in a solid film and the very low amplified spontaneous emission threshold. *Appl. Phys. Lett.* **86**, 071110 (2005).
163. Dias, F. B. *et al.* Triplet Harvesting with 100% Efficiency by Way of Thermally Activated Delayed Fluorescence in Charge Transfer OLED Emitters. *Adv. Mater.* **25**, 3707–3714 (2013).
164. Zhang, N. *et al.* The effect of delocalization on the exchange energy in meta- and para-linked Pt-containing carbazole polymers and monomers. *J. Chem. Phys.* **124**, (2006).
165. Shi, J. *et al.* Solid State Luminescence Enhancement in π-Conjugated Materials: Unraveling the Mechanism beyond the Framework of AIE/AIEE. *J. Phys. Chem. C* **121**, 23166–23183 (2017).
166. Samuel, I. D. W. & Turnbull, G. A. Organic Semiconductor Lasers. *Chem. Rev.* **107**, 1272–1295 (2007).
167. Miasojedovas, A. *et al.* Concentration effects on emission of bay-substituted perylene diimide derivatives in a polymer matrix. *Dyes Pigments* **92**, 1285–1291 (2012).
168. Tsiminis, G. *et al.* Low-threshold organic laser based on an oligofluorene truxene with low optical losses. *Appl. Phys. Lett.* **94**, (2009).

169. Wallikewitz, B. H., Hertel, D. & Meerholz, K. Cross-Linkable Polyspirobifluorenes: A Material Class Featuring Good OLED Performance and Low Amplified Spontaneous Emission Thresholds. *Chem. Mater.* **21**, 2912–2919 (2009).
170. Heliotis, G., Bradley, D. D. C., Turnbull, G. A. & Samuel, I. D. W. Light amplification and gain in polyfluorene waveguides. *Appl. Phys. Lett.* **81**, 415–417 (2002).
171. Calzado, E. M., Boj, P. G. & Díaz-García, M. A. Amplified Spontaneous Emission Properties of Semiconducting Organic Materials. *Int. J. Mol. Sci.* **11**, 2546–2565 (2010).
172. Resta, V. *et al.* Nanoparticle-doped electrospun fiber random lasers with spatially extended light modes. *Opt Express* **25**, 24604–24614 (2017).
173. Montinaro, M. *et al.* Diverse Regimes of Mode Intensity Correlation in Nanofiber Random Lasers through Nanoparticle Doping. *ACS Photonics* **5**, 1026–1033 (2018).
174. Yang, Y., Turnbull, G. A. & Samuel, I. D. W. Hybrid optoelectronics: A polymer laser pumped by a nitride light-emitting diode. *Appl. Phys. Lett.* **92**, (2008).
175. Kazlauskas, K. *et al.* Fluorene- and benzofluorene-cored oligomers as low threshold and high gain amplifying media. *Appl. Phys. Lett.* **107**, 043301 (2015).
176. Karabunarliev, S., Bittner, E. R. & Baumgarten, M. Franck–Condon spectra and electron-libration coupling in para-polyphenyls. *J. Chem. Phys.* **114**, 5863 (2001).
177. Kreiza, G. *et al.* Bifluorene Single Crystals with Extremely Low-Threshold Amplified Spontaneous Emission. *Adv. Opt. Mater.* **5**, 1600823 (2017).
178. Schumacher, S. *et al.* Effect of exciton self-trapping and molecular conformation on photophysical properties of oligofluorenes. *J. Chem. Phys.* **131**, 154906 (2009).
179. Kukhta, N. A., da Silva Filho, D. A., Volyniuk, D., Grazulevicius, J. V. & Sini, G. Can Fluorenone-Based Compounds Emit in the Blue Region? Impact of the Conjugation Length and the Ground-State Aggregation. *Chem. Mater.* **29**, 1695–1707 (2017).
180. Estrada, L. A., Yarnell, J. E. & Neckers, D. C. Revisiting Fluorenone Photophysics via Dipolar Fluorenone Derivatives. *J. Phys. Chem. A* **115**, 6366–6375 (2011).
181. Yuan, M.-S. *et al.* Fluorenone Organic Crystals: Two-Color Luminescence Switching and Reversible Phase Transformations between π–π Stacking-Directed Packing and Hydrogen Bond-Directed Packing. *Chem. Mater.* **26**, 2467–2477 (2014).
182. Hayes, S. C. & Silva, C. Analysis of the excited-state absorption spectral bandshape of oligofluorenes. *J. Chem. Phys.* **132**, 214510 (2010).

183. Ling, S., Schumacher, S., Galbraith, I. & Paterson, M. J. Excited-State Absorption of Conjugated Polymers in the Near-Infrared and Visible: A Computational Study of Oligofluorenes. *J. Phys. Chem. C* **117**, 6889–6895 (2013).
184. Lee, G., Kim, J., Kim, S. Y., Kim, D. E. & Joo, T. Vibrational Spectrum of an Excited State and Huang–Rhys Factors by Coherent Wave Packets in Time-Resolved Fluorescence Spectroscopy. *ChemPhysChem* **18**, 670–676 (2017).
185. Kayal, S., Roy, K. & Umapathy, S. Femtosecond coherent nuclear dynamics of excited tetraphenylethylene: Ultrafast transient absorption and ultrafast Raman loss spectroscopic studies. *J. Chem. Phys.* **148**, 024301 (2018).
186. Wang, H. *et al.* Cyano-Substituted Oligo(p-phenylene vinylene) Single Crystals: A Promising Laser Material. *Adv. Funct. Mater.* **21**, 3770–3777 (2011).
187. Qu, S., Lu, Q., Wu, S., Wang, L. & Liu, X. Two dimensional directed π–π interactions in a linear shaped bi-1,3,4-oxadiazole derivative to achieve organic single crystal with highly polarized fluorescence and amplified spontaneous emissions. *J. Mater. Chem.* **22**, 24605–24609 (2012).
188. Wang, K. *et al.* Organic Polymorphs: One-Compound-Based Crystals with Molecular-Conformation- and Packing-Dependent Luminescent Properties. *Adv. Mater.* **26**, 6168–6173 (2014).
189. Okada, D. *et al.* π-Electronic Co-crystal Microcavities with Selective Vibronic-Mode Light Amplification: Toward Förster Resonance Energy Transfer Lasing. *Nano Lett.* **18**, 4396–4402 (2018).
190. Lunt, R. R., Benziger, J. B. & Forrest, S. R. Relationship between Crystalline Order and Exciton Diffusion Length in Molecular Organic Semiconductors. *Adv. Mater.* **22**, 1233–1236 (2010).
191. Parashchuk, O. D. *et al.* Molecular Self-Doping Controls Luminescence of Pure Organic Single Crystals. *Adv. Funct. Mater.* **28**, 1800116 (2018).
192. Zhan, X. *et al.* Fluorenyl-substituted silole molecules: geometric, electronic, optical, and device properties. *J Mater Chem* **18**, 3157–3166 (2008).
193. Gierschner, J., Mack, H.-G., Lüer, L. & Oelkrug, D. Fluorescence and absorption spectra of oligophenylenevinylenes: Vibronic coupling, band shapes, and solvatochromism. *J. Chem. Phys.* **116**, 8596–8609 (2002).
194. Baronas, P. *et al.* Low-Threshold Light Amplification in Bifluorene Single Crystals: Role of the Trap States. *ACS Appl. Mater. Interfaces* **10**, 2768–2775 (2018).
195. Hennebicq, E. *et al.* Exciton Migration in Rigid-Rod Conjugated Polymers: An Improved Förster Model. *J. Am. Chem. Soc.* **127**, 4744–4762 (2005).

196. de Sousa, L. E. *et al.* Role of Exciton Density in Organic Materials: Diffusion Length, Lifetime, and Quantum Efficiency. *Chem. Mater.* (2019) doi:10.1021/acs.chemmater.9b01281.
197. Menke, S. M. & Holmes, R. J. Exciton diffusion in organic photovoltaic cells. *Energy Env. Sci* **7**, 499–512 (2014).
198. Hedley, G. J., Ruseckas, A. & Samuel, I. D. W. Light Harvesting for Organic Photovoltaics. *Chem. Rev.* **117**, 796–837 (2017).
199. Hayashi, K. *et al.* Suppression of roll-off characteristics of organic light-emitting diodes by narrowing current injection/transport area to 50 nm. *Appl. Phys. Lett.* **106**, 093301 (2015).
200. Nakanotani, H., Sasabe, H. & Adachi, C. Singlet-singlet and singlet-heat annihilations in fluorescence-based organic light-emitting diodes under steady-state high current density. *Appl. Phys. Lett.* **86**, 213506 (2005).
201. Dong, H., Zhang, C. & Zhao, Y. S. Host–guest composite organic microlasers. *J. Mater. Chem. C* **5**, 5600–5609 (2017).
202. Zhang, Q. *et al.* Host Exciton Confinement for Enhanced Förster-Transfer-Blend Gain Media Yielding Highly Efficient Yellow-Green Lasers. *Adv. Funct. Mater.* **28**, 1705824 (2018).
203. Lin, J. D. A. *et al.* Systematic study of exciton diffusion length in organic semiconductors by six experimental methods. *Mater. Horiz.* **1**, 280 (2014).
204. Engel, E., Leo, K. & Hoffmann, M. Ultrafast relaxation and exciton–exciton annihilation in PTCDA thin films at high excitation densities. *Chem. Phys.* **325**, 170–177 (2006).
205. Tamai, Y., Ohkita, H., Benten, H. & Ito, S. Exciton Diffusion in Conjugated Polymers: From Fundamental Understanding to Improvement in Photovoltaic Conversion Efficiency. *J. Phys. Chem. Lett.* **6**, 3417–3428 (2015).
206. Shaw, P. E., Ruseckas, A. & Samuel, I. D. W. Exciton Diffusion Measurements in Poly(3-hexylthiophene). *Adv. Mater.* **20**, 3516–3520 (2008).
207. Akselrod, G. M. *et al.* Visualization of exciton transport in ordered and disordered molecular solids. *Nat. Commun.* **5**, (2014).
208. Zhu, T., Wan, Y. & Huang, L. Direct Imaging of Frenkel Exciton Transport by Ultrafast Microscopy. *Acc. Chem. Res.* **50**, 1725–1733 (2017).
209. Salcedo, J. R., Siegman, A. E., Dlott, D. D. & Fayer, M. D. Dynamics of energy transport in molecular crystals: the picosecond transient-grating method. *Phys. Rev. Lett.* **41**, 131 (1978).
210. Rose, T. S., Righini, R. & Fayer, M. D. Picosecond transient grating measurements of singlet exciton transport in anthracene single crystals. *Chem. Phys. Lett.* **106**, 13–19 (1984).
211. Xie, W., Menke, S. M., Frisbie, C. D. & Holmes, R. J. Experimental Characterization of Charge and Exciton Transport in Organic

Semiconductors. in *The WSPC Reference on Organic Electronics: Organic Semiconductors* 231–291 (WORLD SCIENTIFIC, 2016). doi:10.1142/9789813148598_0008.

212. Marciniak, H. *et al.* Photoexcitation dynamics in polyfluorene-based thin films: Energy transfer and amplified spontaneous emission. *Phys. Rev. B* **85**, (2012).
213. Stehr, V., Engels, B., Deibel, C. & Fink, R. F. Anisotropy of singlet exciton diffusion in organic semiconductor crystals from *ab initio* approaches. *J. Chem. Phys.* **140**, 024503 (2014).
214. Meth, J. S., Marshall, C. D. & Fayer, M. D. An examination of radiative and nonradiative excitation transport in thin anthracene crystals: Transient grating experiments. *Solid State Commun.* **74**, 281–284 (1990).
215. Kenkre, V. M., Parris, P. E. & Schmid, D. Investigation of the appropriateness of sensitized luminescence to determine exciton motion parameters in pure molecular crystals. *Phys. Rev. B* **32**, 4946–4955 (1985).
216. Ruseckas, A. *et al.* Singlet energy transfer and singlet-singlet annihilation in light-emitting blends of organic semiconductors. *Appl. Phys. Lett.* **95**, 183305 (2009).
217. King, S. M., Dai, D., Rothe, C. & Monkman, A. P. Exciton annihilation in a polyfluorene: Low threshold for singlet-singlet annihilation and the absence of singlet-triplet annihilation. *Phys. Rev. B* **76**, (2007).
218. Shaw, P. E., Ruseckas, A., Peet, J., Bazan, G. C. & Samuel, I. D. W. Exciton–Exciton Annihilation in Mixed-Phase Polyfluorene Films. *Adv. Funct. Mater.* **20**, 155–161 (2010).
219. Powell, R. C. & Soos, Z. G. Singlet exciton energy transfer in organic solids. *J. Lumin.* **11**, 1–45 (1975).
220. Sun, M.-J. *et al.* Photoluminescent Anisotropy Amplification in Polymorphic Organic Nanocrystals by Light-Harvesting Energy Transfer. *J. Am. Chem. Soc.* **141**, 6157–6161 (2019).
221. Ding, R. *et al.* High-Color-Rendering and High-Efficiency White Organic Light-Emitting Devices Based on Double-Doped Organic Single Crystals. *Adv. Funct. Mater.* **29**, 1807606 (2019).
222. Wu, J.-J. *et al.* Tunable Emission Color and Morphology of Organic Microcrystals by a “Cocrystal” Approach. *Adv. Opt. Mater.* **6**, 1701300 (2018).
223. Dong, H. *et al.* Organic Microcrystal Vibronic Lasers with Full-Spectrum Tunable Output beyond the Franck-Condon Principle. *Angew. Chem.* **130**, 3162–3166 (2018).
224. Tanaka, S. *et al.* Enhancement of the Exciton Coherence Size in Organic Semiconductor by Alkyl Chain Substitution. *J. Phys. Chem. C* **120**, 7941–7948 (2016).

225. Wong, K. F., Bagchi, B. & Rossky, P. J. Distance and Orientation Dependence of Excitation Transfer Rates in Conjugated Systems: Beyond the Förster Theory. *J. Phys. Chem. A* **108**, 5752–5763 (2004).
226. Wang, H. *et al.* Doped Organic Crystals with High Efficiency, Color-Tunable Emission toward Laser Application. *Cryst. Growth Des.* **9**, 4945–4950 (2009).
227. Gierschner, J. & Park, S. Y. Luminescent distyrylbenzenes: tailoring molecular structure and crystalline morphology. *J. Mater. Chem. C* **1**, 5818 (2013).
228. Spano, F. C. & Yamagata, H. Vibronic Coupling in J-Aggregates and Beyond: A Direct Means of Determining the Exciton Coherence Length from the Photoluminescence Spectrum. *J. Phys. Chem. B* **115**, 5133–5143 (2011).
229. van Stokkum, I. H. M., Larsen, D. S. & van Grondelle, R. Global and target analysis of time-resolved spectra. *Biochim. Biophys. Acta BBA - Bioenerg.* **1657**, 82–104 (2004).
230. Stehr, V., Fink, R. F., Engels, B., Pflaum, J. & Deibel, C. Singlet Exciton Diffusion in Organic Crystals Based on Marcus Transfer Rates. *J. Chem. Theory Comput.* **10**, 1242–1255 (2014).
231. Arias, D. H. *et al.* Thermally-Limited Exciton Delocalization in Superradiant Molecular Aggregates. *J. Phys. Chem. B* **117**, 4553–4559 (2013).
232. Baronas, P. *et al.* Enhanced Energy Transfer in Doped Bifluorene Single Crystals: Prospects for Organic Lasers. *Adv. Opt. Mater.* 1901670 (2020) doi:10.1002/adom.201901670.
233. Yamagata, H. & Spano, F. C. Vibronic coupling in quantum wires: Applications to polydiacetylene. *J. Chem. Phys.* **135**, 054906 (2011).
234. Kallinger, C. *et al.* Picosecond amplified spontaneous emission bursts from a molecularly doped organic semiconductor. *J. Appl. Phys.* **91**, 6367–6370 (2002).
235. Gärtner, C., Karnutsch, C., Lemmer, U. & Pflumm, C. The influence of annihilation processes on the threshold current density of organic laser diodes. *J. Appl. Phys.* **101**, 023107 (2007).
236. Chénais, S. & Forget, S. Recent advances in solid-state organic lasers. *Polym. Int.* **61**, 390–406 (2012).
237. Grivas, C. & Pollnau, M. Organic solid-state integrated amplifiers and lasers. *Laser Photonics Rev.* **6**, 419–462 (2012).
238. Yamaguchi, Y., Vacek, G. & Schaefer, H. F. Low-lying triplet electronic states of acetylene:cis3B2 and3A2,trans3Buand3Au. *Theor. Chim. Acta* **86**, 97–113 (1993).
239. Zhao, L. *et al.* Singlet-Triplet Exciton Annihilation Nearly Suppressed in Organic Semiconductor Laser Materials Using Oxygen as a Triplet Quencher. *IEEE J. Sel. Top. Quantum Electron.* **22**, 26–34 (2016).

240. Kéna-Cohen, S. *et al.* Plasmonic Sinks for the Selective Removal of Long-Lived States. *ACS Nano* **5**, 9958–9965 (2011).
241. Jiang, Y. *et al.* Low-Threshold Organic Semiconductor Lasers with the Aid of Phosphorescent Ir(III) Complexes as Triplet Sensitizers. *Adv. Funct. Mater.* **29**, 1806719 (2019).
242. Kirch, A., Gmelch, M. & Reineke, S. Simultaneous Singlet–Singlet and Triplet–Singlet Förster Resonance Energy Transfer from a Single Donor Material. *J. Phys. Chem. Lett.* **10**, 310–315 (2019).
243. Hertel, D., Bässler, H., Guentner, R. & Scherf, U. Triplet-triplet annihilation in a poly(fluorene)-derivative. *J. Chem. Phys.* **115**, 10007–10013 (2001).
244. Wallikewitz, B. H., Kabra, D., Gélinas, S. & Friend, R. H. Triplet dynamics in fluorescent polymer light-emitting diodes. *Phys. Rev. B* **85**, 045209 (2012).

PAULIUS BARONAS | CV

Birthdate	1990/06/29
Email	Paulius.baronas@ff.vu.lt; Paulius.baron@gmail.com

EDUCATION

2015 - 2019
PhD in Physics
Vilnius University, Institute of Photonics and Nanotechnology

2013 - 2015
Master‘s degree in Materials Technology
Vilnius University, Department of Physics
Studies: Optoelectronic Material and Technology
Thesis: Ultrafast dynamics of photo induced electron transfer in iron complex based solar cells. Supervised by Prof. Villy Sundström (Lund University)

2009 - 2013
Bachelor’s degree in Physics
Vilnius University, Department of Physics
Studies: Nuclear Energy Physics
Thesis: Multifunctional carbazole and fluorene derivatives for OLED applications. Supervised by Prof. Saulius Juršėnas.

RESEARCH / WORK EXPERIENCE

2013 - Present
Junior researcher
Vilnius University, Institute of Photonics and Nanothechnology

September – November 2018
Visiting researcher
Murdoch university, Department of Physics, Perth, Australia.
Two month internship based on Lithuanian research council grant.
Supervisor: Almantas Pivrikas
Research topic: Investigation charge carrier transport in organic single crystals employing photo-current measurements.

January 2015 - May 2015
Visiting researcher
Lund University, Department of Chemical Physics, Lund, Sweden.
Four month internship based on Erasmus+ exchange programme
Research topic: Investigation of charge transfer mechanisms in Dye sensitized solar cell (DSSC) employing ultrafast transient absorption („pump-probe“) spectroscopic technique.

January - June 2014
Visiting researcher
Lund University, Department of Chemical Physics, Lund, Sweden.
Five month internship based on Erasmus+ exchange programme
Supervisor: Arkady Yartsev
Research topic: Time resolved photoluminescence study of charge generation, transfer and recombination in bulk-heterojunction (BHJ) polymer solar cells.

June – September 2012	Student intern Vilnius University, Department of Semiconductor Physics Two month research project based on national initiative „Promotion of Students' Scientific Activities“ by the Research Council of Lithuania Supervisor: Saulius Juršėnas Research topic: Luminescent carbazole and fluorene derivatives for optoelectronic applications

PARTICIPATION IN SCIENTIFIC PROJECTS

2018 - Present	“Development of advanced optoelectronic materials via smart molecular engineering”, SMART, The Research Council of Lithuania (2018-2022). Junior researcher for conducting ultrafast spectroscopy measurements on potential organic laser materials.
2018 - Present	“Triplet state engineering in organic optoelectronics compounds”, Global Grant, The Research Council of Lithuania (2018-2022). Junior researcher for conducting time-resolved spectroscopic measurements on potential organic triplet-converting materials.
2017 - Present	“Light up-conversion efficiency enhancement in organic thin films for optoelectronic applications”, Researcher teams' projects, The Research Council of Lithuania (2017 - 2020). Engineer for conducting time-resolved spectroscopic measurements on potential organic triplet-converting materials.
2015 – 2017	“Towards organic laser transistor", Lithuania – Japan scientific research programme, The Research Council of Lithuania (2015 - 2017). Engineer for conducting ultrafast spectroscopy measurements on potential organic laser materials.
2014 - 2015	“Control of the photo-physical properties of multifunctional molecular systems” Global Grant, The Research Council of Lithuania (2012-2015). Engineer for conducting time-resolved spectroscopic measurements on potential organic triplet-converting materials.
2013 - 2015	“Flexible structure bearing bifluorene compounds for optoelectronics industry, BiFluorenas“, EU structural funds (2013-2015). Engineer for conducting spectroscopic measurements on potential organic laser materials.

AWARDS

Best contributed talk in the field of semiconductors (Open Readings 2017)

PUBLICATIONS

I. **P. Baronas**, K. Kazlauskas, G. Kreiza, V. Jankauskas, A. Tomkevičienė, J. Simokaitienė, J. V. Grazulevicius, S. Juršėnas, "Differently linked fluorene-carbazole triads for light amplification", *Dyes and Pigments*, 123, 370-379 (2015).

II. G. Kreiza, **P. Baronas**, E. Radiunas, P. Adomėnas, O. Adomėnienė, K. Kazlauskas, J. C. Ribierre, C. Adachi, S. Juršėnas, "Bifluorene single crystals with extremely low-threshold amplified spontaneous emission", *Adv. Opt. Mater.* 5, 1600823 (2017).

III. **P. Baronas**, G. Kreiza, P. Adomėnas, O. Adomėnienė, K. Kazlauskas, C. Adachi and S. Juršėnas, "Low-Threshold Light Amplification in Bifluorene Single Crystals: Role of the Trap States", *ACS Appl. Mater. Interfaces* 10, 2768-2775 (2018).

IV. **P. Baronas**, P. Ščajev, V. Čerkasovas, G. Kreiza, P. Adomėnas, O. Adomėnienė, K. Kazlauskas, J. C. Ribierre, C. Adachi and S. Juršėnas, "Exciton Diffusion in Bifluorene Single Crystals Studied by Light Induced Transient Grating Technique", *Appl. Phys. Lett.* 112, 033302 (2018).

V. **P. Baronas**, G. Kreiza, M. Mamada, S. Maedera, P. Adomėnas, O. Adomėnienė, K. Kazlauskas, C. Adachi and S. Juršėnas, "Enhanced energy transfer in doped bifluorene single crystals: prospects for organic lasers", *Adv. Opt. Mater.* 1901670 (2019).

NOTES

NOTES

Vilniaus universiteto leidykla
Saulėtekio al. 9, LT-10222 Vilnius
El. p. info@leidykla.vu.lt,
www.leidykla.vu.lt
Tiražas 30 egz.